



TECHNISCHE  
UNIVERSITÄT  
WIEN

DISSERTATION

# Demonstrator System for the Phase-I Trigger Readout Upgrade of the ATLAS Liquid Argon Calorimeter at the LHC

ausgeführt zum Zwecke der Erlangung des akademischen Grades  
einer Doktorin der Naturwissenschaften unter Leitung von

Univ.-Doz. Dr.techn. Dipl.-Ing. Claudia-Elisabeth Wulz

E141

Technische Universität Wien

eingereicht an der Technischen Universität Wien  
Fakultät für Physik

von

Mag. rer. nat. Adriana Milic

Matrikelnummer 0601928

[milic.adriana@gmail.com](mailto:milic.adriana@gmail.com)

37 rue de Geneve, F-01630 Saint Genis-Pouilly

Genf, am 28. August 2016



# Contents

<b>Kurzfassung</b>	<b>viii</b>
<b>Abstract</b>	<b>x</b>
<b>1 Introduction</b>	<b>13</b>
<b>2 A Toroidal LHC Apparatus - ATLAS</b>	<b>16</b>
2.1 Structure of the ATLAS detector . . . . .	16
2.2 Inner detector . . . . .	16
2.3 Calorimetry . . . . .	18
2.4 Muon system . . . . .	19
2.5 Magnet system . . . . .	21
2.6 Trigger system . . . . .	22
2.7 Data acquisition . . . . .	24
2.8 The ATLAS coordinate system . . . . .	24
<b>3 The Liquid Argon Calorimeter in ATLAS</b>	<b>26</b>
3.1 Calorimeters . . . . .	26
3.2 Physics of calorimetry . . . . .	26
3.2.1 Energy measurement . . . . .	26
3.2.2 Electromagnetic showers . . . . .	28
3.2.2.1 Bremsstrahlung . . . . .	28
3.2.2.2 Pair production . . . . .	29
3.2.2.3 Photoelectric effect . . . . .	29
3.2.2.4 Rayleigh and Compton scattering . . . . .	29
3.2.3 Radiation length . . . . .	30
3.2.4 Performance of the LAr calorimeter . . . . .	30
3.3 Structure of the ATLAS calorimeters . . . . .	30
3.3.1 Barrel calorimeter . . . . .	32
3.3.2 Barrel presampler . . . . .	32
3.3.3 Granularity of the samplings . . . . .	33
3.4 Electronic signal processing . . . . .	34
3.4.1 Readout electrodes . . . . .	34
3.4.2 Shaping, pile-up and electronics noise . . . . .	35
3.4.3 Electronics calibration . . . . .	37
3.4.4 Temperature and purity monitoring . . . . .	37
3.5 Readout and trigger system . . . . .	38
3.6 Front end electronics . . . . .	38
3.7 Back end electronics . . . . .	39
3.8 L1-Trigger readout . . . . .	40

<b>4</b>	<b>The Trigger Readout Phase-I Upgrade of the ATLAS Liquid Argon Calorimeter</b>	<b>43</b>
4.1	Physics requirements and expected performance . . . . .	43
4.1.1	Super Cell energy reconstruction . . . . .	44
4.1.2	Super Cell energy resolution . . . . .	44
4.1.3	Level-1 trigger performance studies . . . . .	45
4.1.3.1	Shower shape analysis . . . . .	45
4.1.3.2	Multi-dimensional optimization of shower shape variables . . . . .	46
4.1.3.3	Photon performance . . . . .	47
4.1.3.4	Expected trigger rates . . . . .	48
4.1.4	Impact on Higgs physics and other physics channels . . . . .	48
4.1.4.1	$H \rightarrow \tau\tau$ . . . . .	48
4.1.4.2	$H \rightarrow b\bar{b}$ in associated $(W/Z)H$ production . . . . .	50
4.1.4.3	$H \rightarrow WW^*$ . . . . .	50
4.1.4.4	Diboson and Triboson production and quartic couplings . . . . .	51
4.1.4.5	Supersymmetric (SUSY) particles . . . . .	51
4.2	Implementation of the upgrade of the trigger readout system . . . . .	52
4.3	Front end electronics . . . . .	52
4.3.1	Modifications to the front end crate . . . . .	53
4.3.2	LTDB . . . . .	54
4.3.2.1	Analogue signal treatment . . . . .	54
4.3.2.2	Digital signal treatment . . . . .	55
4.3.2.3	Power supply . . . . .	56
4.4	Back end electronics . . . . .	56
4.4.1	Introduction . . . . .	56
4.4.2	LDPS electronics components . . . . .	57
4.4.3	LDPB board pre-prototype . . . . .	58
4.4.4	Data flow through the back end system . . . . .	58
4.4.5	Firmware on AMC . . . . .	59
4.5	Towards the ATLAS LAr calorimeter Phase-II upgrade . . . . .	59
<b>5</b>	<b>Bunch-crossing Multiplexing studies</b>	<b>63</b>
5.1	Introduction . . . . .	63
5.2	Implementation of BCMUX . . . . .	64
5.3	Simplified BCMUX algorithm . . . . .	65
5.3.0.1	Profile of probability for electrons . . . . .	66
5.3.0.2	Profile of probability for jets . . . . .	66
5.3.0.3	Effect on $R_\eta$ . . . . .	67
5.3.0.4	Different quantizations for electrons . . . . .	67

<b>6</b>	<b>Demonstrator System tests</b>	<b>70</b>
6.1	Test setup . . . . .	70
6.2	Data taking . . . . .	72
6.3	Measurements . . . . .	73
6.3.1	Total noise and coherent noise . . . . .	73
6.3.2	Autocorrelation matrix . . . . .	74
6.3.3	Cross-talk on trigger readout . . . . .	74
6.4	Tests of the current readout system . . . . .	74
6.4.1	Results for main readout . . . . .	75
6.4.1.1	Total noise per channel . . . . .	75
6.4.1.2	Coherent noise . . . . .	75
6.4.2	Results for trigger readout . . . . .	75
6.4.2.1	Total noise . . . . .	75
6.4.2.2	Correlation coefficient between trigger towers . . . . .	79
6.4.2.3	Cross-talk . . . . .	79
6.5	Tests of the upgraded trigger readout . . . . .	79
6.5.1	Results for main readout . . . . .	81
6.5.1.1	Total noise per channel . . . . .	81
6.5.1.2	Coherent noise . . . . .	81
6.5.2	Results for Trigger Readout . . . . .	84
6.5.2.1	Total noise . . . . .	84
6.5.2.2	Correlation coefficient between trigger towers . . . . .	84
6.5.2.3	Cross-talk . . . . .	87
6.5.2.4	Linearity and saturation point of trigger receiver output . . . . .	87
6.5.2.5	Measurements with different LTDB configurations . . . . .	90
6.6	Functionality of the BNL LTDB . . . . .	90
6.7	Measurements with the Saclay/LAL LTDB . . . . .	92
6.8	Conclusions on demonstrator tests . . . . .	92
6.9	Installation of the demonstrator system in ATLAS . . . . .	93
6.10	Tests of the demonstrator system in ATLAS . . . . .	94
6.10.1	Connectivity . . . . .	94
6.10.2	Total noise on main readout and trigger readout path . . . . .	94
6.10.3	Coherent noise fraction . . . . .	96
6.10.4	Total noise and pedestal on LTDB . . . . .	96
6.10.5	Amplitude shapes . . . . .	96
6.10.6	Conclusion on demonstrator installation . . . . .	98
<b>7</b>	<b>Calibration of the Demonstrator System</b>	<b>99</b>
7.1	Calibration system in ATLAS . . . . .	99
7.2	Data encoding . . . . .	100
7.2.1	Header formats . . . . .	101
7.3	Energy reconstruction of a calorimeter cell . . . . .	102
7.3.1	Principle of energy reconstruction . . . . .	102
7.3.2	Optimal Filtering Coefficients computation . . . . .	102

7.3.3	Conversion of signal amplitude to energy . . . . .	105
7.3.3.1	Electronic gain . . . . .	105
7.3.3.2	Sampling fraction . . . . .	106
7.3.3.3	Current to energy conversion factor . . . . .	106
7.3.4	Electronics calibration . . . . .	106
7.3.4.1	Pedestal run . . . . .	107
7.3.4.2	Ramp run . . . . .	107
7.3.4.3	Delay run . . . . .	107
7.4	Athena framework . . . . .	108
7.5	LAr calorimeter reconstruction software . . . . .	108
7.5.1	Event data objects . . . . .	108
7.5.2	Implementation . . . . .	109
7.6	Demonstrator data format . . . . .	110
7.7	Athena byte stream converter . . . . .	110
7.8	Calibration runs for demonstrator system . . . . .	111
7.9	Obtained calibration constants . . . . .	112
<b>8</b>	<b>Physics runs with the demonstrator system</b>	<b>115</b>
8.1	Trigger coverage . . . . .	115
8.2	Proton-proton runs . . . . .	115
<b>9</b>	<b>Impact of an Extended ATLAS Tracker on <math>W^\pm W^\pm</math> Vector Boson Scattering at a High-Luminosity LHC</b>	<b>119</b>
9.1	Vector boson scattering at the HL-LHC . . . . .	119
9.2	Theoretical overview of vector boson scattering . . . . .	119
9.2.1	Same-sign $W^\pm W^\pm$ scattering . . . . .	120
9.2.2	Backgrounds . . . . .	121
9.3	LHC and ATLAS ITk upgrade . . . . .	123
9.4	Monte Carlo simulation . . . . .	123
9.4.1	Sample generation . . . . .	123
9.4.2	Upgrade Smearing Functions . . . . .	123
9.4.3	Event selection . . . . .	124
9.4.4	The significance method . . . . .	125
9.5	Object validation . . . . .	126
9.5.1	Leptons . . . . .	126
9.5.2	Jets and $E_T^{miss}$ . . . . .	128
9.5.3	Pile-up subtraction . . . . .	128
9.6	Performance studies . . . . .	129
9.6.1	Leptons . . . . .	129
9.6.2	Additional leptons . . . . .	129
9.6.3	Jets . . . . .	132
9.6.4	Pile-up . . . . .	132
9.6.5	Pile-up suppression . . . . .	134
9.7	Results . . . . .	134

10 Conclusions	141
References	cxlii
Acknowledgements	cxlvii
Curriculum Vitae	cxlix

## Kurzfassung

ATLAS ist einer von zwei Mehrzweckdetektoren am Large Hadron Collider (LHC), dem großen Hadronenspeicherring am CERN (Europäische Organisation für Teilchenphysik), der darauf ausgelegt wurde, ein breites Spektrum an physikalischen Phänomenen zu ergründen, angefangen von Extradimensionen und Dunkler Materie, Supersymmetrie und anderen Szenarien jenseits des Standardmodells, bis zum Higgs Boson, das 2012 entdeckt wurde.

Der LHC ist ein Teilchenbeschleuniger, der Protonen mit Protonen bei einer Schwerpunktenenergie von bis zu 14 TeV zur Kollision bringt. Er wird Spitzenluminositäten von  $\mathcal{L} \approx 5 - 7 \times 10^{34} \text{cm}^{-2}\text{s}^{-1}$  im Zuge der Aufrüstung zum High-Luminosity LHC (HL-LHC), die um 2026 geplant ist, erreichen.

Eine Aufrüstung der Experimente am LHC ist ebenfalls im Gange. Die erste Aufrüstungsphase (Phase-I), die auch das Hauptthema dieser Dissertation ist, ist teilweise beendet. Diese erlaubt ATLAS, die bisherige Sensitivität gegenüber neuen physikalischen Phänomenen trotz höherer Luminosität und kontinuierlich schwieriger werdenden experimentellen Bedingungen beizubehalten. Insbesondere ist es wichtig, ähnliche Schwellenwerte des Triggers für Energie und Impuls beizubehalten. Das wird durch die Erhöhung der Granularität der Kalorimeter Level-1 Triggersysteme und dem Hinzufügen neuer Müonentrigger und Spurdetektoren in der Region hoher Rapidität erreicht. Präzisionsmessungen der Kopplungen des Higgs Bosons, sowie die Suche nach supersymmetrischen oder anderen Teilchen ist in einem großen Teil des Phasenraums auf die effiziente Selektion von Leptonen mit niedrigem Transversalimpuls angewiesen. Zusätzlich wird eine Reihe von Detektoren, die in dem Bereich sehr hoher Rapidität installiert werden, es erlauben, auch Ereignisse in dieser Region zu messen.

Das ATLAS Experiment verwendet ein ausgeklügeltes System für den Trigger und die Datenerfassung bei der Datennahme. Der Trigger wählt die Ereignisse aus, die dauerhaft gespeichert und für Physikanalysen verwendet werden. Die anfängliche Rate von 40 MHz wird nach zahlreichen Zwischenstufen auf 100 – 200 Hz reduziert und gespeichert. Mit der Aufrüstung von ATLAS muss auch das Triggersystem verbessert werden, um das volle Potential des LHC ausschöpfen zu können und um nicht Ereignisse, die dem Auffinden interessanter Physik dienen könnten, zu verlieren.

Diese Dissertation stellt die Aufrüstung des ATLAS Flüssigargon-Kalorimeters (LAr) im Rahmen der Phase-I dar. Deren Ziel ist es, Daten höherer Granularität, Auflösung und mit longitudinaler Information von Teilchenschauern für die Level-1 Triggerprozessoren bereitzustellen. Die Aufrüstung wird die Energieauflösung des Triggersystems und die Selektionseffizienz für Elektronen, Photonen,  $\tau$ -Leptonen,



Teilchenjets und für fehlende Transversalenergie erhöhen und gleichzeitig die Unterdrückung von überlagerten Ereignissen niedriger Energie und mit niedrigem Transversalimpuls (Pile-Up) verbessern.

Um das neue System für die Phase-I Aufrüstung bereits in diesem Abschnitt der Datennahme testen zu können, wurde im Rahmen dieser Dissertation ein Prototyp in einem kleinen Teil von ATLAS eingebaut, der parallel zu dem jetzigen System läuft. Auf diese Weise konnten bereits zahlreiche Untersuchungen durchgeführt werden, wie beispielsweise der Vergleich von Ereignissen, die von dem alten und dem neuen System gemessen wurden.

Der zweite Teil dieser Arbeit beinhaltet die Ergebnisse der Evaluierung der möglichen Auswirkungen von mehreren Verbesserungsszenarien des Spurdetektors von ATLAS für den HL-LHC auf die elektroschwache Streuung von  $WW$  Vektorbosonen mit gleicher Ladung. Die Evaluierung dient der Optimierung der Phase-II Projekte. Das Ergebnis unterstreicht die Wichtigkeit der Rekonstruktion von Teilchenjets in der Region hoher Rapidität bei einem Szenario mit im Mittel bis zu 200 Wechselwirkungen pro LHC Teilchenstrahl-Kreuzung. Somit liefert dieser Zerfallskanal ein gutes Argument, die derzeitigen Pläne des ATLAS Spurdetektors auszudehnen. Diese Analyse ist ein hervorragender Maßstab für den Nutzen der Aufrüstungsszenarien der Phase-II, insbesondere für jene im Bereich hoher Rapidität.

## Abstract

ATLAS is one of the two general-purpose detectors at the Large Hadron Collider (LHC), designed to search for a large range of physics phenomena, from extra dimensions and dark matter, supersymmetry and other beyond standard model scenarios, to the Higgs boson, which was discovered in 2012.

The LHC is a particle accelerator providing proton-proton collisions at centre-of-mass energies of up to 14 TeV, which will reach peak instantaneous luminosities of  $\mathcal{L} \approx 5 - 7 \times 10^{34} \text{cm}^{-2}\text{s}^{-1}$  in the course of its planned high-luminosity (HL-LHC) upgrade which will be completed around 2026.

Upgrades of the experiments are also under way. The Phase-I upgrade, part of which is the main topic of this thesis, is already partially terminated. It will allow ATLAS to keep its sensitivity for new physics phenomena in spite of the growing luminosity and thus more challenging experimental conditions. In particular, similar momentum or energy trigger thresholds as during the first running period of the LHC may be maintained. This is achieved by increasing the granularity of the calorimeter Level-1 trigger systems and by introducing new muon trigger and tracking detectors in the forward direction. Precision measurements of the couplings of the Higgs boson, as well as searches for supersymmetric or other particles in a large region of the parameter space, rely on the capability of efficiently selecting leptons with low transverse momenta. Additionally, a new set of very far forward detectors will enable ATLAS to explore events with signatures of jets or leptons in the high rapidity region.

The ATLAS experiment records data using a sophisticated trigger and data acquisition system. The trigger selects collision events for permanent storage and physics analysis. The initial rate of 40 MHz is reduced in several stages to 100-200 Hz of data which is saved. With the upgrade of ATLAS, the trigger system needs to be upgraded as well, in order to make full use of the LHC's potential and not to lose events interesting for physics.

This thesis presents the ATLAS Liquid Argon (LAr) calorimeter Phase-I upgrade whose objective is to provide higher-granularity, higher-resolution and longitudinal shower shape information from the calorimeter to the Level-1 trigger processors. The upgrade will improve the trigger energy resolution and efficiency for selecting electrons, photons,  $\tau$  leptons, jets and missing transverse momentum, while enhancing discrimination against underlying events with low energy and transverse momentum (pile-up). In order to be able to test the Phase-I upgrade system already in the current data taking period of the LHC, in the framework of this thesis a demonstrator system was installed in a small part of the ATLAS detector, running in parallel with the legacy trigger readout. In this way, several

measurements could already be performed on the new system, as matching events measured by the currently employed ATLAS Level-1 trigger to events measured by the new system.

The second part of the thesis presents results of an evaluation of the potential impact of several ATLAS Inner Tracker upgrade scenarios for the HL-LHC on the electroweak same-sign  $WW$  vector boson scattering channel, intended to aid the optimization of the Phase-II upgrade projects.

The outcome emphasizes the importance of forward jet reconstruction in case of high pile-up scenarios of up to an average of 200 superimposed interactions per LHC beam crossing. Hence, this channel provides a strong argument to expand the plans of the current Inner Tracker upgrade.

This analysis provides an excellent measure for the benefit of several Phase-II upgrade scenarios, particularly in the forward region.



# 1 Introduction

One of the objectives in physics today is to explain and possibly unify all fundamental forces. The Standard Model of particle physics [1, 2, 3], whose ingredients are fermions, gauge bosons, and the Higgs boson [4, 5], provides a description of three of these forces - the strong, the weak and the electromagnetic one. Gravity is not described by the Standard Model, and so are many other observed phenomena which indicates that the Standard Model, although a very successful quantum field theory, is not complete. It neither explains for example why there are exactly three generations of quarks and leptons, nor is it able to accommodate neutrino masses, dark matter, and dark energy, and it relies on several input parameters whose values cannot be derived from fundamental principles.

CERN (European Organisation for Nuclear Research) is one of the experimental institutions, whose task it is to study the predictions of mathematical models such as the Standard Model and find hints for a more comprehensive theory which can clarify the questions we are still faced with. CERN is home of the LHC [6], the world's most powerful particle accelerator.

The ATLAS detector is designed to perform a wide variety of measurements, from Standard Model measurements to precision measurements of the properties of the Higgs boson, new exotic and supersymmetrical particles. It has been constructed at the LHC, located underground in a large cavern excavated at one of the LHC's intersection points (Figure 1). The LHC currently delivers peak luminosities of  $2 - 3 \times 10^{34} \text{cm}^{-2}\text{s}^{-1}$  and with a bunch spacing of 25 ns the collision rate is 40 MHz.

The other big detectors located at the LHC are ALICE [7], LHCb [8], and CMS [9], with CMS also being an all-purpose detector like ATLAS. In order for ATLAS to be able to reconstruct the full range of particles and missing transverse energy ( $E_T^{\text{miss}}$ ) from undetected particles, maximum possible coverage and minimum energy loss through crack regions must be ensured. For feasible storage, the data rate is reduced by the ATLAS three-level trigger system. During a run, for every event a rapid decision whether the data should be stored, is made. The data is distributed and analysed around the world with the computing grid [10].

From 2009-2013 (Run 1), the LHC was operating at 70% of the nominal luminosity and delivered in total  $30 \text{fb}^{-1}$  of integrated luminosity to ATLAS and CMS. The first long shut down (LS1, Phase-0), during which a big part of the work for this thesis was accomplished, the Phase-I demonstrator for the electromagnetic calorimeter of ATLAS was installed. In Run 2, which started in February 2015 and is still ongoing, the LHC is working at nominal luminosity. Run 2 is expected to finish in 2018 and will be followed by another long shut down (LS2, Phase-I), in which several upgrade systems will be installed on the detector for Run 3 (2020-2023). After Run 3 the installations for the HL-LHC will take place where the LHC is expected to reach a luminosity of up to  $5 \times 10^{34} \text{cm}^{-2}\text{s}^{-1}$ .

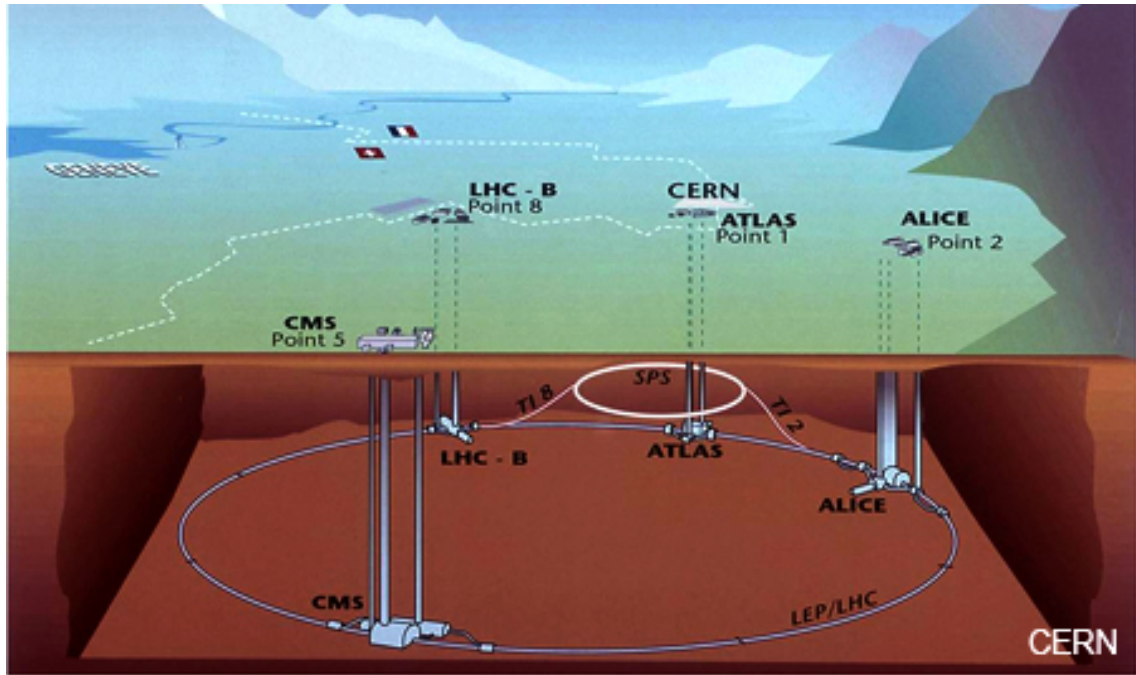


Figure 1: The LHC is contained in a circular tunnel, with a circumference of 27 kilometres and at a depth ranging from 50 to 175 metres underground.

In Figure 2 the detailed schedule of the LHC is shown.

This thesis is structured in the following way:

Chapter 2 introduces the ATLAS detector and its main sub-detectors. The magnet system, trigger system and data acquisition are described as well.

In Chapter 3 a detailed description of the LAr calorimeter of ATLAS is given. A summary of the performance of LAr is discussed and the main components of the front and back end electronics are introduced.

Chapter 4 describes the idea and purpose of the ATLAS LAr calorimeter Phase-I upgrade. The expected performances and requirements are studied and the upgraded electronic components are discussed.

A bandwidth reduction study completed for the upgraded system is explained in Chapter 5.

In Chapter 6 detailed results of the tests of the upgraded system before the installation on ATLAS are given. The installation on the detector is described briefly and first calibration data taken with the demonstrator are presented.

# LHC / HL-LHC Plan

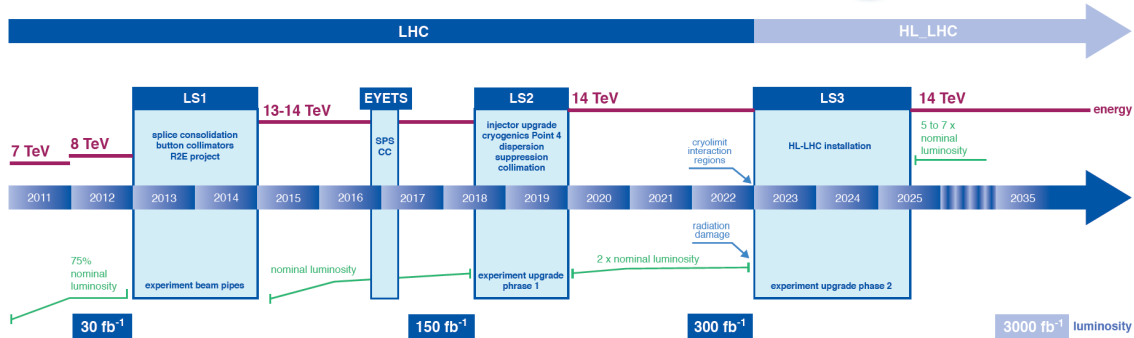


Figure 2: The LHC schedule up to the HL-LHC. [11]

Chapter 7 describes the framework and data format necessary to calibrate the demonstrator system with the existing ATLAS offline software reconstruction tools.

First results from data taken with the demonstrator during physics runs are given in Chapter 8. ATLAS and demonstrator events have been matched in order to draw comparisons of the data taken.

Chapter 9 presents a study completed for the ATLAS Phase-II upgrade. The impact of several scenarios for a future upgraded ATLAS Inner Tracker is evaluated for the electroweak production of same-electric-charge WW scattering events at the HL-LHC at  $\sqrt{s} = 14$  TeV.

## 2 A Toroidal LHC Apparatus - ATLAS

### 2.1 Structure of the ATLAS detector

ATLAS has a cylindrical shape, it is 25 m in diameter and 44 m long. It weighs approximately 7000 tons. The structure of the detector can be seen in Figure 3.

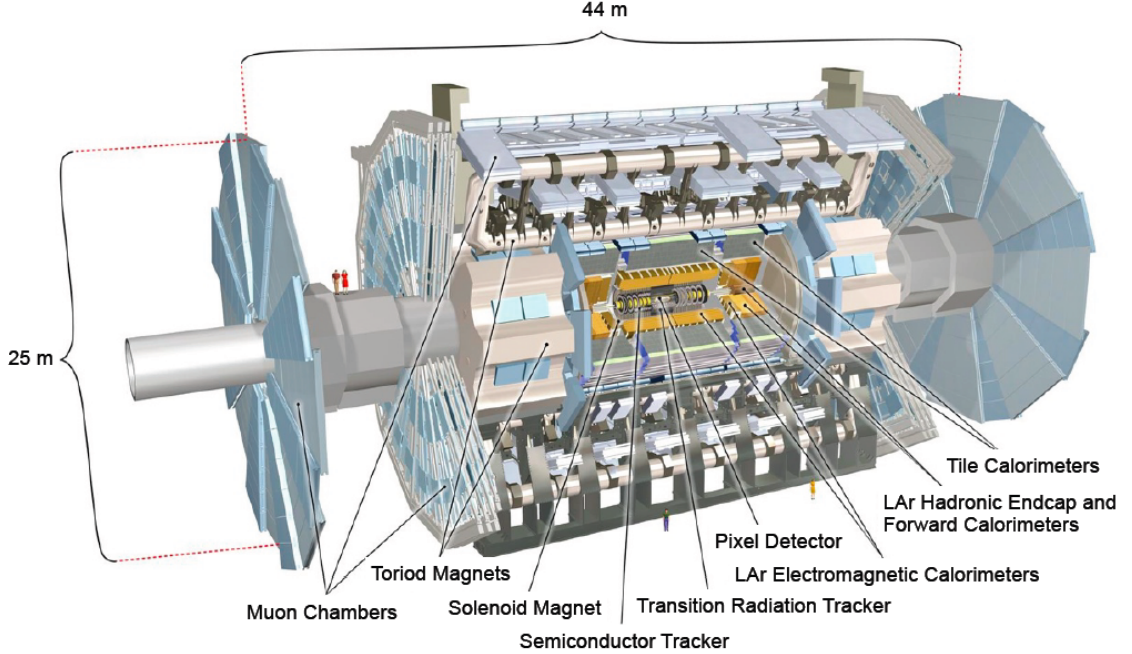


Figure 3: A schematic drawing of the ATLAS detector is shown in this picture [12].

The detector consists of three major components: the inner detector (ID) or tracker, the calorimeters and the muon system. The tracker is surrounded by a superconducting solenoid and for the muon system there are a barrel and an endcap toroid outside the calorimeter system.

### 2.2 Inner detector

The ID covers a pseudorapidity range of  $|\eta| < 2.5$  and performs particle tracking in order to measure particle transverse momentum and trajectories. The high momentum resolution and precision pattern recognition enables the reconstruction of both primary and secondary vertices [13]. As shown in Figure 4, the three sub-detectors of the ID are the Pixel Detector (PD) [14], the Semiconductor Tracker (SCT) [15], and the Transition Radiation Tracker (TRT) [16]. Closest to the beam pipe a new detector was inserted during Phase-0, the Insertable Barrel Layer (IBL) detector [17].

The PD lies closest to the beam pipe and consists of three layers parallel to the beam within the barrel region and three disks perpendicular to the beam in the endcap region. The PD reads out pixels of  $50 \mu\text{m} \times 400 \mu\text{m}$  size. It has 80 million



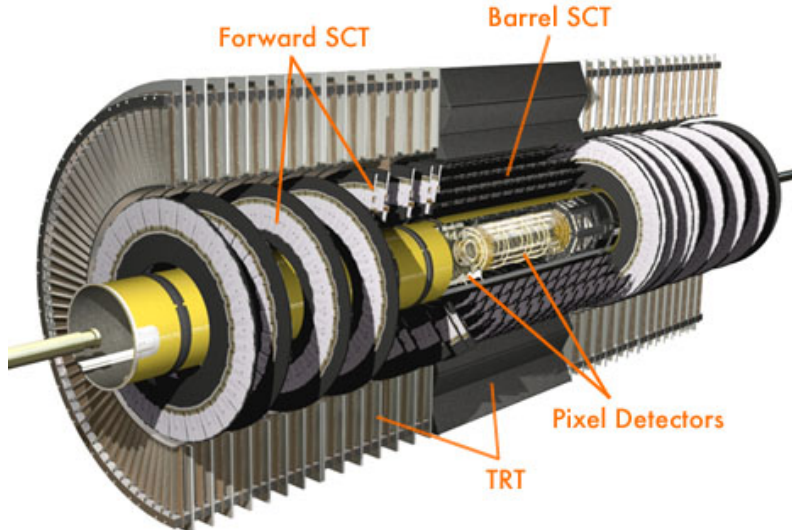


Figure 4: Cut-away view of the ATLAS inner detector without the IBL detector which was added during Phase-0.

channels and 1744 modules. Each module consists of 47232 pixels and is around  $250 \mu\text{m}$  thick.

The PD and the SCT are silicon detectors. When a charged particle passes through, the number of electron-hole pairs created in the silicon is proportional to the deposited energy. The holes drift because of the applied voltage towards the cathode, where the current is collected and amplified. If the signal is above a certain threshold, a hit is recorded with the location of the pixel and a timestamp. By joining multiple hits, the path of the particle can be reconstructed and its origin and momentum can be calculated.

The SCT is placed outside the PD and is built up of a barrel made of four cylinders and two endcaps which contain nine disks each. In total there are 6.3 million readout channels in the SCT. It is built up of readout strips of  $80 \mu\text{m}$  pitch each.

The TRT is placed outside the SCT and has a coverage of up to  $|\eta| < 2$ . It is made of drift tubes (straws) which can operate at high rates due to their small diameter and the isolation of the sense wires within individual gas volumes. Xenon gas is used to detect transition radiation photons created in a radiator between the straws. Each straw is 4 mm in diameter and equipped with a  $30 \mu\text{m}$  diameter gold-plated Tungsten-Rhenium wire. In the barrel, the drift tubes are parallel to the beam while in the endcap they are arranged radially. Highly relativistic electrons are likely to emit transition radiation when crossing the boundary between media with different dielectric constants in the TRT, while more massive particles like pions emit less transition radiation. This fact is used to improve electron identification.

In addition to the transition radiation, a charged particle ionises the gas within a straw and creates an electric signal which is used for tracking. The drift time of the ionisation radiation is longer than the one of the transition radiation. Hence, these

two types of radiation can be separated. In order to allow proper separation, the drift time is also measured. Although the TRT is around ten times less accurate than the PD and the SCT, it contributes significantly to the momentum measurement. That is because on the one hand, the TRT covers the largest area in radius within the tracking system and on the other hand, collects up to 36 hits per track which is possible because of the layout of the straws.

As mentioned before, a new detector, the IBL, was added to the ATLAS tracking system in Phase-0. It was only possible to integrate it by shrinking the diameter of the beam pipe. The insertion gap between the inner supporting tube of the beam pipe and the IBL detector is only 0.2 mm and the gap between the supporting tube and the PD is 1.9 mm. With higher luminosity in Run 2, significant radiation damage of the inner layers of the detector will occur, which means that ATLAS would have had significant losses in its tracking efficiency. The idea was to minimize risks by creating an insertable layer instead of replacing the existing B-layer, the innermost layer of the PD. A schematic drawing of the IBL can be seen in Figure 5.

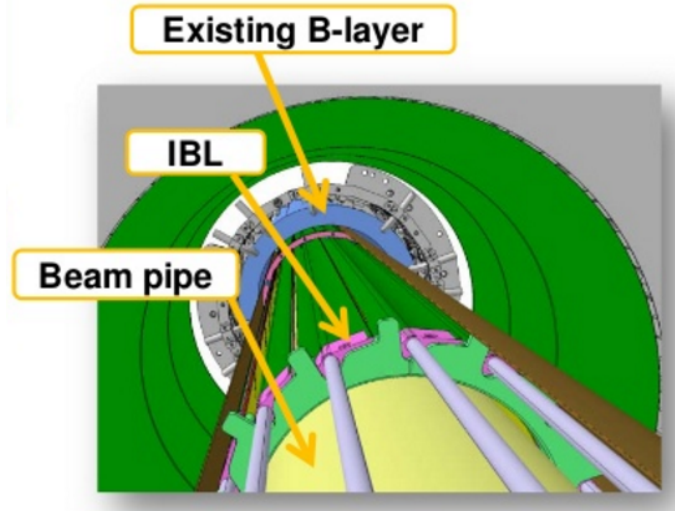


Figure 5: A schematic view of the PD, the IBL and the beam pipe [18].

## 2.3 Calorimetry

The ATLAS calorimeters are designed to measure the energy and position of electromagnetically interacting particles such as electrons and photons and hadronically interacting particles such as pions and others producing for example jets, to give an accurate estimation of the  $E_T^{\text{miss}}$  and to contribute to the particle identification [19].

The ATLAS calorimetry system consists of several sub-detectors, all fully symmetric in  $\phi$ . They are designed to measure energy deposits of both charged and neutral particles within  $|\eta| < 4.9$ . The structure of the ATLAS calorimeters is shown in Figure 6.

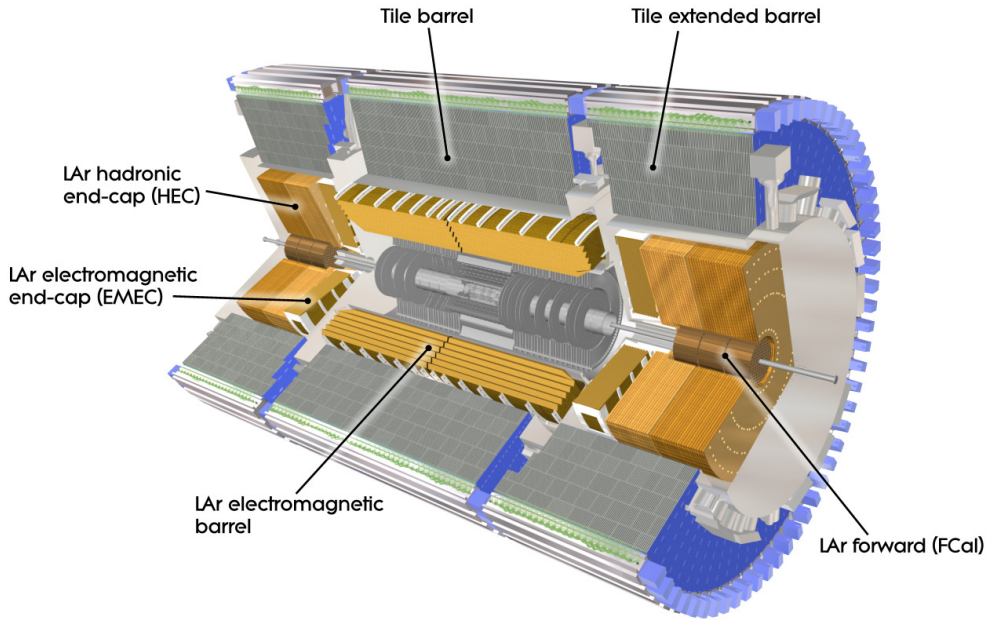


Figure 6: Cut-away view of the ATLAS calorimeter system.

All ATLAS calorimeters are sampling calorimeters. Thus, absorber sheets generating particle showers are alternated with layers of active material to perform energy measurements.

An incident particle produces showers in stages, losing energy until the shower is completely absorbed. By summing up all the energy within the concerned calorimeter volume, the initial energy of the particle can be measured. In the electromagnetic calorimeter and the endcap of the hadronic calorimeter (HEC), liquid argon is used as active medium. In the barrel region of the hadronic calorimeter scintillating tiles are used. Liquid argon is constantly flowing and does not suffer from radiation damage as opposed to the tiles and is therefore preferable in the region close to the interaction point and the forward region. The absorbers are made of lead in the barrel and of copper in the hadronic endcap.

Since only a fraction of the shower energy can be measured in the active material, the calibration of the calorimetry system is crucially important.

The electromagnetic calorimeter in ATLAS is the principal subject of this thesis. A more detailed description follows in Section 3.

## 2.4 Muon system

The muon spectrometer [20] provides muon momentum measurements using detection of the muon tracks. The magnetic field is generated by the large barrel toroid in  $|\eta| < 1.4$  and two smaller endcap magnets in  $1.6 < |\eta| < 2.7$ , which results in a superposition of both fields in the transition region  $1.4 < |\eta| < 1.6$ .

The muon chambers are arranged in three cylindrical layers parallel to the beam

pipe in the barrel region and perpendicular to the beam, also in three layers, in the transition and endcap regions.

For accurate muon momentum measurement, Thin Gap Chambers (TGCs) and Resistive Plate Chambers (RPCs) are used. TGCs are arranged into disks in the endcap region ( $1.05 < |\eta| < 2.4$ ). Depending on the type of the chamber, the TGCs contain two or three 2.8 mm gaps filled with a mixture of  $CO_2$  and  $C_5H_{12}$ . Passing muons ionize this gas mixture and the charge is collected by wires placed in the middle of the gap.

RPCs used for triggering in the central region ( $|\eta| < 1.05$ ) are arranged around the barrel in three double layers. The two innermost layers are close together (7820 and 8365 mm in R) and provide a trigger for muons with a transverse momentum between 6 and 9 GeV. The third layer at 10229 mm is only used for muons with a transverse momentum between 9 and 35 GeV. The RPCs comprise a 2 mm gas gap between an anode and a cathode plate, with metallic strips on the outer sides of the plates for readout.

Monitor Drift Tubes (MDTs) [21] and Cathode Strip Chambers (CSCs) [22] provide measurements of track segments. The MDTs consist of three or four layers of aluminium drift tubes of 30 mm in radius placed on each side of the muon chamber. The tubes are filled with a mixture of argon,  $CO_2$  and water vapor. The anode wire is placed at the center of the tubes. The chambers vary in length from 1 to 6 m and in width from 1 to 2 m. The MDTs cover a region of  $|\eta| < 2.4$ . The necessary 80  $\mu\text{m}$  position resolution per tube layer is achieved by a laser alignment system which is built into the detector.

The CSCs cover a region of  $2 < |\eta| < 2.7$ . They are made of sixteen multi-wire proportional chambers on each endcap disk. The chambers are also filled with a mixture of argon and  $CO_2$  with anode wires running radially. The cathode strips run radially on one side of the chambers and transversely on the other side. Only the cathode strips are read out and provide measurements in  $\eta$  and  $\phi$  for each hit.

This momentum measurement is independent of any muon momentum measurement in the ID, since the toroidal magnet system is independent of the solenoid in the ID. Hence, ATLAS can make two independent transverse measurements for muons.

The stand-alone muon momentum measurement needs a precision of 30  $\mu\text{m}$  in the relative alignment of chambers both within each projective tower and between consecutive layers in immediately adjacent towers. The alignment is based on the optical monitoring of deviations from straight lines.

The initial position accuracy required for the relative positioning of non-adjacent towers is a few millimetres and was established during installation of the chambers. The relative alignment of the barrel and forward regions relies on high-momentum muon trajectories taken with the magnetic field switched off.

The strength of the magnetic field along the muon trajectory has to be determined to an accuracy of a few per mill. The field is continuously monitored by approximately 1800 Hall sensors distributed throughout the spectrometers. Their measurements are compared with magnetic field simulations. The comparisons are used for calculating the positions of the toroid coils and account for magnetic

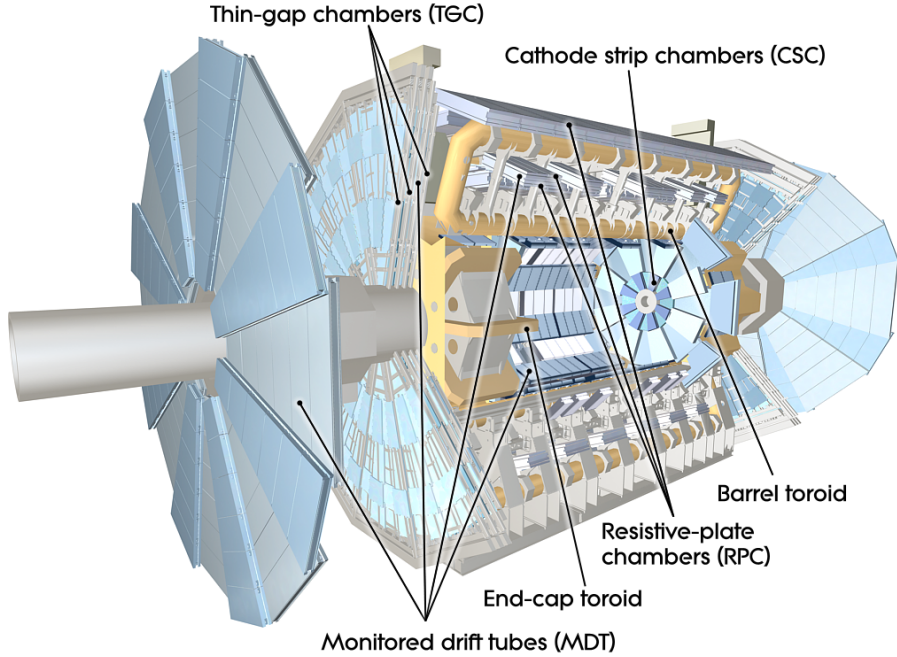


Figure 7: Cut-away view of the ATLAS muon system.

perturbations induced by nearby metallic structures.

## 2.5 Magnet system

The ATLAS magnet system, as shown in Figure 8, consists of

- A solenoid which provides a 2 T magnetic flux density for the ID.
- A barrel toroid and two endcap toroids which produce a magnetic flux density of approximately 0.5 T and 1 T for the muon detectors in the central and endcap regions, respectively.

In order to achieve the desired calorimeter performance, it was necessary to keep the material thickness in front of the calorimeter as low as possible. This required the solenoid windings and the LAr calorimeter to be in the same vacuum vessel. The magnetic flux of the magnet is returned by the HCAL and its girder structure.

The barrel toroid and the endcap toroids consist of eight coils each. The coils are assembled radially around the beam axis. The coil system of the endcap toroid is rotated by  $22.5^\circ$  with respect to the barrel toroid coil. In this way, radial overlap between the two coil systems is provided and the bending power optimized. Each endcap toroid is housed in one large cryostat. The barrel toroids are housed in eight cryostats.

The bending power is characterized by the field integral  $\int B dl$ , where B is the field component normal to the muon direction. The integral is computed along an infinite-momentum muon trajectory between the inner- and outermost

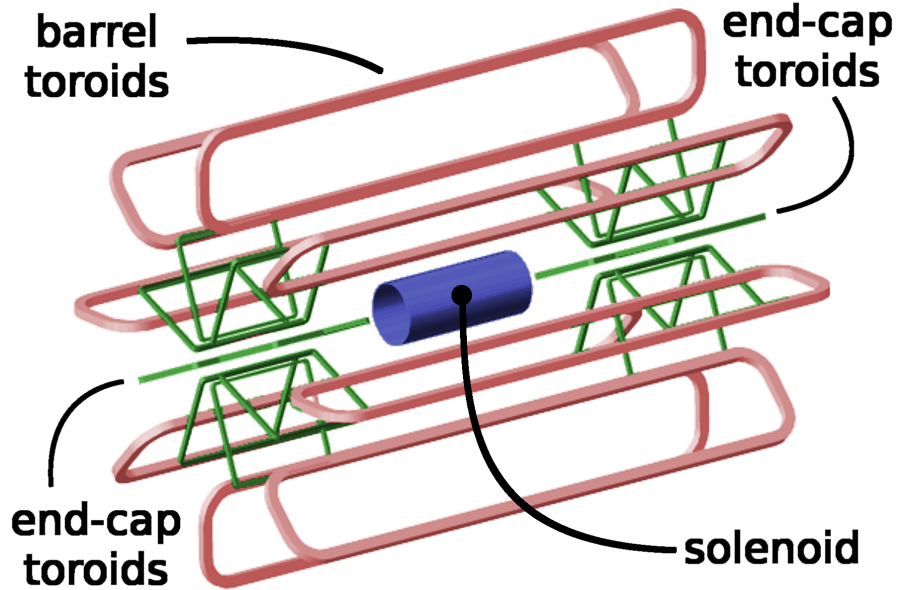


Figure 8: The ATLAS magnet system consists of eight barrel and endcap toroid coils each. The solenoid winding lies inside the calorimeter volume.

muon chamber planes. The barrel toroid provides 1.5 to 5.5 Tm of bending power in  $0 < |\eta| < 1.4$ . The endcap toroids provide approximately 1 to 7.5 Tm in  $1.6 < |\eta| < 2.7$ . In the overlap region ( $1.4 < |\eta| < 1.6$ ) the bending power is lower.

## 2.6 Trigger system

The bunch crossing rate at the LHC was 20 MHz during Run 1 and was increased to 40 MHz for Run 2. Most of the collisions produced in bunch crossings are not head-on collisions, but so-called soft or low transverse momentum interactions and produce events which are not of interest to be studied further. Therefore, the ATLAS trigger system has been developed to select and store only interesting events, reducing the event rate from 40 MHz to approximately 200 Hz.

The trigger looks for events with leptons with high transverse momentum,  $\tau$  leptons or high  $E_T^{\text{miss}}$ . If the event signature does not have any of these features, the event is discarded. As shown in Figure 9, the ATLAS trigger system operates in three stages. The Level-1 trigger is implemented in hardware and reduces the rate from 40 MHz to below 100 kHz. It uses a limited amount of the total detector information and makes a decision within about  $2.5 \mu\text{s}$ . The two following trigger stages, the Level-2 trigger [23] and the event filter (EF) [24], are software-based [25].

The Level-2 trigger has an execution time of about 10 ms and reduces the rate to 1-2 kHz. The EF needs about one second to make a decision and lowers the rate further to 100-200 Hz, which are saved on tape.

The Level-1 trigger selects Regions of Interest (RoIs) areas in the detector containing potentially interesting physics objects. For the identification of electrons and photons within the electromagnetic calorimeter at Level-1, the trigger towers,

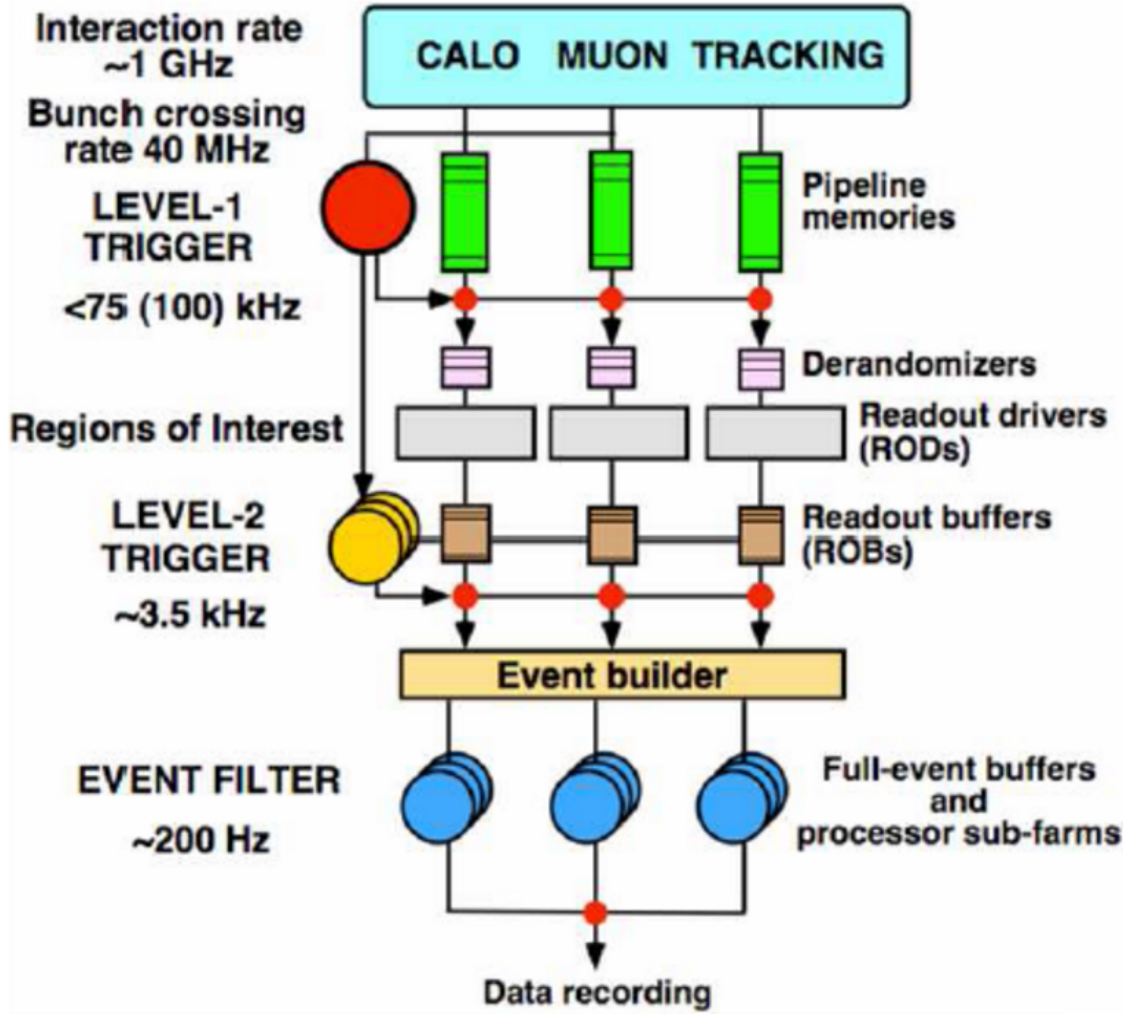


Figure 9: The ATLAS trigger system consists of three stages, of which the first one (Level-1 trigger) is implemented in hardware and the following two (Level-2 trigger and event filter) in software [26].

which span  $0.1 \times 0.1$  in  $\Delta\eta \times \Delta\phi$ , are used together with the appropriate isolation criteria.

The Level-1 muon trigger utilizes measurements of tracks from RPCs in the barrel region and TGCs in the endcap regions of the muon spectrometer. RPCs and TGCs rapidly provide information to the trigger. MDTs and CGCs are not fast enough, but extremely precise and thus used in offline muon reconstruction. The Level-1 trigger decisions are also made based on  $E_T^{\text{miss}}$  and the scalar sum of the transverse momentum of all jets, called  $H_T$ .

The RoIs identified by the Level-1 trigger are used to seed the Level-2 trigger, which uses more sophisticated reconstruction algorithms and have in general tighter criteria on the transverse momentum of the objects. It also uses the full calorimeter granularity and information from the ID, the MDTs and the CSCs of the muon

spectrometers. At Level-2, the event rate can be reduced by applying so-called *prescales*. By applying them the events which satisfy the trigger requirements, the rates are reduced by a certain factor which is chosen beforehand. However, most of the physics analyses prefer unprescaled triggers.

Events which pass the Level-2 trigger are sent to the EF which performs a full offline analysis to accurately select events containing the physics objects of interest.

After the EF, the events are separated into *streams*, of which each contains the output from several different trigger chains. Apart from the physics streams, there are also streams of events triggering on empty bunch crossings. They are used for calibration and detector related studies.

The streams are transferred to the data processing center *Tier 0* at CERN, where the offline event reconstruction is taking place. The output is distributed and saved to computing centres around the world. During this offline re-reconstruction, additional data monitoring and algorithms are applied which would not have been possible during the online reconstruction due to the high time consumption.

The calibration streams are processed first in order to provide new calibration to the detectors within 24 hours.

## 2.7 Data acquisition

The Readout Drivers (RODs), which are described in more detail in Chapter 3.6, gather information from several on-detector (front end) data streams. After an event is accepted by the Level-1 trigger, the data from the pipelines is transferred off the detector to the RODs. Digitized signals are formatted as raw data and transferred to the data acquisition (DAQ) system [25].

The readout system of the DAQ receives and temporarily stores the data in local buffers. The Level-2 trigger then selects events with their associated ROIs, which are transferred to the event-building system and then to the EF for final selection.

## 2.8 The ATLAS coordinate system

The origin of the ATLAS coordinate system is defined at the nominal interaction point of the beam. The  $z$ -axis points in beam direction. The  $x$ -axis points towards the center of the LHC ring, while the  $y$ -axis points away from the centre of the earth. Usually, angular coordinates are used. The azimuthal angle  $\phi$  is measured in the  $xy$ -plane:

$$\phi = \arctan\left(\frac{x}{y}\right) \quad (1)$$

The polar angle  $\theta$  is between the  $z$ -axis and the  $xy$ -plane.

$$\theta = \arctan\left(\frac{\sqrt{x^2 + y^2}}{z}\right) \quad (2)$$

The pseudorapidity  $\eta$  is given by



$$\eta = -\ln(\tan(\frac{\theta}{2})) \quad (3)$$

Another three important quantities which will be referred to throughout this thesis are the projection of the particle momentum on the  $xy$ -plane, the so-called transverse momentum

$$p_T = \sqrt{p_x^2 + p_y^2} = |p|\sin\theta, \quad (4)$$

the transverse energy

$$E_T = E\sin\theta \quad (5)$$

and

$$\Delta R = \sqrt{\Delta\eta^2 + \Delta\phi^2} \quad (6)$$

which corresponds to the distance  $\eta - \phi$  between energy deposits.

## 3 The Liquid Argon Calorimeter in ATLAS

### 3.1 Calorimeters

Calorimeters measure the energy of incident particles which interact with the calorimeter material and are usually completely absorbed. The particle produces a cascade of secondary particles which induce a signal that is proportional to the energy of the primary particle.

There are two types of calorimeters; electromagnetic and hadronic ones. Electromagnetic calorimeters mainly measure the energy of photons and electrons, hadronic calorimeters the energies of hadrons such as protons, pions or jets, which are produced via strong interaction by a quark or gluon. In particle physics detectors, the electromagnetic calorimeter is situated in front of the hadronic calorimeter, because hadrons do not lose a lot of energy when traversing the electromagnetic part, while photons or electrons are completely absorbed.

Both hadronic and electromagnetic calorimeters can be further classified as sampling and homogeneous calorimeters. Homogeneous calorimeters are made up of one single material which absorbs the particle and produces a measurable signal. In sampling calorimeters there are alternating layers of absorber and active material. The absorber is a dense material which causes the particle to lose a large fraction of energy, whereas in the active medium a signal is produced when charged particles pass through. The sampling calorimeters allow for compact calorimeters which can absorb the whole energy of an incident particle.

### 3.2 Physics of calorimetry

#### 3.2.1 Energy measurement

Particles which traverse the calorimeter permanently lose energy by ionizing the material they pass through. The electron-ion pairs which are created in the active material of the calorimeter (liquid argon in the case of ATLAS [27]) are separated by an electric field and drift towards the electrodes. There they induce a signal whose height is proportional to the number of pairs.

The energy  $E$  of the incident particle is proportional to the number of particles  $N$  in the electromagnetic shower.  $N$  fluctuates statistically and since the total ionization signal is proportional to  $N$ , the fluctuations of the reconstructed energy  $\Delta E$  can be expressed as follows [27]

$$\frac{\Delta E}{E} \propto \frac{\Delta N}{N} \propto \frac{\sqrt{N}}{N} \propto \frac{1}{\sqrt{N}} \propto \frac{1}{\sqrt{E}}. \quad (7)$$

As a result, the energy resolution of calorimeters improves with increasing particle energy if taking only statistical arguments into consideration.

In a real calorimeter one has to account for instrumentation effects and noise:

$$\frac{\sigma}{E} = \frac{a}{\sqrt{E}} \oplus \frac{b}{E} \oplus c \quad (8)$$

$a$  is the sampling or stochastic term, which is in the range between 8 – 11% [28], and a direct reflection of the sampling frequency. Homogeneous calorimeters have a very small stochastic term, because the whole shower is absorbed in the active material of the calorimeter. Sampling calorimeters have a higher stochastic term because the energy deposited in the active material fluctuates from event to event. The presampler in the LAr calorimeter was added to avoid a worsening of this term at low energies by correcting for energy losses in the dead material upstream.

$b$  is the combined noise term and depends on the optimization between electronics and pile-up noise since they vary in opposite directions with the shaping time. Detectors based on collecting charged particles have higher noise terms, because of the preamplifier required in the electronics readout chain. The noise term is important for the performance at particle energies lower than 20 GeV.

The constant term  $c$  is important at high energies. It is more sensitive to the skill put into the construction, calibration, and operation of the detector. It sums up effects caused by material non-uniformities, imperfections of mechanical structures, temperature gradients, radiation damage, etc.

$\oplus$  indicates the quadratic sum. The energy resolution for the LAr calorimeter in ATLAS is shown in Figure 10 [29].

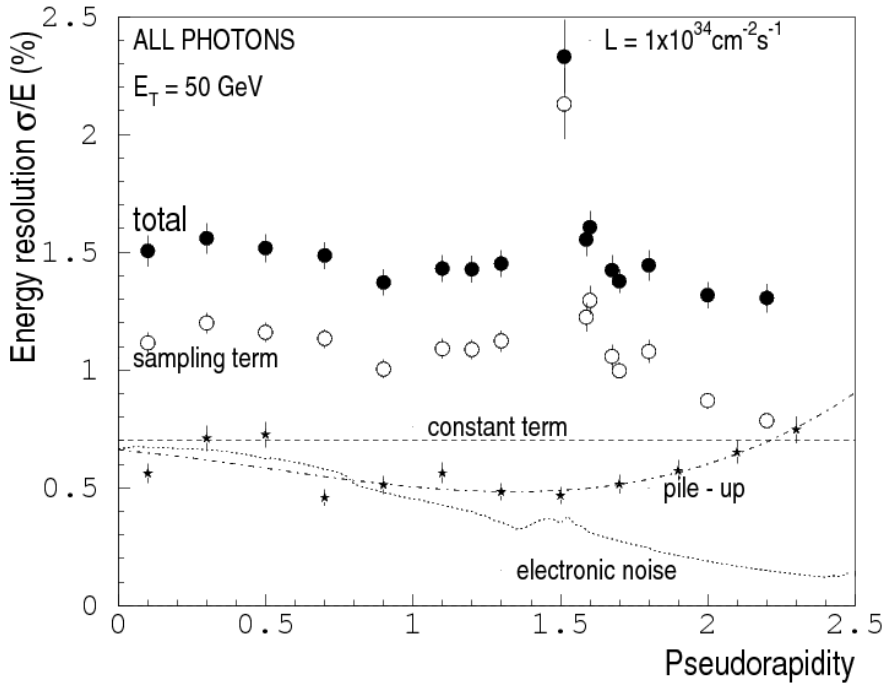


Figure 10: The energy resolution as a fraction of the total energy is shown as a function of  $\eta$  for 50 GeV  $E_T$  photons.

In a sampling calorimeter like the LAr calorimeter, only a fraction of the total energy is deposited in the active part. The ratio of the energy deposited in the active material divided by the total energy deposited is called the *Sampling Fraction*:

$$S_f = \frac{E_{\text{active}}}{E_{\text{active}} + E_{\text{passive}}} \quad (9)$$

In order to obtain the total energy deposited in a sampling calorimeter, one has to divide the energy measured by the sampling fraction.

### 3.2.2 Electromagnetic showers

When an electron or positron passes through matter it may emit bremsstrahlung. The photons emitted during this process cause electron-positron pair production. In this way, a cascade of particles with decreasing energy builds up until the energy of the particles falls below the threshold for pair production. The remaining energy is dissipated by excitation and ionization.

In Figure 11 the impact of the different processes contributing to the energy loss of photons and electrons/positrons are shown.

There are only a few tracks that traverse many layers of the calorimeter and deposit a fraction of their energy in the active region. The vast majority of incident particles in an electromagnetic shower has little energy and a very short range, typically much smaller than the thickness of the layers [30]. The picture of many electron tracks passing several calorimeter layers would be misleading. On the other hand, a muon will pass many layers, losing a comparably small fraction of its energy by ionization and produce only a few secondary particles.

The shower depth increases logarithmically with the particle's energy. Therefore, calorimeters are relatively compact devices, even for LHC energies in the TeV range.

Electromagnetic showers have also a transversal spread due to the multiple scattering processes of photons and electrons/positrons. The Moliere radius gives a good measure of the lateral shower spread. It is given by

$$R_M = X_0 \frac{21 \text{ MeV}}{E_c} \quad (10)$$

where  $E_c$  is the critical energy which is approximately  $E_c = 800\text{MeV}/(Z + 1.2)$  [31] and  $X_0$  is the radiation length.

A short description of the most important processes is in the following.

**3.2.2.1 Bremsstrahlung** An electron or positron with energy  $E_{\text{init}}$  passing through matter loses most of its energy as a result of the deceleration through the interaction with the Coulomb field of atomic nuclei. The spectrum of the emitted photons follows the function  $1/E_{\text{init}}$ . Usually, the emitted photon carries only a fraction of the initial energy of the particle.

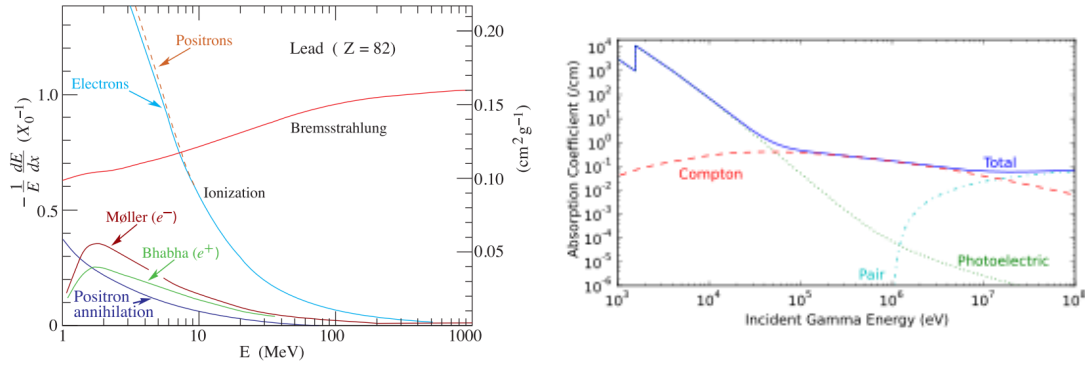


Figure 11: On the left side, the fractional energy loss of electrons per radiation length as function of the electron energy is shown [32]. On the right side, the photon absorption coefficient in lead as function of the energy showing the contributions of the different scattering processes is depicted [33]

**3.2.2.2 Pair production** If the energy of a photon is twice the rest mass of an electron, it can produce an electron-positron pair in the field of a charged particle. The cross-section for pair production increases with increasing energy of the incident particle and reaches a plateau for energies above 10 GeV. This process contributes significantly to the energy loss of particles if they have an energy of above a few MeV and pass through materials with a low atomic number.

**3.2.2.3 Photoelectric effect** In this process, an atom absorbs a photon which leaves it in an excited state. The atom returns to the ground state by emitting X-rays or so-called Auger electrons. The cross-section for the process increases with the number of available electrons. Hence, it gets bigger in material with high  $Z$  and scales with  $Z^n$  for  $n = 4$  or  $5$ . For energies higher than a few MeV the cross-section decreases with  $E^{-3}$ .

**3.2.2.4 Rayleigh and Compton scattering** Rayleigh scattering occurs when the energy of the incident particle is smaller than the energy of the particle it is scattered on. The process is dominantly elastic, hence, the incoming particle hardly loses any of its energy, but only gets deflected. Rayleigh scattering is relevant for particle energies below 1 MeV.

If a particle undergoes Compton scattering, it will lose energy and transfer it to the atomic electron it was scattered on. In most cases the electron will enter an unbound state. For energy ranges between a couple of hundred keV and few MeV Compton scattering is the most probable process to occur in most absorber materials. The cross-section for Compton scattering is approximately proportional to the  $Z$  value of the absorber material. With increasing energy of the incident particle, the cross-section decreases with  $1/E$ .

### 3.2.3 Radiation length

The radiation length  $X_0$  is a characteristic of each material and a convenient way to measure the energy loss of a high energy electromagnetic particle when it is passing through the material.

For electrons, one radiation length is defined as the mean distance over which a high energy electron's energy ( $E > 1$  GeV) is reduced to  $1/e$  of its previous value through bremsstrahlung.

Photons lose most of their energy through pair production. Hence, for photons the energy is decreased to  $1/e$  after travelling the mean free path  $x = \frac{9}{7} X_0$ .

$X_0$  is measured in  $\text{g} \cdot \text{cm}^{-2}$ . For a material consisting of a single type of nuclei, it can be approximated by [34]:

$$X_0 = \frac{716.4 \cdot A}{Z(Z+1) \ln \frac{287}{\sqrt{Z}}} \text{g} \cdot \text{cm}^{-2} \quad (11)$$

where  $Z$  is the atomic and  $A$  the mass number of the nucleus.

For the measurement of the energy of an electromagnetic shower it is crucial that the calorimeter is thick enough in terms of radiation lengths to absorb the whole energy of the particles. For this, a material with high atomic number  $Z$  has to be chosen. The ATLAS electromagnetic calorimeter is about 22 radiation lengths thick. To absorb 99% of the energy of a 300 GeV electron in the calorimeter, a thickness of about  $25 X_0$  is sufficient.

### 3.2.4 Performance of the LAr calorimeter

Thanks to its high granularity, the electromagnetic calorimeter provides electron and photon identification and a good rejection of the jet background. The transversal shower shape in the front layer of the calorimeter can then be used to distinguish photons from  $\pi^0$ s. The strips of the front layer allow for  $\pi^0$  rejection by a factor  $> 3$  for a 90% photon efficiency [35]. The jet rejection at  $> 20$  GeV is expected to be about 5000, which is needed to eliminate the QCD background in the  $H \rightarrow \gamma\gamma$  channel.

The strips also contribute to the photon angular measurement in  $\eta$  with an accuracy of  $\frac{50 \text{ mrad}}{\sqrt{E}}$ , essential for  $H \rightarrow \tau\tau$ .

For jet reconstruction, coherent noise may hamper the performance for jets and missing  $E_T$ , which both require summing up a large number of channels.

The benchmark for the whole ATLAS calorimeter, the missing  $p_T$  resolution for the pseudoscalar supersymmetric Higgs boson  $A \rightarrow \tau\tau$  has been estimated to be about 7 GeV for each transverse component, allowing a mass resolution of about 20 GeV at 150 GeV [19].

## 3.3 Structure of the ATLAS calorimeters

A two-dimensional view of both electromagnetic and hadronic calorimeters is shown in Figure 12. The geometry of the barrel cryostat can be seen in Figure 13.

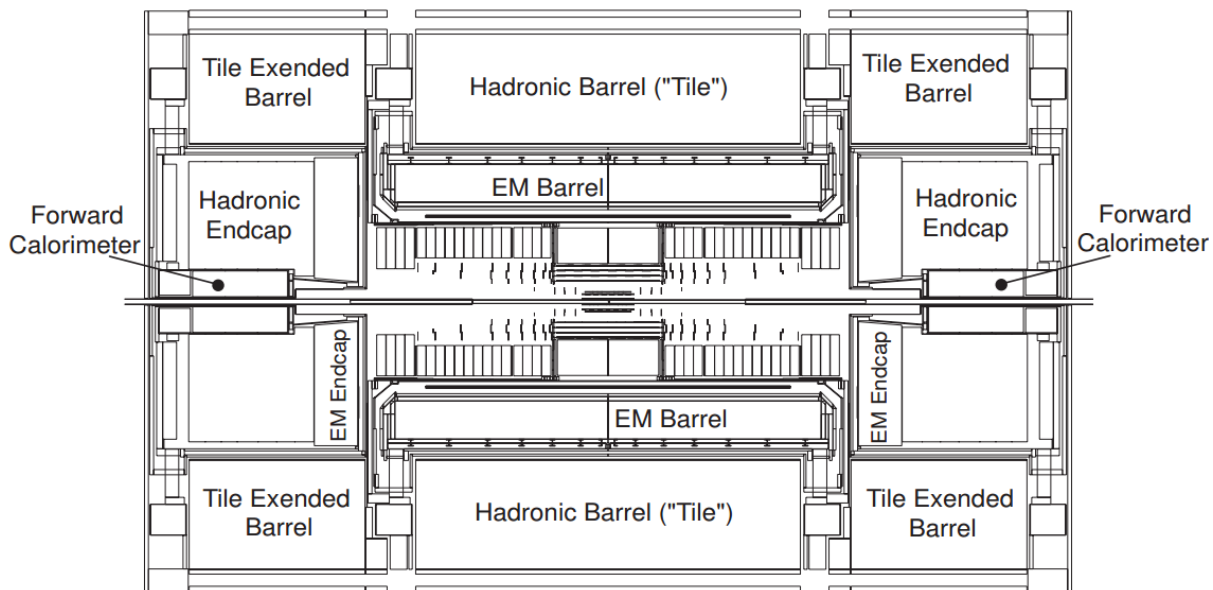


Figure 12: 2D view of the electromagnetic and hadronic calorimeters in ATLAS.

All calorimeters used in ATLAS are sampling calorimeters. The main properties of the various sub-systems are listed in the following:

- **Electromagnetic calorimeter** The electromagnetic barrel has a coverage of up to  $|\eta| = 1.475$ . The electromagnetic endcaps range from  $1.375 < |\eta| < 3.2$  on both sides of the detector. Both are built from lead absorbers interleaved with liquid argon as active material. An extensive description of the working principle is in the following sections.
- **Hadronic barrel Calorimeter** The central barrel part covers the rapidity region of up to  $|\eta| = 1.0$  and the extended barrel goes up to  $|\eta| = 1.7$  on each side. The gap between the central and the extended barrel is needed to guide cable services from the Inner Detector and the electromagnetic calorimeter outside the detector. In order to estimate the energy lost in this region, scintillators are placed in the gap.

The Hadronic Barrel Calorimeter consists of steel absorbers which are interlaced with scintillating tiles for readout.

- **Hadronic endcap calorimeter** The Hadronic endcap uses as well liquid argon as active material, although the absorbers are not accordion shaped, but are flat copper plates. It is placed in the same cryostat as the electromagnetic endcap and covers a pseudo-rapidity range of  $1.5 < |\eta| < 3.2$ .
- **Forward Calorimeter** The Forward calorimeter is used for hadronic and electromagnetic calorimetry in the pseudo-rapidity region between 3.2 and 4.9. It is located around the beam pipe, in the inner bore of the hadronic

endcap. Also here the liquid argon technology is used, but the active gaps are made much thinner in order to cope with the higher counting rate. As absorber material copper and tungsten are used.

Since the Phase-I demonstrator was installed in the barrel part of the Liquid Argon calorimeter, there is a detailed description of the barrel in the following.

### 3.3.1 Barrel calorimeter

The central cryostat contains the barrel electromagnetic calorimeter, the superconducting solenoid and is supporting the tracking system. The magnet was integrated in the same cryostat in order to minimize the material in front of the calorimeter. At  $\eta = 0$  a traversing particle sees about  $2.3 X_0$  of material before it reaches the calorimeter. For larger  $\eta$  the amount of material in front of the calorimeter increases, because the particle track becomes longer.

The barrel consists of two identical half-barrels with a gap of a few millimetres. Each half-barrel consists of 1024 absorbers with readout electrodes in between. The absorbers and electrodes are accordion-shaped with the folds approximately perpendicular to the incoming particle tracks. The folding angles of the absorbers and electrodes decrease with increasing radius, leaving a constant gap of about 4.5 mm between two neighbours and allowing a hermetically uniform azimuthal coverage. The readout electrodes which are 300  $\mu\text{m}$  thick, are centred in this gap by honeycomb spacers, defining two liquid argon gaps of 2.1 mm each.

The readout cells are defined in  $\eta$  by etching of the readout boards and in  $\phi$  by grouping together four adjacent boards. The readout and calibration signals are routed through the cold-to-warm feedthroughs. The barrel cryostat has 32 feedthroughs at each end.

The geometry of the cryostat and the integration of the calorimeter can be seen in Figure 13.

### 3.3.2 Barrel presampler

The presampler becomes necessary to correct for energy losses upstream the calorimeter.

The barrel presampler is a 1 cm deep liquid argon active layer instrumented with electrodes which lie in the  $(r, \phi)$ -plane. It is subdivided into 32 identical azimuthal sectors, each spanning  $\pi/32$  in  $\phi$ , per half-barrel.

In the transition region between the barrel and the endcap at  $\eta = 1.4$  a scintillator layer is used between the cryostats to recover jet energy measurements.

The presampler readout has a granularity of  $\Delta\eta = 0.025$  and  $\Delta\phi = 0.1$ .

At  $|\eta| > 1.8$  the presampler is no longer needed due to a more limited amount of dead material and the higher energy of particles at a given  $p_T$ .



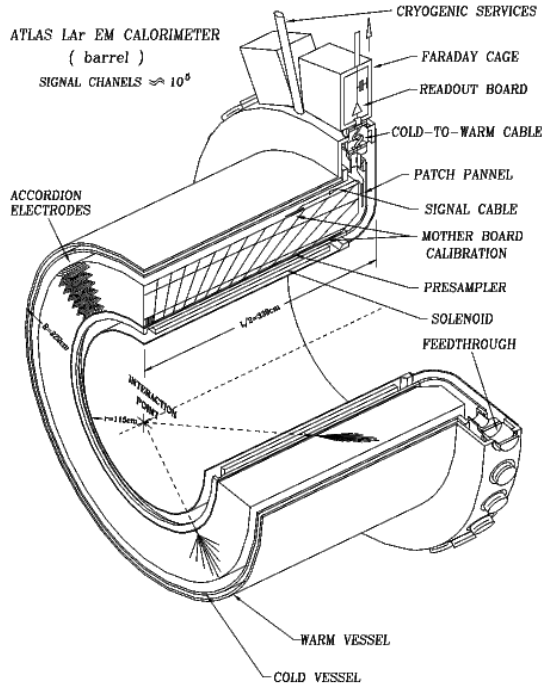


Figure 13: Barrel cryostat

### 3.3.3 Granularity of the samplings

Precision physics can hardly be expanded beyond  $|\eta| = 2.5$ . For that reason the endcap has a coarser granularity than the barrel and only two samplings in depth.

The characteristics of the three longitudinal samplings are the following:

- The front layer is optimized for the rejection of  $\pi^0$  up to  $E_T = 50$  GeV and measuring the pointing of photons. It ends at  $X_0 \approx 6$ , including  $\approx 1.6 X_0$  of dead material in front of the active part of the calorimeter.
- The middle layer is optimized to absorb most of the energy of electromagnetic showers. It goes from 6 to 24  $X_0$ .
- The back layer covers the depth beyond 22  $X_0$  (close to  $\eta = 0$  the second sampling is reduced to 22  $X_0$  to leave a minimum of 2  $X_0$  for the third sampling). Its main purpose it to catch shower tails.

The granularity of all samplings is summed up in Table 1.

In the endcaps a given  $\eta$ -bin becomes narrower when going to larger  $\eta$ . Practical considerations led to limit the strip pitch to 5 mm. For  $\eta > 1.8$  the strip size becomes  $\frac{1}{6}$  of the tower size and for  $\eta > 2.0$  it becomes  $\frac{1}{4}$  of the tower size.

The total number of channels in the electromagnetic calorimeter is 182468. For the trigger towers in the central region 60 elementary cells are summed up to one trigger tower unit. At high  $\eta$  this number decreases. For  $\eta > 2.5$ , 8 elementary cells are summed up to one trigger unit. The dimensions of the trigger towers in

Table 1: Granularity of the samplings of the liquid argon barrel calorimeter.

Sampling	$\Delta\eta$	$\Delta\phi$	Depth in $X_0$
Presampler	0.025	$2\pi/64$	1.7
Front	0.025/8	$2\pi/64$	2.5-4.5
Middle	0.025	$2\pi/256$	16.5-19
Back	0.05	$2\pi/256$	1.4-7

this region are  $\Delta\eta \times \Delta\phi = 0.2 \times 0.2$ , whereas in the central part they are  $0.1 \times 0.1$ . The granularity of the front, middle and back layer and the separation into trigger towers can be seen in Figure 14.

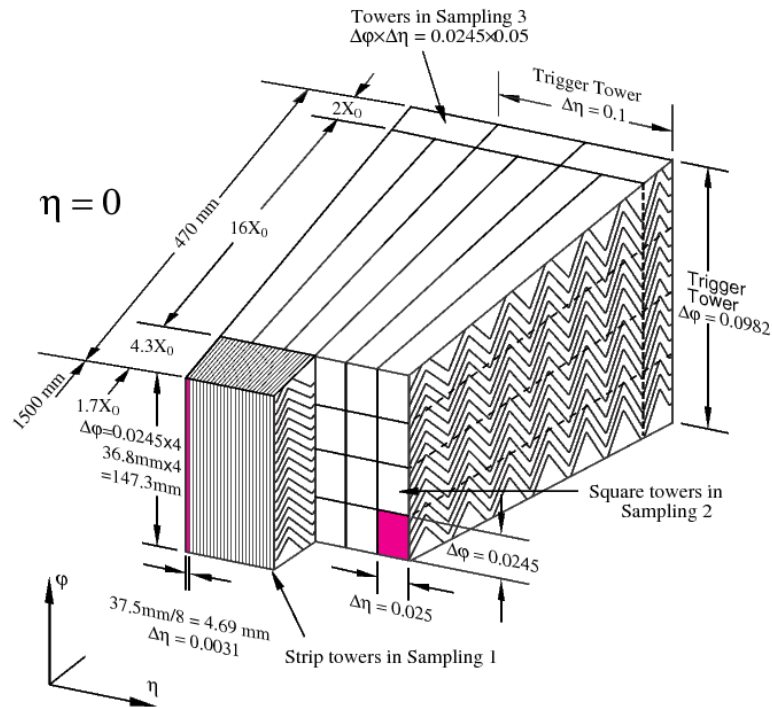


Figure 14: The structure of a LAr calorimeter barrel module is shown in this picture. The layers (presampler: PS, front: 1, middle: 2, and back: 3) can be seen as well as their granularity in  $\phi$  and  $\eta$  [36].

### 3.4 Electronic signal processing

#### 3.4.1 Readout electrodes

In the calorimeter, signal electrodes are alternated with the absorber plates. The readout electrodes are made up of three layers of copper separated by polyamide (Figure 15). To the outer layers of the electrode high voltage is applied which creates an electric field in the gaps. Currents induced capacitively by electrons drifting in

the gaps are collected from the central layer. Hence, the currents from both gaps surrounding the electrode are summed.

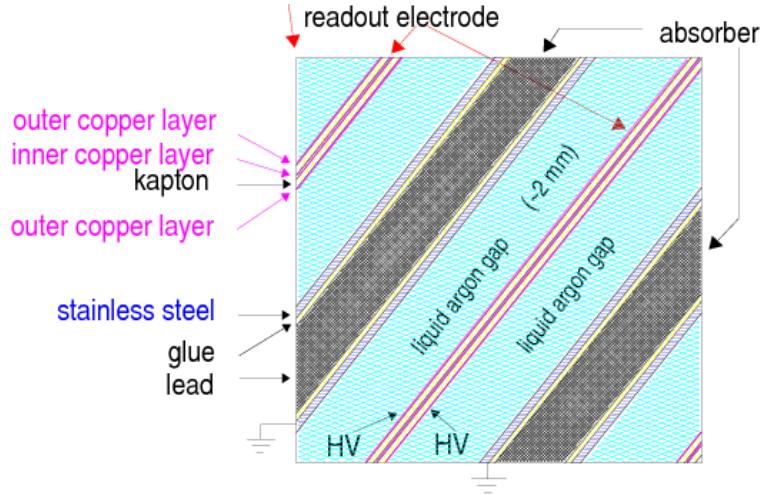


Figure 15: Signal layer for barrel electrode [37].

Printed circuits at the electrode edges provide the connection between neighbouring electrodes in  $\phi$  to obtain the suitable granularity and also the connection to the output cables. The output cables run towards the feedthroughs over the printed circuits, parallel to the beam axis.

Figure 16 shows the signal layer of the barrel electrode ( $0 \leq \eta \leq 1.45$ ). Each high-voltage line supplies a zone covering  $\Delta\eta = 0.2$  and  $\Delta\phi = 0.1$ . It is brought over the electrode through resistive bridges through a bus of 6 mm. Two resistors in parallel, each of  $1 \text{ M}\Omega$ , connect the bus to each cell in the middle and back layer.

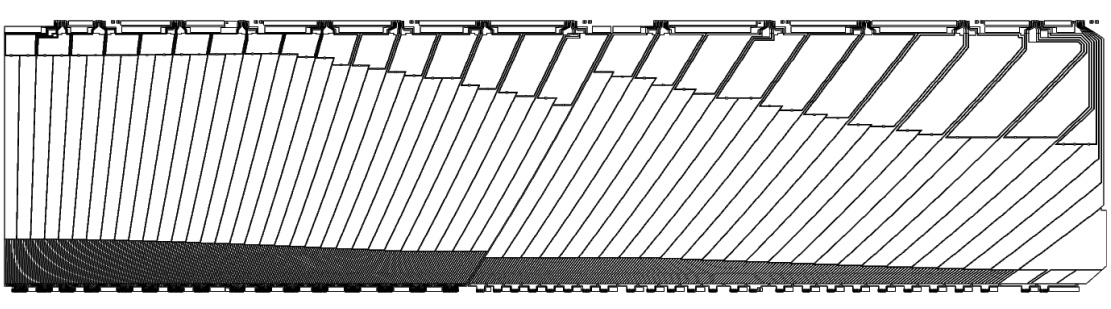


Figure 16: Signal layer for barrel electrode

### 3.4.2 Shaping, pile-up and electronics noise

Primarily, pile-up results from energy deposited in the calorimeter by particles produced in soft interactions. The average number of charged (neutral, after  $\pi^0$  decays) particles per  $\eta$  interval is 7.5 (7.9) and their average  $p_T$  is 460 (290) MeV, as can be seen in Figures 17a and 17b.

Due to the solenoidal field charged particles with a  $p_T < 360$  MeV are trapped inside the cavity.

Assuming an inelastic cross-section of 70 mb, an average luminosity of  $10^{34} \text{cm}^{-2} \text{s}^{-1}$  and an average filling factor of the LHC of 2835 active bunches over 3564 clock cycles, one gets 23 inelastic events per active crossing.

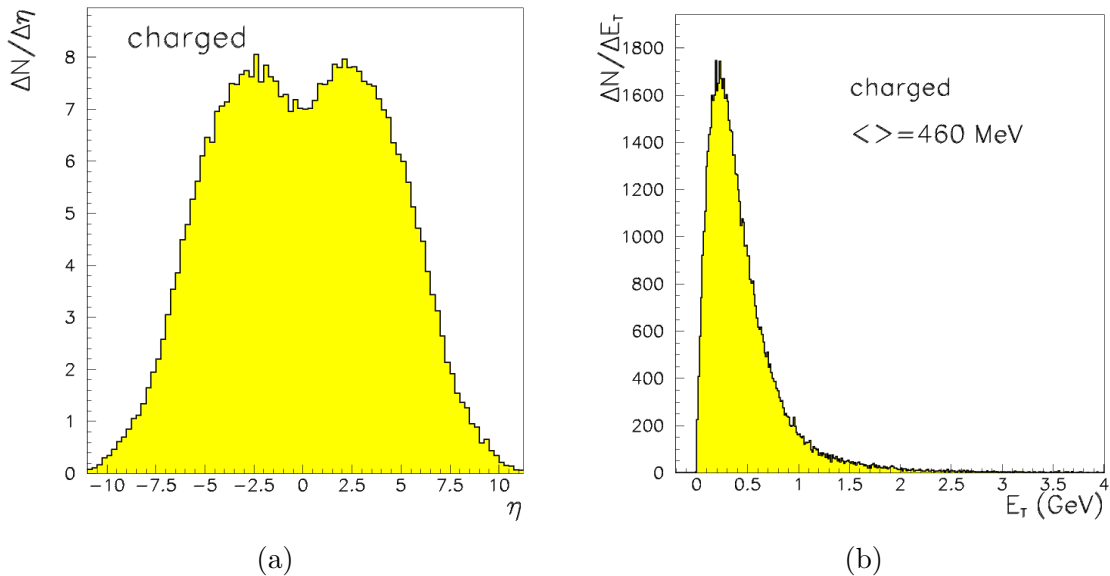


Figure 17: The charged track multiplicity as a function of pseudo-rapidity for minimum-bias events is shown on the left side. In the right picture the transverse energy distribution of charged particles for minimum-bias events is shown. [28]

The average signal in any calorimeter cell is 0, although because of the reflection of the high- $p_T$  tail, its value in  $E_T$  is -50 MeV in an electromagnetic cluster ( $3 \times 5$  cells in the middle layer). The RMS of the energy deposit (= pile-up) is directly proportional to the pile-up sum

$$I = \left( \sum_i \frac{f_i^2}{f_{max}^2} \right)^{\frac{1}{2}} \quad (12)$$

where  $f_i$  is the relative amplitude of all bunch crossings contributing to the signal and  $f_{max}$  is the peak amplitude.

In an electromagnetic cluster the RMS of the transverse energy deposition is typically 300 MeV. Hence, it contributes significantly to the calorimeter resolution.

One way to reduce this is to make the signal response faster by making the peaking time  $t_p$  shorter. Since this increases the thermal noise one has to optimize between pile-up and thermal noise (Figure 18). The chosen shaping time gives an optimum response (minimal sum for electronics and pile-up noise) when operating at the nominal high luminosity.

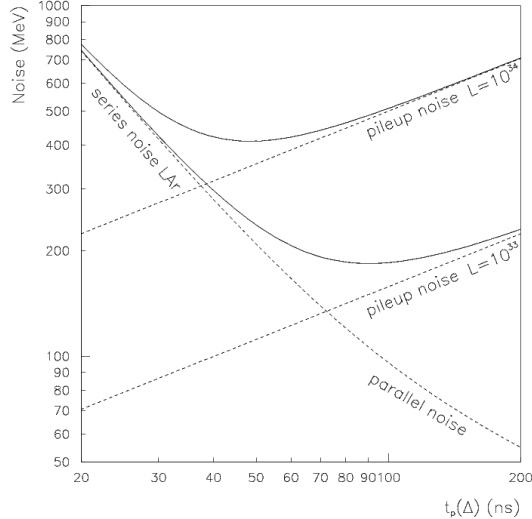


Figure 18: Optimization of the shaping time [38].

### 3.4.3 Electronics calibration

For an accurate calibration, the calibration signal has to resemble as much as possible the physics signal. It has to be fast (electromagnetic showers induce signals with rise times of  $< 1$  ns) and should have a decay time equal to the drift time in the gap.

The LAr calibration system sends voltage pulses to precision resistors located on boards close to the calorimeter cells. One has to correct for some systematic effects in the calibration like the non-uniformity of dead material in front of the presampler or some liquid temperature gradient. In the overall calibration LAr relies on physics event samples.

Since the given level of precision required for the hadronic and forward calorimeters is lower than for the electromagnetic calorimeter, there were some simplifications to be made.

When calibrating these calorimeters, all parts of a readout tower are pulsed simultaneously. In the forward calorimeter the calibration resistors are located close to the blocking capacitors due to the high level of radiation.

In Chapter 7 the calibration will be discussed more in detail.

### 3.4.4 Temperature and purity monitoring

The calorimeter signal depends on the temperature of the liquid argon only through the liquid density with a sensitivity of  $\approx 0.5\%$  per Kelvin. The signal is directly proportional to the electron drift speed in the gaps, which is also temperature dependent. The temperature dependence there is  $-2\%$  per Kelvin. Therefore, a uniform liquid temperature bath is important. What LAr aims for is a  $\Delta T < 0.3$  K between any two points of the calorimeter. That corresponds to the energy resolution term of  $< 0.2\%$ .

For the purity monitoring test cells in various places of each cryostat are used for measurements. Electronegative impurities occur because of outgassing of calorimeter material under irradiation.

### 3.5 Readout and trigger system

The current LAr readout electronics system can record energies in a range from  $\approx 50$  MeV to  $\approx 3$  TeV. The system samples the triangular-shaped signals at 40 MHz. Upon a L1-Trigger accept it sends digitized samples for each bunch crossing up to a maximum L1-Trigger rate of 75 kHz in Run 1 of LHC data taking. In Run 2 the system is operating with a trigger rate of 100 kHz.

An overview of the LAr readout architecture is shown in Figure 19. It is composed of the front end (FE) electronics placed close to the detector and the back end (BE) electronics located in the electronics cavern (USA-15).

### 3.6 Front end electronics

The 58 FE crates are mounted directly on the LAr cryostats, both in the gap between the barrel and endcap calorimeters and on the outer face of the endcap cryostats. The high voltage of  $\approx 2$  kV, which is necessary to power the readout boards, is brought from outside using warm feedthroughs located on top of each cryostat. The on-detector electronics needs to be radiation hard and has been qualified in terms of radiation tolerance for up to 10 years of operation at the LHC, equivalent to an integrated luminosity of 700 - 1000 fb<sup>-1</sup>.

As shown in Figure 19, each FE crate contains:

- **Front End Boards (FEBs)** These boards read out and digitize the LAr calorimeter signals. Each FEB is a 10-layer printed circuit board (PCB) that processes the signals from 128 channels in a specific layer of the calorimeter. The detector signals go through a whole chain of analogue processing. The raw signals are amplified and then split and further amplified by shaper chips to produce three overlapping linear gain scales with gain ratios of about 10. Gain selector chips choose the gain for each channel based on the peak sampled value of each signal. Fast bipolar shaping is performed with a time constant  $\tau = RC = 13ns$  and the shaped signals are sampled at the LHC bunch crossing frequency of 40 MHz. Switched capacitor array analogue pipeline chips hold the signals in a buffer. Upon a L1-Trigger accept, typically five samples per channel are read out from the switched capacitor array and digitized using a 12-bit analogue-to-digital converter (ADC). The digitized data are formatted, multiplexed, serialized and then transmitted optically via a 1.6 Gbps fibre optical link off the detector to the back end electronics. A detailed description of the boards can be found in [38].
- **Layer Sum Boards (LSB)** Part of the analogue signals are first summed in the shapers and then on the LSBs. Then, they are forwarded to the LTDB via the baseplane.

- **Tower Builder Boards (TBB)** Analogue signal sums from different FEBs are sent over the backplane in the FE crate to the TBB, which adds up the signals to trigger towers with a size of  $\Delta\eta \times \Delta\phi = 0.1 \times 0.1$ . The signals are then sent to the L1 calorimeter trigger system.
- **Calibration Boards** The calibration boards deliver a pulse to the LAr cells whose shape is close to the triangular-shaped signal, but has an exponential decay due to the inductively injected current.
- **Controller Boards** The controller boards receive and distribute the 40 MHz LHC clock and other configuration and control signals.

Signals for the first level trigger are formed by analogue sums and correspond to trigger units of  $\Delta\eta \times \Delta\phi = 0.1 \times 0.1$  in the electromagnetic barrel. The summing is performed in three steps: shaper chip, front end board (FEB) and Tower Builder Board (TBB).

The resulting analogue sums are connected by twisted pairs of cables to USA-15 where they are digitized at 80 MHz. <sup>1</sup>

### 3.7 Back end electronics

The back end electronics filters, formats, and monitors the digitized calorimeter signals and reconstructs the  $E_T$ .

The digitized samples are transferred by a 1.6 Gb optical link to the back end. The VME-based Readout Driver (ROD) crate contains:

- **Readout Driver Boards (RODs)** The RODs [39] recover the output of the FEBs at the L1-Trigger rate and compute quantities such as the energy, time phase and quality of the signal. These quantities are then sent via optical fibres to the data acquisition (DAQ) system. The memory is separated into one part for writing incoming data and another part for data read by the digital signal processor (DSP). Each DSP can perform  $5.7 \times 10^9$  instructions per second. This means that at a L1-Trigger rate of 75 kHz the calculations must be performed within 13  $\mu s$ . An optimal filtering algorithm is used to calculate the energy deposited in the calorimeter from the digitized samples. Above a given energy threshold, the time of the energy deposition and the quality of the pulse are also estimated. The quality factor quantifies whether a pulse matches the expected shape or whether it may have been mismeasured.
- **CPU Board** The CPU board is a VME processor that controls the ROD crate.
- **SPAC Master Board** The SPAC Master Board is a module to configure and load parameters into the boards in the FE crate or to read back registers. Configuration and monitoring are done using the **Serial Protocol for ATLAS Calorimeters (SPAC)** [40].

---

<sup>1</sup>The analogue pipelines have 144 cells, covering a maximal latency time of 2.5  $\mu s$ .

- **Trigger Busy Module (TBM)** The TBM receives the trigger, timing and TTC signals, including the LHC clock and other synchronous commands.

### 3.8 L1-Trigger readout

The architecture of the L1 calorimeter (L1Calo) system is depicted in Figure 21. It receives analogue signals from the TBBs and equivalent signals from the Tile Calorimeter system.

The system contains:

- **Pre-processor Module (PPM)** The PPMs sample the analogue trigger tower signals at 80 MHz, identify the bunch crossing using the pulse shape and use a look-up table to compute the transverse energy. The digitized data is then transmitted to the CPMs and JEMs.
- **Cluster Processor Module (CPM)** Each CPM identifies isolated electron, photon and  $\tau$  lepton candidates from the  $\Delta\eta \times \Delta\phi = 0.1 \times 0.1$  granularity energy deposits in a given calorimeter region. An ROI is defined using a sliding window algorithm and electromagnetic and hadronic isolation quantities are computed from the surrounding clusters.
- **Jet Energy Module (JEM)** Each JEM identifies energetic jet candidates from  $\Delta\eta \times \Delta\phi = 0.2 \times 0.2$  jet elements in a given calorimeter region. Also here a ROI is defined, and in addition, the sum of the total transverse energy and the missing transverse energy are also computed.
- **Common Merger Module (CMM)** The results from the CPMs and JEMs are transmitted over crate backplanes and summed in CMMs before being sent to the Central Trigger Processor (CTP).

After a L1-Trigger accept, the L1Calo modules provide readout data and ROIs to the High-Level Trigger (HLT) system via the readout drivers.



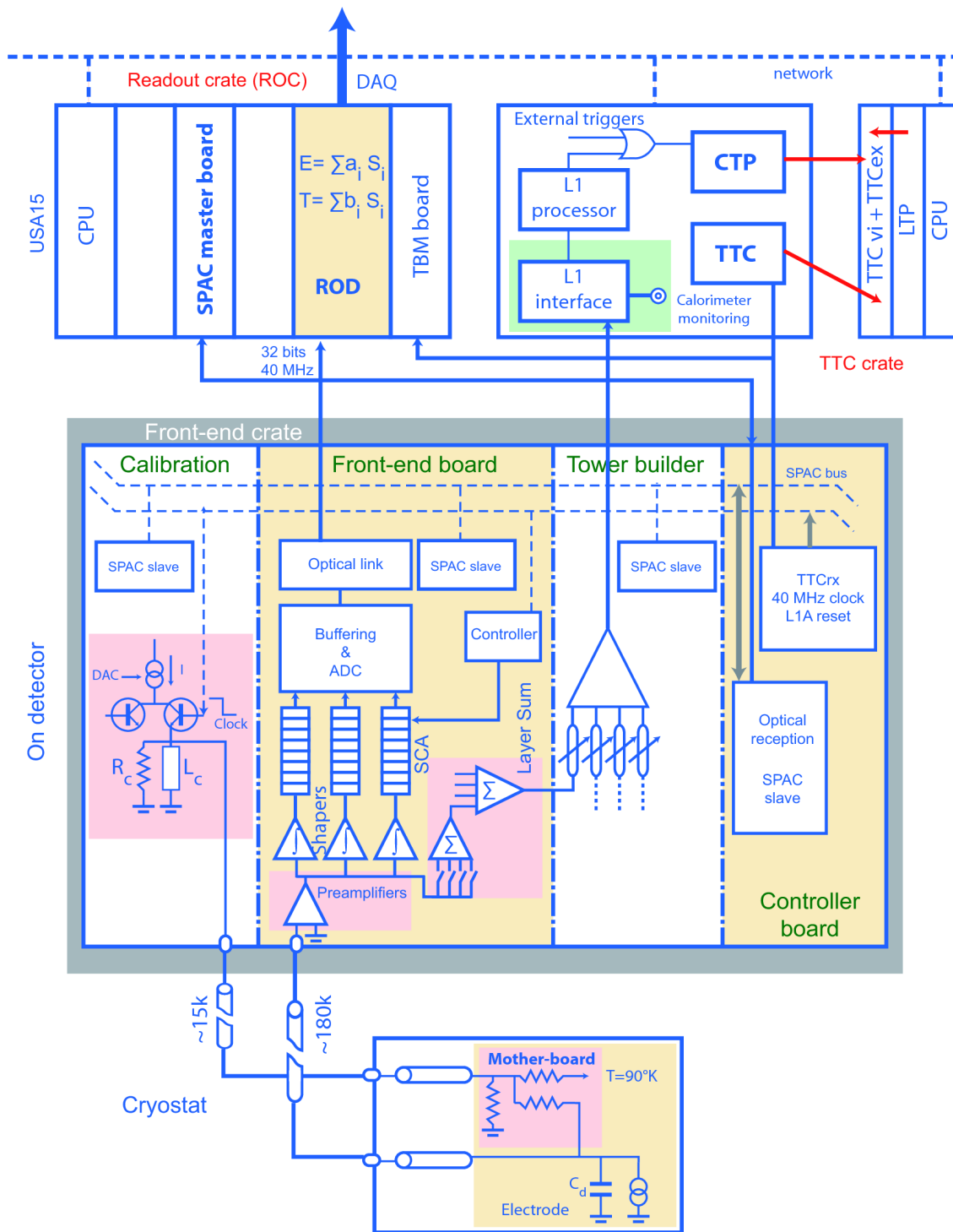


Figure 19: Schematic block diagram of the current LAr readout electronics [39].

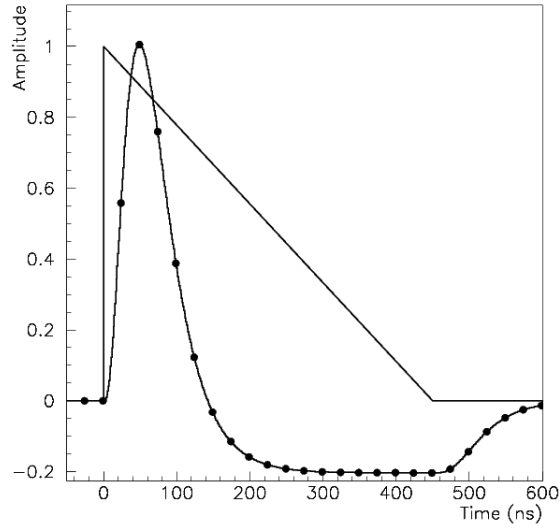


Figure 20: The signal from the detector is of triangular shape. After shaping and amplification the smooth curve is obtained [38]. The rising edge of the calibration signal is similar to the triangular shape of the detector signal, but it has an exponential decay.

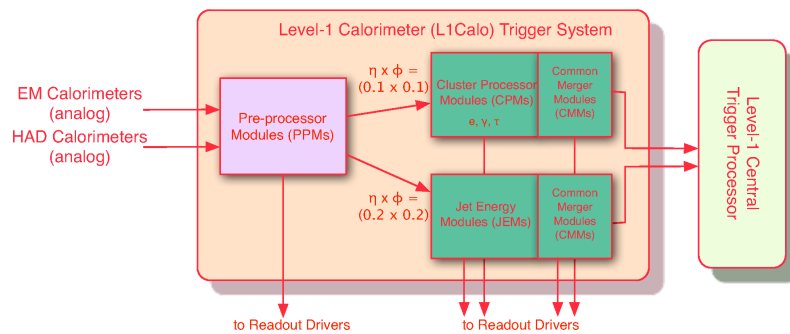


Figure 21: Schematic block diagram of the L1Calo system.

## 4 The Trigger Readout Phase-I Upgrade of the ATLAS Liquid Argon Calorimeter

The existing calorimeter trigger information is based on the sum of the energy deposition across the longitudinal layers of the calorimeter in units as big as  $\Delta\eta \times \Delta\phi = 0.1 \times 0.1$ , the so-called *trigger towers*. The new finer granularity scheme is based on *Super Cells*, which will provide information for each layer of the calorimeter and finer segmentation ( $\Delta\eta \times \Delta\phi = 0.025 \times 0.1$  in the middle and front layer and  $\Delta\eta \times \Delta\phi = 0.1 \times 0.1$  in the presampler and back layer) of the trigger readout of the EM barrel and endcap.

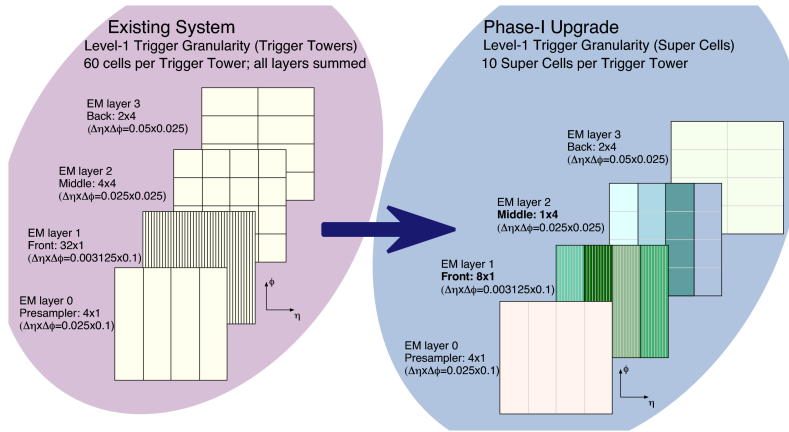


Figure 22: Comparison of the Trigger Tower and Super Cell segmentation.

### 4.1 Physics requirements and expected performance

After the discovery of the 125 GeV Higgs boson, probing the details of the electroweak symmetry breaking is one of the major goals for the LHC experiments. The Phase-I upgrade of ATLAS [41] will provide the detector with the necessary tools to make the required measurements of the Higgs boson and look for new physics including Supersymmetry and extra dimensions. The improvements are essential given the expected higher instantaneous luminosity and pile-up conditions of the upgraded LHC.

The ultimate goal of the upgrade is to improve the performance of the Level-1 single object triggers based on the calorimeter information. This can be achieved by:

- Enabling the use of shower-shape variables for a more effective identification of electrons, photons and  $\tau$  leptons.
- Sharpening the EM, jet and  $E_T^{\text{miss}}$  efficiency turn-on curves.

For this performance improvements, the following upgrades will be done:

- The new trigger units, the Super Cells, which are formed in the front end electronics and available to the Level-1 trigger, are finer than the old units and longitudinal information of showers will also become available.
- The quantization scale and dynamic range of the digitizers of the Super Cells will be improved by a factor of  $> 4$  for each  $\eta$ -region and all layers of the calorimeter.
- The deposited transverse energy will be calculated through optimized algorithms, as it is done currently in the Liquid Argon Readout Drivers (RODs) in the main readout.

#### 4.1.1 Super Cell energy reconstruction

The energy deposited in the calorimeter cells by particle showers has to be reconstructed and assigned to the correct bunch crossing. The reconstruction algorithm is based on a linear combination of the signal samples. The coefficients minimize electronics and pile-up noise by having precise knowledge of the pulse shape. As luminosity increases, pile-up becomes the dominant contribution of the total noise in most calorimeter regions, as shown in Figure 23a for Phase-I and 23b for Phase-II. In all performance studies the Super Cell energy is reconstructed by summing the energies of the individual cells belonging to it.

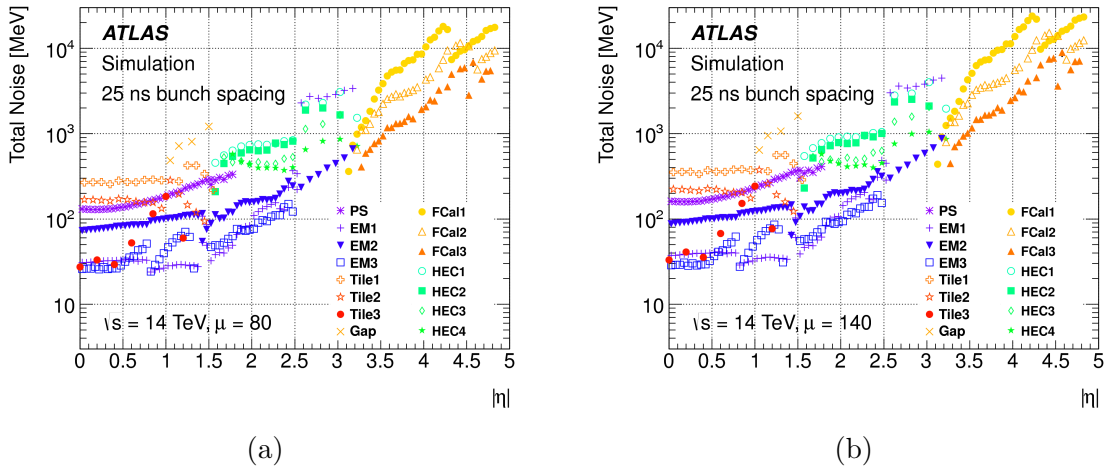


Figure 23: Simulated noise of the transverse energy per Super Cell in the four layers of the calorimeter as function of  $|\eta|$  for Phase-I and Phase-II.

#### 4.1.2 Super Cell energy resolution

The transverse energy  $E_T$  in each Super Cell is obtained through applying an optimal filtering algorithm to the raw input data with a quantization scale of 125 MeV in the middle layer and 32 MeV elsewhere. The correlation of the EM clusters formed from the Super Cells and the  $E_T$  from the offline reconstructed transverse energy

$E_T^{\text{off}}$  of electrons is shown in Figure 24a and 24b. It is shown that the resolution improvement results in an improved efficiency for EM objects in the trigger for a given offline  $E_T$ .

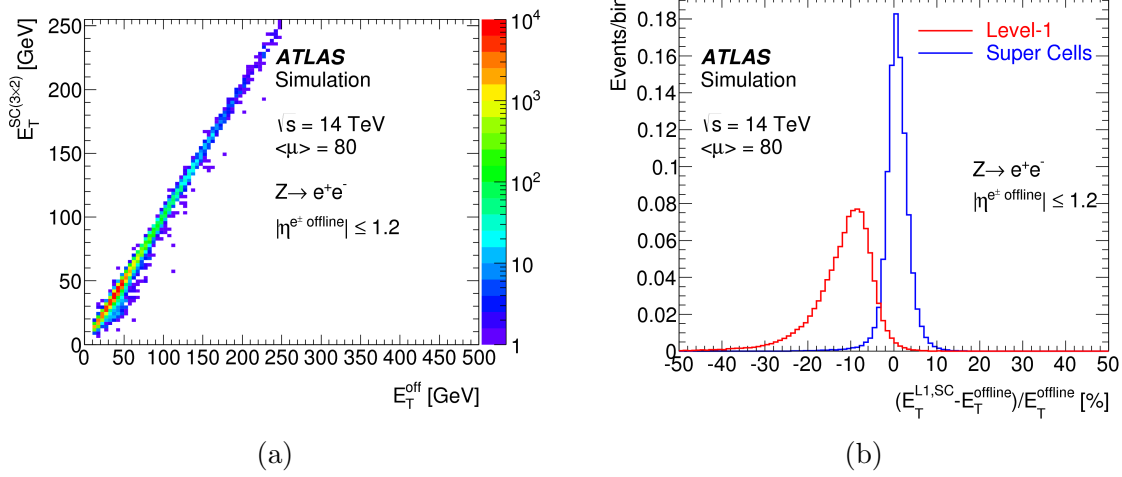


Figure 24: Super Cell energy correlation between offline and online reconstruction.

Assuming a least significant bit of 32 MeV and 125 MeV in the front and middle layer, respectively,  $E_T$  values of up to 102 GeV and 400 GeV in the corresponding calorimeter layers will be processed without loss of precision having a 12-bit dynamic range.

### 4.1.3 Level-1 trigger performance studies

The performance studies are based on simulations made with Geant4. The trigger efficiency for the various physics objects is evaluated using samples of signal overlaid with an average of 80 minimum-bias events ( $\langle \mu \rangle = 80$ ) to reproduce the pile-up conditions expected during Run 3. Rejection of background and trigger rates are obtained from a sample of overlapping minimum-bias events with also  $\langle \mu \rangle = 80$ . For keeping the trigger rates low in Run 3 and the low- $p_T$  thresholds at their present value, additional discriminating criteria are introduced to separate electrons and photons from jets. EM showers can be distinguished from the background of QCD jets due to the electrons and photons by using shower shape variables.

Here, some of the variables which reduce the trigger rates significantly, are presented.

**4.1.3.1 Shower shape analysis** The performance of the following three discriminating variables, chosen for their importance to offline electron identification, is investigated.

$R_\eta$  is the transverse energy measured in a  $3 \times 2$  group of Super Cells in  $\eta \times \phi$  in the middle layer (2), centred around the highest-energy Super Cell, divided by the energy measured in a  $7 \times 2$  group in the same layer:

$$R_\eta = \frac{E_{T,\Delta\eta\times\Delta\phi=0.075\times 0.2}^{(2)}}{E_{T,\Delta\eta\times\Delta\phi=0.175\times 0.2}^{(2)}} \quad (13)$$

$f_3$  is the transverse energy measured in the back layer (3) in an area of size  $\Delta\eta \times \Delta\phi = 0.2 \times 0.2$  divided by the energy deposited in all three layers. The size of the area in which the energies are reconstructed in the front (1) and middle (2) layer is  $\Delta\eta \times \Delta\phi = 0.075 \times 0.2$ :

$$f_3 = \frac{E_{T,\Delta\eta\times\Delta\phi=0.2\times 0.2}^{(3)}}{E_{T,\Delta\eta\times\Delta\phi=0.075\times 0.2}^{(1)} + E_{T,\Delta\eta\times\Delta\phi=0.075\times 0.2}^{(2)} + E_{T,\Delta\eta\times\Delta\phi=0.2\times 0.2}^{(3)}} \quad (14)$$

$\omega_{\eta,2}$  is the spread of the shower in the middle layer (2) in a  $3 \times 2$  Super Cell region, where the sums run over the Super Cells, defined as:

$$\omega_{\eta,2} = \sqrt{\frac{\sum (E_T^2 \times \eta^2)_{\Delta\eta\times\Delta\phi=0.075\times 0.2}}{E_{T,\Delta\eta\times\Delta\phi=0.075\times 0.2}^{(2)}} - \left(\frac{\sum (E_T^2 \times \eta)_{\Delta\eta\times\Delta\phi=0.075\times 0.2}}{E_{T,\Delta\eta\times\Delta\phi=0.075\times 0.2}^{(2)}}\right)^2} \quad (15)$$

In Figure 25 and 26 the distribution of the aforementioned variables for electrons from  $Z \rightarrow e^+e^-$  events is shown.  $R_\eta$  is narrow for electrons and broader for jets.  $\omega_{\eta,2}$  and  $f_3$  is narrower for EM than for hadronic showers.

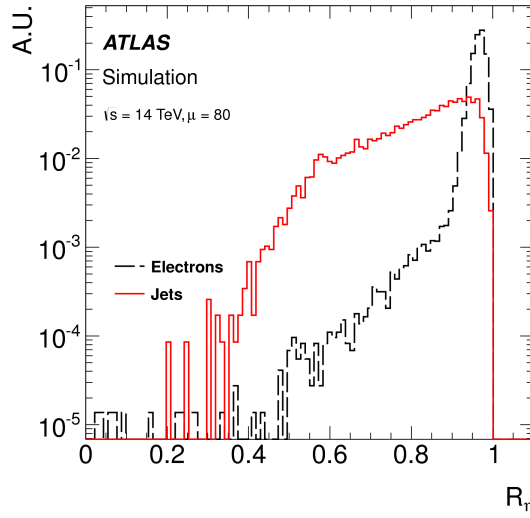


Figure 25: The distribution of  $R_\eta$  for electrons and jets.

**4.1.3.2 Multi-dimensional optimization of shower shape variables** In order to minimize the trigger rate while keeping a high signal efficiency, an optimization of the discriminating variables  $R_\eta, \omega_{\eta,2}$  and  $f_3$  is performed. Additionally, hadronic isolation ( $HadCore \leq 1 \text{ GeV}$ ) is required for each electron

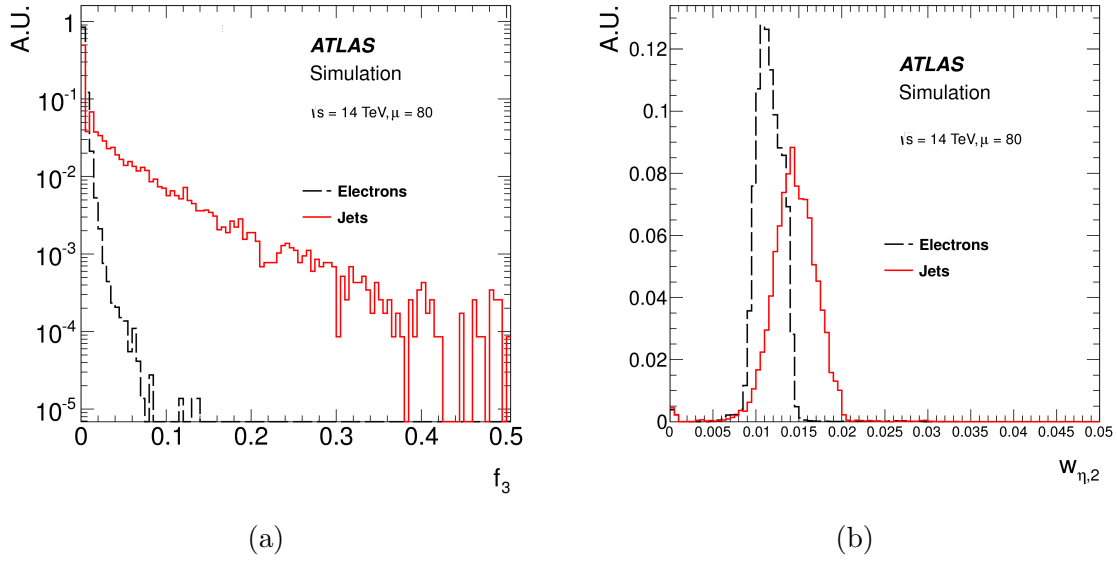


Figure 26: The distribution of  $f_3$  is shown on the left and of  $\omega_{\eta,2}$  on the right.

candidate. *HadCore* is defined as the transverse energy deposited in a  $\Delta\eta \times \Delta\phi = 0.2 \times 0.2$  region of the hadronic calorimeter behind the EM shower. All trigger efficiencies are computed as the fraction of offline electrons with  $p_T > 20$  GeV in the signal sample reconstructed with tight identification requirements that pass the trigger selection.

The dependence of the signal efficiency on the parameter  $R_\eta$  is shown in Figure 27a. Figure 27b shows the corresponding trigger rates as measured from simulated  $\langle \mu \rangle = 80$  events.

The dependence of the trigger rate on  $E_T$  is shown in Figure 28 with applied cuts of optimized values for *HadCore*,  $\omega_{\eta,2}$ ,  $R_\eta$  and  $f_3$ . The use of these new variables allows for a decrease of the trigger rate by up to a factor of 4 for  $p_T \approx 20$  GeV for the same electron efficiency.

The optimized parameters were chosen to be  $R_\eta \geq 0.93$ ,  $\omega_{\eta,2} < 0.0146$  and  $f_3 \leq 0.02$ , yielding a trigger efficiency of 95%. The trigger rates can be further reduced by raising the  $E_T$  threshold.

Additionally to the aforementioned improvements, the better Level-1 EM resolution due to the possible application of layer weights, will sharpen the trigger turn-on curves and further lower the offline threshold. This will lead to an increased signal acceptance for many physics channels, as discussed in section 4.1.4.

**4.1.3.3 Photon performance** Due to the importance of high-sensitivity measurements of the Higgs Boson in the  $\gamma\gamma$  decay mode, it was important to ensure a high photon trigger efficiency with the optimized EM shower shape variables. Simulated  $H \rightarrow \gamma\gamma$  events with a leading photon  $p_T > 40$  GeV have been studied [28]. With the working point at  $R_\eta > 0.93$  and  $\omega_{\eta,2} < 0.0146$  obtained from a  $Z \rightarrow e^+e^-$  sample with electron  $p_T > 20$  GeV the single photon efficiency is

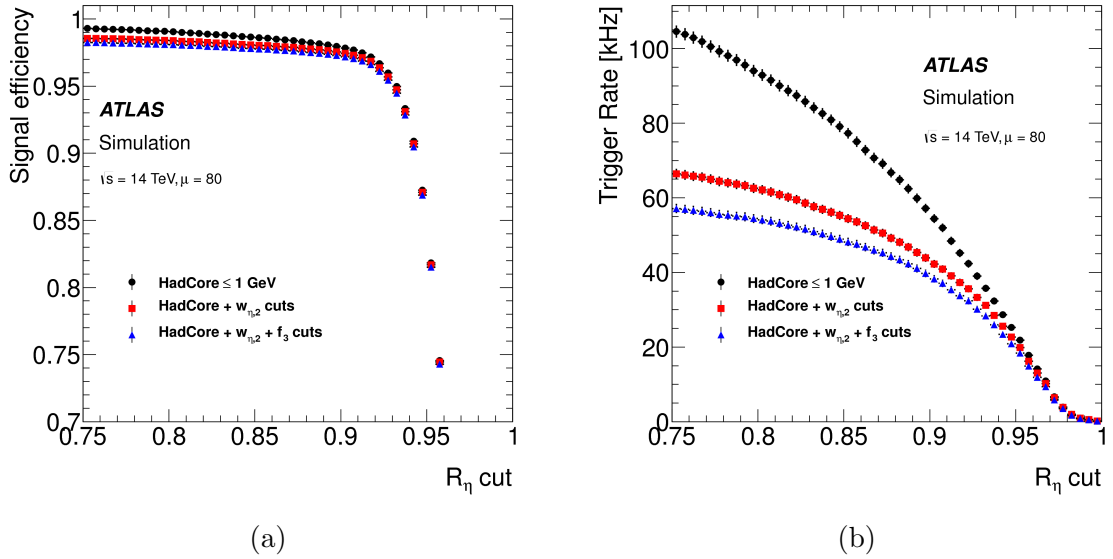


Figure 27: Dependence of the signal efficiency on  $R_\eta$  with *HadCore* requirement and successive cuts on optimized values of  $\omega_{\eta,2}$  and  $f_3$  is shown on the left. On the right one can see the dependence of the trigger rate on  $R_\eta$  with *HadCore* requirement and successive cuts on optimized values of  $\omega_{\eta,2}$  and  $f_3$ .

calculated to be 97.5 %, the di-photon efficiency 94.9 % and the electron efficiency 95 %. The working point was chosen such as to yield the same electron efficiency as during Run 1 conditions.

**4.1.3.4 Expected trigger rates** Some of the expected trigger rates for Run 2 and preliminary results for Run 3 including the improved trigger performance due to the Phase-I upgrade are shown in Table 2.

The final trigger menu for LHC Run 3 will be further developed in the future, using the experience gained during Run 2. However, the menu presented here is used as a guideline for the next Section (4.1.4) to demonstrate the impact of the Liquid Argon Phase-I upgrade on the physics potential in Run 3.

#### 4.1.4 Impact on Higgs physics and other physics channels

The trigger performance results shown were applied to a crucial component of the physics program at the upgraded LHC to show that the Level-1 ATLAS trigger system can deal with the high luminosities and pile-up conditions. The improvements in the single and multi-lepton,  $\tau$ , jets and  $E_T^{\text{miss}}$  triggers are expected to have an impact on many other measurements and searches for new physics.

**4.1.4.1  $H \rightarrow \tau\tau$**  Vector boson fusion (VBF) provides a distinct experimental signature for Higgs boson decays to  $\tau$  leptons due to the additional forward jets present in the final state. Here, the case is taken into account where one  $\tau$  lepton decays leptonically and the other decays hadronically. Signal events consist of one



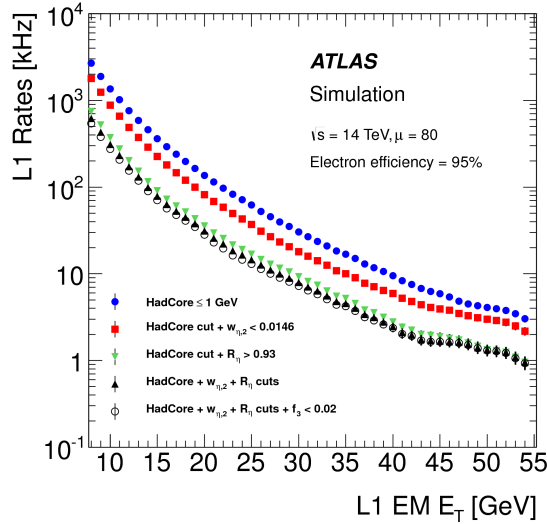


Figure 28: Trigger rates for  $\mathcal{L} = 3 \times 10^{34} \text{ cm}^{-2} \text{ s}^{-1}$  as a function of  $E_T$  thresholds with optimized requirements on  $HadCore$ ,  $\omega_{\eta,2}$ ,  $R_{\eta}$  and  $f_3$ .

	Run 1		Run 2			Run 3		
	Offl. $p_T$ thld. [GeV]	Rate [kHz]		Offl. $p_T$ thld. [GeV]	Rate [kHz]		Offl. $p_T$ thld. [GeV]	Rate [kHz]
EM30	37	130	EM80	100	2.5	EM80	100	2.5
EM total		270			18			20
J75	200	34	J100	200	7.0	J100	200	7.0
Jet / $E_{T,total}^{miss}$		306			25			25

Table 2: Trigger rates of Run 1 and expected trigger rates for Run 2 and Run 3.

isolated electron, one  $\tau_{had}$  candidate, two jets and  $E_T^{miss}$ . The trigger that can record these events is either a single electron trigger or a multi-object trigger such as an electron +  $\tau_{had}$  + jet trigger. Since the electron is a decay product of the  $\tau$  lepton, its  $p_T$  tends to be soft. The  $p_T$  distributions of both the electrons and  $\tau$  leptons are shown in Figure 29.

Table 3 illustrates the impact of various trigger selection criteria. Raising the  $p_T$  requirements for the electron candidate from 20 GeV to 25 GeV and for the  $\tau_{had}$  candidate from 40 GeV to 50 GeV results into a decrease of the signal acceptance by 37%. The loss of acceptance observed when applying all other selection criteria that are used in the analysis of the Run 1 data, but with the above higher thresholds is very similar. For this channel the impact of the Liquid Argon Phase-I upgrade is significant.

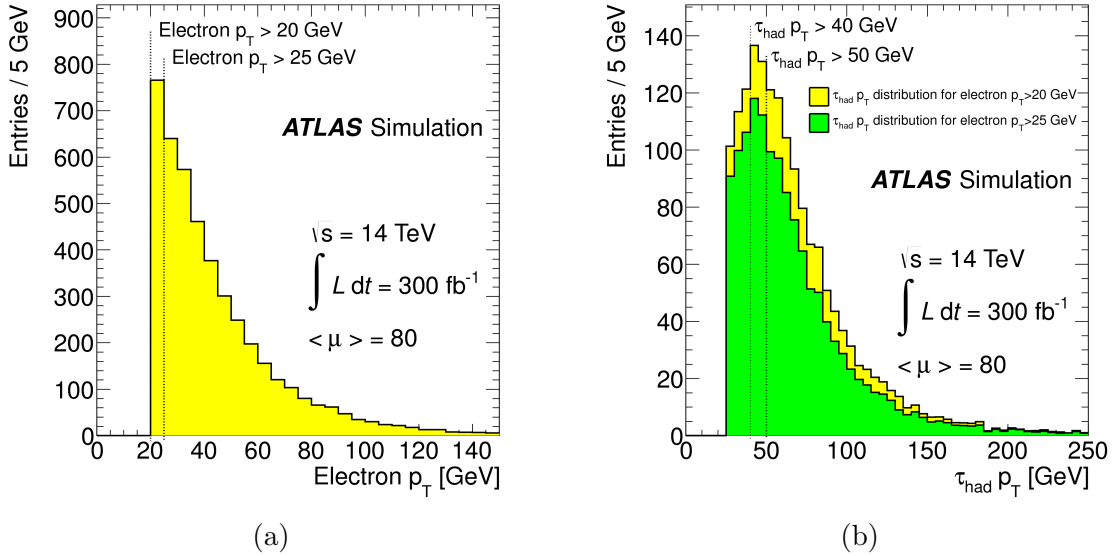


Figure 29: Distribution of electron- (left) and  $\tau - p_T$  (right) after applying a  $p_T > 20$  GeV cut for the left and  $p_T > 25$  GeV for the right plot. For the plots a sample with simulated  $H \rightarrow \tau\tau$  events, where one  $\tau$  decays to an electron and neutrinos and the other  $\tau$  decays hadronically, was used. The offline selection criteria achievable with the Liquid Argon Phase-I upgrade (electron  $p_T > 20$  GeV and  $\tau_{had} p_T > 40$  GeV) as well as those assuming Run 2 conditions (electron  $p_T > 25$  GeV and  $\tau_{had} p_T > 50$  GeV) are indicated with dashed lines.

**4.1.4.2  $H \rightarrow b\bar{b}$  in associated  $(W/Z)H$  production** The  $H \rightarrow b\bar{b}$  decay mode is predicted to have the largest branching fraction (58%) for  $m_H = 125$  GeV in the Standard Model. Associated production of a Higgs boson with a vector boson,  $W$  or  $Z$ , offers a viable possibility to search for these decays because leptonic decays of the vector boson can be efficiently used for triggering and background reduction purposes.

One of the decays of this category is the  $2H \rightarrow \nu\nu b\bar{b}$  decay. It relies on the  $E_T^{miss}$  trigger. For the 2012 data, the offline event selection includes the requirement  $E_T^{miss} > 120$  GeV, corresponding to 85 – 90% trigger efficiency. The higher Level-1  $E_T^{miss}$  thresholds will require raising the offline requirement to  $E_T^{miss} > 200$  GeV. However, with the proposed Liquid Argon Phase-I upgrade an offline requirement of  $E_T^{miss} > 160$  GeV can be achieved. This increase will reduce the signal acceptance by 47% compared to the present analysis. The background is dominated by  $t\bar{t}$  and  $Zb\bar{b}$  and is also reduced by higher  $E_T^{miss}$  thresholds.

**4.1.4.3  $H \rightarrow WW^*$**  This decay mode is of great interest since it directly accesses the  $W$  boson coupling which is central to the Higgs mechanism. The simulated samples have been used to estimate the signal acceptance and significance for different offline selection criteria applied to the leptons compatible with the trigger thresholds used. Di-lepton triggers with 80% efficiency and single-lepton triggers

Trigger requirement	$p_T(e) > 20 \text{ GeV}$ $p_T(\tau) > 40 \text{ GeV}$	$p_T(e) > 25 \text{ GeV}$ $p_T(\tau) > 50 \text{ GeV}$
$e^-$ selection efficiency	$(25.4 \pm 0.2)\%$	$(21.0 \pm 0.2)\%$
$e^-$ and $\tau$ selection efficiencies	$(7.5 \pm 0.1)\%$	$(4.7 \pm 0.1)\%$
Relative acceptance	1	$0.631 \pm 0.015$

Table 3: Efficiency of electron  $p_T$  and  $\tau$   $p_T$  selections for VBF  $H \rightarrow \tau\tau$  events which decay as described in the paragraph before. The last row shows the acceptance loss when raising the electron  $p_T$  selection from 20 to 25 GeV and the  $\tau$   $p_T$  selection from 40 to 50 GeV.

with 90% efficiency are used to include events with the lowest possible  $p_T$  of the sub-leading lepton.

For Run 2, the requirement on the  $p_T$  cuts will become more stringent. Without the Phase-I upgrade this would translate into a considerable signal acceptance loss of 24% for the  $e\nu e\nu$  channel and 12% for the  $e\nu\mu\nu$  channel. The acceptance loss with the proposed selection criteria will only be 3% for  $e\nu e\nu$  and 7% for  $e\nu\mu\nu$ .

#### 4.1.4.4 Diboson and Triboson production and quartic couplings

Processes like  $W\gamma$ ,  $Z\gamma$ ,  $W^\pm W^\pm$ ,  $WZ$  and  $ZZ$  have been studied during Run 1 and their more detailed studies will profit from the lower dilepton and trilepton trigger thresholds.

Quartic couplings which are linked with the mechanism of electroweak symmetry breaking are either probed in vector boson scattering processes like  $W^\pm W^\pm$ ,  $WZ$  and  $ZZ$  with additional forward jets or in triboson production like  $W\gamma\gamma$  etc. Vector boson scattering has not yet been observed in Run 1 and is a major goal of the future LHC program.

#### 4.1.4.5 Supersymmetric (SUSY) particles

The lepton triggers are crucial for searches for electroweak production of SUSY particles, for example the pair production of neutralinos, charginos and sleptons. SUSY searches will benefit from the lower lepton thresholds in the single lepton,  $\tau$ +lepton and multi-lepton triggers. Also the top squark search relies mostly on the single and dilepton triggers.

Searches for strong production of SUSY particles without leptons, for SUSY with degenerate mass spectra and for graviton emission or pair production of dark matter particles rely mostly on the capability of triggering on  $E_T^{\text{miss}}$  in association with jets. Similarly, in SUSY the primary benefit of a lower  $E_T^{\text{miss}}$  requirement is for scenarios where the squarks, gluinos, sleptons, charginos and neutralinos are not much heavier than the Lightest Supersymmetric Particle (LSP).

## 4.2 Implementation of the upgrade of the trigger readout system

The signal to the upgrade branch of the Liquid Argon system starts to split from the old trigger readout path in the linear mixer of the FEBs, as can be seen in Figure 30. The signals for the new path are summed on the LSBs to 4 Super Cells each for the middle and front layer and to one Super Cell for presampler and back layer. These signals are transmitted via the new baseplane to the *LAr Trigger Digitizer Board* (LTDB) where they are digitized and transmitted to the back end via optical links. In order to keep the old trigger readout path operational, the analogue signals are summed to the granularity of the legacy trigger and fed back to the TBB, where they are summed to trigger towers.

The thresholds of the Level-1 trigger system are in units of transverse energy, whereas the signals from the calorimeters are proportional to energy. In the existing system, the conversion factor of  $\sin\Theta$  is applied to signals in the trigger chain in several steps:

- Through the choice of the preamplifier.
- Through the gain of the linear mixer in the FEBs for all calorimeters.
- Through the  $\eta$ -dependent gains that are applied in the TBB for the EM calorimeters.

In the upgraded system, the choice of preamplifiers and gains in the FEBs will remain unchanged. How the  $\eta$ -dependent gains will be applied is not yet decided; they may be included in the analogue section of the LTDB or as a factor in the calibration constant which is applied in the back end electronics.

## 4.3 Front end electronics

The Phase-I upgrade requires the following modifications in the front end electronics:

- New LSBs: The current LSBs are plugged on the FEBs to produce  $\Delta\eta \times \Delta\phi = 0.1 \times 0.1$  analogue sum signals in a given layer of the calorimeter. The new LSBs produce finer granularity Super Cell signals in the front and middle layers.
- New Baseplane: The new baseplane will allocate new slots for the LTDBs. A much larger number of signals are transferred from the FEBs to the LTDB than currently in the trigger chain. The LSB also routes the legacy trigger signals to the TBB or TDB (Tower Driver Board, the counterpart of the TBB in the endcaps).
- LTDB: The LTDB receives Super Cell signals, digitizes them and transmits them to the back end digital processors. It also forms layer sum signals and sends them to the TBB. Thus, the analogue trigger chain remains operational.

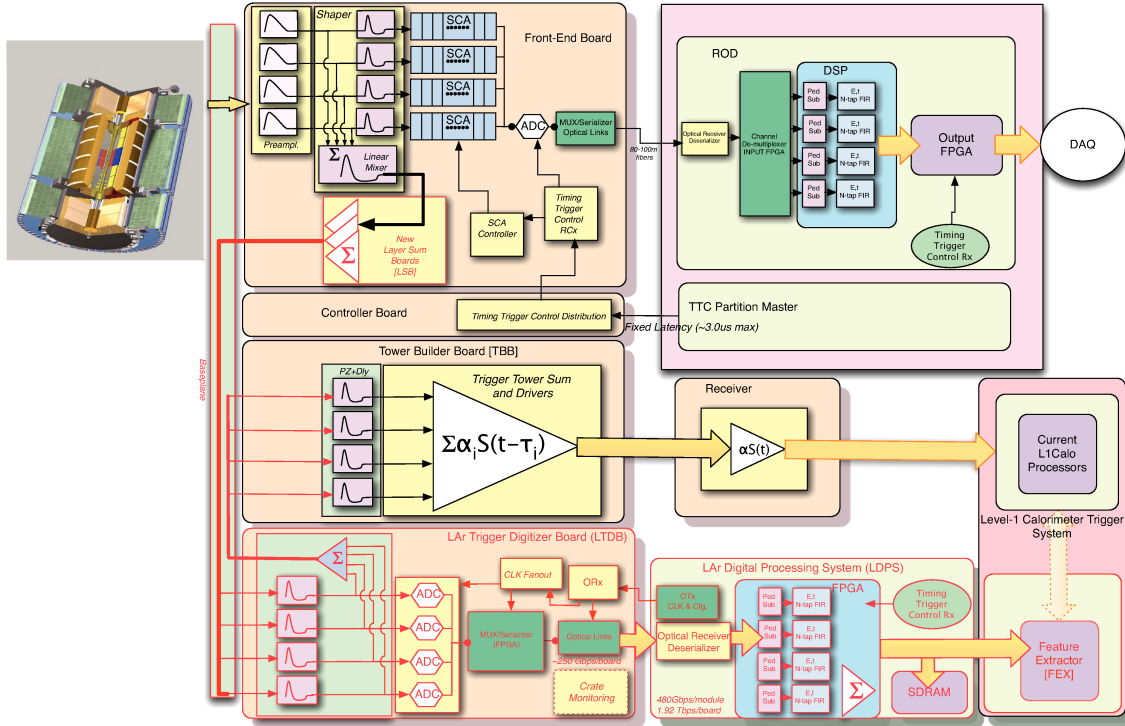


Figure 30: The new components of the architecture of the liquid argon Phase-I trigger readout upgrade are indicated by the red outlines and arrows.

#### 4.3.1 Modifications to the front end crate

In order to replace the baseplane, it will be necessary to unplug the so-called warm cables, which form the connection between the cryostat feedthrough and the baseplane. Then they will have to be repositioned to their new slot positions and reconnected to the replacement baseplane.

The new baseplane will be similar to the one used so far, but will have some additional features:

- There will be three high-density hard metric connectors for each of the LTDB slots as well as higher density baseplane interconnects between the analogue signal outputs of the FEB, the LTDB and the legacy TBB inputs.
- Routing of the signals will be more complex for the new baseplane. Super Cell signals will be transmitted to the LTDB. For the cases where the Super Cell is identical to the trigger tower (the so-called spectator channels), the signal goes directly from the FEB to both the LTDB and the TBB or TDB.
- Certain signal groups for some calorimeter sections may only be partially used or not used at all. Designated LTDB inputs are grounded on the baseplane when not used, LTDB outputs are left unconnected on the baseplane.

In order to dispatch the optical link signals from UX15 to USA-15 one fibre cable will be installed for each FEC. The mapping of cables to the back end electronics

modules (LDPBs as shown in Figure 30) will be guided by optimal placing of the Super Cells to trigger towers in an adjacent  $\eta \times \phi$  space.

### 4.3.2 LTDB

The LTDB will be responsible for the formation of the legacy layer sum signals as well as the digitization of the Super Cell signals. Each LTDB will process up to 320 Super Cell signals. There are typically 10 Super Cells per trigger tower in the barrel part, but less in the endcaps. A schematic block diagram of the proposed LTDB is shown in Figure 31.

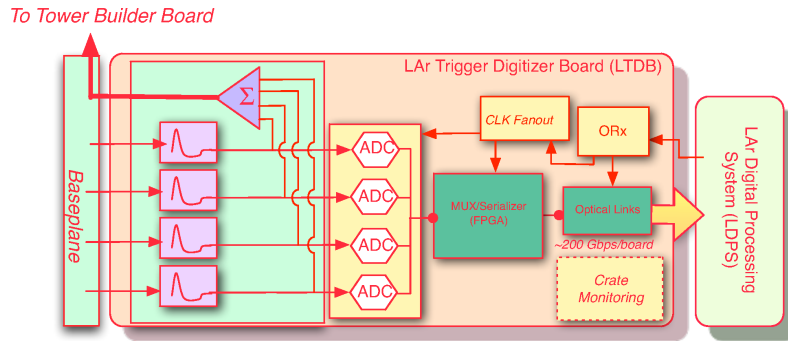


Figure 31: Schematic block diagram of the LAr Trigger Digitizer Board (LTDB). The analogue signals transmitted from the detector front end through the baseplane to the LTDB are digitized and sent to the LAr Digital Processing System (LDPS) via optical links. In order to keep the legacy trigger readout operational the analogue signals are routed to the TBB where they are summed.

There is one LTDB per baseplane in each EMB, HEC and EMEC Standard Crate, but in the EMEC Special and FCal crate, two are required. In total, 124 LTDBs will be installed in the system.

**4.3.2.1 Analogue signal treatment** The analogue section of the LTDB has to provide the appropriate gain, shaping and offset such that the 12-bit dynamic range of the ADC operates without sacrificing the value of the signal to noise ratio. Thus, the quantization error should not exceed the intrinsic electronic noise arising from the preamplifiers, the linear mixer and the summing amplifiers.

The Phase-I upgrade must also maintain the functionality of the trigger chain. In layers where the size of the Super Cell is the same as that of the legacy trigger tower, the signals are sent directly to both the TBB/TDB and the LTDB.

When the baseplane signals from the LSB have a finer granularity in  $\eta$  than a single trigger tower, the signals must be received from the baseplane with a low-impedance termination. They are used for the generation of ADC signals and summed in groups of four to provide the TBB with signals corresponding to trigger towers.

The cases summarized are:

- Spectator signals: The TBB/TDB signal is unchanged from the one used in the current system and the LTDB utilizes it to create digitized representations. This can occur two ways: low-impedance mode (the signal from the LSB is terminated in  $50\ \Omega$  at the LTDB) and high-impedance mode (the signal from the LSB is terminated in  $50\ \Omega$  at the TBB/TDB and the LTDB receives it using a high-impedance tap).
- Summed signals: The LTDB terminates a set of four signals from the baseplane and sums them together, the summed output being transmitted to the TBB.

To perform these different functions, the LTDB must have two different analogue signal processing configurations. A block diagram illustrating these functions is shown in Figure 32.

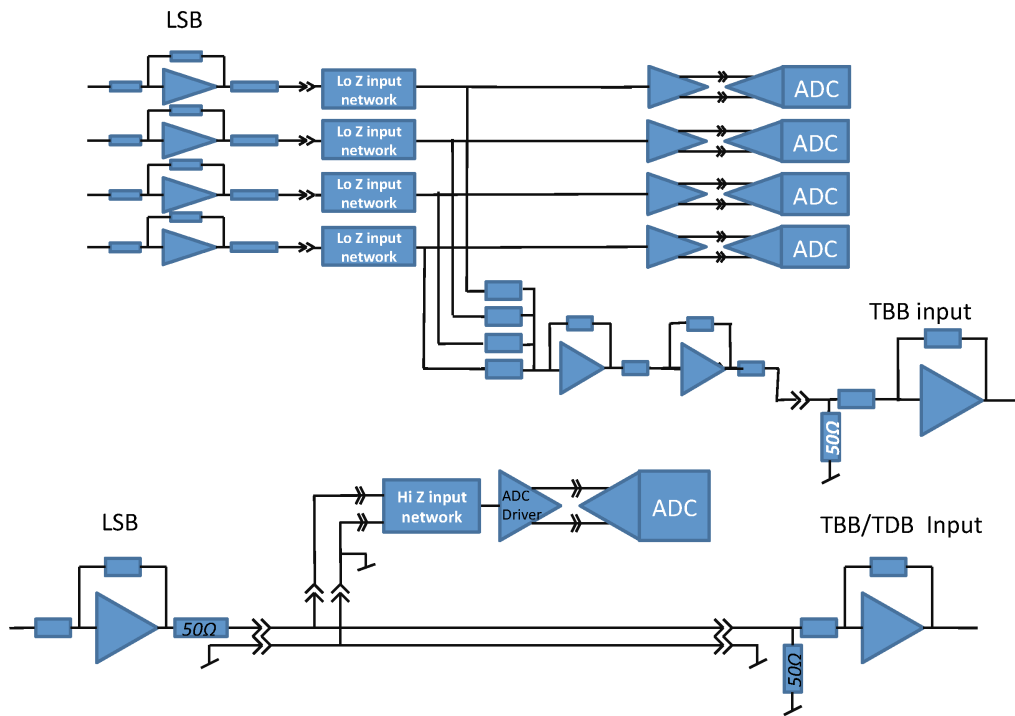


Figure 32: Schematic block diagram of the analogue section of the LTDB.

**4.3.2.2 Digital signal treatment** A block diagram of the LTDB digital section is shown in Figure 33. There are two signal flow paths: the data link and the control (TTC) link. The digital processing chain which drives the data link is responsible for signal digitization and transmission.

The Super Cell signals are multiplexed and serialized in LOCx2 and transmitted via the optical transmitter [42]. The TTC link is responsible for transmission of clock signals, slow control and monitoring communications.

The TTC signals are delivered to the LTDB via optical fibres. The control link consists of three components, as illustrated in Fig. 33: the VTRx, the GBTx and

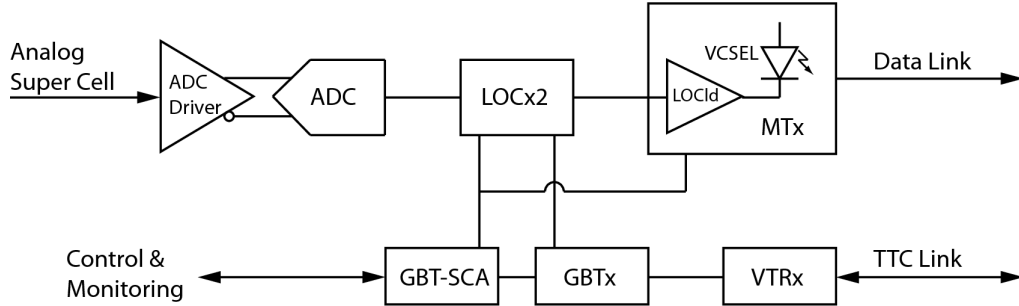


Figure 33: Schematic block diagram of the digital section of the LTDB.

the GBT-SCA (Slow Control Adapter). Each SCA has 32 channels of slow ADCs for monitoring purposes. The bunch-crossing ID counters in the LOCx2 need to be reset synchronously within an LHC clock cycle. The GBTx data output, which is synchronous to the LHC clock, will be used as a reset. Super Cell signals must be digitized at 40 MHz by the ADC on the LTDB. Digital data from the ADC are prepared for high speed serial transmission over fibre. Data of 8 ADC channels are multiplexed into a bit stream of 5.12 Gbps and sent out of the LOCx2. This signal is amplified, converted into an optical signal on a VCSEL and launched into an optical fibre. The elements where these operations are performed are mounted on the so-called MTx.

**4.3.2.3 Power supply** The electrical power required by the front end electronics is delivered by a *Low Voltage Power Supply* (LVPS). The LVPS is made of DC-DC converters mounted on the detector adjacent to the corresponding FEC and powered by 280 VDC generated in USA-15.

During Phase-I operation, the LTDBs will need to draw their power from the LVPS on the detector. The current power consumption is less than 75% of the total 3.2 kW these supplies can deliver. Thus, sufficient power reserve for the LTDB operation is available.

## 4.4 Back end electronics

### 4.4.1 Introduction

The LDPS, which is the back end electronics system of the Phase-I upgrade, receives the digital signals from the LTDBs, computes the transverse energy for each Super Cell ( $E_T^{\text{SuperCell}}$ ) every 25 ns and transmits them to the Level-1 calorimeter trigger system (L1Calo). A block diagram of the LDPS is shown in Figure 34.

The LDPS receives about 25 Tbps and transmits approximately 41 Tbps over optical fibres to the L1Calo system. It has to be integrated in the ATLAS data acquisition system and synchronized with the LHC clock.

The LDPS is made up of 31 LAr Digital Processing Blades (LDPBs) housed in three ATCA (Advanced Telecom Computer Architecture) shelves. Each LDPB is



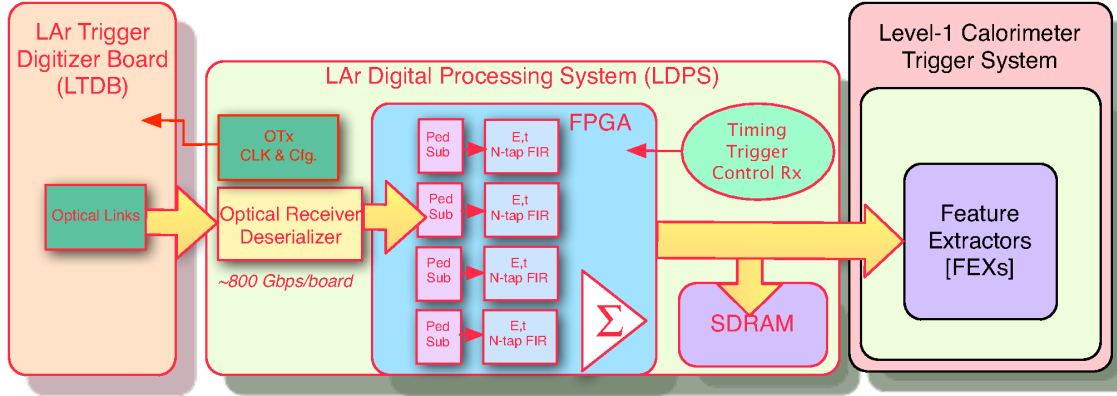


Figure 34: Illustration of the LDPS, which receives the Super Cell signals from the LTDBs, extracts the  $E_T^{\text{SuperCell}}$  and transmits the values to the L1Calo system.

made of one carrier board equipped with four Advanced Mezzanine Cards (AMCs), which contain a powerful FPGA which processes data of up to 320 Super Cells.

In addition to the data transmission, the LDPS must distribute the ATLAS trigger, Timing and Control (TTC) signals to the LTDB and LDPBs, configure the boards in the system, monitor the TDAQ system and send hardware status information to the ATLAS Detector and Control System (DCS) [43].

#### 4.4.2 LDPS electronics components

The ATCA platform is 12 or 13 rack units high and houses up to 14 boards. Each LDPB consists of an ATCA carrier board equipped with four AMCs. The design of the AMC is build around one FPGA, as shown in Figure 35.

The chosen FPGA must have 54 transceivers, 48 for signals, 4 for one fast link and up to 2 for the GBT link. The GBT links are used between the LDPBs and the *Front End Link Interface eXchange* (FELIX) [44] and between FELIX and TDAQ for sending data to ATLAS events. The FPGA receivers are running at 5.12 Gbps and the transmitters at 11.2 Gbps.

As mentioned before and as shown in Figure 36, each LDPB carrier board holds four AMCs.

The main components on the carrier board are the following (colors are referring to those in Figure 36):

- *FPGA* (brown): The FPGA interfaces the high-speed link coming from the AMCs to the 10/40 GbE network for data monitoring and transmits the TTC information (green) from the GBT link (red) to the AMCs.
- *GbE switch* (light blue): Configuration, monitoring and reprogramming of the AMCs and carrier FPGAs are done through the GbE switch. It also interconnects the AMCs, IPMC and carrier FPGA with the ATCA switches.
- *IPMC* (purple): The IPMC [45] is in communication with the shelf manager through the IPMB.

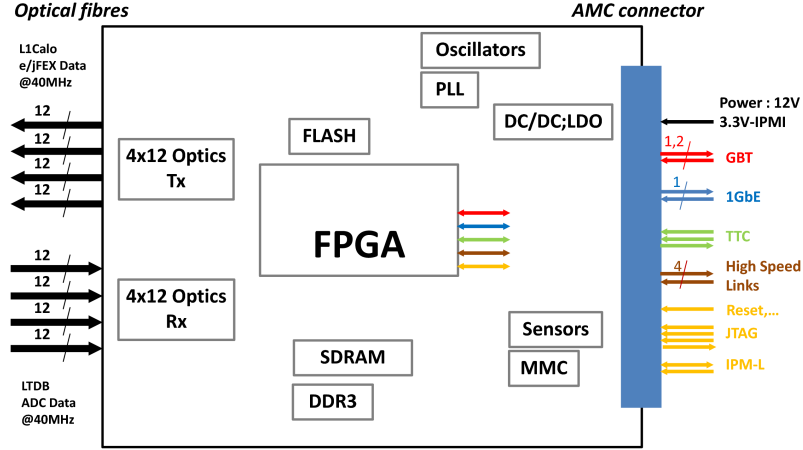


Figure 35: The AMC, built around a high-bandwidth FPGA, transmits data over  $4 \times 12$  optical fibres. The DC/DC converter and Low Drop Out (LDO) regulator perform the power conversion from the AMC 12 V supply to the necessary voltages for the components. Each GBT link uses an FPGA transceiver and connects it to the carrier board. The GbE link serves for configuration and monitoring of the AMC and for reprogramming the Flash memory. TTC commands are routed from the carrier board to the AMC FPGA.

- *ATCA power block* (dark blue): The power block provides power to the carrier components and the AMCs from the 48 V shelf power.

#### 4.4.3 LDPB board pre-prototype

In order to test a possible LDPB layout, four ATCA boards have been built and tested with fibres running up to 8.6 Gbps. A photograph of one of the boards can be seen in Figure 37. Two of the boards have been used for the demonstrator tests at the EMF (see Chapter 6) and two have been installed in USA-15 for the ATLAS demonstrator.

#### 4.4.4 Data flow through the back end system

In Figure 38, the flow of the signals through the back end system, which is described in detail in the following, is shown.

The ADC Data from the LTDBs are transmitted to the AMCs at a rate of  $\approx 25$  Tbps at 40 MHz. From the AMCs the  $E_T^{\text{SuperCell}}$  data are transmitted at about 41 Tbps to the *eFEX* and *jFEX* (electron and jet feature extractor) [46] systems of L1Calo. A part of the ADC and e/jFEX data are transmitted to the PC farm for data monitoring. For the monitoring of the LTDB slow control data are transferred to the Partition Master PC. The needed data for monitoring the LDPB and ATCA status are sent from the shelf manager to the DCS.

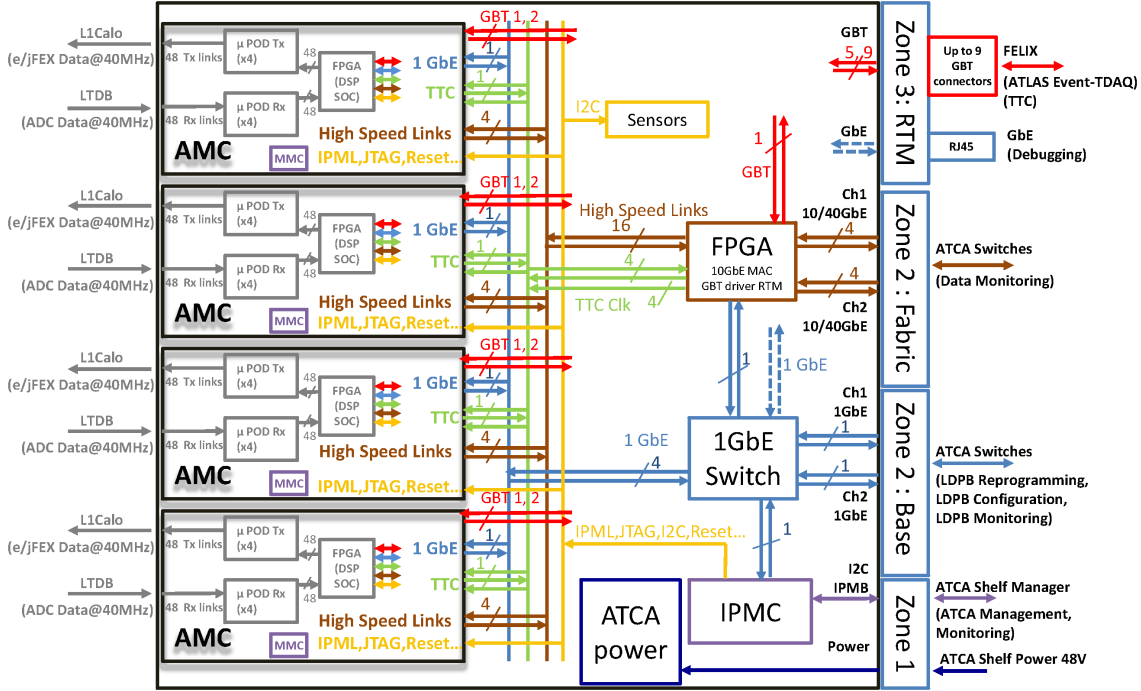


Figure 36: The block diagram shows a carrier board on which four AMCs are mounted.

#### 4.4.5 Firmware on AMC

The firmware on the AMC handles several high speed links in the input from the LTDB. Every 25 ns the  $\Sigma E_T^{\text{SuperCell}}$  is reconstructed by applying a filtering algorithm. The results are sent to the L1Calo FEXs and the readout and monitoring data are buffered until a Level-1 accept is received, in which case the data is sent to TDAQ.

The first step the firmware has to perform is the deserialization and demultiplexing of the incoming data. Then the Super Cell transverse algorithms are calculated with dedicated filtering algorithms. The  $\Sigma E_T^{\text{SuperCell}}$  are then encoded into 10 bit words. In case of saturated pulses, which have a different shape than nominal pulses, a transverse energy might be assigned to the wrong bunch crossing. Therefore, this information is recuperated from a neighbouring Super Cell in case of saturation.

Super Cells will be grouped and summed for transmission for each L1Calo Feature Extraction (FEX). As mentioned before, the input waveform data and the filtering output have to be buffered pending a Level-1 accept. Hence, the FPGA has to have sufficient memory resources.

### 4.5 Towards the ATLAS LAr calorimeter Phase-II upgrade

During long shutdown 2, which will start in 2019, the upgraded trigger electronics for the ATLAS Liquid Argon calorimeter will be installed and in long shut down 3 the main readout electronics will be completely replaced in order to continue

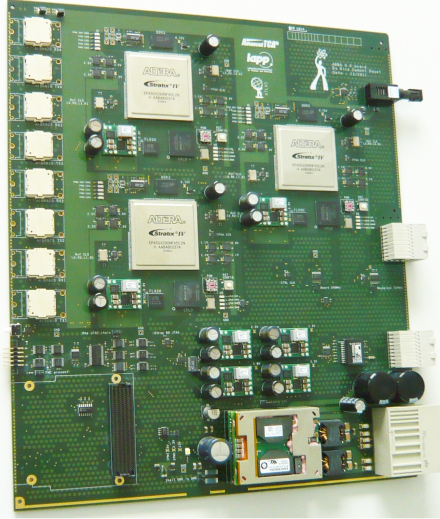


Figure 37: The LDPB pre-prototype, equipped with three FPGAs, has a size of  $322 \text{ mm} \times 280 \text{ mm}$ .

operation at the full potential during the HL-LHC run.

Figure 39 shows the readout architecture planned for the Phase-II upgrades:

- The Phase-I upgrade components will be maintained during the HL-LHC run.
- The trigger electronics used during Run 1 and 2 (greyed out in the figure) will be decommissioned.
- The main readout electronics will be completely replaced by new FEBs, which will digitize the signals at each bunch crossing and send them over fast optical links to the back end electronics .

The hardware-based first level trigger will be divided into a Level-0 and Level-1 sub-system:

- The Level-0 trigger calorimeter trigger is made out of the LTDB, the LDPS, and the FEX systems which will be installed during long shutdown 2 (see Section 4.4). The rate is expected to be around 1 MHz and the latency approximately  $10 \mu\text{s}$ .
- The Level-1 trigger will access the full granularity detector information to further enhance discrimination against backgrounds. The Level-1 trigger is expected to work at a rate of around 40 kHz and a latency of approximately  $30 \mu\text{s}$ .

The Phase-I upgrade project is fully compatible with the overall ATLAS upgrade described in [47].

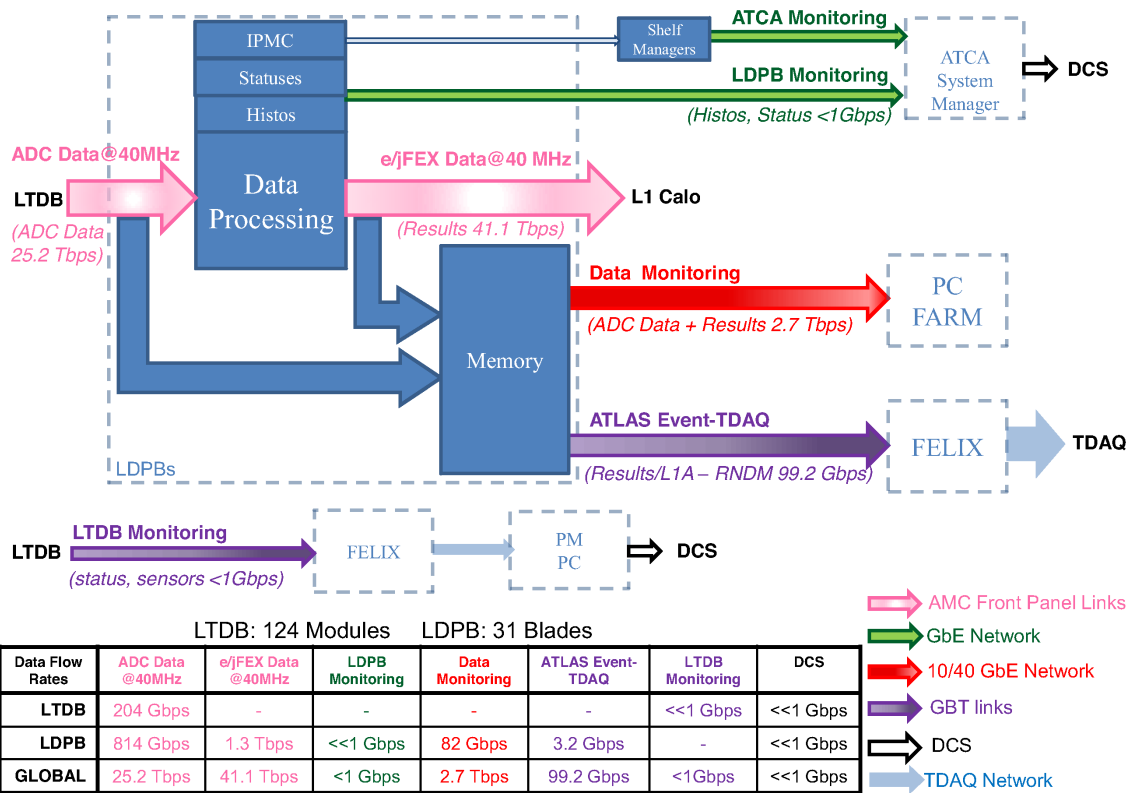


Figure 38: The data paths of the LDPBs are shown. The data sources are represented by blue boxes, the hardware elements by dashed lines.

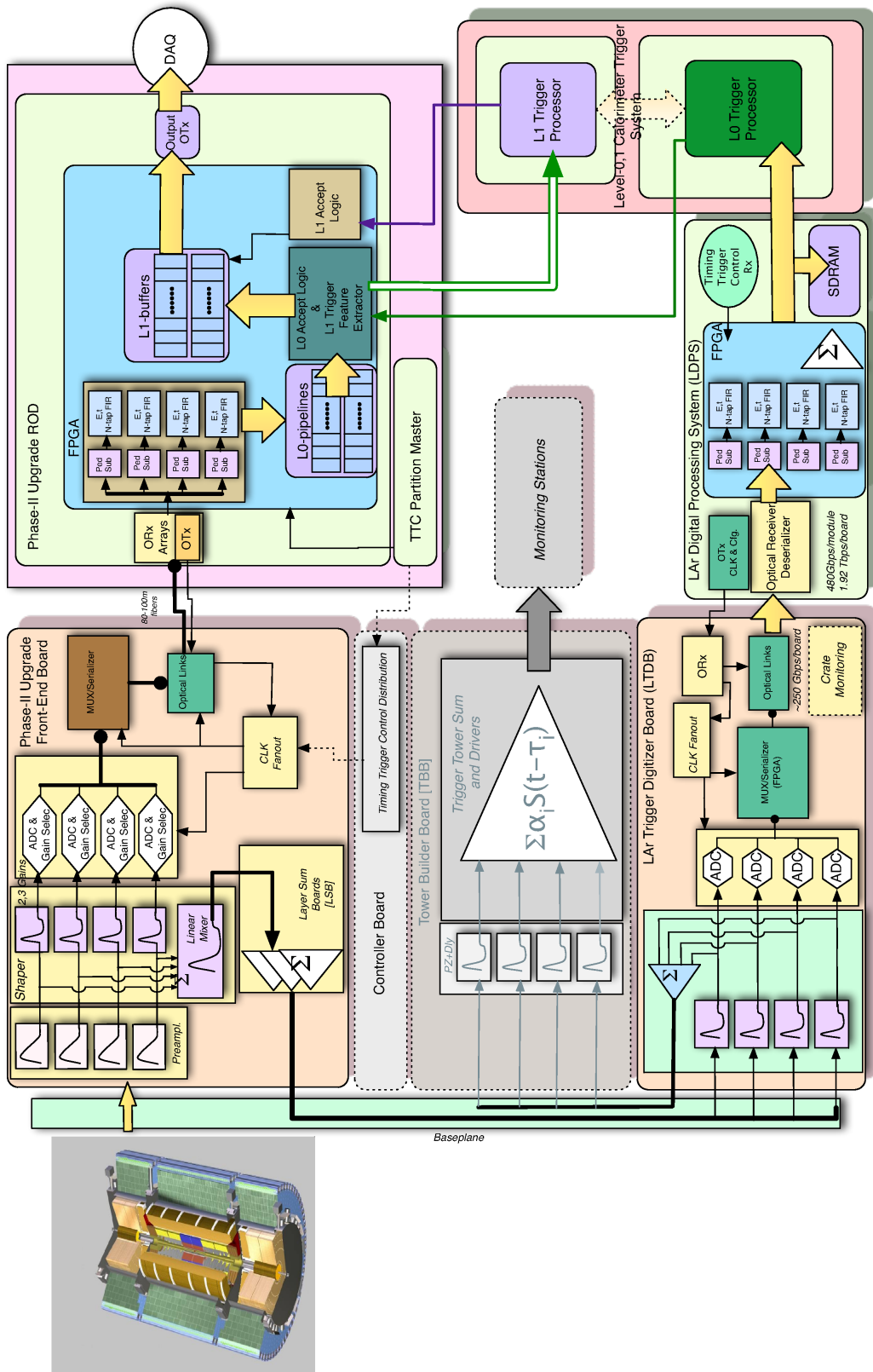


Figure 39: Schematic block diagram of the Liquid Argon readout architecture for Phase-II. The Front End Boards will be replaced and the trigger readout used during Run 1 and 2 will be decommissioned.

## 5 Bunch-crossing Multiplexing studies

### 5.1 Introduction

For each LHC bunch-crossing, the current Level-1 calorimeter trigger system has to decide whether a potentially interesting interaction has occurred in the detector. Every 25 ns the following information is extracted by the so-called pre-processor:

- The transverse energy deposited in a trigger tower during an interaction.
- The corresponding bunch-crossing for that energy deposition.

The energy deposition is then examined by the cluster processors to see if the patterns match the expectations for interesting interactions.

For each of the  $\approx 7200$  trigger towers an analogue signal is sent to the Level-1 calorimeter trigger. The height of the signal corresponds to the deposited transverse energy and the position of the maximum identifies the bunch-crossing. The pulse shape for non-saturated pulses is a linear function of the amplitude, which means that it is not energy dependent.

The linear transverse energy range of a trigger tower goes up to 250 GeV. After that point saturation of the trigger tower signals will occur. Saturation distorts the shape of the analogue signal. Unlike for the non-saturated pulses, the saturated ones are energy dependent and their shape changes with the amplitude. Hence, there is a dedicated algorithm for finding the corresponding bunch-crossing for saturated pulses which is capable of dealing with distorted pulse shapes.

The bunch-crossing multiplexing (BCMUX) algorithm is a data transmission scheme which doubles the serial link bandwidth from the pre-processor to the cluster processor. It makes use of the nature of the non-saturated BCID algorithm which produces empty time slices after it has identified a bunch-crossing. This empty time slice can be used to transmit the energy value of a neighbouring trigger tower. The big advantage of the algorithm is that it halves the number of transceiver chips, connectors and cables from about 7200 to 3600. This has a large implication for the architecture of the Level-1 calorimeter trigger which can be significantly reduced in size and lower the overall costs.

For non-saturated pulses, the BCMUX algorithm selects two out of four energy measurements in pairs of two trigger towers and two subsequent bunch-crossings. This algorithm is compatible with the maximum peak-finder algorithm currently used by the pre-processor system.

For the finer granularity Super Cells it may lead to too frequent loss of data because if data is transmitted for one bunch-crossing, the data for the next one may be suppressed. Figure 40 shows the probability that the energy deposited in an electron shower in a Super Cell is higher than the pile-up noise for the front (left) and middle (right) layer of the Liquid Argon calorimeter.

In Super Cells which are two units away from the Super Cell with the highest energy deposit, the pile-up noise might be mistaken for signal in 25 % of the cases. Hence, transmission of all Super Cell data may be preferred to the multiplexing.

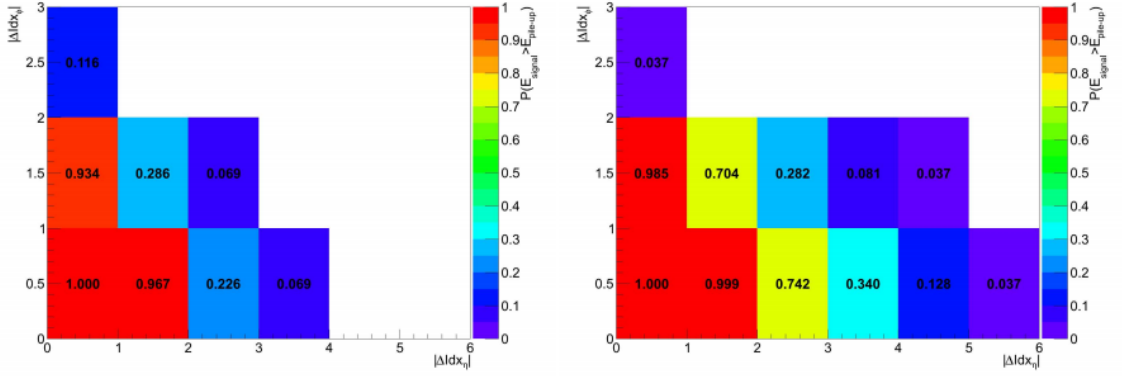


Figure 40: The probability that the energy deposited in an electron shower in a Super Cell is larger than the energy of the pile-up noise for  $\langle \mu \rangle = 200$  for the front (left) and middle (right) layer of the Liquid Argon calorimeter. The Super Cell with the highest energy is in the bottom left corner.

Table 4: Logic table for BCMUX. X (Y) is an 8 bit value of trigger tower A (B).

Case	tower A (8 bit)		tower B (8 bit)		BCMUX output (8+1 bit)	
	$BC_i$	$BC_{i+1}$	$BC_i$	$BC_{i+1}$	$BC_i, \text{flag}_i$	$BC_{i+1}, \text{flag}_{i+1}$
1	0	-	0	-	0,0	-
2	X	0	0	0	X,0	0,1
3	X	0	0	Y	X,0	Y,1
4	X	0	Y	0	X,0	Y,0
5	0	X	Y	0	Y,1	X,1
6	0	0	Y	0	Y,1	0,1

A further problem could be that jets are mistaken for electrons when looking at the parameter  $R_\eta$ , which was introduced in equation 13.

## 5.2 Implementation of BCMUX

The peak finder algorithm takes three consecutive samples and compares them. If the following condition is not fulfilled

$$P_{t+1} \leq P_t > P_{t-1} \quad (16)$$

where  $P_t$  is the digitized pulse amplitude of a trigger tower signal at time slice  $t$ , it will set all  $P_i$  to zero. Hence, the bunch-crossing after a pulse is always empty. The BCMUX scheme uses that empty slices to transmit the values of a neighbouring trigger tower.

The digital input data to the BCMUX scheme are two 8 bit trigger tower channels A and B and a flag bit which identifies the transmitted trigger tower and the corresponding time slice.



Table 4 shows all possible logic states for the BCMUX scheme. On the first bunch-crossing ( $BC_i$ ), the first non-zero trigger tower data out of A and B are sent out with a flag bit indicating whether it was A or B. On the second bunch-crossing ( $BC_{i+1}$ ) the other tower is sent with a flag bit indicating whether it was the same bunch-crossing ( $BC_i$ ) or the one after. This means that the flag bit has two different meanings for the two bunch-crossings. It indicates the trigger tower at the first and the bunch-crossing at the second bunch-crossing. At the receiving end, the data words have to be demultiplexed. The first time slice is buffered until the second time slice arrives which introduces additional 25 ns to the trigger latency.

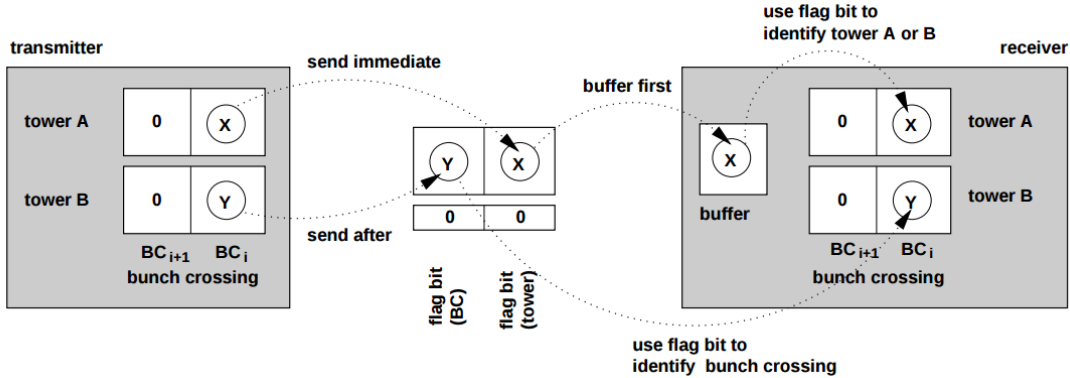


Figure 41: Illustration of the logic state 4 of Table 4. Figure from [48].

For the logic state 4 in Table 4 the BCMUX scheme is illustrated in Figure 41. The multiplexing of two trigger tower channels A and B and the buffering of the first bunch-crossing is shown as well as the demultiplexing at the receiver end.

### 5.3 Simplified BCMUX algorithm

For the study presented here, the BCMUX algorithm was somewhat simplified and the worst case scenario evaluated. One event was analyzed at a time, hence, there was no multiplexing of bunch-crossings. Positive energies within electron or jet showers were set to zero with a probability depending on how big the energy deposition is. Negative energies were zeroed out. All energies were quantized with the least significant bit being 125 MeV. Also the effect of smaller quantization values was studied. Only the calorimeter middle layer was considered for this study, because most of the particle energy is deposited there and usually the value for the  $R_\eta$  variable is computed within this layer.

First the probability was estimated that pile-up is higher than signal for all Super Cells in an  $R_\eta$  cluster (Figure 42). With that probability a particular energy was set to 0. The probabilities were estimated for four separate  $\eta$  slices (0-1.4, 1.4-1.8, 1.8-2.5) for both electrons and jets.

The samples used for the study are Monte Carlo min-bias samples with a pile-up of  $\langle \mu \rangle = 80$  for the evaluation of the effect of the bandwidth reduction on jets and  $Z \rightarrow e^+e^-$  samples for the evaluation of the electrons.

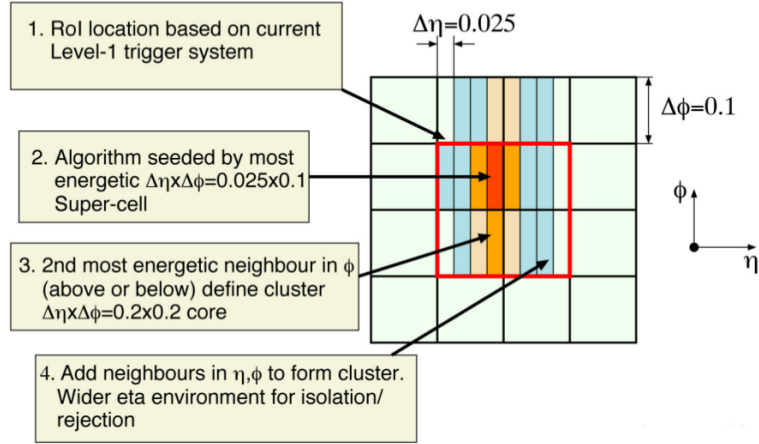


Figure 42: One  $R_\eta$  cluster is defined by taking the most energetic Super Cell found in an RoI which is defined by the Level-1 trigger system. The second most energetic neighbouring Super Cell in  $\phi$  defines the cluster core, around which neighbours in  $\eta$  and  $\phi$  are added to form the complete cluster.

**5.3.0.1 Profile of probability for electrons** For electrons with a  $p_T > 30$  GeV the probability was computed that the energy deposited by it is zeroed out because of the underlying pile-up. The results are shown for the Super Cell neighbours in  $\phi$  and  $\eta$  in Figure 43 and 44. In addition the Super Cell transverse energy distribution in GeV is shown below the probability pattern plots for all  $\eta$  slices.

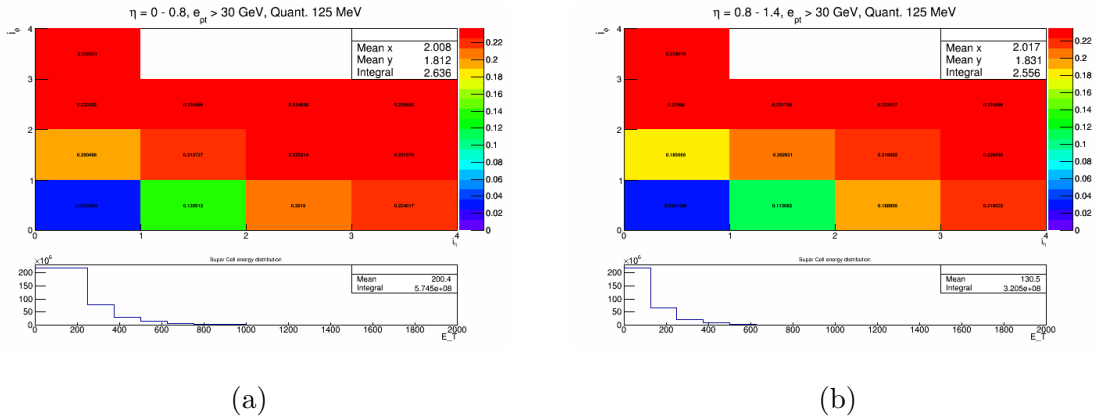
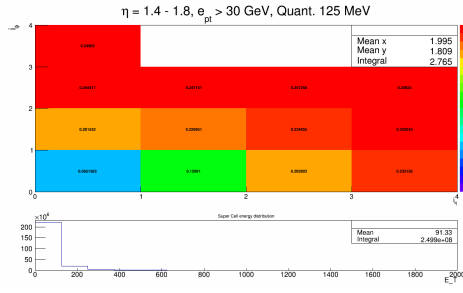


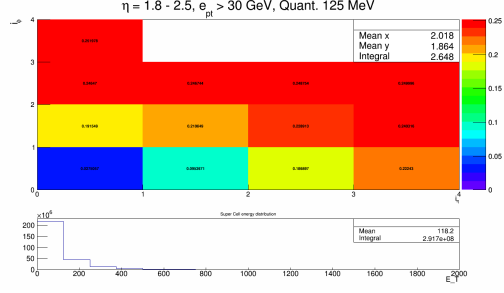
Figure 43: Pattern of probability for electrons for  $\eta$  slice 0-0.8 (left) and  $\eta$  slice 0.8-1.4 (right).

The probability that the first neighbour in  $\phi$  or  $\eta$  is mistaken for pile-up is 10-20%. The probabilities for the second neighbours range already above 20%.

**5.3.0.2 Profile of probability for jets** For jets with a  $p_T > 10$  GeV the probability was computed that the energy deposited by it is zeroed out because of



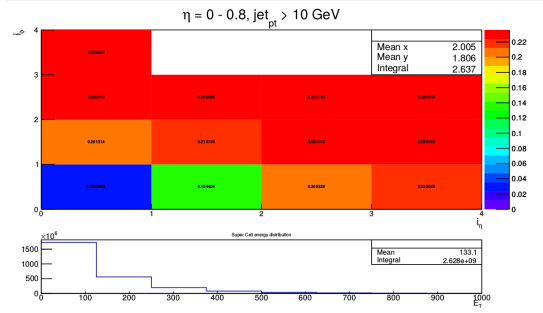
(a)



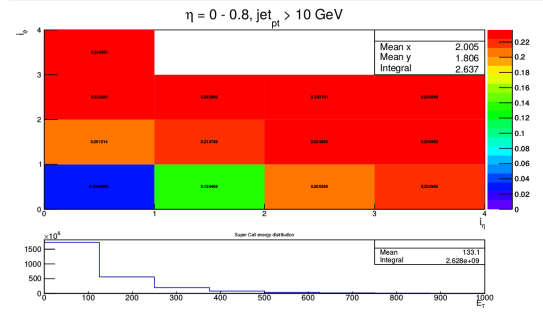
(b)

Figure 44: Pattern of probability for electrons for  $\eta$  slice 1.4-1.8 (left) and  $\eta$  slice 1.8-2.5 (right).

the underlying pile-up. The results are shown for the Super Cell neighbours in  $\phi$  and  $\eta$  in Figure 45 and 46, including the Super Cell energy distribution in GeV below each probability pattern plot.



(a)



(b)

Figure 45: Pattern of probability for jets for  $\eta$  slice 0-0.8 (left) and  $\eta$  slice 0.8-1.4 (right).

As for electrons, the probability that the first neighbour in  $\phi$  or  $\eta$  is mistaken for pile-up is 10-20% and for the second neighbours above 20%.

**5.3.0.3 Effect on  $R_\eta$**  The next step was to compare the distributions of  $R_\eta$  with and without the bandwidth reduction. Comparisons were done for both electrons and jets. Only the distributions for  $\eta = 0 - 0.8$  are shown here because the results are equivalent to the distributions in the other  $\eta$  slices.

As can be seen from the distributions in Figure 47,  $R_\eta$  and  $R_{\eta, \text{mux}}$  are identical for both electrons and jets. The reason is that with a LSB of 125 MeV, most energies in the  $R_{7 \times 2}$  region are anyway cancelled out because the cell energies are low, as explained in Figure 48.

**5.3.0.4 Different quantizations for electrons** The effect of different quantization schemes on the  $R_\eta$  and  $R_{\eta, \text{mux}}$  distributions was determined for

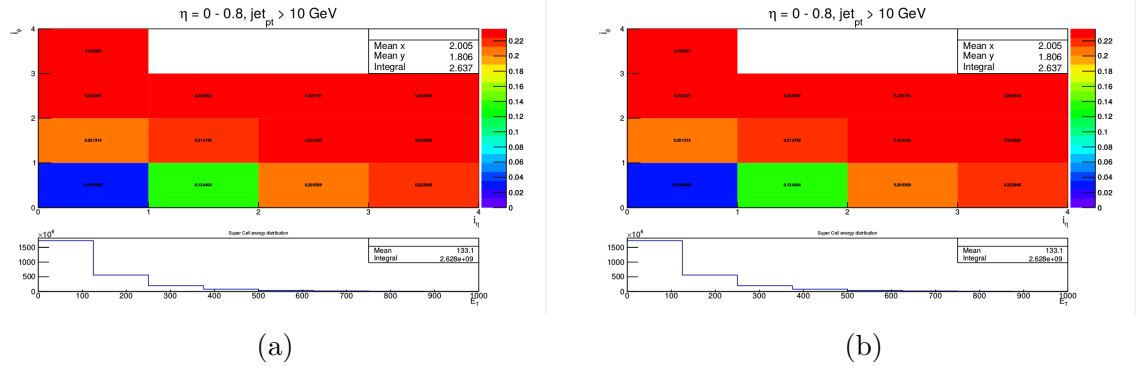


Figure 46: Pattern of probability for jets for  $\eta$  slice 1.4-1.8 (left) and  $\eta$  slice 1.8-2.5 (right).

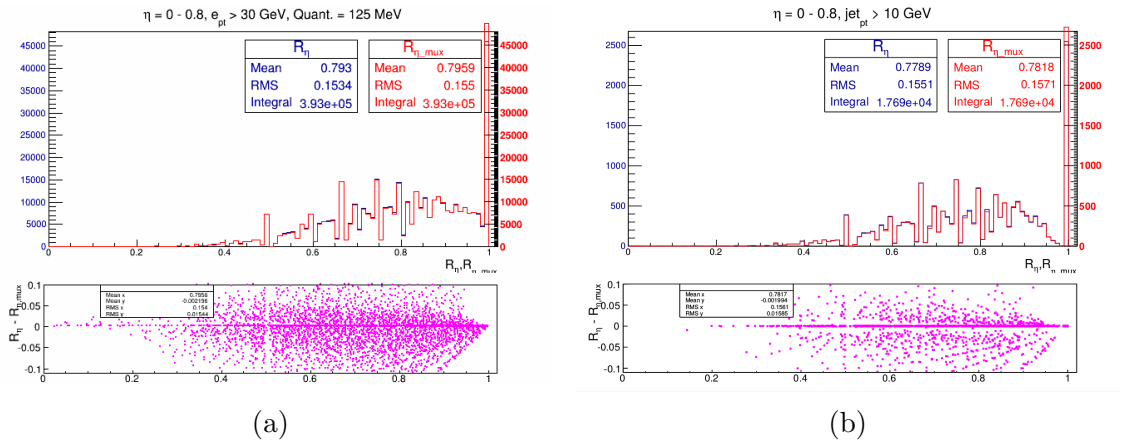


Figure 47: Comparison of  $R_\eta$  and  $R_{\eta,mux}$  for electrons (left) and jets (right) for  $\eta = 0 - 0.8$ . Under the distributions the difference of the two values is depicted.

electrons with a  $p_T > 30 \text{ GeV}$ . In Figure 49 the distributions for a quantization with different quantizations are shown.

$R_\eta$  increases with increasing quantization due to the fact that more energies in the  $R_{7 \times 2}$  region get cancelled out the larger the LSB. Hence,  $R_{7 \times 2}$  and  $R_{3 \times 2}$  approach each other and the ratio of the both increases. For many events the ratio is 1, therefore the presence of the large peak at 1 which decreases with decreasing values for the LSB.

There is again no difference seen between  $R_\eta$  and  $R_{\eta,mux}$ .

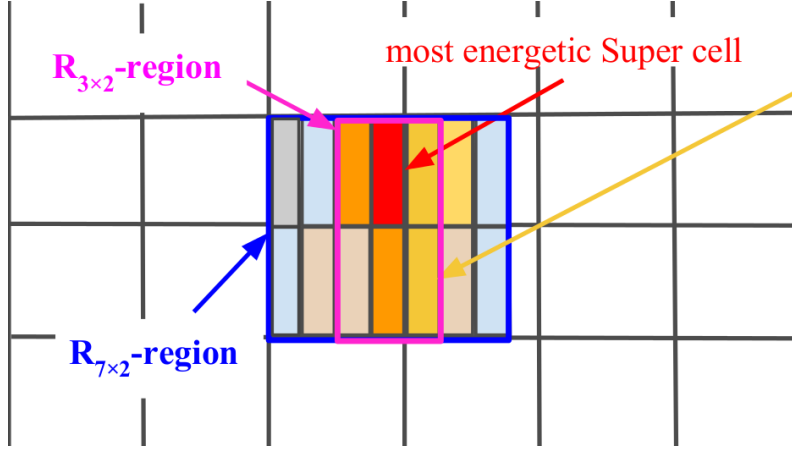


Figure 48: The light blue Super Cells indicate energy deposits which were so low that it was set to 0 due to the quantization. For most energy deposits, the energies in the  $R_{7 \times 2}$  region are set to 0. Therefore, the bandwidth reduction has barely an effect on  $R_\eta$ .

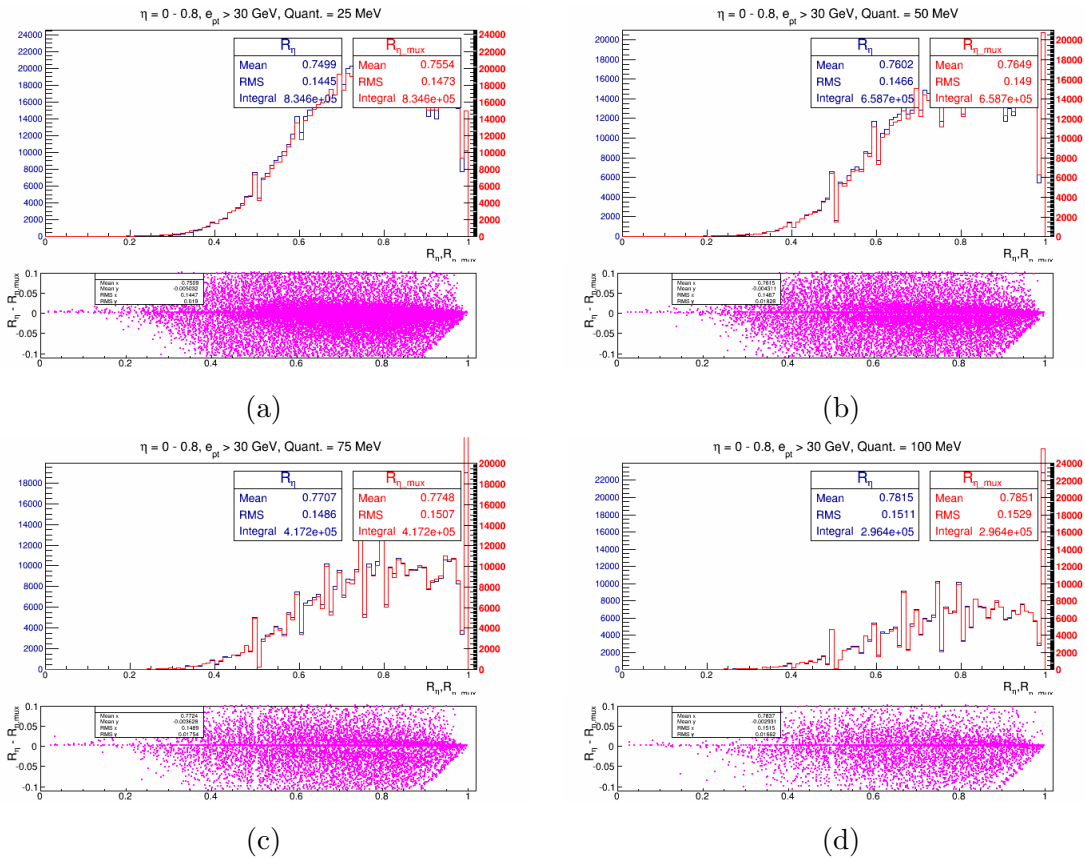


Figure 49: Comparison of  $R_\eta$  and  $R_{\eta, max}$  for electrons with  $p_t > 30$  GeV. The energy quantizations are 25, 50, 75 and 100 MeV. Below each distribution there is the difference between  $R_\eta$  and  $R_{\eta, max}$  shown.

## 6 Demonstrator System tests

### 6.1 Test setup

At the Liquid Argon Electronic Maintenance Facility (EMF) a barrel FEC was set up. Half of it was equipped with boards and a readout system equivalent to the system operating in ATLAS. It was used to establish a setup comparable to ATLAS and after that ensure that new components of the upgraded system do not degrade the performance of the ATLAS main readout and the legacy trigger readout. Furthermore, the proper functionality of the new baseplane, LTDB demonstrator and LSBs was tested. A schematic diagram of the test setup is shown in Figure 50.

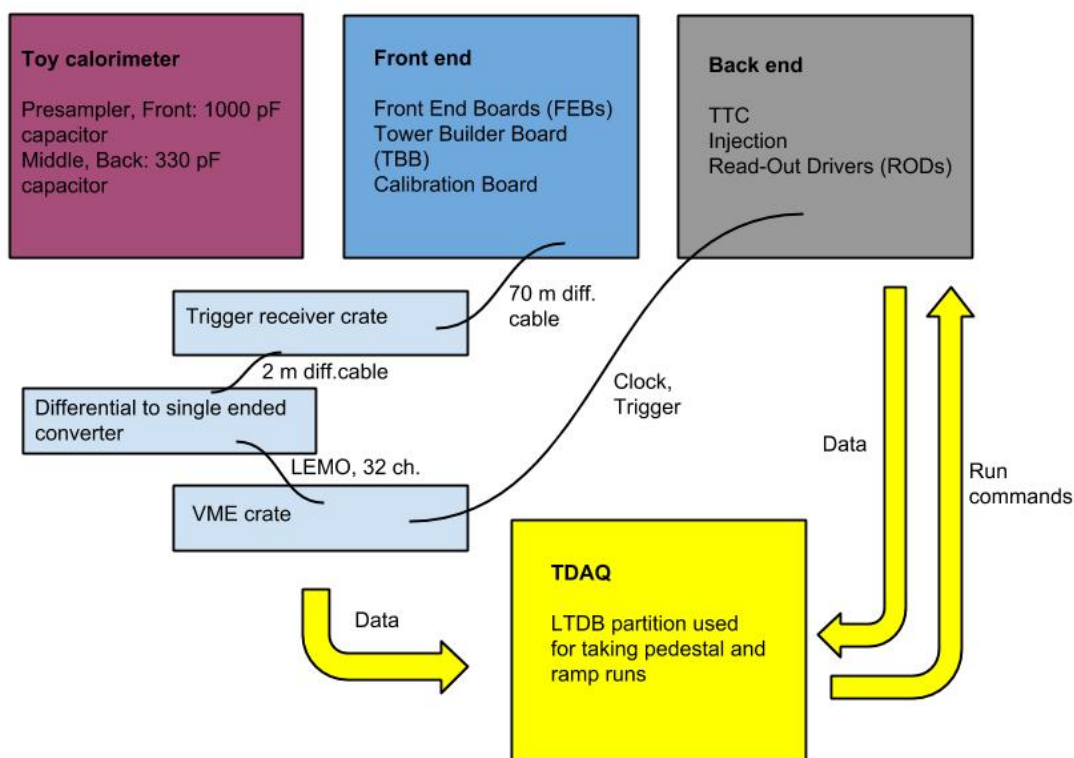


Figure 50: Setup at the EMF. The "toy calorimeter" is a calibration distribution board sending signals to the front end. The trigger readout path and the back end readout were equivalent to the system installed in ATLAS, as well as the TDAQ system.

The calorimeter cells were simulated by a load which was plugged at the back of the baseplane and provided the possibility to use the calibration system for injecting signals into the FEBs as if coming from the calorimeter (thus, the term *toy calorimeter*).

The configuration of the boards in the front end which was used to establish a baseline of the current system in ATLAS is shown in Figure 51.

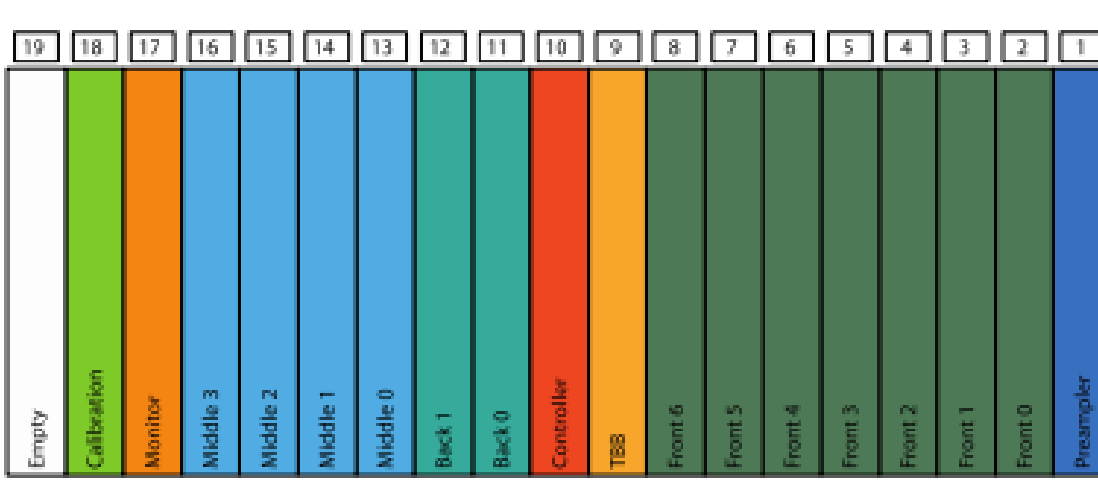


Figure 51: The slot assignment of the boards as is it in the EM barrel and as it was first in the test setup is shown. The left slot is empty and was used later on for adding the LTDB to the crate.

There is one calibration, one monitor and one controller board per half FEC. Additionally, there is one TBB, used to sum the signals coming from the FEBs to units corresponding to trigger towers and sending them to the trigger receiver crate. There is one FEB (PS0) reading out the presampler of the calorimeter, seven FEBs (F0-6) reading out the front layer, four FEBs (M0-3) reading out the cells from the middle layer and two boards (B0,1) receiving the signals from the back layer.

The FEC used in the setup was an EM barrel crate. Hence, there were 30 trigger towers which in total cover a region of  $\Delta\eta \times \Delta\phi = 1.55 \times 0.2$ . A layout for the cabling of the trigger towers in the FEBs reading out the middle and back layer is shown in Figure 52.

The FEC was connected to the trigger receiver crate with a 70 m twisted pairs cable. Through a differential-to-single-ended converter and optic connectors, the signal from the front end was routed to a set of flash ADC where it was digitized.<sup>2</sup>

After the digitization the signal was recorded by the TDAQ system [51].

Also the back end readout was identical to the readout in ATLAS. Hence, the main readout of the FEBs through the TDAQ system could be done as on the detector. The data which was taken was read in through the ATLAS offline computing framework *Athena* (see Section 7.4).

The back end also provided a TTC signal to the VME crate containing the flash ADCs for triggering.

<sup>2</sup>A flash ADC is a type of analogue-to-digital converter and the fastest way to convert an analogue to a digital signal. For an N-bit converter, the circuit employs  $2^N - 1$  comparators. A resistive-divider with  $2^N$  resistors provides the reference voltage. The input voltages are compared successively to the reference voltages. Each comparator produces a 1 when its analogue input voltage is higher than the reference voltage applied to it. Otherwise, the comparator output is 0. Thus, the point where the code changes from ones to zeros is the point at which the input signal becomes smaller than the respective comparator reference-voltage levels [49, 50].

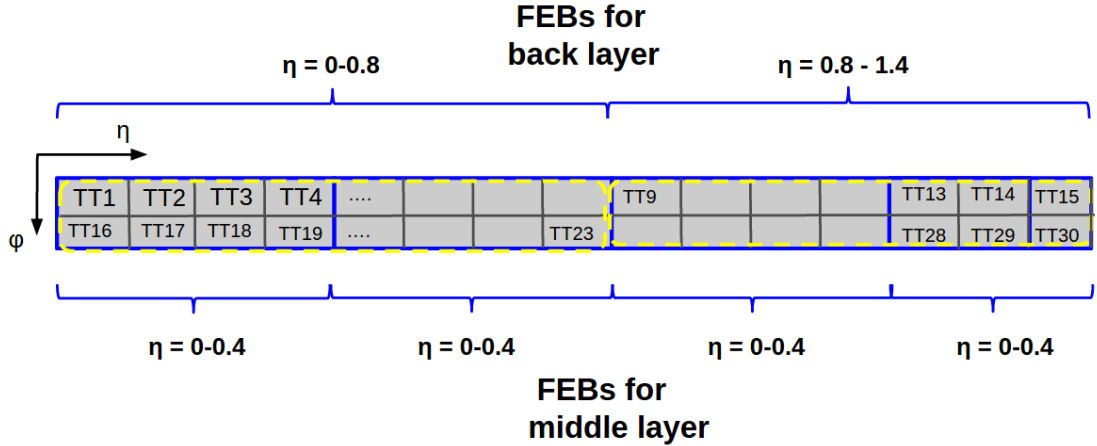


Figure 52: In total there were signals of 30 trigger towers per half FEC to be fed to the trigger receiver crate. There are two FEBs reading out the back layer and four FEBs reading out the middle layer. Their  $\eta$  and  $\phi$  extension is indicated in the drawing. There is one FEB reading out the signals from the presampler and seven FEBs reading the signal from the front layer.

For the EMF a separate *LTDB Partition* was set up in the TDAQ software. The TDAQ software is used for the configuration of all electronic components and their control and takes care of the data monitoring and readout. The run commands such as number of events to be taken, number of triggers, the amplitude of the injection signal, etc. were sent from the LTDB partition to the back end.

For the trigger readout, the flash ADCs were “masked“ as FEBs in order to be able to use the same Athena code to read the data from the flash ADCs. The masking required setting the proper data headers, which are described in detail in Section 7.2.1.

The mapping of the calibration board to the FEBs was one to one, meaning that channel 1 of the calibration board pulses channel 1 of all FEBs, channel 2 pulses channel 2 of all FEBs, etc. On the detector this is done in a different way in order to minimize cross-talk effects between the calorimeter cells when the calibration is performed.

## 6.2 Data taking

There are three types of calibration runs which can be taken with the TDAQ partition:

- Pedestal run
- Ramp run
- Delay run



They are described in detail in Section 7.3.4.

The parameters such as DAC and delay values and the number of triggers were set in dedicated files, which were read in by the LTDB partition. The shaper switches, which operate between the shapers making the sums of the cells on the FEBs and the TBB, were whether directly set in the LAr Master panel <sup>3</sup> or via a script, which was less error-prone than setting the switches manually.

There were several runs to be taken for the various measurements which had to be performed.

## 6.3 Measurements

In order to evaluate the total noise per channel on the main readout and the coherent noise on the main readout pedestal runs were taken. Pedestal runs were also used in order to evaluate the autocorrelation in time in one channel.

For measuring the electronics cross-talk on the trigger readout, two kind of cross-talk runs were taken which are described in detail in the following.

### 6.3.1 Total noise and coherent noise

The total noise was computed by taking the root mean square (RMS) of the pedestal. It includes both coherent and not coherent noise.

Since coherent noise can cause fake energy in large areas of the detector which would introduce errors on the energy measurement, it has to be kept below 5%, according to ATLAS requirements.

In order to spot areas with increased coherent noise, the correlation coefficients for each FEB were evaluated and plots for all channels of one board were made. The correlation coefficients for each pair of channels were computed in the following way:

$$\rho_{xy} = \frac{\sigma_{xy}}{\sigma_x \sigma_y} \quad (17)$$

with

$$\sigma_{xy} = \frac{1}{N} \sum_{i=1}^n (x_i - \mu_x)(y_i - \mu_y). \quad (18)$$

Here,  $x_i$  is the event  $i$  in channel  $x$ ,  $y_i$  is the event  $i$  in channel  $y$ ,  $\mu_x$  and  $\mu_y$  are the means for channel  $x$  and  $y$  and  $\sigma_x$  and  $\sigma_y$  are the variances for channel  $x$  and  $y$ .

This method was very useful when coherent noise induced by various factors such as wrongly laid cables or bad grounding increased. Usually, the correlation coefficients for the channels at the edges of the board would increase.

For numerical evaluation of the coherent noise the coherent noise fraction was computed by:

---

<sup>3</sup>Monitoring of the readout of LAr centers on this application, where general run information such as duration and run number is displayed. In addition to various software alarms and detector settings, the Master panel is also used to manage LAr calorimeter calibration runs.

$$\rho_{\text{coh}} = \frac{\sqrt{\sigma_{\Sigma_{i \in \mathcal{A}}}^2 - N_{i \in \mathcal{A}} \cdot \langle \sigma_{i \in \mathcal{A}}^2 \rangle}}{N_{i \in \mathcal{A}} \cdot \langle \sigma_{i \in \mathcal{A}} \rangle}. \quad (19)$$

$\mathcal{A}$  is the entity of channels over which the coherent noise is computed (in case of a FEB 128 channels). For computing the coherent noise of a half FEC,  $\mathcal{A}$  is the number of all channels of all FEBs in the half FEC.

In the numerator of formula 19, there is the total noise of all channels minus the incoherent noise per channel.

### 6.3.2 Autocorrelation matrix

The autocorrelation referred to here is the correlation between two time samples with distance  $n+1$  time slices within the same channel computed over all samples and all events for each channel. Like the correlation coefficients, it is useful for spotting channels with increased coherent noise. The autocorrelation matrix  $V_{ij}$  is also an essential input to the Optimal Filtering Coefficients (OFC) computation described in Section 7.3.2. The matrix elements are computed by the following formula:

$$V_{ij} = \langle s_i * s_j \rangle, \quad (20)$$

where  $s_i$  are the pedestal subtracted ADC counts in sample  $i$  and the brackets stand for the mean value over the total number of events.

### 6.3.3 Cross-talk on trigger readout

In order to measure the cross-talk between two trigger towers, a signal was injected in certain cells of one of the trigger towers. The cross-talk signals in the other trigger towers were measured and compared to the injected signal. The cross-talk was evaluated by dividing the signal in the not pulsed trigger towers by the amplitude of the injected signal.

The signal was not injected into all cells of the “agressor“ trigger tower, but in the inner or outer cells of one layer, as it is shown in Figure 53. This was done in order to ensure that the electronics cross-talk was at the same level for both pulsing patterns. In terms of detector cross-talk the outer cell pulsing would cause in principle a much higher cross-talk because of the cross-talk between the detector cells.

In order to control that just the signal from the trigger tower pulsed reaches the TBB, we enabled or disabled the shaper switches. The main readout was not affected by the shaper switch settings.

## 6.4 Tests of the current readout system

As mentioned in the previous section, the first aim was to establish a benchmark with a setup which was very close to the original setup in ATLAS. Additionally, a

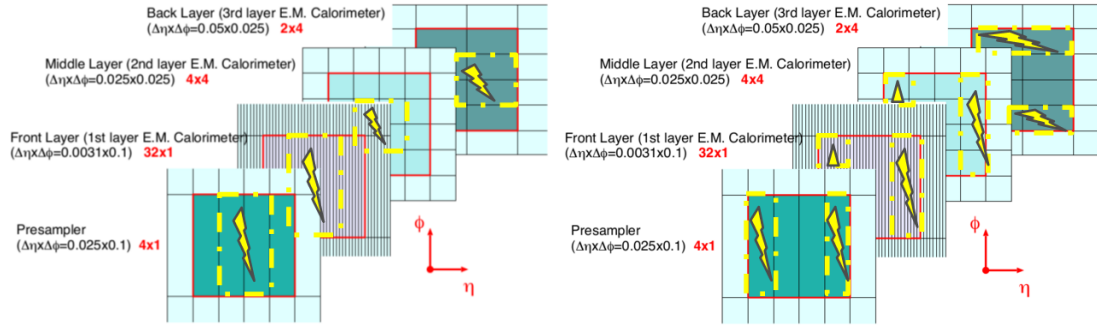


Figure 53: On the left side, the pulsing pattern for when the inner cells are pulsed is shown. On the right side the pulsing of the outer cells is shown. Both are expected to have the same level of cross-talk to other trigger towers.

test system for the LTDB demonstrator was set up. It was used to do first noise measurements, test all channels with pulse injection and verify the synchronisation with the TTC clock. A picture of the complete setup can be seen in Figure 54.

## 6.4.1 Results for main readout

### 6.4.1.1 Total noise per channel

For computing the total noise a run with 40000 events and 8 samples was used. The total noise for all channels of all FEBs is shown on the left side in Figure 55. For comparison, the total noise of the ATLAS readout is shown on the right side. The different slots read out different layers in the calorimeter. Slot 1 contains the board which reads out the cells of the presampler, slots 2-7 belong to the front layer, slot 8 and 9 to the back layer and slot 10-13 to the middle layer.

The mean values of the noise measured in ATLAS and in the current and upgraded test setup is shown in Section 6.5 in Table 5.

The RMS of the total noise is shown separately for all FEBs in Figure 56.

### 6.4.1.2 Coherent noise

For each FEB, the correlation coefficients were computed to spot increased coherent noise on board edges, etc. One of the plots is shown in Figure 57 where none of the values is increased. For each of the FEBs the values were computed and controlled for increased correlation coefficients.

The coherent noise fraction on the main readout for all FEBs in the crate is shown in Figure 58.

## 6.4.2 Results for trigger readout

### 6.4.2.1 Total noise

The total noise on the trigger readout was measured via the noise on the pedestal of the flash ADCs. Figure 59 shows the total noise for all 30 trigger towers which were read out. For the computation a pedestal with 5000 events and 8 samples was used.

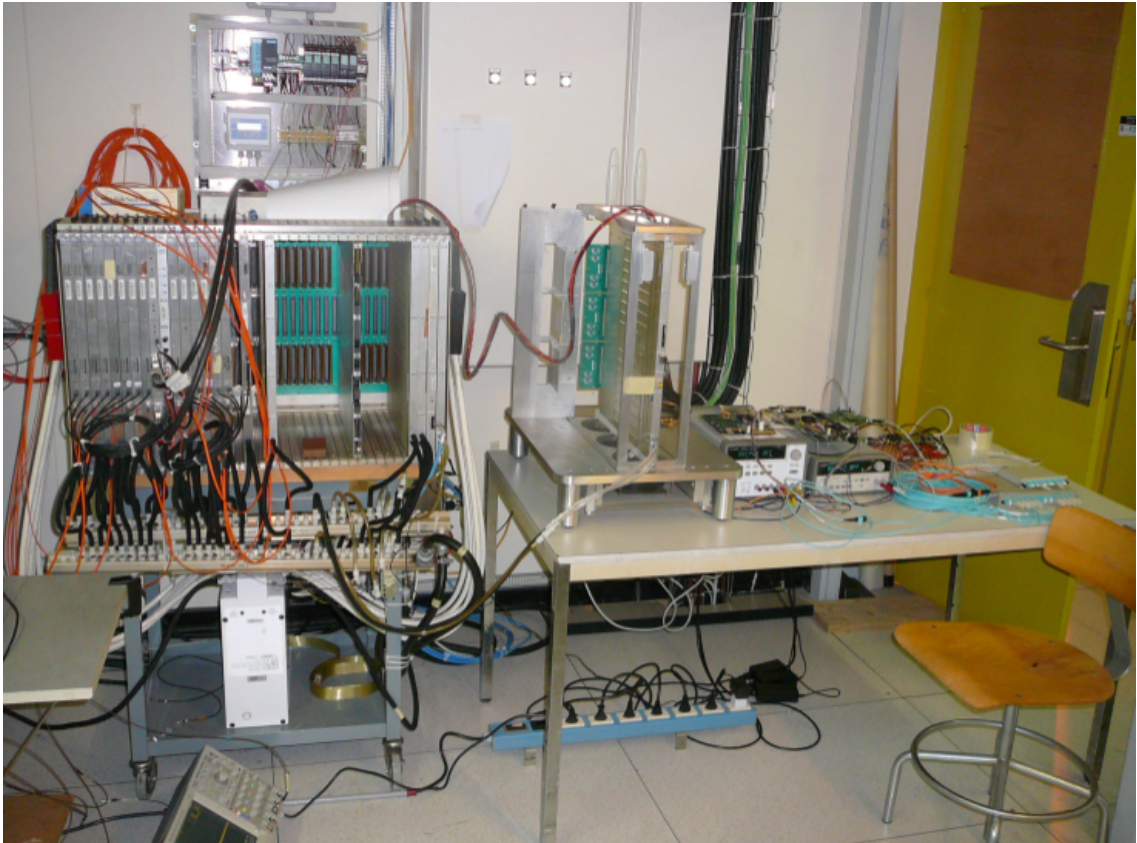


Figure 54: Setup at the EMF: On the left side the half full FEC can be seen. On the right side on the table the LTDB test setup is assembled.

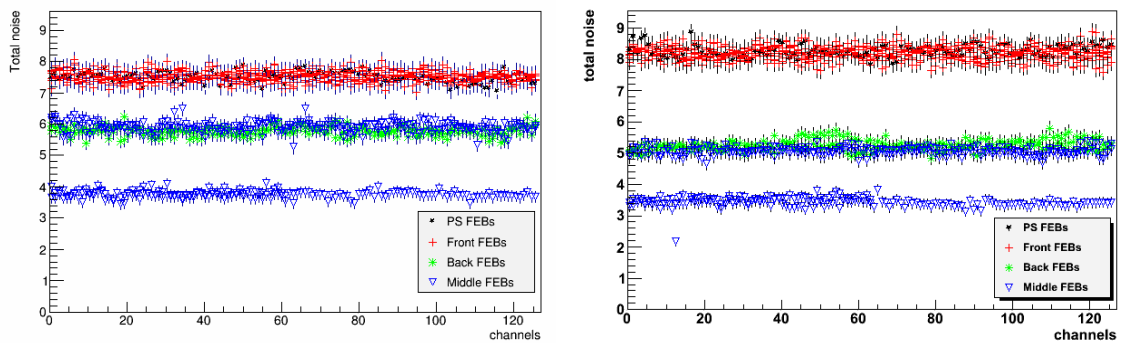


Figure 55: On the left side, the total noise in ADC counts for the channels of all FEBs is shown for a run of 40000 events and 8 samples. On the right side, the total noise, in ADC counts as well, for the readout in ATLAS is shown for comparison. There are three bands because of the different capacitances used and pre-amplifier resistances for the FEBs reading out the different layers and eta-regions of the detector. Hence, one can conclude that an equivalent setup to ATLAS was established in terms of total noise [52].

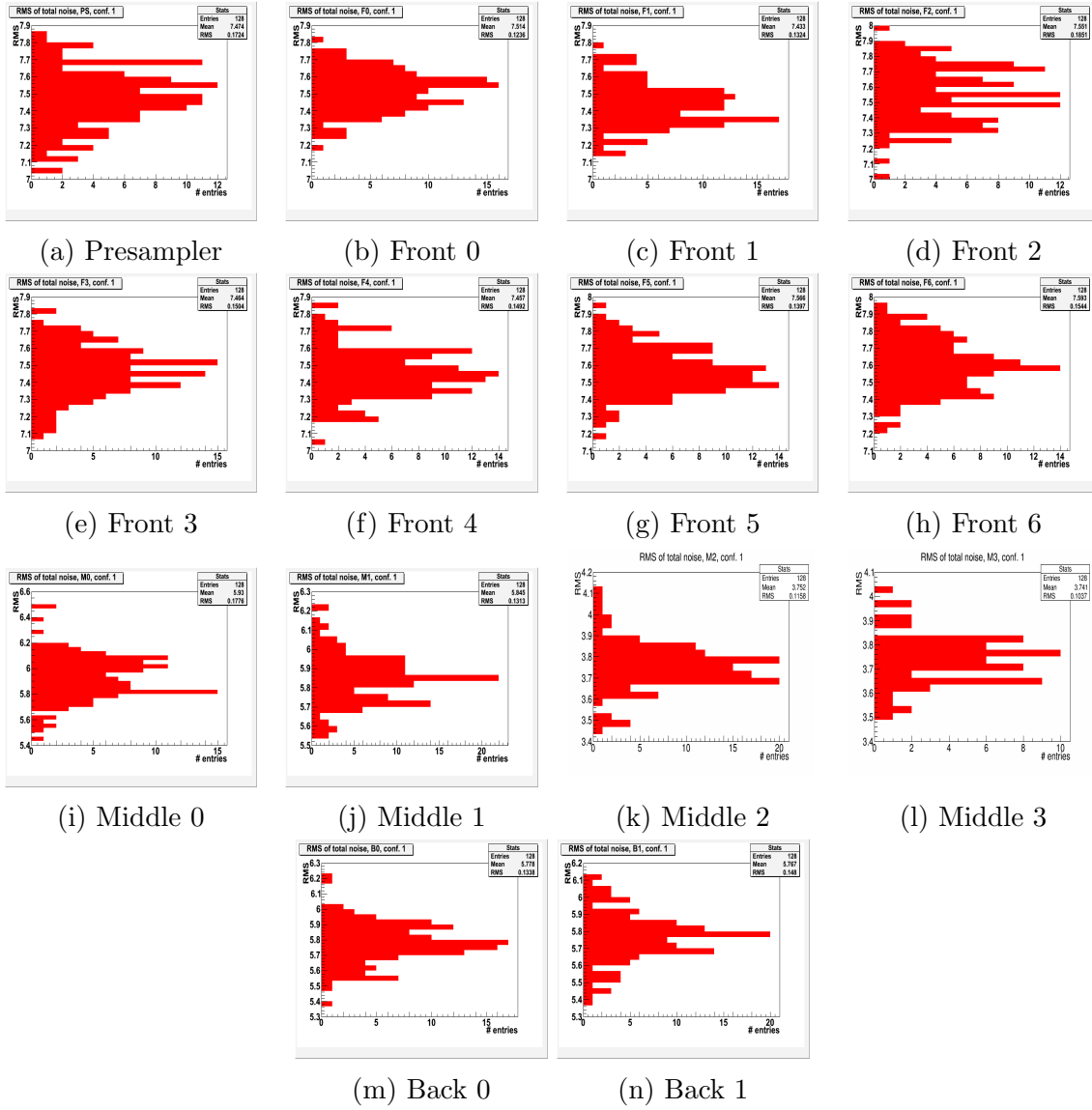


Figure 56: The RMS on the total noise for each FEB is shown.

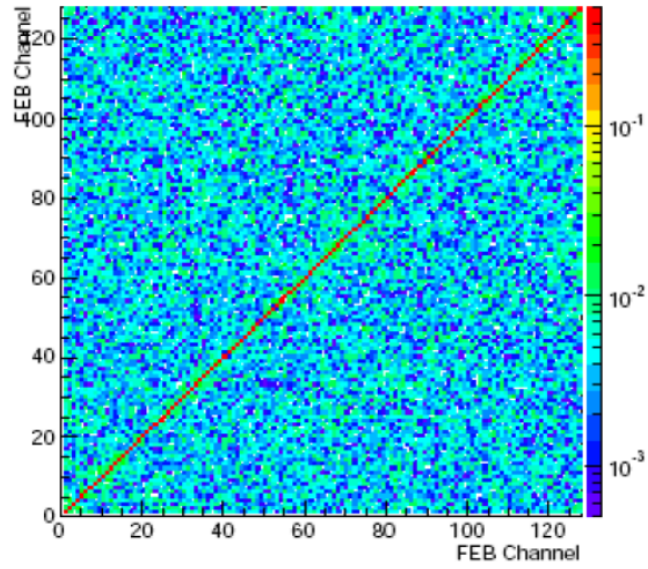


Figure 57: Correlation coefficients for all channels of one FEB are shown in this plot. The correlation coefficient of a channel with itself is 1.

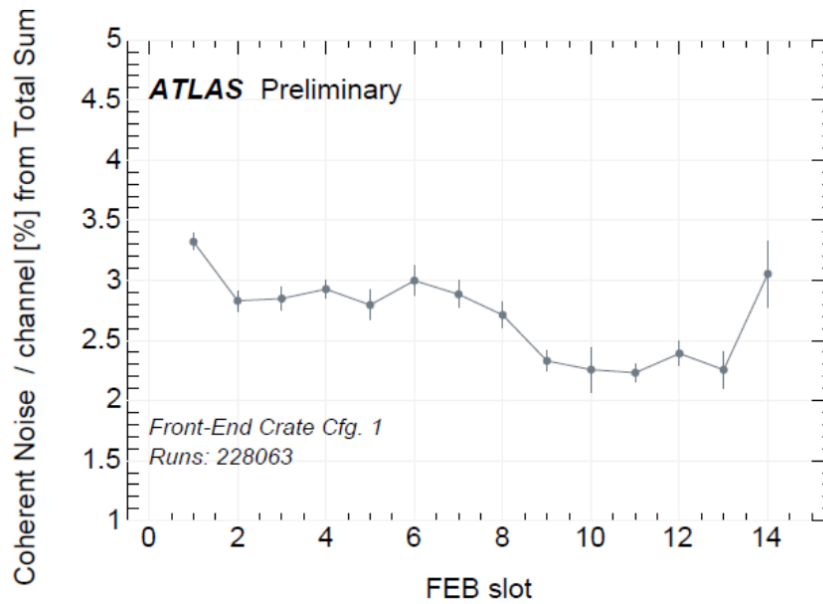


Figure 58: The coherent noise fraction over all channels per FEB is shown for all FEBs in the FEC of the test setup. The differences of the noise for the different FEBs is caused by the different capacitances and pre-amplifier resistances used for the different layers. The ATLAS requirement of the coherent noise being under 5% was met.

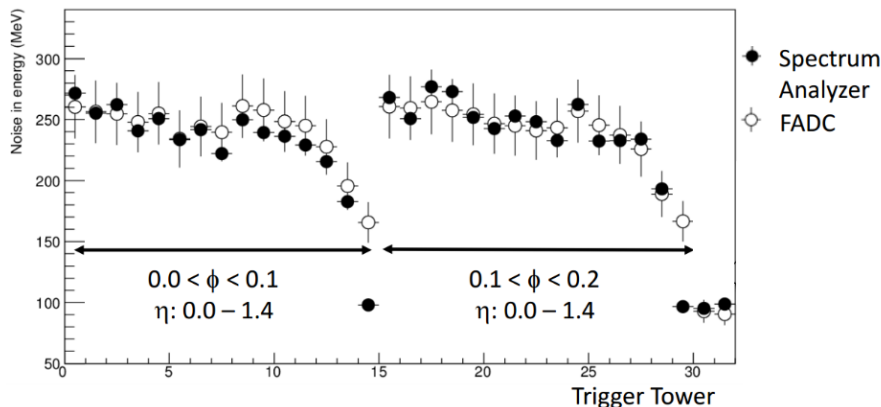


Figure 59: The RMS measured on the trigger readout path is shown. The values represented by the full circles were measured with a spectrum analyzer, the values shown in open circles were measured with the flash ADCs [52].

The total noise on the flash ADCs was measured independently with a spectrum analyzer and via the pedestal taken on the flash ADC output.

For the spectrum analyzer, the total noise is computed by measuring the width of the integrated spectrum. In Figure 60 the noise spectrum for one of the trigger towers is shown.

#### 6.4.2.2 Correlation coefficient between trigger towers

The correlation coefficient which was computed as described in Section 6.3.1 is shown in Figure 61 for all 30 trigger towers. The correlation of a trigger tower with itself is 1, if there is no correlation at all between two trigger towers it is 0.

The RMS of the correlation coefficient was evaluated to be  $6.5 \times 10^{-3}$ .

#### 6.4.2.3 Cross-talk

As described before, the cross-talk was evaluated by dividing the amplitude of the signal when injecting the pulse by the signal height of the neighbouring trigger towers at the peak sample. For both pulsing patterns the results are shown in Figure 62. The RMS of the distribution of the values was evaluated to be 0.12% for the pulsing of the inner cells with a maximal value of +0.73% and for pulsing the inner cells 0.13% with a maximal value of +0.75%.

### 6.5 Tests of the upgraded trigger readout

After obtaining satisfactory results with the setup equivalent to ATLAS, all components which were necessary to go to the upgraded system were installed. The LSBs for all FEBs except for the presampler were replaced, the newly designed baseplane was installed and the LTDB demonstrator was put in the crate and powered.

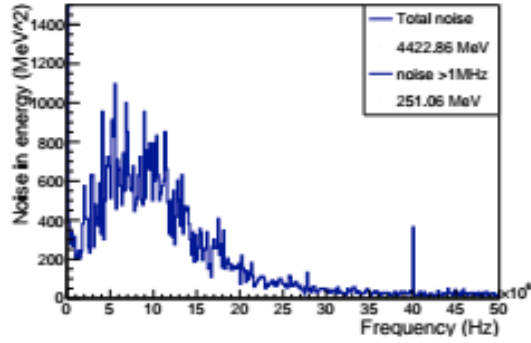


Figure 60: The spectrum of one of the trigger towers measured by a spectrum analyzer during configuration one is shown here. The integrated spectrum was estimated to be about 244 MeV for this particular trigger tower. The peak at 40 MHz was subtracted in order to obtain this value because it is caused by the TTC clock and irrelevant for the noise. However, for the noise shown in the plot the value was computed including the spike.

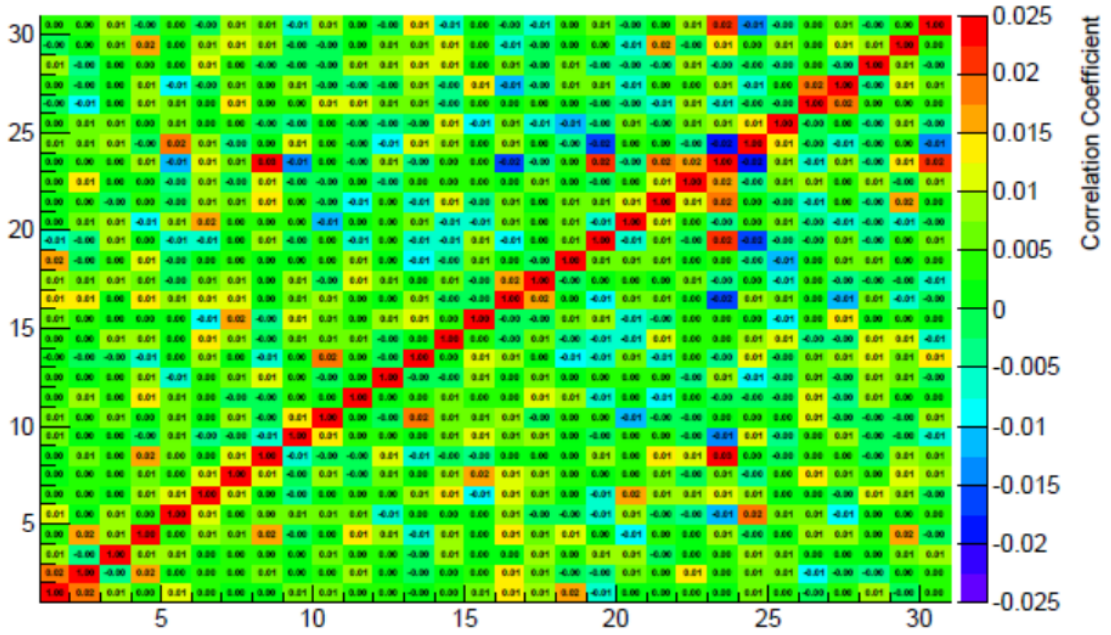


Figure 61: The correlation coefficient for all 30 trigger towers of the test setup is shown. The correlation of a trigger tower with itself must be 1. For the trigger towers 1-15, the average value of the coherent noise fraction was about  $6.27 \pm 0.4\%$ , for trigger towers 16-30  $4.56 \pm 0.52\%$  and for all trigger towers  $5.40 \pm 0.23\%$ .



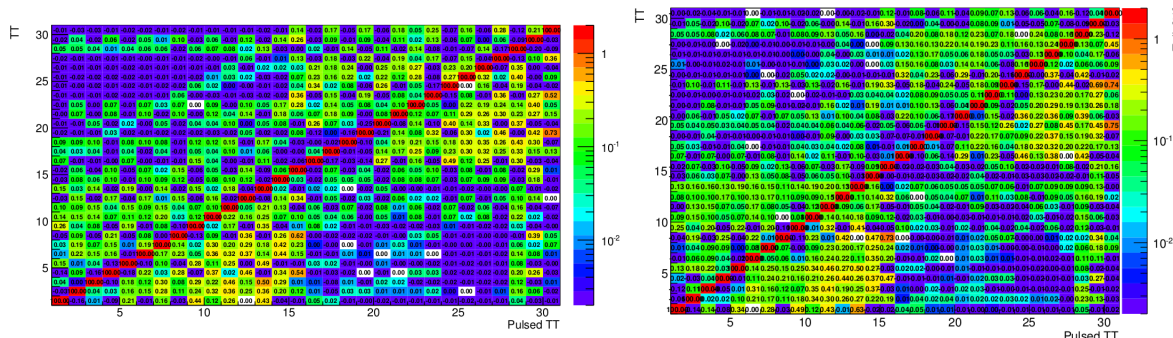


Figure 62: The cross-talk between trigger towers for the two different pulsing patterns are shown. On the left side, the cross-talk pulsing all trigger towers in all layers in the inner cells is evaluated. On the right side, the trigger towers were pulsed across all layers in the outer cells.

The new LSBs are summing the signals from the linear mixer. For the front and middle layer they are summed to four Super Cells per trigger tower and for the back layer and presampler to one signal per trigger tower.

Since the slot configuration allowed for an additional board in the crate (Figure 63), a new baseplane was designed for the new board configuration. The LTDB was then installed in the crate with the new baseplane.

The new baseplane was installed on the right side of the FEC. Subsequently, all FEBs and additional boards were inserted on the other side of the crate, as can be seen in Figure 64.

A schematic diagram of the readout scheme at the EMF is depicted in Figure 65.

### 6.5.1 Results for main readout

The results for the upgraded system will be shown in comparison to the results which were obtained with the tests of the current readout system.

#### 6.5.1.1 Total noise per channel

For the computation of the total noise again a run with 40000 events and 8 samples was used. In the following plots for the total noise, the same number of events and samples was used.

Figure 66 shows the total noise for all channels of all FEBs for the upgraded system (left), and the results which were obtained with the old setup (right).

Table 5 summarizes the noise levels for the ATLAS readout, and the current and the upgraded setup at the EMF.

#### 6.5.1.2 Coherent noise

The coherent noise fraction, as defined in 19, is shown in Figure 67. The plot shows the coherent noise fraction on the main readout for all FEBs in the crate for

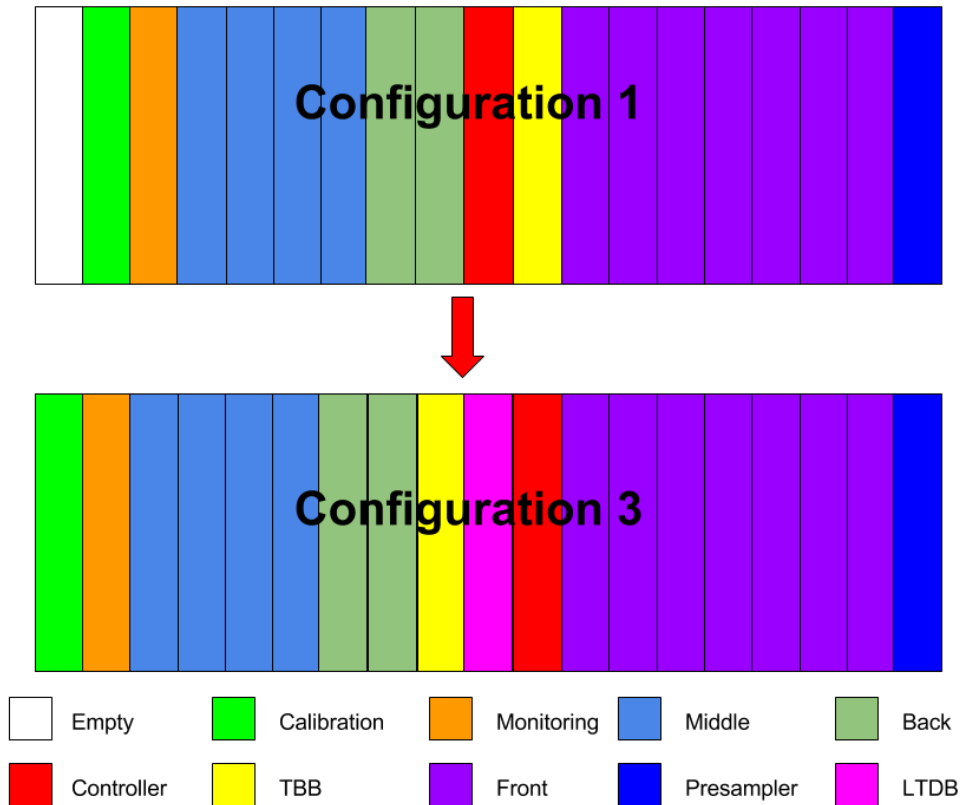


Figure 63: The slot configuration for the old and upgraded system are shown. In the current ATLAS system, there is a free slot on one side of the crate. For the new configuration, a new baseplane was designed. It allowed to shift the calibration board, monitor board, several FEBS and the TBB to one side. In this way a free slot was obtained in the middle of the crate in which the LTDB could be installed.

Table 5: Comparison of the noise levels in ADC counts of ATLAS, the test setup with the current readout system and the upgraded system. FEBS reading out the same layer were compared. The noise for all setups are at the same level.

	# of FEBS	ATLAS	Current setup	Upgraded setup
Presampler	1	8.1	7.4	7.5
Front	7	8.1	7.5	7.5
Middle	4	3.4-5.1	3.7-5.9	3.7-5.9
Back	2	5.4	5.8	5.7

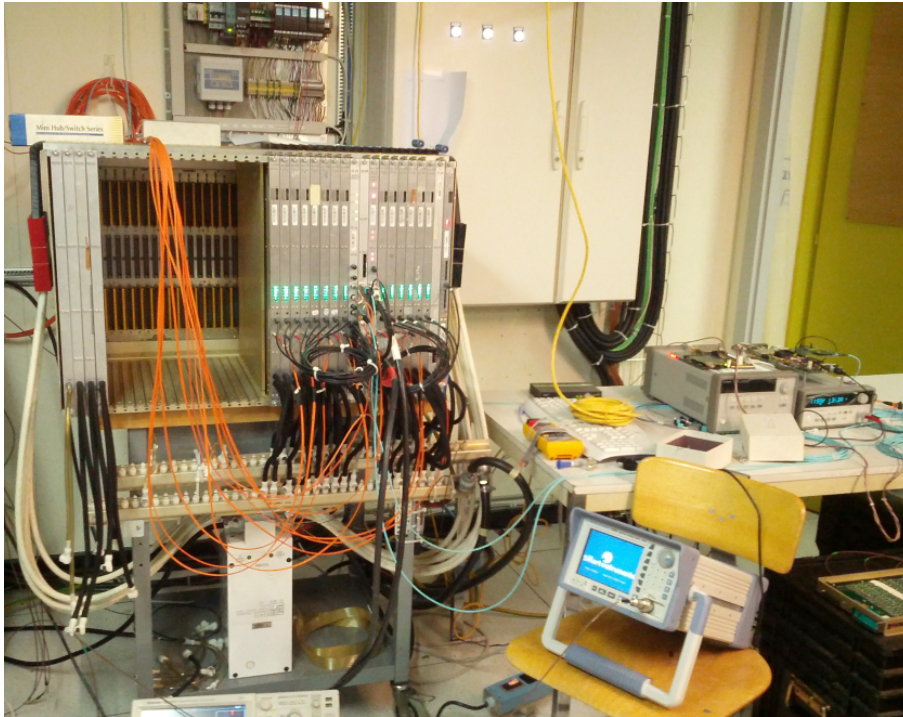


Figure 64: For the setup of the new system, the baseplane was installed on the other side of the crate. On the LTDB the light blue optical fibers are connected leading to the back end.

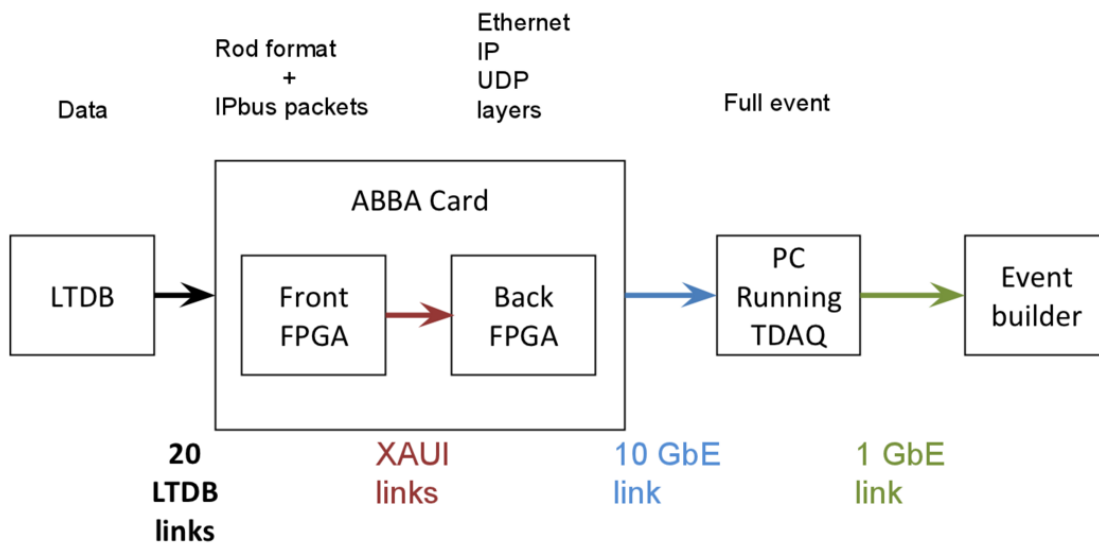


Figure 65

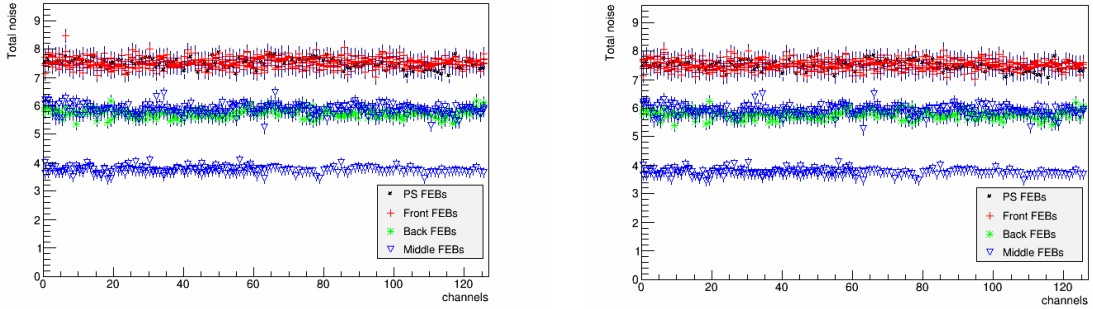


Figure 66: On the left side, the total noise in ADC counts for the channels of all FEBS is shown for a run of 40000 events and 8 samples for the upgraded system. On the right side, the total noise, as well in ADC counts, for the old readout system is shown for comparison. The noise levels are the same.

Table 6: Comparison of the coherent noise fractions of the test setup with the current readout system and the upgraded system.

Trigger Tower	Current setup	Upgraded setup
1-15	$6.27 \pm 0.40\%$	$8.09 \pm 0.31\%$
16-30	$4.56 \pm 0.52\%$	$6.91 \pm 0.36\%$
1-30	$5.40 \pm 0.23\%$	$6.92 \pm 0.2\%$

the current and upgraded test setup .

## 6.5.2 Results for Trigger Readout

### 6.5.2.1 Total noise

Figure 68 shows the total noise for all 30 channels of the trigger readout for both the current and upgraded test setup. For the computation of the noise a pedestal with 5000 events and 8 samples was used for both setups. The total noise on the flash ADCs was measured independently with a spectrum analyzer and via the pedestal taken on the flash ADC output for the current system. For the upgraded system, only the noise measured by the flash ADCs was evaluated.

### 6.5.2.2 Correlation coefficient between trigger towers

The correlation coefficient was computed for both the current and upgraded setup (Figure 69) for all 30 trigger towers.

A summary of the coherent noise fraction for all trigger towers for both test configurations is shown in Table 6. There is a slight increase for the Phase-I readout system, but since there is no requirement on the level of the coherent noise in ATLAS and the difference measured between the two setups was minimal, the small increase of the coherent noise fraction is acceptable.

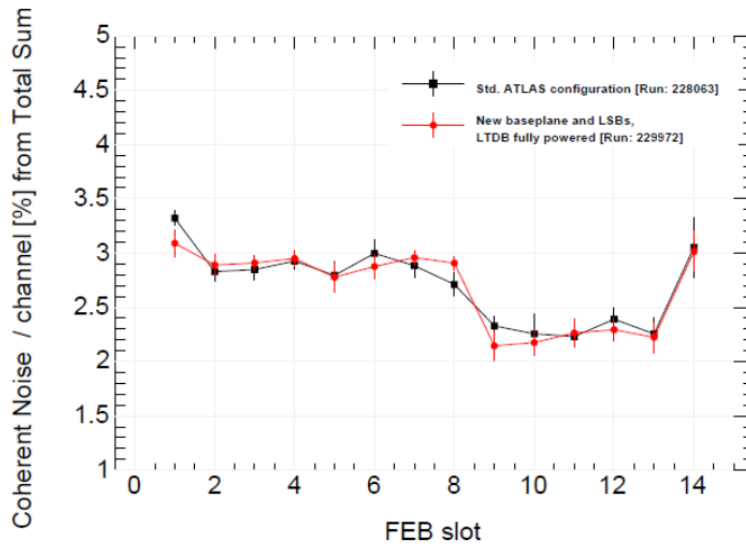


Figure 67: The coherent noise fraction over all channels per FEB is shown for all FEBs in the FEC for both setup configurations. For both configurations the coherent noise fraction is below 5% as required by ATLAS.

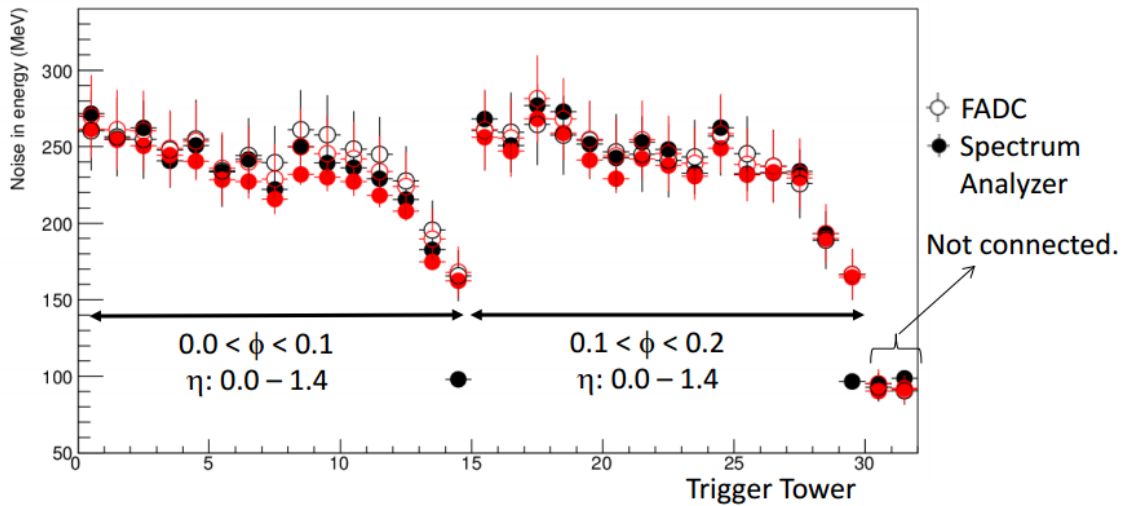


Figure 68: The RMS of the pedestal measured on the trigger readout path for both test configurations is shown. The values represented by the black circles were measured with the current setup (with a spectrum analyzer for the full circles and with the flash ADCs for the open circles). In comparison to that, the total noise measured with the upgraded system is shown in red full circles.

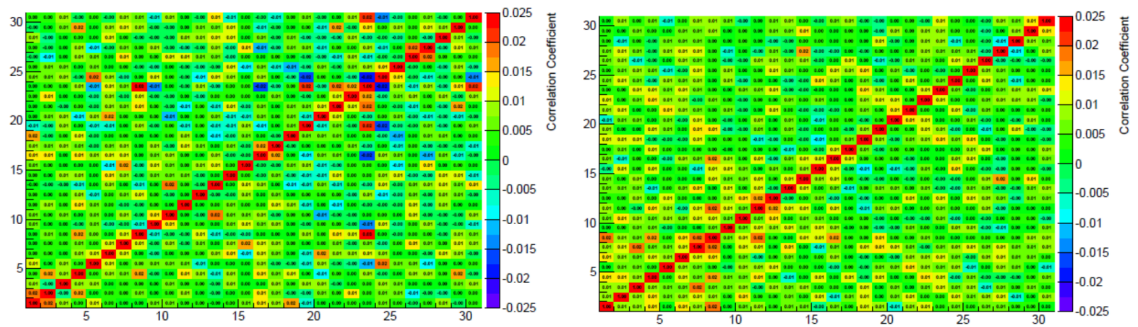


Figure 69: The correlation coefficient for all 30 trigger towers of the current setup is shown on the left, for the upgraded system on the right side. The RMS on the correlation coefficient measurement is  $6.5 \times 10^{-3}$  for the current setup and  $5.2 \times 10^{-3}$  for the upgraded setup.

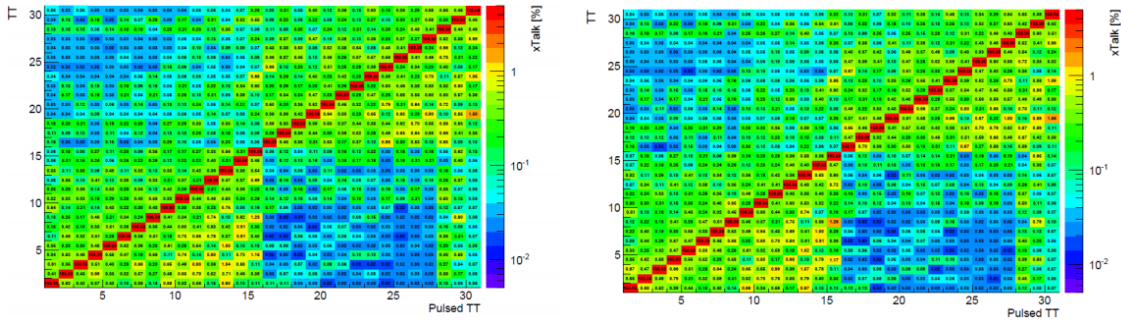


Figure 70: The cross-talk between trigger towers for the two different test configurations was evaluated. On the left side, the cross-talk for the current setup and on the right side, the results for the upgraded system are shown.

### 6.5.2.3 Cross-talk

The results for the current setup and the upgraded setup are shown in Figure 70. Since it was evaluated that the two pulsing patterns provide equal results, we used the “outer cells pulsing“ for the upgraded system tests.

For the current system, the RMS of the distribution of the values was evaluated to be 0.12% with a maximal value of +0.70%. For the upgraded system, the RMS was 0.12% with a maximal value of +0.77%. Hence, it was proven that there is no difference in the size of the cross-talk.

### 6.5.2.4 Linearity and saturation point of trigger receiver output

According to [29], the integral linearity of the whole trigger summing chain, including the transmission to the electronics cavern is better than 2% over the range of 0-256 GeV in  $E_T$ . Hence, it had to be verified that the trigger receiver output is linear up to the aforementioned value of  $E_T$ . In order to prove the linearity, each trigger tower was pulsed with a DAC value of a known corresponding energy. The peak height at the trigger receiver output was measured and plotted against the injected energy.

In Figure 71 two pulses measured with an oscilloscope at the trigger receiver output are shown. The upper pulse corresponds to an  $E_T$  of 256 GeV. Four cells of the trigger tower were pulsed with a DAC value of 1105. The lower pulse, which corresponds to an  $E_T$  of 350 GeV, shows already some distortion at the peak.

In Figure 72 the injected energy is plotted against the DAC value. The saturation point is defined as the  $E_T$  value where the function deviates from the linear fit by more than 2%. The range for the linear fit, as indicated on the plot, is 0 - 180 GeV.

The saturation points of all trigger towers were measured. The ATLAS requirement on the saturation is that the data point at the energy of 256 GeV has to deviate less than 5 % from the linear fit. In Figure 73, the deviation from the integrated linearity fit function is shown. The red line indicates where the deviation is greater than 5 %, the blue line where it is greater than 2%. For the ATLAS requirement of 5 % the saturation for all trigger towers occurs well above 256 GeV.

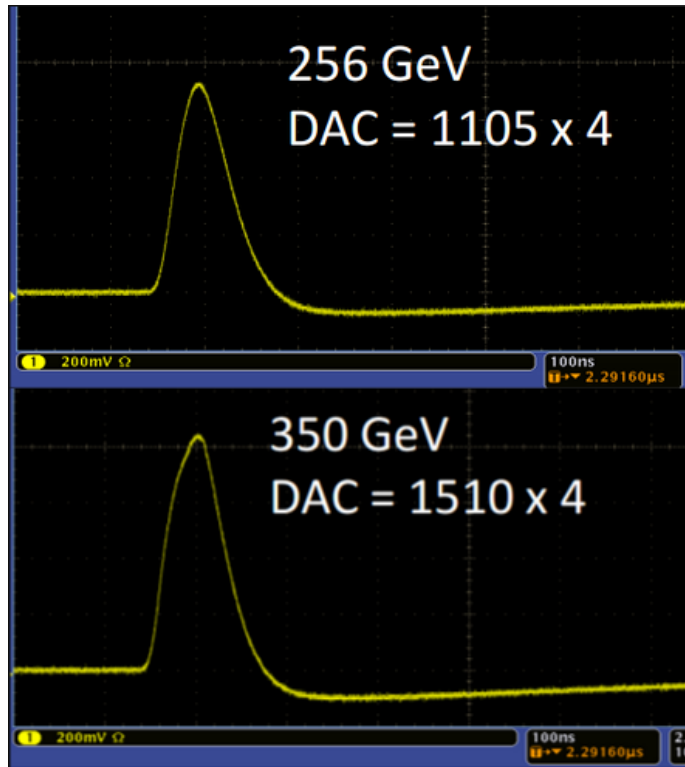


Figure 71: On the top, the measured pulse with a DAC value corresponding to the energy of 256 GeV in  $E_T$  is shown. At the bottom, a DAC equal to 350 GeV in  $E_T$  was injected. At the top of the pulse the effect of saturation and hence pulse distortion can be seen.



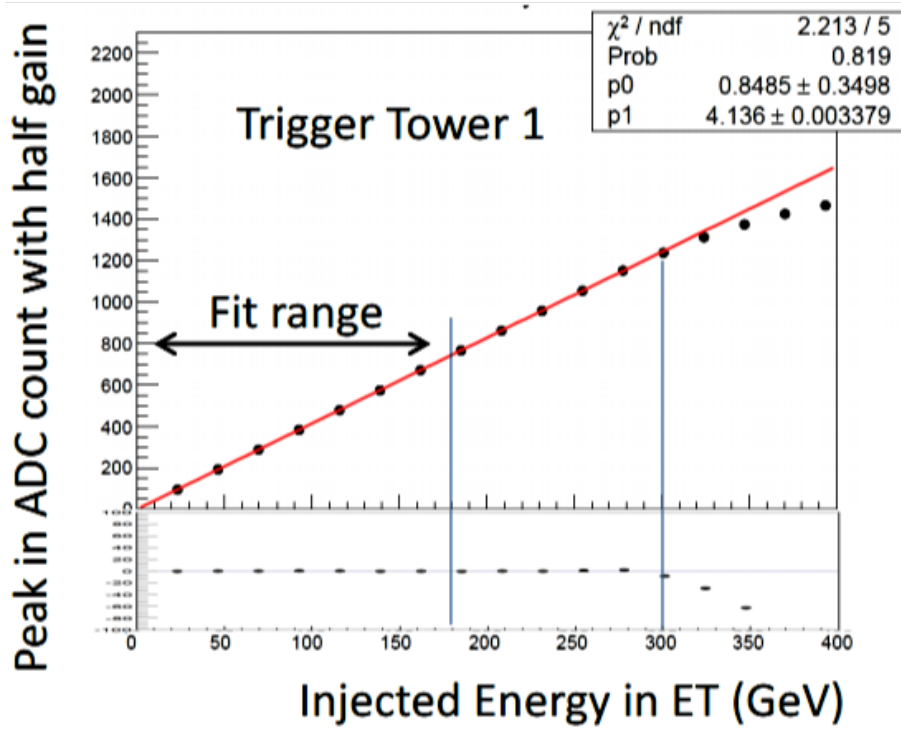


Figure 72: The injected energy in  $E_T$  is plotted against the DAC value. The saturation point is well over the required 256 GeV. The linearity of the trigger readout starts degrading at approximately 300 GeV.

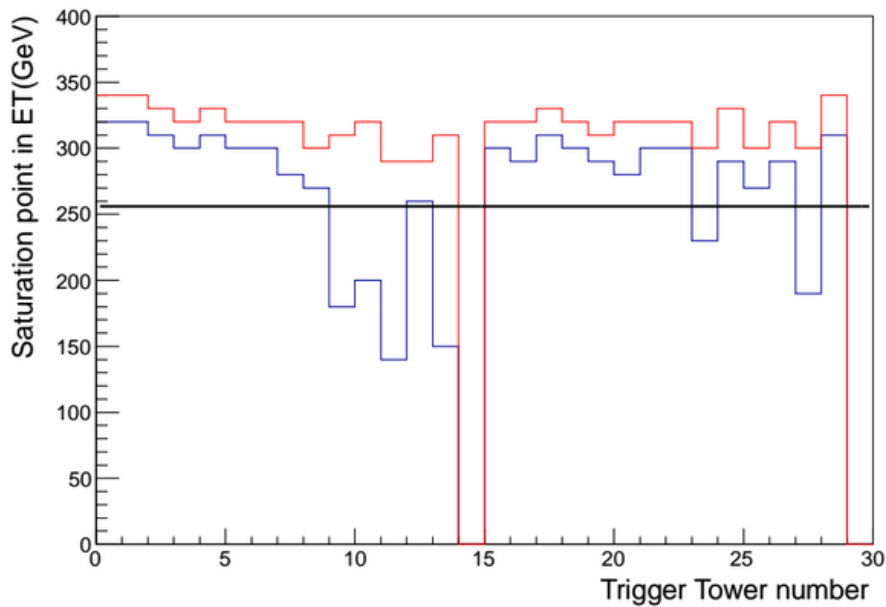


Figure 73: Deviation of the integrated linearity fit function from the saturation point of each trigger tower. The blue line represents 2 % deviation, the red line 5 %.

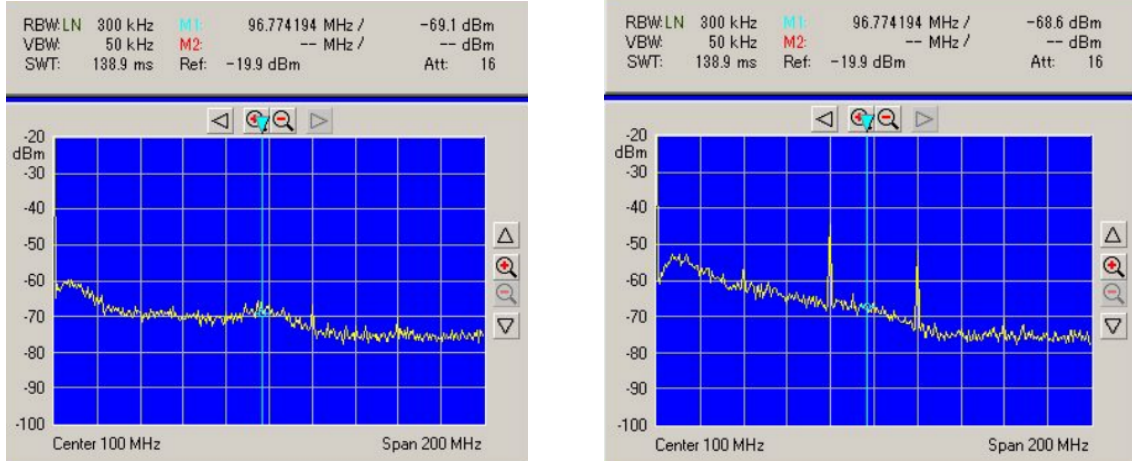


Figure 74: Noise spectrum measured on the output of the TBB with the digital part of the LTDB switched off (left) and on (right).

### 6.5.2.5 Measurements with different LTDB configurations

There were two LTDB pre-prototypes designed for the Phase-I demonstrator. One was produced at the Brookhaven National Laboratories (BNL) and the other one at Saclay/LAL. They will be referred to as BNL and Saclay/LAL LTDB.

After performing all aforementioned measurements, the frequency spectrum of the output of the TBB was measured through a differential to single-ended converter. When the digital part of the LTDB was switched off, there was no unexpected noise contribution to the measured spectrum, as can be seen in the left Figure of 74. However, when the digital part was switched on, a noise synchronized with the TTC clock could be measured, which is shown on the right of Figure 74. The biggest contributions were at 80 and 120 MHz. When the digital part of the LTDB was turned off, this additional noise disappeared. This noise contributions were beyond the measured spectrum and did not appear in the TBB output or main readout, as shown in Figure 68 and Figure 75, respectively.

In addition to the measurement of the frequency spectra of the output of the TBB, the coherent noise fraction was measured with the LTDB fully powered (analogue and digital part switched on) and with just the analogue part switched on (Figure 75). The values are also compared to the standard ATLAS configuration and were measured to be the same.

## 6.6 Functionality of the BNL LTDB

In addition to evaluating the impact of the LTDB on the main readout and trigger readout, the functionality of the LTDB itself was exercised. The pedestal for all 320 channels and calibration pulses sent to the LTDB through the FEBs with the calibration board was measured (Figure 76).

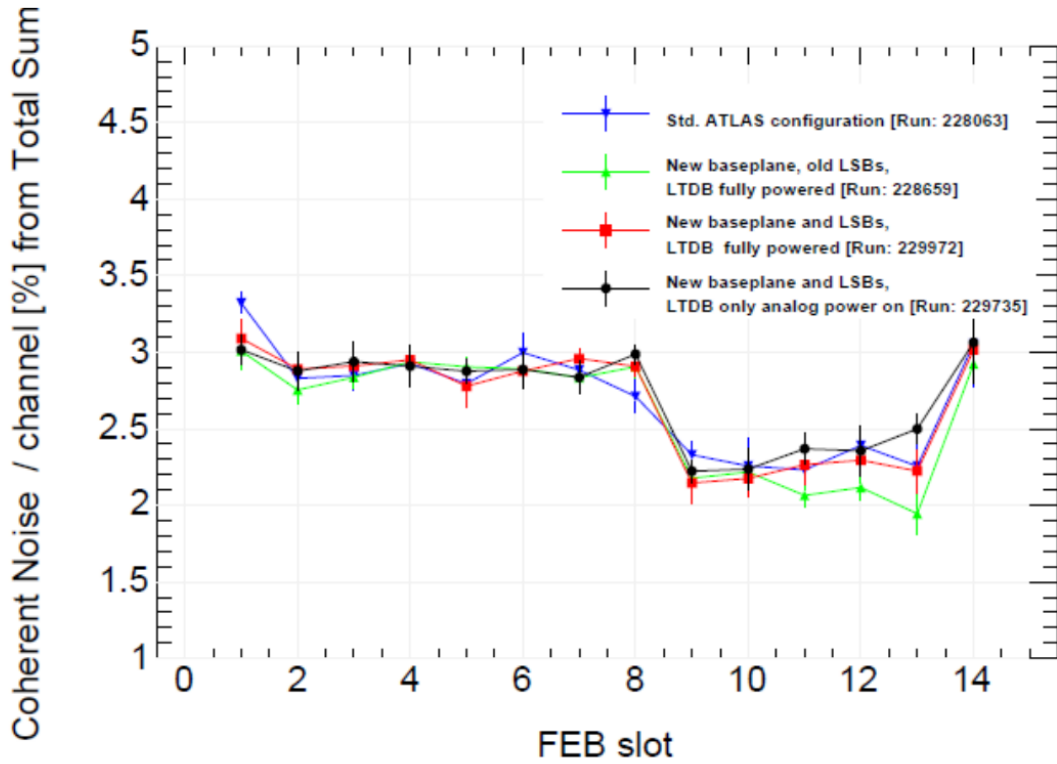


Figure 75: Coherent noise as a fraction of the total noise per channel for different configurations of the LTDB. The configuration where the LTDB is fully powered and the new baseplane and LSBs are installed is what is called here the upgraded trigger readout system.

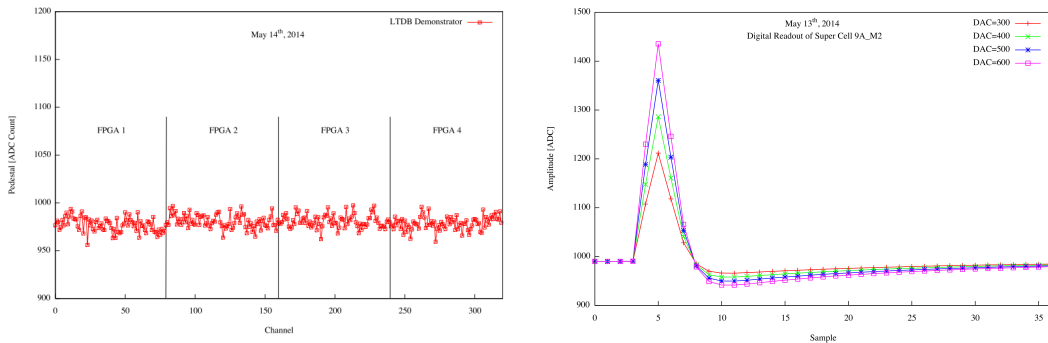


Figure 76: On the left, the pedestal of each channel of the LTDB measured at the EMF is shown. On the right, a pulse sent to the LTDB by the calibration system is shown. One channel of the FEBs was pulsed with four different DAC values. The signal on the LTDB channel corresponds to one Super Cell signal. The number of samples was adjusted to cover the pulse.

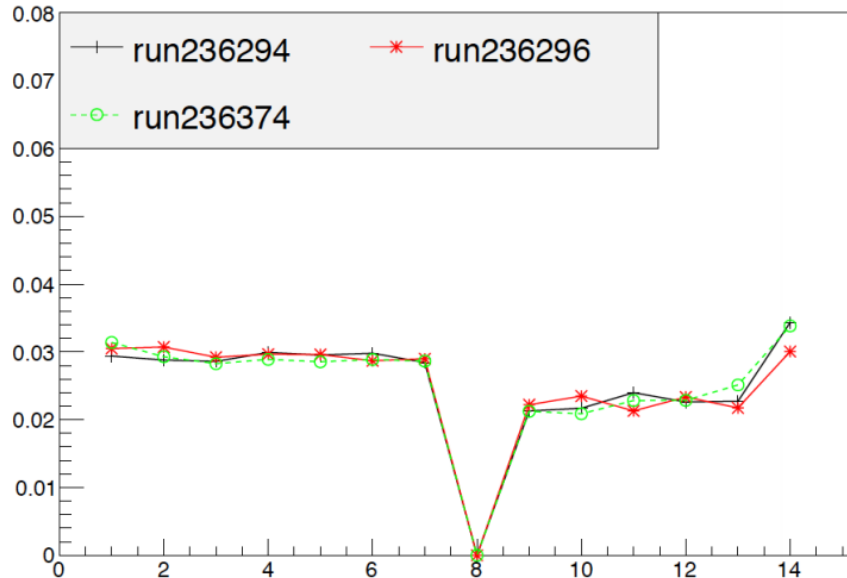


Figure 77: Coherent noise as a fraction of the total noise per channel for the Saclay/LAL LTDB. Because of a problem with the optical link in slot 8, the coherent noise for this board could not be evaluated. Per run 40000 events were taken. The three runs were taken with the same settings for more statistics.

## 6.7 Measurements with the Saclay/LAL LTDB

As for the BNL LTDB, the same tests were done for the other LTDB pre-prototype from Saclay/LAL. After installing it in the FEC at the EMF, the noise, coherent noise, cross-talk, linearity and saturation point were measured and the connectivity was tested.

The coherent noise fraction for all FEBs in the EMF crate was evaluated. Since the optical link for the FEB in slot 8 was not working properly, the coherent noise for that board could not be measured. However, the other FEBs were measured to have a coherent noise fraction comparable to the one of the BNL LTDB (Figure 77).

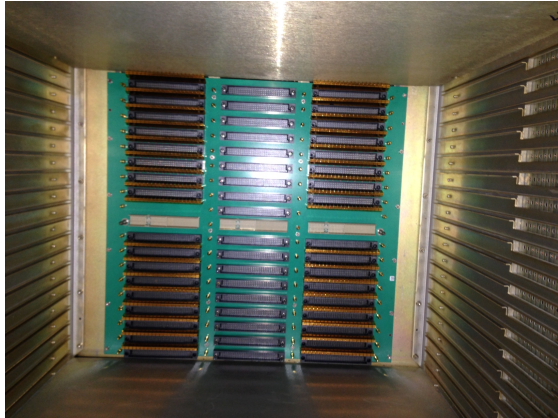
After all tests with the Saclay/LAL LTDB at the EMF, it was concluded that also this LTDB could be installed on the detector.

## 6.8 Conclusions on demonstrator tests

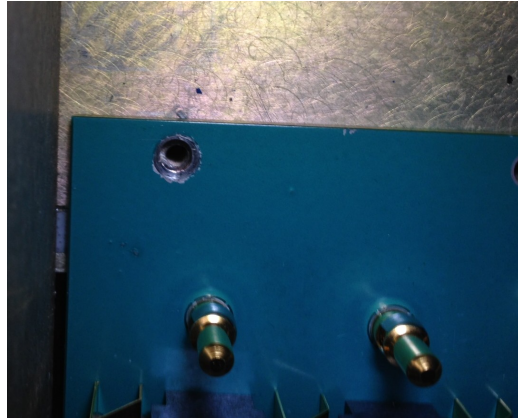
The test setup at the EMF was established with sufficient sensitivity to qualify the Liquid Argon demonstrator readout to be comparable to the ATLAS readout. All tests were performed with the ATLAS standard readout and, after that, with the Phase-I readout electronics.

The main readout was tested in terms of total noise and coherent noise and was evaluated to be the same for both configurations.

On the analogue trigger output, the connectivity with the new baseplane was verified to be correct. Furthermore, the saturation, total noise level, coherent noise



(a)



(b)

Figure 78: On the left side, the demonstrator crate after the extraction of the FEBs is shown. On the right side, an edge of the baseplane before screwing it to the pedestal is depicted.

level and cross-talk were evaluated to be the same for both configurations.

All results measured pass the required ATLAS thresholds and it was concluded that the installation of the demonstrator does not degrade the performance of the main readout and trigger legacy system.

## 6.9 Installation of the demonstrator system in ATLAS

After the successful tests at the EMF, the demonstrator was installed in ATLAS in one of the barrel FECs of the side A top area of the detector. One FEC covers a region of  $0 < \eta < 1.475$  and  $0.4$  in  $\phi$ .

In order to install the demonstrator system, the FEBs from the demonstrator crate were extracted, equipped with new LSBs and again inserted, the new baseplanes and the LTDBs were installed in the demonstrator crate before the detector closure.

The two baseplanes installed had been tested at the EMF before installation. In Figure 78a a half FEC after the extraction of the FEBs can be seen. In Figure 78b, one corner of the baseplane with the drilled holes is shown. The whole baseplane has 24 holes to be screwed to the pedestal. The holes were just big enough for the screws to fit through and did not match exactly the holes on the pedestal. It is important to note that the next time when installing a baseplane it would be most convenient to slightly enlarge the holes to leave more latitude.

Furthermore, plugging the connectors of the warm cables to the baseplane turned out to be quite time consuming because one had to reach through the pedestal opening cover to connect the warm cables between the feedthrough and the baseplane (Figure 79).

In Figure 80, the demonstrator crate with all FEBs can be seen. On the right side of the crate, the first LTDB has been installed. The green lights show the



Figure 79: Connecting the warm cables to the baseplane by reaching through the pedestal.

proper configuration of the FEBs. The blue cables are the optical fibres connecting the LTDB to the back end. The second LTDB was installed shortly before the access to the detector was lost.

## 6.10 Tests of the demonstrator system in ATLAS

In order to verify the proper installation of the demonstrator, calibration data was taken both via the standard readout and with the LTDB within the LAr calibration infrastructure.

In a similar way as in the tests at the EMF, the total noise and coherent noise fraction, the connectivity and in addition the amplitude shapes were measured and compared to those of the neighbouring crates in order to verify that the values measured with the demonstrator crate were similar to the other crates.

### 6.10.1 Connectivity

As a first step, the connectivity of the demonstrator crate was tested by operating the shaper switches which act between the FEBs and the TBB. For trigger towers which showed a signal where expected the connectivity was verified.

### 6.10.2 Total noise on main readout and trigger readout path

The total noise on the FEB channels of the neighbouring crate was compared to the total noise of the demonstrator crate, as shown in Figure 81. The noise levels are expected to be the same since the FEBs in both crates read out regions of the calorimeter which are close to each other. When comparing the plots it can be seen

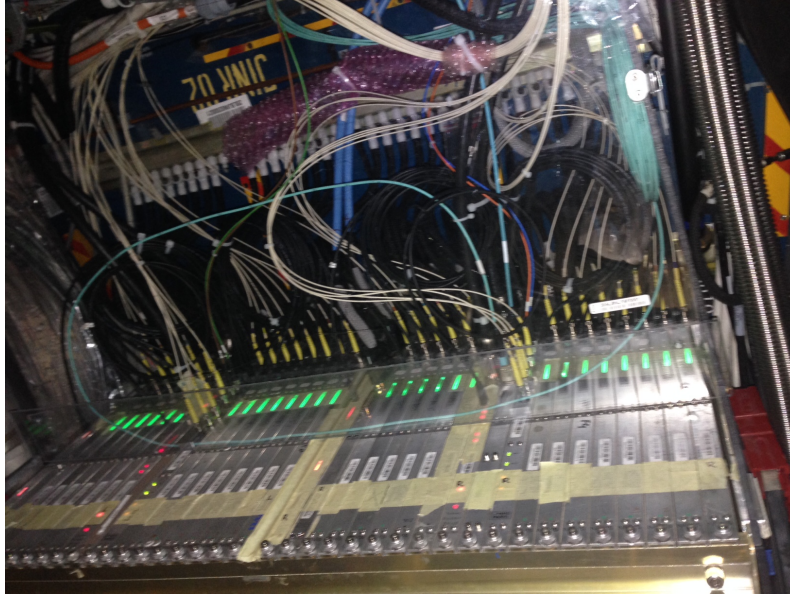


Figure 80: Full crate on the ATLAS detector equipped with all FEBs and one LTDB on the right side. The other LTDB for the other half was installed approximately one month later.

that the noise levels are the same and there was no additional noise introduced by the demonstrator crate.

The L1Calo system measured the total noise of all crates seen in the trigger readout path. The map for the total noise is shown in Figure 82. The total noise was measured with the shaper switches opened and closed. In the region of the demonstrator crate ( $0 < \eta < 1.475$  and  $1.8 < \phi < 2.2$ ) there is no increase of the total noise measured by the L1Calo system.

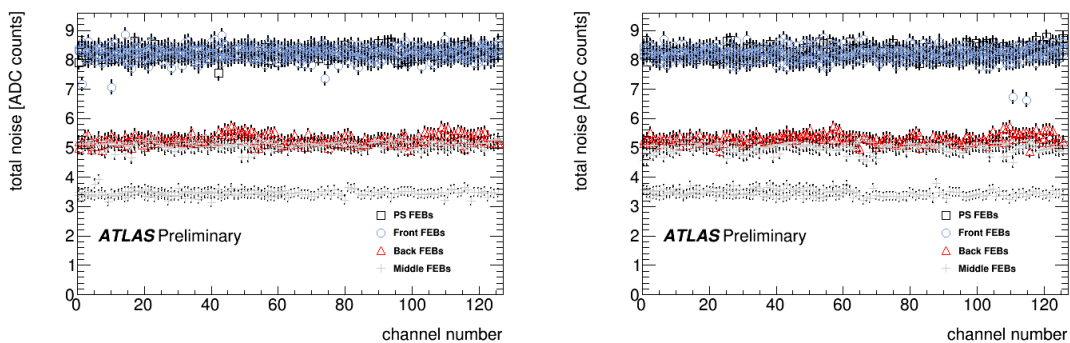


Figure 81: On the left side the RMS for all channels of the FEBs of the demonstrator crate can be seen. On the right side the same for the neighbouring crate I05 is shown.

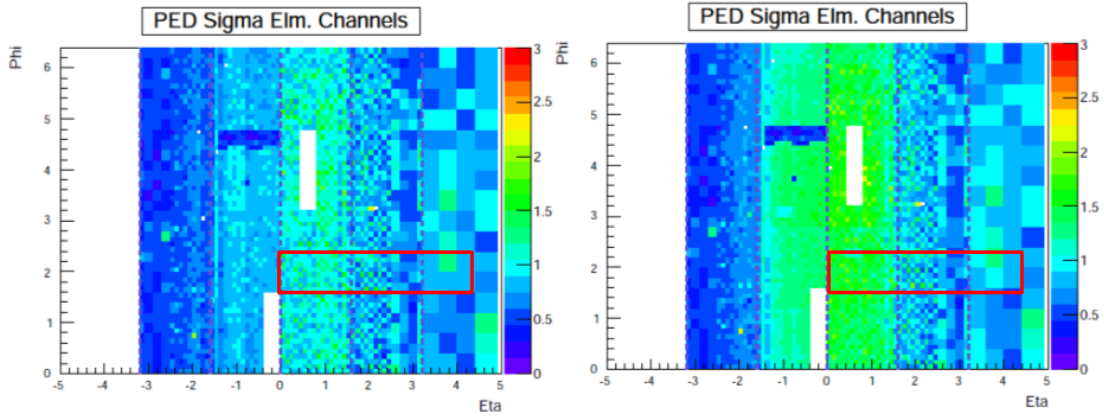


Figure 82: On the left, the total noise with the shaper switches opened is shown. On the right, the total noise with the shaper switches closed is depicted. The red box indicates where the demonstrator region is. When the shaper switches are closed, the noise from the detector can also be seen. Thus, the total noise level increases. However, there is no particular increase of the noise in the demonstrator region.

### 6.10.3 Coherent noise fraction

The coherent noise was computed as a fraction of the total noise for the demonstrator crate and the two neighbouring crates, as shown in Figure 83. Feedthroughs 9 and 10 belong to the demonstrator crate I06, feedthroughs 7 and 8 to I05 and feedthroughs 11 and 12 to I07. The last entry shown in the plot (slot 15) is the coherent noise fraction of the whole half-crate. For all feedthroughs the values are comparable and there is no increase of the coherent noise fraction for the demonstrator crate per FEB. The coherent noise depends on the FEB type and is slightly higher for the PS in slot 1 than for the front layer FEBs (slots 2-7). It is lower for the back layer FEBs in slot 8 and 9 and increases for the middle layer FEBs in slots 10 to 14. The FEB in slot 14 has half the number of channels in comparison to the other middle FEBs, hence, the coherent noise for that board is decreased. Also the coherent noise of one half-crate of the demonstrator, which is equal to one feedthrough, does not show an increase in comparison to the other feedthroughs (shown in slot 15).

### 6.10.4 Total noise and pedestal on LTDB

In addition to the total noise measured on the FEBs, the pedestal of the signal through the LTDB and its RMS was measured as well. In Figure 84 the total noise and pedestal of the 12-bit ADC of the 320 channels of one of the LTDBs installed in the demonstrator crate is shown. One ADC count corresponds to roughly 125 MeV.

### 6.10.5 Amplitude shapes

The amplitude shapes are the peak values taken from the calibration pulses for all channels of a board or an entire crate.



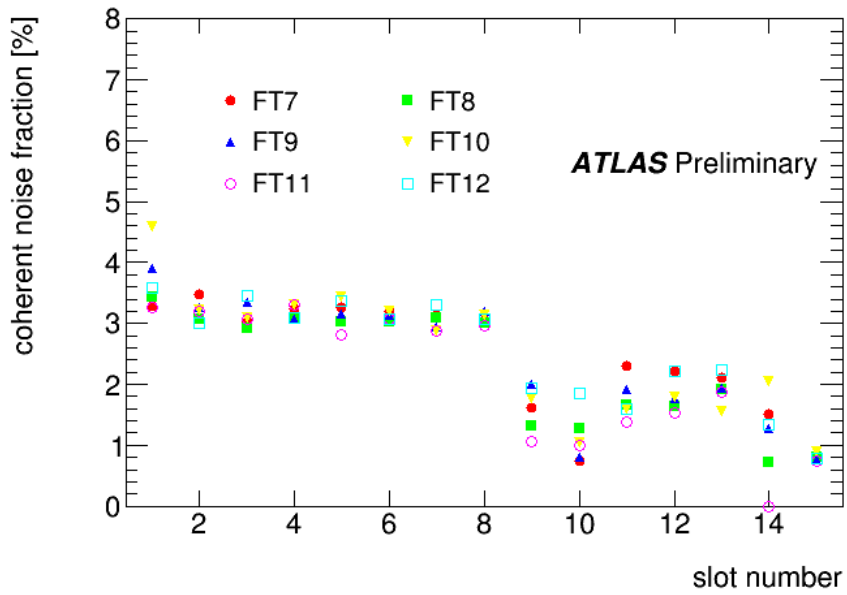


Figure 83: Coherent noise fraction for each FEB for the feedthroughs (FT) of the demonstrator crate (FT 9 and 10) and the two neighbouring crates [52].

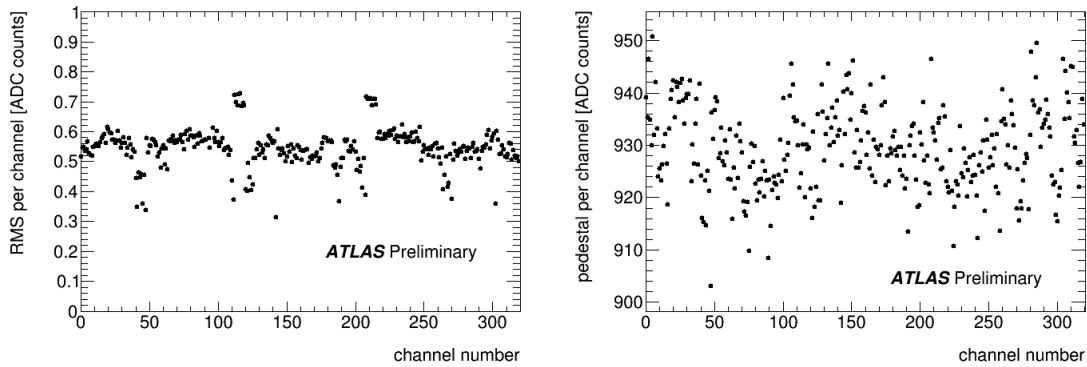


Figure 84: On the left side the RMS for all channels of the LTDB can be seen. On the right side the pedestal values for all channels of the LTDB are shown [52].

The amplitude shapes for neighbouring crates are expected to be similar because they usually read out adjacent regions of the calorimeter. Therefore, the amplitude shapes of the demonstrator crate were compared to those of the neighbouring crate (Figure 85). A small shift in amplitudes could be observed also among other crates. Hence, the shapes for the demonstrator crate are as expected.

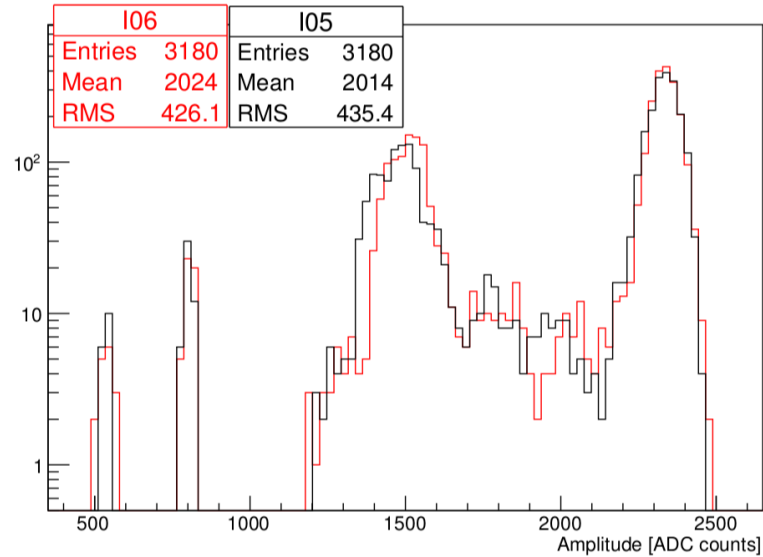


Figure 85: Amplitude shapes for the demonstrator crate I06 and the neighbouring crate I05. Here the peak values of the pulses read out during a ramp run are plotted for all channels of the boards in a half crate.

### 6.10.6 Conclusion on demonstrator installation

After the installation of the demonstrator on ATLAS, the connectivity, the total noise and the coherent noise fraction on the main readout and the trigger path, the total noise and pedestal on the LTDB (with digital part switched on and off) and the amplitude shapes were measured. All values were verified to be as expected. Hence, the proper installation of the demonstrator front end system was verified and the attention was moved to the back end.

## 7 Calibration of the Demonstrator System

### 7.1 Calibration system in ATLAS

For the LAr calorimeter, a precise calibration system is used allowing to measure the response of the readout electronics and extract the calibration constants needed for the energy calculation. In this way, it can be avoided that the stability and uniformity of the ionization signal deteriorates.

This is accomplished by injecting a current pulse of a known shape and amplitude (similar to the current generated by the ionization pulse) close to the point where the ionization current is picked up. In Figure 86, the electronic components of the calibration system are schematically drawn.

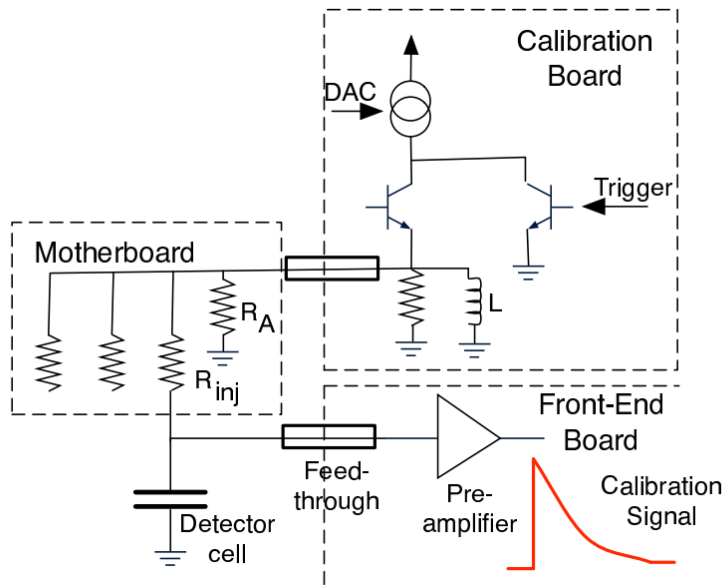


Figure 86: The electronics of the calibration system is depicted here. By switching the inductance  $L$ , a calibration pulse is generated which is split among several calorimeter cells via a network of resistances located on the motherboard. Figure from [53].

A uniform, stable and linear signal whose shape is close to the triangular ionization signal of the calorimeter is provided to all channels. The calibration board contains 128 identical channels. A precise current  $I_p$  is built from a custom Digital-to-Analog Converter (DAC) ASIC with 16-bit dynamic range. The voltage pulse is converted to current using an external 0.1% resistor [54]. The calibration signal has a short rise time and an exponential decay (in contrast to that, the ionization signal has a linear decay). It is produced by interrupting a current, which is set via a DAC, through an inductance. The DAC value determines the amplitude of the signal. The calibration board is located in the FECs, together with the FEBs. The network of resistors to distribute the signal to several calorimeter cells is inside

the cryostat, as close as possible to the calorimeter cells. The values of the resistors depend on the dynamic range of the cells. The resistors for the front layer have a value of 3 k $\Omega$ , the ones for the back layer 1 k $\Omega$ . The values for the resistors of the middle layer change values with  $\eta$ . They are 1 k $\Omega$  for  $\eta < 0.8$  and 500  $\Omega$  for higher  $\eta$ .

It is also possible to delay the calibration pulse relatively to the readout in steps of 1 ns thanks to a delay chip on the calibration board.

Hence, the three parameters which can be set on the calibration board are the DAC value, the delay and the pulsing pattern which determines which cells are being pulsed.

## 7.2 Data encoding

The raw data acquired by the ATLAS subdetectors are written to data files and stored at CERN tape archives. The byte streams produced by boards located in the back end are compiled by the Readout Drivers (RODs), which differ for each subdetector, and the common ATLAS Data Acquisition System. The byte stream format, called *Eformat*, is a hierarchical system of fragments [55].

Each fragment consists of a header and many sub-fragments. The outermost fragment is the *Event fragment*, which contains several *ROB fragments*. The Event and ROB fragment has a header with the event formatting information needed to decode it. Optionally, there might be also a trailer with a checksum. Each ROB fragment maps on a single *ROD fragment*. The ROD fragments contain the raw data and are specific to the sub-detector systems. The encoding of the data within the ROD fragment is up to the sub-detectors. A schematic illustration of the structure of the Eformat is shown in Figure 87

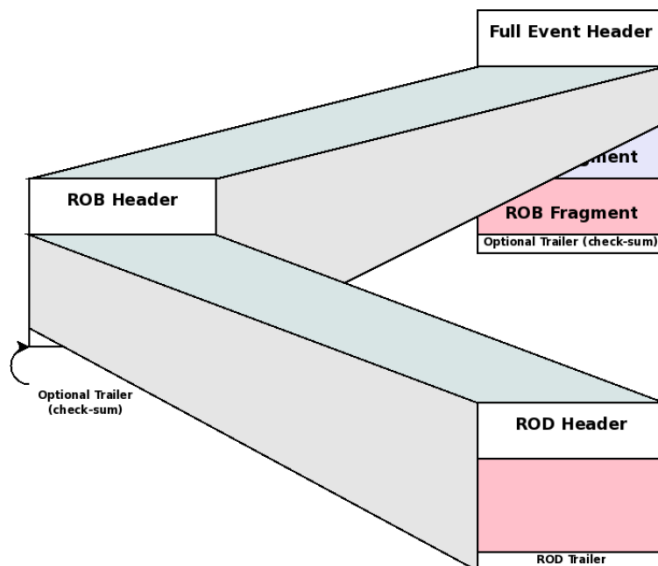


Figure 87: Class diagram of the raw event data format.

### 7.2.1 Header formats

As shown in Table 7, the ROB header is composed of a generic and a specific part. The generic part is the same for the Event and ROB fragment. It is slightly different for the ROD fragment.

Generic header part	
	Start of header marker
	Total fragment size
	Total header size
	Format version number
	Source identifier
	Number of status elements (n)
	Status element [0]
	...
	Status element [n-1]
	Check sum type
Specific header part	
	Specific header [0]
	Specific header [m]

Table 7: Listing of words in the ROB fragment header.

In the following, the elements of the generic part are described in detail:

- *Start of header marker*: This element indicates the start of a fragment. Its value is unique for each type of fragment.
- *Total fragment size*: The total number of words in the whole fragment.
- *Total header size*: Total number of words in the header.
- *Format version number*: Format version of the fragment.
- *Source identifier*: This element consists of the sub-detector ID and the Module ID. It is unique across whole ATLAS.
- *Number of status elements*: Number of status elements in the header.
- *Status elements*: These data words contain information about the status of the data within the fragment.
- *Check sum type*: This element indicates if there is a check sum in the trailer and, in case it is present, what type of check sum there is.

The ROD data format is shown in Table 8.

Header	
	Start of header marker
	Total header size
	Format version number
	Source identifier
	Run number
	Status element [0]
	...
	Status element [n-1]
	Check sum type
	Specific header part
	Specific header [0]
	Specific header [m]
Payload	
	Data elements
	Status elements
Trailer	
	Number of status elements
	Number of data elements
	Status block position

Table 8: Listing of words in the ROD fragment header.

## 7.3 Energy reconstruction of a calorimeter cell

### 7.3.1 Principle of energy reconstruction

The ADC samples of the ionization signal together with the constants calculated from the calibration data taken during dedicated calibration runs are the basis for the energy calculation. As can be seen in Figure 20, the LAr signal has an undershoot caused by the shaper on the FEB. In order to accommodate for that, the ADC has a pedestal of about 1000 counts which has to be subtracted from the samples. For computing the peak of the ionization signal, the *Optimal Filtering Method* is used (described in Section 7.3.2). After obtaining the amplitude of the signal, an ADC to energy conversion factor is applied, which takes into account the electronics gain, the current to energy conversion factor and the sampling fraction of the calorimeter.

Three gains can be set in the readout chain: high, medium and low.

### 7.3.2 Optimal Filtering Coefficients computation

The Optimal Filtering (OF) [56] is used for computing the peak of the ionization signal in calorimeters operating in high luminosity environment while minimizing the contribution of thermal and pile-up noise.

The general approach for the determination of amplitude and timing from the samples uses the autocorrelation function of the samples. This is a function of the ratio of the thermal to pile-up noise amplitudes, to maximize the SNR in order to determine the time origin and the amplitude of the signal.

The peaking time of shaped signals is 20 ns or greater. The entire waveform is dwelling for at least 400 ns, typically the drift time of electrons in the detector planes. Collisions occur at intervals much shorter than the dwell time, and hence pile-up effects will play an important role.

As mentioned before and as it was discussed in Section 3.4.2, the two principal sources of noise which must be considered for liquid ionization calorimeters operating in a high luminosity environment are

- Series thermal noise, whose amplitude depends only upon the characteristics of the detector and the signal processing circuitry. Because usually units of transverse energy are used, all signals from the calorimeter are weighted with  $\sin\theta$ , so the thermal noise becomes negligible at large  $\eta$ .
- Pile-up noise, which is due to the constant bombardment of calorimeter cells by products of collision reactions with high cross-sections. Pile-up signals are generated at beam crossing frequency. The number spectrum of the events is given by a Poisson distribution. Its mean value  $N_i$  for event type  $i$  is related to the cross-section  $\sigma_i$ , the bunch spacing  $T_c$ , and the collider luminosity  $\mathcal{L}$  by the formula  $\overline{N}_i = \mathcal{L}T_c\sigma_i$ .

The waveforms  $g(t)$  to be analysed are produced by the convolution of the current waveform from the ionization with the impulse response of the circuit in the readout chain and are given by:

$$g(t) = \frac{1}{q_s} h(t) * i(t) = \frac{1}{q_s} \int_{-\infty}^{\infty} i(t-u)h(u)du \quad (21)$$

In this equation,  $q_s$  is the integrated signal charge,  $i(t)$  the function of the ionization current and  $h(t)$  the impulse response of the readout circuit.

The quantity which characterizes the impulse response time is the measurement time  $t_m$ . It represents the time of integration of the current and is defined as

$$t_m = \int_0^{\tau_{zc}} h(t)dt. \quad (22)$$

$\tau_{zc}$  is the zero-crossing point of the first lobe of the impulse response, as can be seen in Fig. 88.

Because of the short spacings between bunch crossings and the many events per collision, the ability to correlate signals in time depends on the extraction of the timing information from the signal itself. Intuitively, one expects that the timing resolution improves and the effect of event pile-up is reduced if the measurement time is decreased. However, such a reduction leads to a deterioration in the SNR due to two effects:

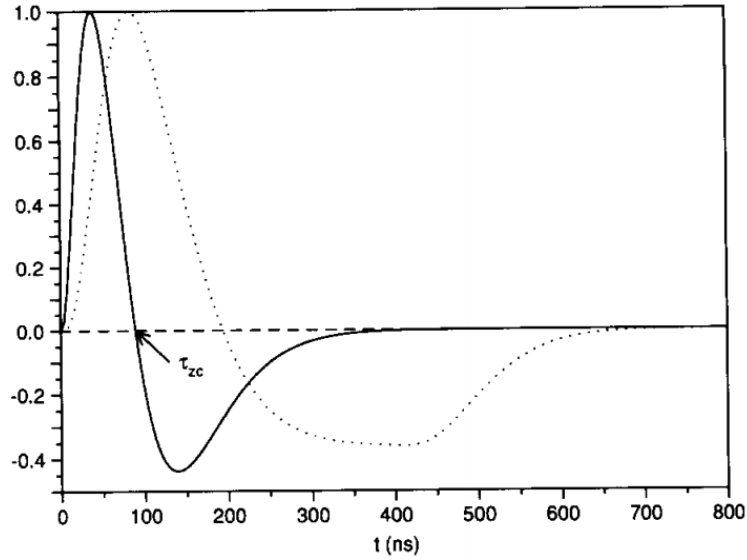


Figure 88: The shape of the impulse response and the signal waveform for the case of  $t_m = 50$  ns and a drift time of 400 ns is shown here. The point  $\tau_{zc}$  where the lobe crosses zero is used for the calculation of the measurement time  $t_m$ . The amplitude is normalized to 1 [56].

- The thermal noise increases as the bandwidth of the system is increased.
- As  $t_m$  is decreased, a smaller fraction of the charge deposited in the calorimeter is utilized in the signal processing. This leads to a reduction of the signal height, and a corresponding increase in the thermal noise.

It is crucial to understand how to choose the optimum for the shaping time  $t_m$ , considering the two effects of thermal and pile-up noise. For determining the amplitude and timing information from a set of measured samples, it is assumed that the form of the signal at the output of the pre-filter is known, except for its amplitude  $A$  and time origin  $\tau$ . The expression for the signal samples at  $t_i$  is given by

$$S_i = Ag(t_i - \tau). \quad (23)$$

Here, the signal shape  $g$  is the convolution of the impulse response  $h(t)$  with the drift current  $i(t)$ .

OF refers to the formation of linear combinations of signal samples to recover the signal parameters, namely the amplitude  $A$  and start time  $\tau$ , while minimizing the effects of noise. Hence, coefficients  $a$  and  $b$  are defined and form the linear sums  $u$  and  $v$  of signal samples  $s$ :

$$A = \sum_{i=1, \dots, n} a_i s_i \quad (24)$$

$$A\tau = \sum b_i s_i, \quad (25)$$



where  $a_i$  and  $b_i$  are the optimal filtering coefficients and  $s_i$  are the samples with the pedestal subtracted.

The shape of the signal is known, so that the samples  $s_i$  will have values

$$s_i = Ag(t_i - \tau) = Ag_i - A\tau g'_i + n_i \quad (26)$$

where  $n_i$  is a noise component.

$g_i$ ,  $g'_i$  and  $n_i$  differ from cell to cell. Hence, there is a set of OFCs per calorimeter channel and per shaper gain.

The expectation value of  $u(v)$  is required to be  $A(A\tau)$ , hence, the following equations are obtained:

$$A = \langle u \rangle = \sum_i (Aa_i g_i - A\tau a_i g'_i + \langle n_i \rangle) \quad (27)$$

$$A\tau = \langle v \rangle = \sum_i (Ab_i g_i - A\tau b_i g'_i + \langle n_i \rangle) \quad (28)$$

The noise averages to 0 and the variances of the parameters  $u$  and  $v$  are given by

$$\text{Var}(u) = \sum_{ij} a_i a_j \langle n_i n_j \rangle = \sum_{ij} a_i a_j R_{ij} \quad (29)$$

$$\text{Var}(v) = \sum_{ij} b_i b_j \langle n_i n_j \rangle = \sum_{ij} b_i b_j R_{ij} \quad (30)$$

The expectation value  $\langle n_i n_j \rangle = R_{ij}$  is the autocorrelation function evaluated at time  $t_i - t_j$ .

After minimizing the above functions using Lagrange multipliers  $\lambda$ , a set of linear equations is obtained. The solutions for  $a_i \equiv a$  and  $b_i \equiv b$  are the following:

$$a = \lambda Vg + \kappa Vg' \quad (31)$$

$$b = \mu Vg + \rho Vg' \quad (32)$$

The matrix  $V$  is the inverse of the autocorrelation matrix  $R \equiv R_{ij}$ .

### 7.3.3 Conversion of signal amplitude to energy

For obtaining the cell energy in MeV, the following quantities have to be measured:

#### 7.3.3.1 Electronic gain

The relation between ADC counts and ionization current is measured on a regular basis by the calibration system. As an output, the fit of ADC values to DAC values is obtained, which is in first approximation a linear function and, if looking into more details, a higher order polynomial to account for non-linearities in the readout electronics. The relation between the used DAC value, the injected current  $I_{\text{inj}}$  and the injection resistor  $R_{\text{inj}}$  is given by the following equation:

$$\frac{I_{\text{inj}}}{DAC} = \frac{5V}{(2^{16} - 1)R_{\text{inj}}} \quad (33)$$

### 7.3.3.2 Sampling fraction

The sampling fraction is defined as the ratio of the energy deposit in the active regions of the calorimeter and the total energy deposit. It can be obtained from Monte Carlo simulations.

### 7.3.3.3 Current to energy conversion factor

The conversion factor from the energy deposit to the induced current can be calculated from the drift time and the average energy needed to produce an electron/ion pair (23.6 eV for argon). The energy deposit of one eV frees electrons and ions with a total charge of  $e/W$ , where  $e$  is the elementary charge. Since the ions drift very slowly, they can be neglected in the calculation. The electrons induce a current at the signal electrode. As they get absorbed at the anode, the current decreases which leads to the observed triangular shape of the ionization signal.

The peak current per deposited charge  $q$  is given by

$$I = \frac{q \cdot v}{d}, \quad (34)$$

where  $v$  is the drifting velocity of the electrons over the distance  $d$ .

The drift time  $t_d$  is given by  $t_d = \frac{d}{v}$  and the charge per deposited eV by  $\frac{q}{E} = \frac{e}{W}$ . When replacing  $v$  and  $q$  in equation 34, the following expression is obtained:

$$\frac{I}{E} = \frac{e}{t_d \cdot W} \quad (35)$$

The drift velocity  $v$  is dependent on the electric field and the temperature of the liquid argon. It was measured during the design phase of the calorimeter and can be described by an empirical formula, as discussed in [57].

The values entering equation 34 at a nominal liquid argon temperature of 89.3 K, a given gap width and a voltage of 2 kV are summarized in Table 9. The numbers given in this table are only valid for the sections of the calorimeter where the electric field is homogeneous and recombination of the electron/ion pairs can be neglected.

Region	Gap width [mm]	Drift velocity [m/s]	I/E [nA/MeV]
Presampler	2.00	4593	15.6
Accordion	2.12	4508	14.4

Table 9: Drift velocities and I/E factor computed for the presampler and accordion.

### 7.3.4 Electronics calibration

The calibration has to provide the best possible energy measurement for the offline physics analysis and the trigger system.

The electronics constants mentioned in the previous sections are obtained by dedicated calibration runs. They may vary with time and are measured individually

for each cell and each gain. The following types of runs are taken for the electronics calibration:

#### 7.3.4.1 Pedestal run

Runs without injected charge are used to monitor the noise level and establish a pedestal, the ADC values which would be read out without any input signal. This corresponds to approximately 1000 ADC counts to accommodate for the undershoot of the shaper. During physics runs, random triggers are used to measure and monitor the pedestal values. On the detector, the pedestal is computed for each cell and shaper gain by an average over a given number of periodic triggers and over the number of samples. The noise autocorrelation matrix used for the OF computation is also obtained from the pedestal runs.

#### 7.3.4.2 Ramp run

Each channel is pulsed  $N$  times with a set of given input currents, the DAC values, which can go up to a value of  $\approx 65000$ . For each trigger, the ADC value of each of the samples is read. The mean value and the RMS of these ADC values are computed over the  $N$  triggers for each sample and an averaged calibration wave is obtained for each DAC value.

The data points corresponding to  $\text{DAC} = 0$  are subtracted from the other pulse shapes to remove possible effects for parasitic injection charge which can be up to 1 ADC count.

The ramp is the correlation between the pulse peak and the DAC value by which the cell was pulsed and which corresponds to an electrical current.

From that the ADC peak versus DAC curves are obtained and the ramps extracted.

When taking ramp runs on the detector, neighbouring cells are not pulsed at the same time in order to avoid cross-talk effects.

#### 7.3.4.3 Delay run

As for the ramp runs, each channel is pulsed  $N$  times with a given input current at a given time delay between the calibration pulse and the sampling clock. For the scan of the pulse shape, the readout is delayed in steps of  $\approx 1$  ns with respect to the calibration system. For each trigger, the ADC value of each of the  $N_{\text{samples}}$  samples is read and the mean and RMS of these ADC values over the  $N$  triggers for each sample are computed. The delay is sequentially increased until the sampling period, which is the time interval between two consecutive samples, corresponding to the LHC bunch-crossing period of 24.95 ns, is covered. The averaged samples are arranged in time according to the delay value. Eventually, an averaged profile of the response of the cell to the input DAC is obtained. The readout pedestal is subtracted in the end.

For a given channel, delay waves are acquired at different DAC values. They are used to study the linearity of the electronics, compute the Master Waveforms [58] and to complete the ramps computation.

The pulse shapes obtained from the delay runs are slightly different from the ionization pulse shape for two reasons. First, the calibration pulse has an exponential decay due to the inductance and second, the calibration signal is not injected at the same point as the physics signal. This also leads to slightly different peak heights. Hence, the ramp taken on a calibration pulse is systematically slightly wrong and has to be corrected.

## 7.4 Athena framework

*Athena* is the name of the reconstruction software framework developed by the ATLAS Collaboration [59]. It is an object-oriented C++ based framework that incorporates various other frameworks like ROOT or Pythia. Athena provides several services like histogramming, an event loop manager and allows to implement user algorithms in a flexible way. An Athena job is configured by a *job option file*, that is written in the Python programming language. The job option file defines which services, algorithms, etc. are to be executed and provides the possibility to pass parameters to these services.

## 7.5 LAr calorimeter reconstruction software

The steps which are necessary to get from raw data to physics analysis objects are presented schematically in Figure 89.

### 7.5.1 Event data objects

The data objects that are part of the energy reconstruction process are the following [60]

- *Identifier*: In order to specify a certain calorimeter cell, there are two types of identifiers: The online and the offline identifier. The online identifier describes the position of the cell in the readout system, hence, it contains, detector part, feedthrough number, FEB number and channel number. The offline identifier describes the position in terms of  $\eta$ ,  $\phi$  and layer. The cabling service allows to go from one type of identifier to the other.
- *LArDigit*: This container stores the raw ADC data samples recorded by the FEBs, together with the used gain and the online identifier.
- *LArRawChannel*: This class contains the roughly calibrated energy of a cell, the peak time of the signal and a quality factor. In addition, the online identifier and the gain are stored.
- *LArCell*: The calibrated energy here has a refined calibration, but the identifier used here is the offline identifier. LArCell derives from CaloCell that is the common class for Tile and Liquid Argon cells.

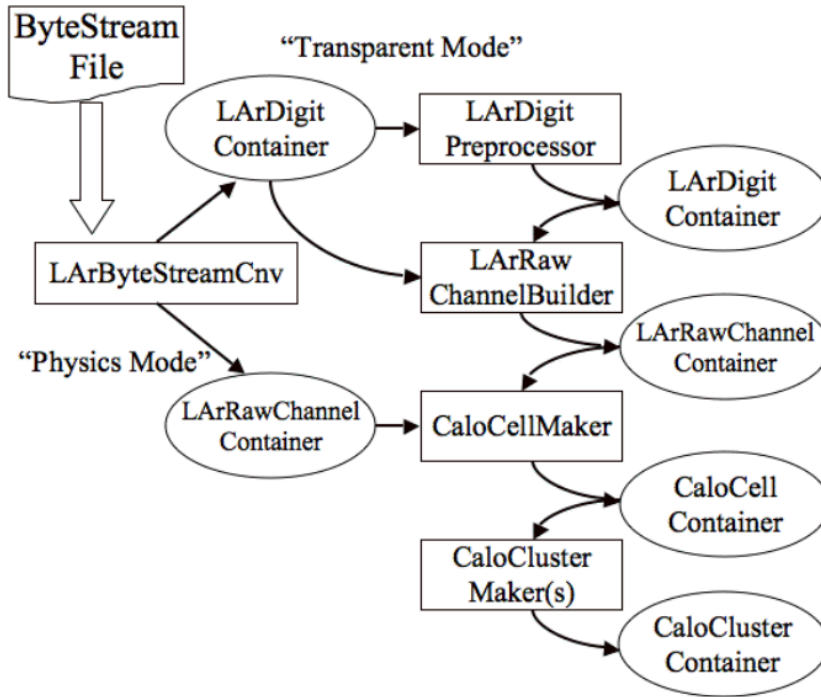


Figure 89: Schematic diagram of the data objects and algorithms used for the calorimeter energy reconstruction. Data objects are depicted as ovals and algorithms as rectangles [60].

- *CaloCluster*: This container stores the energy, size and position of a cluster. This may belong to any of the calorimeters, since, a cluster can span over the boundaries of the Liquid Argon calorimeter.

### 7.5.2 Implementation

The byte stream conversion service for the main readout of LAr reads in the raw data file and discards all headers and trailers in order to reach the payload of a data block. The format of the data in the payload depends on the code running in the DSPs on the RODs (*Transparent*, *Accumulating* and *Physics* mode). In the transparent mode, the samples are written out as they are recorded by the FEBs. In the accumulating mode, the DSP sums the samples of a given number of events in order to compute the averages. In the physics mode OFCs are applied to the samples.

The version number and block type contained in the ROD header allows the code to distinguish between the different modes. The byte stream converter can produce either LArDigits, LArRawChannels or LArCells. LArCells is used for the trigger, LArDigits are produced if the DSP was running in transparent mode and LArRawChannels if it was running in physics mode.

The LArDigitPreprocessor merges containers with different gains into one.

For the cell energy reconstruction, first the peak of the ionization signal is calculated and a rough calibration is done. Subsequently, the calibration is refined by taking into account non-linearities of the electronics and cell dependent corrections. The last step is the formation of cluster of the reconstructed individual cells.

## 7.6 Demonstrator data format

For the demonstrator data taking the system was always working in transparent mode. That means they simply copy the data sent by the LTDB to the byte stream. The energy reconstruction is done by the offline analysis software.

The byte stream written by the board in the back end system of the demonstrator is being composed already at the LTDB. Its format is shown in detail in Table 10.

Word #	Composition of bits
	Sample 0 for channels in fiber 0 and 1
0	fb0_sm0_ch1[11-0] + fb0_sm0_ch0[11-0] + fb1_sm0_ch1[11-4]
1	fb1_sm0_ch1[3-0] + fb1_sm0_ch0[11-0] + fb0_sm0_ch3[11-0] + fb0_sm0_ch2[11-8]
2	fb0_sm0_ch2[7-0] + fb1_sm0_ch3[11-0] + fb1_sm0_ch2[11-0]
3	fb0_sm0_ch5[11-0] + fb0_sm0_ch4[11-0] + fb1_sm0_ch5[11-4]
4	fb1_sm0_ch5[3-0] + fb1_sm0_ch4[11-0] + fb0_sm0_ch7[11-0] + fb0_sm0_ch6[11-8]
5	fb0_sm0_ch6[7-0] + fb1_sm0_ch7[11-0] + fb1_sm0_ch6[11-0]
	Sample 1 for fiber 0 and 1
6	fb0_sm1_ch1[11-0] + fb0_sm1_ch0[11-0] + fb1_sm1_ch1[11-4]
7	fb1_sm1_ch1[3-0] + fb1_sm1_ch0[11-0] + fb0_sm1_ch3[11-4] + fb0_sm1_ch2[11-8]
8	fb0_sm1_ch2[7-0] + fb1_sm1_ch3[11-0] + fb1_sm1_ch2[11-4]
9	fb0_sm1_ch5[11-0] + fb0_sm1_ch4[11-0] + fb1_sm1_ch5[11-4]
10	fb1_sm1_ch5[3-0] + fb1_sm1_ch4[11-0] + fb0_sm1_ch7[11-4] + fb0_sm1_ch2[11-8]
11	fb0_sm1_ch6[7-0] + fb1_sm1_ch7[11-0] + fb1_sm1_ch6[11-4]

Table 10: The bit composition of the words written in the raw data files by the board in the back end is shown in this table. **fb** refers to LTDB fiber, **sm** to sample and **ch** to channel within one LTDB fiber.

If Table 10 was continued, the following 5 words would belong to sample 2 of the same pair of fibres. This continues until all samples of this fiber pair have been transmitted. In the following set of words, the samples for the next fiber pair are transmitted, until all samples for all twenty fibres have been sent.

## 7.7 Athena byte stream converter

The purpose of the byte stream converter is to read in the raw data files written by the board in the back end and rearrange them in a way that one sample is written in one data word.

Each word is then matched with the according channel ID. The pairs of ADC values and IDs is then saved into a LArDigit container, which is used when data is taken in transparent mode.

## 7.8 Calibration runs for demonstrator system

The sequence of DAC and delay values used for the calibration runs for the demonstrator was the same as in the ATLAS standard calibration runs. What was changed were the patterns which were used for pulsing. Instead of pulsing cell by cell as it is done for ATLAS ramp and delay runs, all cells constituting a Super Cell were pulsed.

As for the ATLAS calibration, a pedestal, a ramp and a delay run is needed to compute the OFCs. The demonstrator back end readout consists of two readout board with two FPGAs each. Each FPGA reads out the values of cells with the same  $\phi$  (one " $\phi$ -slice" of the demonstrator region). The runs were taken separately for each FPGA because then the system was more stable and allowed for data taking without event loss.

Although no events were lost, some events showed improper data, as can be seen in Figure 90.

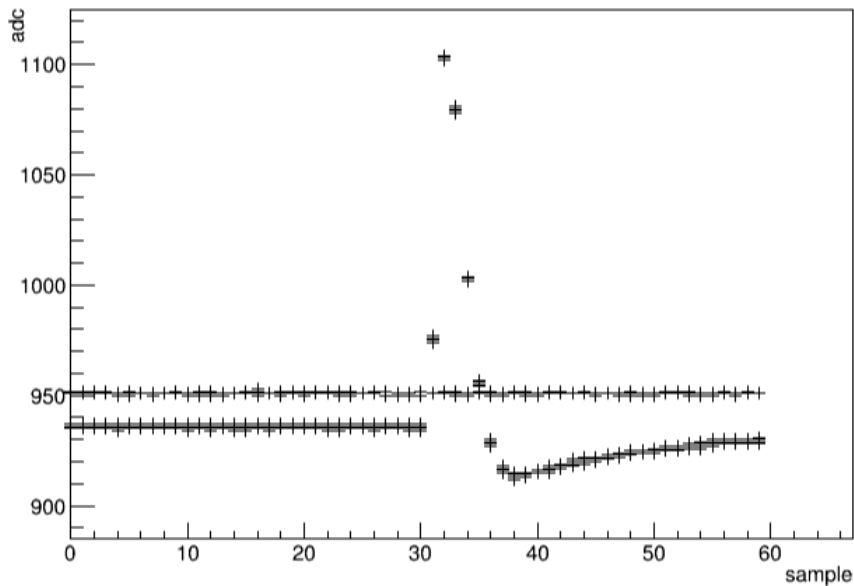


Figure 90: 100 events from a delay run taken with 60 samples and 100 events per delay setting and pulsing pattern. Most events out of the 100 show the expected pulse, but few show just a shifted pedestal instead of the pulse shape.

The reason for the "bad" events was not fully understood, but suspected to occur due to the different triggers used during the delay and ramp runs. For pedestal runs, this kind of misreadings have not been observed.

The events with the shifted pedestal had to be filtered out before they were processed with the calibration framework.

After proper filtering, the obtained pulse shapes from the delay run could be further processed to compute the OF coefficients. The shapes are shown in figure 91.

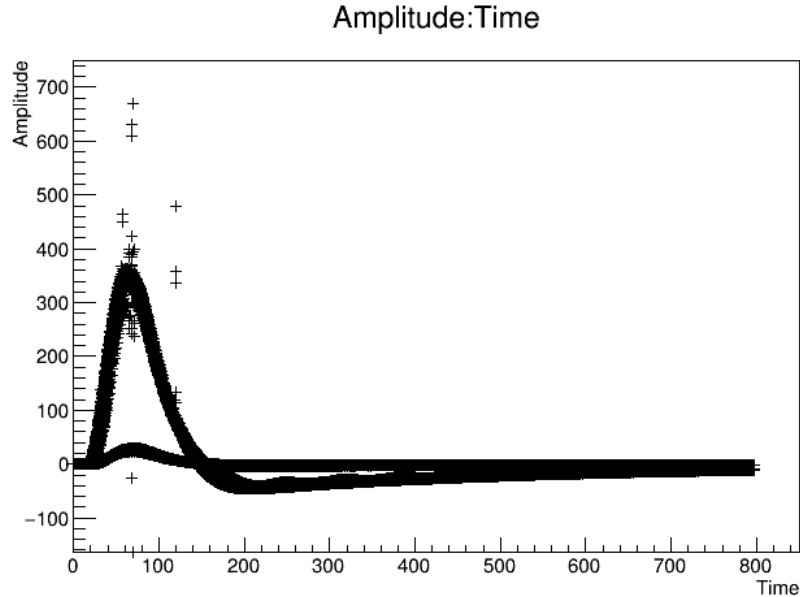


Figure 91: The pulse shapes for one fourth of the channels of the demonstrator are shown in this picture. Some bad readings are still present in the plot, especially on top of the maximum of the pulse, because filtering all of them by hand is not possible. However, they could be used for the computation of the OFCs.

## 7.9 Obtained calibration constants

After taking the needed runs, the data was processed with the byte stream converter. From the pedestal run, the autocorrelation was computed (Figure 92).

With the delay run, the OF coefficients were computed. They are shown in Figure 93.

The structure of the OFCs can be seen when plotting them against the samples in time (Figure 94).



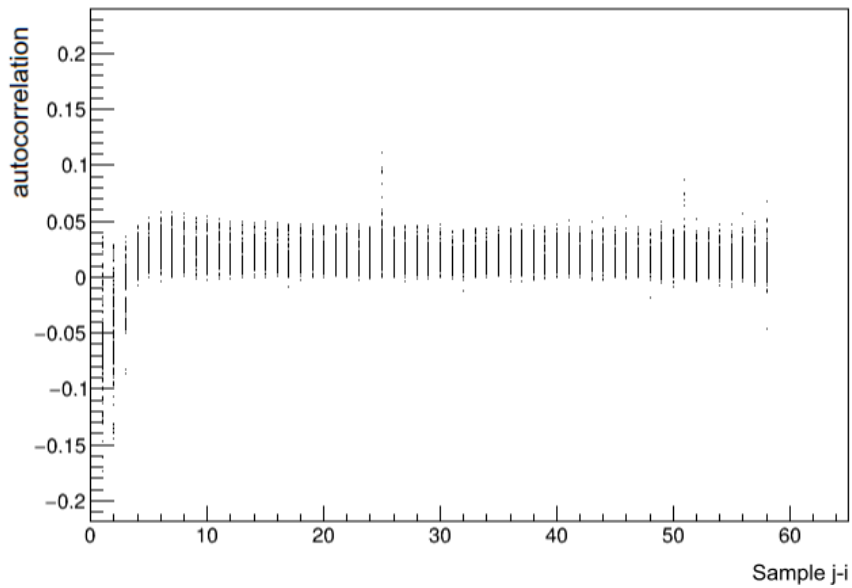


Figure 92: Autocorrelation computed from a pedestal run taken with 60 samples with the demonstrator. Samples which are close to each other in time have a larger autocorrelation value. For samples which are far away from each other the autocorrelation goes as expected to zero.

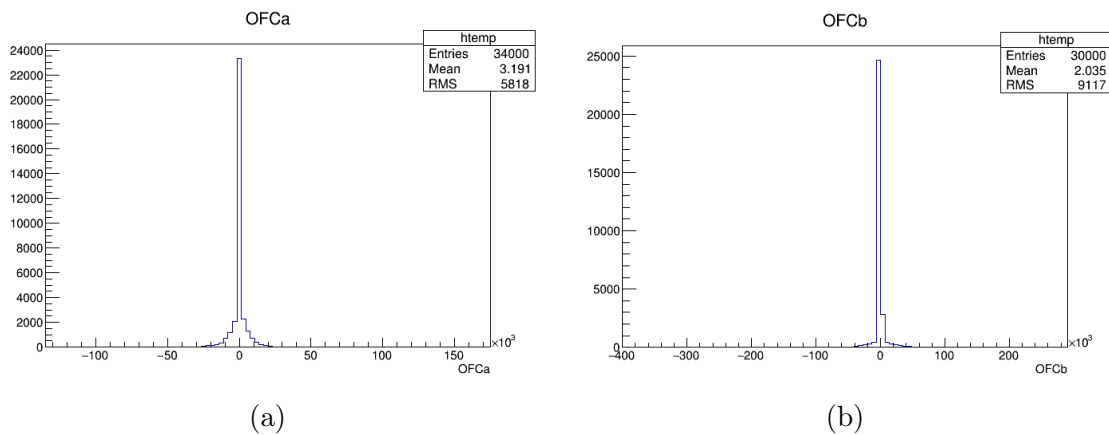
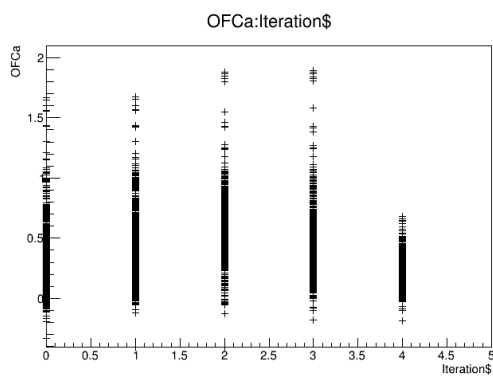
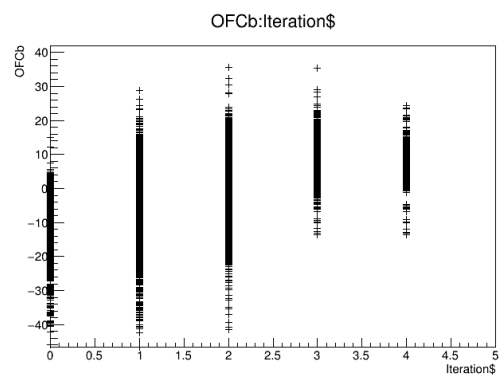


Figure 93: OFCs computed from the delay runs for the Super Cell readout.



(a)



(b)

Figure 94: Here, the OFCs plotted for each of the samples are shown. The shape of the OFCs resembles roughly the pulse shape.

## 8 Physics runs with the demonstrator system

The demonstrator system has been running in parallel with the ATLAS data taking during proton-proton and heavy ion collisions. The main idea of the parasitic running was to compare events from the ATLAS main readout with events recorded by the demonstrator readout. The matching of events was done by comparing the *L1ID*, *BCID* and the *trigger type* from the event header of the demonstrator data and ATLAS data.

The L1ID is a 32 bit number. The last 24 bits correspond to the EVID, which is the event counter. The first 8 bits are assigned to the Event Counter Reset Counter (ECRC). These identifiers are not absolutely unique as in 126000 ATLAS events 8 times the same pair of EVID and ECRC occurs. Hence, also the event signature, for example the  $E_T$ , had to be compared to be able to match the events correctly.

In order to induce the demonstrator back end to read out data, a trigger bit was assigned to trigger in case an event was recorded by the demonstrator region.

Due to instabilities of the firmware, the recording of events was often interrupted in 2015 running. In order to be able to record data again, the FPGAs on the boards in the back end had to be reprogrammed and reset.

### 8.1 Trigger coverage

It was discovered after data taking that the wrong  $\phi$ -slice was chosen for the L1-Calo trigger. Hence, there was no full coverage of the demonstrator region, as is shown in Figure 95. This will be corrected for in the future data taking of the demonstrator.

### 8.2 Proton-proton runs

For the BNL LTDB which is reading out  $\Delta\eta \times \Delta\phi = [0, 1.475] \times [1.8, 1.9]$ , 49000 events were matched to ATLAS events (in total 55000 events for this  $\phi$ -slice were recorded). For the LAL/Saclay LTDB reading out  $\Delta\eta \times \Delta\phi = [0, 1.475] \times [1.9, 2.0]$ , in total 82000 events were matched (from 91000 recorded). All of the data was recorded with 60 samples.

A pulse recorded with the demonstrator readout is shown in Figure 96.

In order to calculate the  $\Delta ADC$ , the mean of the first few leading samples was used to calculate the pedestal. The sample with the maximum ADC value was used as peak sample. Hence, the peak height is given by:

$$\Delta ADC = ADC_{max} - ADC_{ped} \quad (36)$$

In order to obtain the transverse energy  $E_T$  from the ADC values, calibration studies were used.  $E_T$  is obtained by multiplying the ADC value with a calibration constant.

Using this method, the energy depositions were calculated from the demonstrator and the ATLAS main readout. One of the matching events found is shown in Fig. 97.

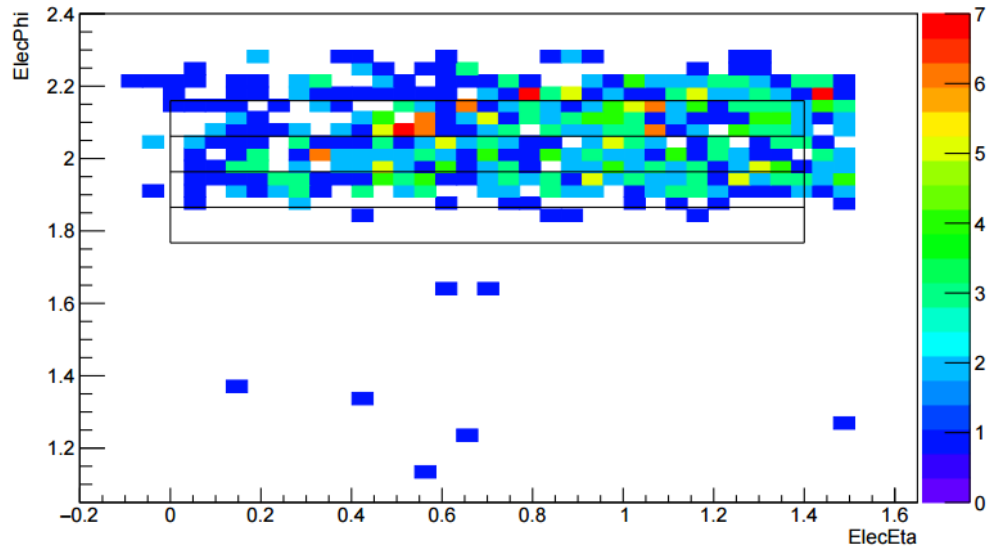


Figure 95: L1-Calo trigger coverage for the trigger used for the demonstrator [61]. The rectangle indicates the demonstrator region. As can be seen, the  $\phi$ -slice at 1.8 is not covered, because the whole region which was triggered on by that trigger type was shifted by 0.1 in  $\phi$ . The scale on the right side shows the number of entries per bin.

With all matched events from all runs from the demonstrator and ATLAS readout a coverage plot was made for the front and middle layer. In total, 8306 events were matched. During data taking, the problem concerning non properly locked fibres was present. Data couldn't be transmitted through this problematic channels during a run, hence, there are many Super cells which appear white in Figure 98.

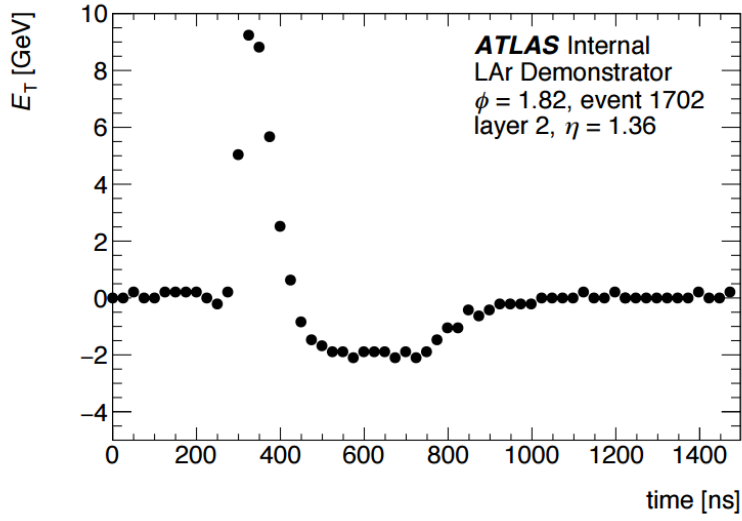


Figure 96: A pulse taken with 60 samples during a proton-proton run.

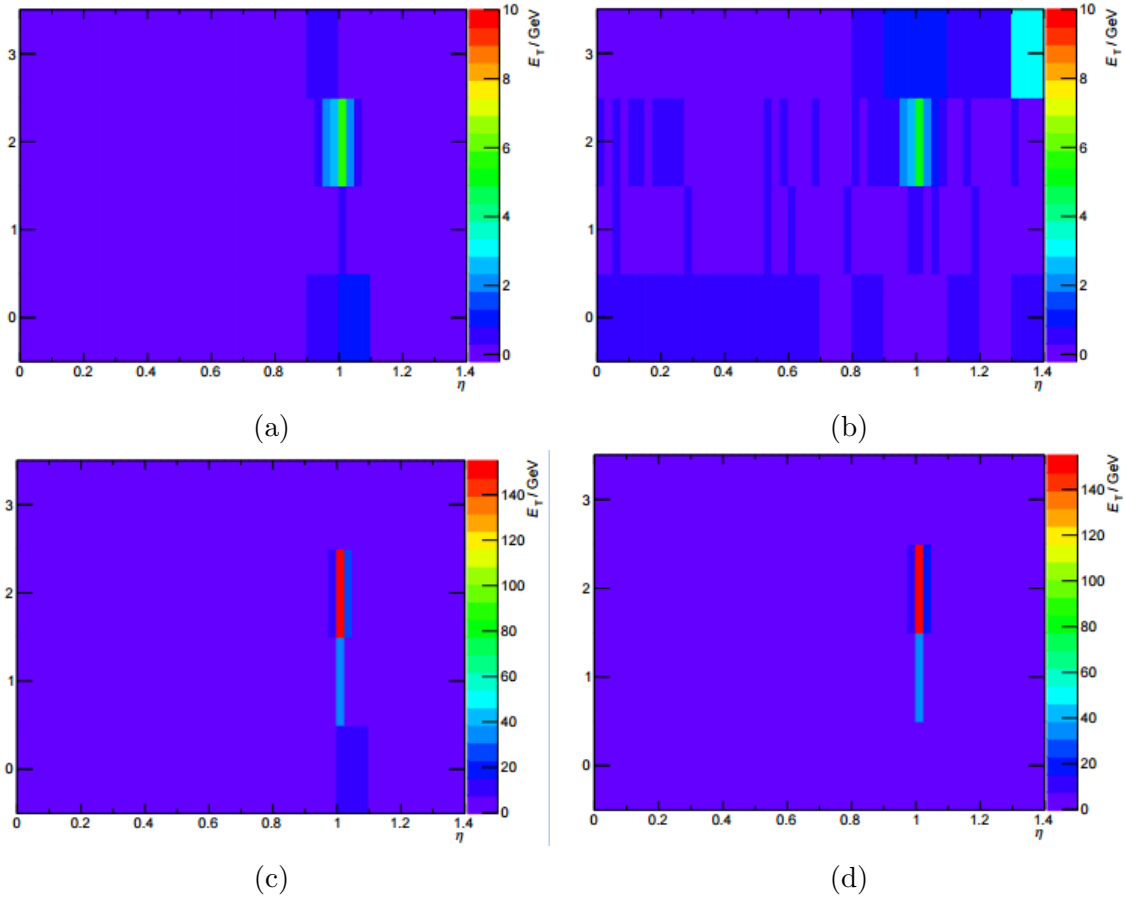


Figure 97: Event displaying an energy deposit recorded in the ATLAS main readout (left side) and the demonstrator readout (right side) [61]. The top plots show the deposit for  $\phi = 1.8$ , the bottom plots for  $\phi = 1.9$ . The left scale indicates the layers in the calorimeter.

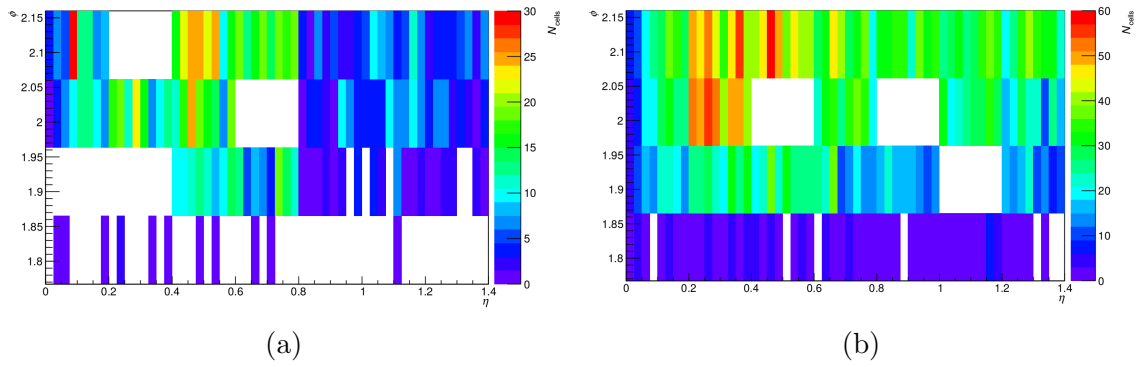


Figure 98: Demonstrator coverage for the front (left) and middle (right) layer of the detector. The white Super cells were these connected to unlocked fibres where data transmission was not possible. In the  $\phi$  slice around 1.8 there are fewer hits due to the wrong coverage of the trigger.

# 9 Impact of an Extended ATLAS Tracker on $W^\pm W^\pm$ Vector Boson Scattering at a High-Luminosity LHC

## 9.1 Vector boson scattering at the HL-LHC

The measurement of Vector Boson Scattering (VBS) provides an excellent opportunity to investigate the nature of Electroweak Symmetry Breaking (EWSB). Additionally, it allows the measurement of possible contributions of New Physics.

In the scope of this work, the potential impact of three ATLAS ITk upgrade scenarios for the HL-LHC [11] on the electroweak  $W^\pm W^\pm$  plus two jets ( $jj$ ) ( $W^\pm W^\pm jj$ -EW) channel was evaluated. The major impact on that analysis comes from the extension of the silicon tracker to pseudorapidities up to  $|\eta| < 2.7, 3.2$  or  $4.0$ , which are referred to as Bronze (Low), Silver (Middle) and Gold (Reference) scenarios, respectively. The values generated by the Monte Carlo simulation were parametrized for the three scenarios with the *Upgrade Smearing Functions* [62].

The results represent the evaluation of the  $W^\pm W^\pm jj$ -EW channel at the HL-LHC based on results from the  $\sqrt{s} = 8$  TeV studies [63, 64]. In this study, the evidence for EW  $W^\pm W^\pm jj$  production was observed with a significance of  $3.6\sigma$ , while  $2.8\sigma$  was expected from calculations from the SM.

In the 8 TeV analysis, the major background of the  $W^\pm W^\pm jj$ -EW channel was  $WZjj$  production where only two leptons were reconstructed. It comprised more than 50 % of the total background of the analysis. In this study, the  $WZjj$  and  $W^\pm W^\pm jj$ -QCD backgrounds were simulated. They were then scaled up to account for the other backgrounds which were not simulated because it was not feasible within the scope of this study.

The backgrounds allow for an assessment of the impact of the pile-up (PU) and lepton acceptance on the  $W^\pm W^\pm jj$ -EW cross-section measurement. The change in performance due to fakes, charge flips, and b-tagging was not taken into account. Hence, the results presented here are a conservative estimate of the benefits of an extended ATLAS tracker on the  $W^\pm W^\pm jj$ -EW channel.

## 9.2 Theoretical overview of vector boson scattering

The spontaneous breaking of the EW symmetry produces three Goldstone bosons which are absorbed into the longitudinal polarisation states of the gauge bosons  $V = W^\pm, Z$ . As a result, the gauge bosons become massive.

The scattering of massive vector bosons  $VV \rightarrow VV$  occurs either through the Higgs boson exchange or through self-interaction of the vector bosons, resulting in triple or quartic gauge couplings - TGC or QGC, respectively (Fig. 99).

In the high energy limit  $E \gg m_V$ , the longitudinal polarisation increases with energy and dominates over transverse components. Hence, it is possible to approximate the VBS as the scattering of its longitudinal components only. The leading term in the VBS amplitude for the gauge terms (top plots of Fig. 99) and the

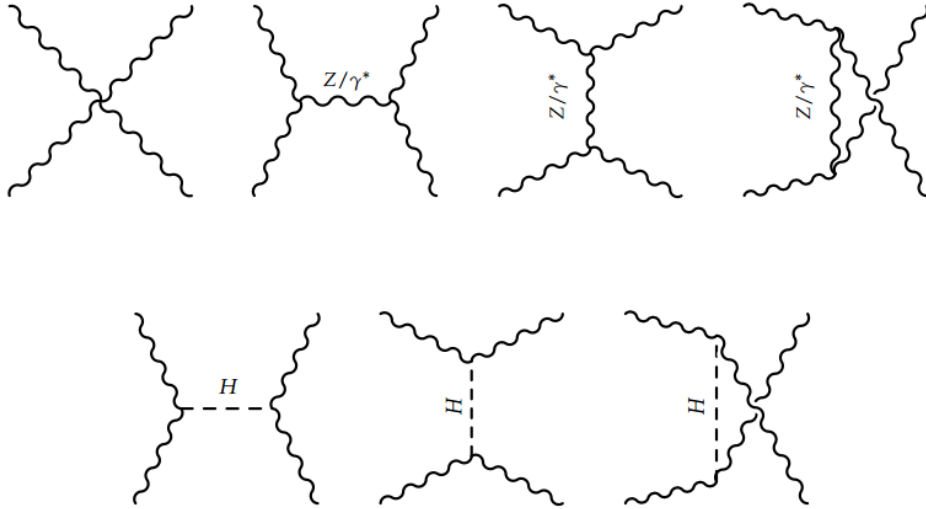


Figure 99: The tree-level graphs for  $VV \rightarrow VV$ . The diagrams on the top show the self-interactions of electroweak gauge bosons and contain triple or quartic gauge couplings. In the bottom plots the interactions including a Higgs boson exchange are depicted. The sine waves represent a vector boson, the dashed lines indicate a Higgs propagation.

scattering amplitude of the Higgs exchange terms (bottom plots of Fig. 99) cancel each other out. Without the Higgs boson, the VBS cross-section would continue to increase at high energies as shown in Fig. 100. This holds only if the properties of the Higgs boson and the values of TGCs and QGCs are as predicted by the SM.

After the discovery of the Higgs boson, it can be probed through the properties of VBS whether the Higgs which was found is a SM Higgs. If the Higgs mechanism alone is not responsible for the EWSB, some New Physics processes should appear at the TeV scale to compensate for the divergent high energy behaviour of the VBS.

Even if the Higgs boson alone is causing the EWSB, it is not excluded that other scalar bosons exist which could alter the Higgs boson couplings. Thus, it is crucial to precisely measure the Higgs and the triple and quartic gauge couplings in order to get a better understanding of the EWSB and possible contributions from New Physics.

### 9.2.1 Same-sign $W^\pm W^\pm$ scattering

In  $pp$  collisions, VBS occurs if two initial quarks radiate vector bosons which scatter, and lead to the final state with two vector bosons and two jets ( $VVjj$ ). VBS is an EW process, however, the  $VVjj$  final state can also be the result of strong interactions. Compared to other VBS processes, the cross-section of EW production dominates in the same-sign  $W^\pm W^\pm$  ( $ssWW$ ) scattering over strong production and is therefore suitable for studying QGCs.

The Feynman diagrams for  $ssWW$  processes can be seen in Fig. 101.



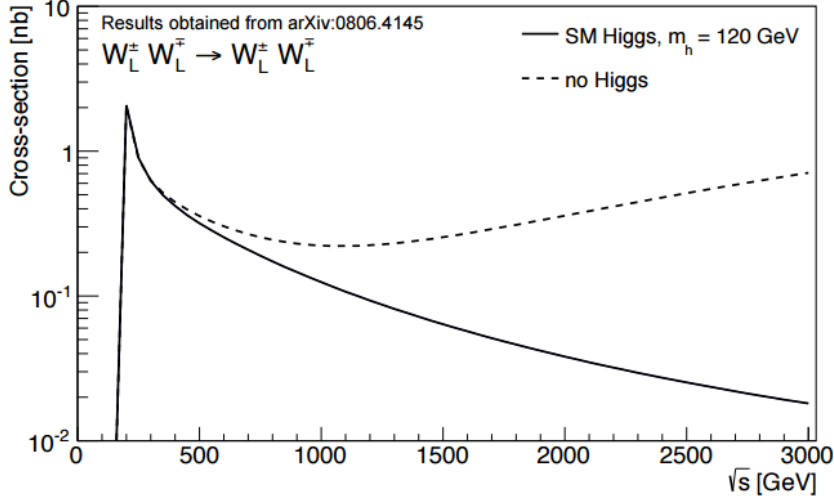


Figure 100: The cross-sections for the VBS with and without the SM Higgs boson diagrams. As can be seen, without a SM Higgs the cross-section would continue to grow for higher energies [65].

The two initial quarks which radiate two  $W$  bosons hadronise into two well separated, highly energetic forward jets with a high invariant mass. The final state  $W^\pm W^\pm jj$  comprises two  $W$ s with the same electric charge. This analysis considers only their leptonic decays into a lepton-neutrino pair. The two final state leptons are energetic and isolated, they have the same electric charge and tend to be in the central rapidity region with respect to the two tag jets. A large missing transverse momentum  $E_T^{miss}$  is expected as well. The event topology is shown in Fig. 102.

## 9.2.2 Backgrounds

In the  $\sqrt{s} = 8$  TeV dataset a signal to background ratio of approximately 1 was observed. The major background contributions are the following:

- *Prompt lepton background:* Additional leptons are not reconstructed or are outside of the experimental acceptance range. 50% of the total background arises from  $WZ/\gamma^* \rightarrow l^\pm l^\mp l^\pm \nu$ , with one missed lepton.
- *Conversion background:* 25% of the total background yields events including  $W\gamma$  production, and processes resulting in oppositely charged prompt leptons where lepton charge identification mainly occurs due to electron bremsstrahlung followed by photon conversion.
- *Non-prompt background:* Leptons from hadronic decays account for 15% of the total background, and  $W^\pm W^\pm jj$ -QCD production yields about 10% of the total background.

The background processes for  $W^\pm W^\pm jj$ -QCD and  $WZ/\gamma^* jj$  were generated in MC. The other processes were either estimated from data in [63] or depend

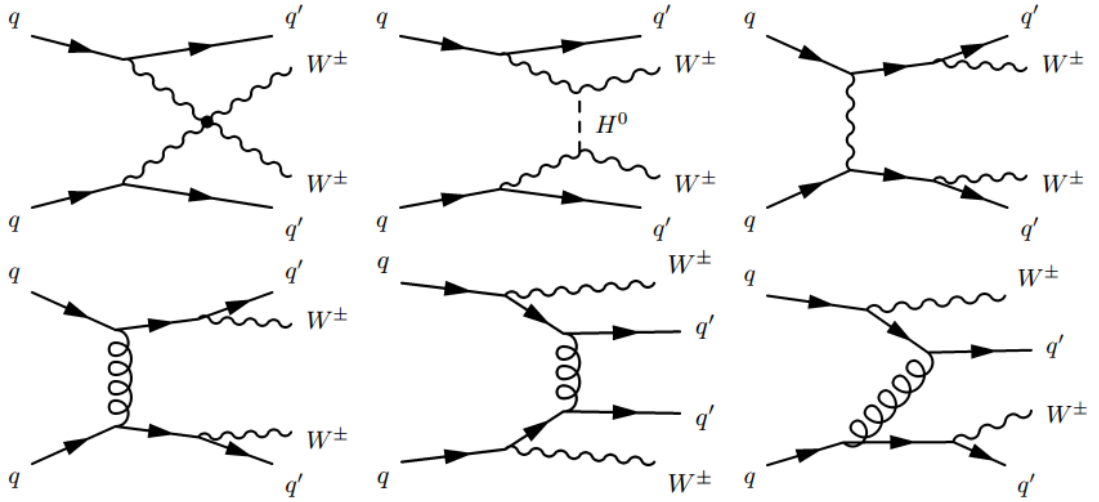


Figure 101: In the top row, the Feynman diagrams for the EW contributions for the  $W^\pm W^\pm jj$  final states are shown (quartic gauge boson coupling, Higgs exchange and non-VBS graph). In the bottom row, the contributions including strong interactions are depicted.

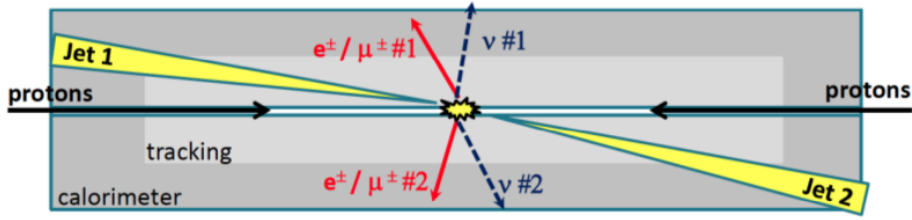


Figure 102: The event topology of the  $W^\pm W^\pm jj$  final state is shown with two isolated leptons, two energetic jets which are well separated in rapidity, and a moderately large  $E_T^{miss}$ .

on the not yet determined material distribution of the future detector. Hence, these backgrounds were not simulated, but their contributions were approximated by scaling up the yields of the other two background processes by a factor of 1.7. This reproduced the total background composition as observed in the VBS signal fiducial volume of the measurement at  $\sqrt{s} = 8$  TeV, assuming that the background composition will be similar at the HL-LHC. However, these contributions might change due to detector effects such as increased material in the forward region, increasing the  $W + \gamma$  background contribution.

In the figures, the  $W^\pm W^\pm jj$  -QCD and  $WZ/\gamma^* jj$  backgrounds are displayed unscaled and the additional backgrounds, called *Other SM bkg.*, are calculated as the sum of  $W^\pm W^\pm jj$  -QCD and  $WZ/\gamma^* jj$  scaled by 1.7.

Table 11: Cross-sections for SM  $ssWW$  signal and background samples.

Process	Final state	Cross-section [fb]
ssWW-EW	$l^\pm\nu l^\pm\nu jj$	15.67
$WZ/\gamma^*$ inclusive	$l^\pm\nu lljj$	469.79
ssWW-QCD	$l^\pm\nu l^\pm\nu jj$	12.02

### 9.3 LHC and ATLAS ITk upgrade

The HL-LHC will operate at  $\sqrt{s} = 14$  TeV at a luminosity of up to  $7 \times 10^{34} \text{cm}^{-2} \text{s}^{-1}$ . This leads to an average of  $\langle \mu \rangle = 140$  interactions per bunch crossing. In total,  $3000 \text{fb}^{-1}$  of integrated luminosity will be collected at the experiments.

In the ATLAS Phase-II upgrade [47] a new tracker will replace the current Inner Detector which has a coverage in pseudorapidity of up to  $|\eta| \leq 2.5$ . There are several upgrade scenarios under consideration to extend the silicon tracker, with coverages in pseudorapidity of up to  $|\eta| \leq 4.0$ . Such an extended tracker is assumed to be accompanied by an extension of the muon system. The ATLAS calorimeter system is already capable of reconstructing electrons up to  $|\eta| \leq 4.9$ . However, in the current configuration, there is no tracking possible beyond  $|\eta| = 2.5$ .

For this study, three scenarios were compared:

- *Nominal tracker* or *Bronze Scenario*  $|\eta| \leq 2.7$
- *Medium tracker* or *Silver Scenario*  $|\eta| \leq 3.2$
- *Extended tracker* or *Gold Scenario*  $|\eta| \leq 4.0$

### 9.4 Monte Carlo simulation

#### 9.4.1 Sample generation

For generating the Monte Carlo samples, the MADGRAPH [66] generator interfaced with Pythia [67] for hadronization, parton showering and underlying event modelling was used. The signal process  $W^\pm W^\pm jj$  -EW and the background processes  $W^\pm W^\pm jj$  -QCD and  $WZ/\gamma^* jj$  were generated for  $\sqrt{s} = 14$  TeV. Interference between the  $W^\pm W^\pm jj$  -EW and  $W^\pm W^\pm jj$  -QCD processes were neglected in this study. It was estimated in [63] that the impact would increase the combined cross-section by  $(7 \pm 4\%)$  in the VBS signal phase space.

The cross-sections for the Standard Model signal and background samples are presented in the Table 11.

#### 9.4.2 Upgrade Smearing Functions

The generated truth events were processed with the *Upgrade Smearing Functions* using tag 02-04-01 [68]. The results are based on performance parametrizations which were evaluated using data from a fully simulated ATLAS detector in each of the three considered upgrade scenarios.

For this analysis, electron, muon, jet, and missing transverse energy objects were used. The electron energy is smeared, followed by application of a single electron

trigger efficiency and an ID efficiency. Similarly, the muon  $p_T$  is smeared, and a single muon trigger efficiency and ID efficiency are applied subsequently. Jet energies and  $E_T^{miss}$  are also smeared.

Fully simulated PU events are added event by event, based on the mean PU value specified. In order to minimize processing time, a threshold of PU jet  $p_T > 30$  GeV was applied. There is a separate PU library for each value of  $\langle\mu\rangle$ . After adding the PU, a *track confirmation* tool is implemented to remove PU and hard scattered (HS) jets in the region where track information can be used to identify PU jets. The track confirmation tool only works for jets with  $p_T < 100$  GeV and in the  $\eta$  region which is covered by the tracker. For these studies, a PU jet efficiency of 2% was selected as the nominal working point. As a consequence, the HS jet efficiency is roughly 85% for HS jet  $p_T < 50$  GeV and 90% for HS jet  $p_T < 100$  GeV. Further details can be found in [62].

### 9.4.3 Event selection

The experimental signature of the  $W^\pm W^\pm jj$  -EW scattering includes two high energy isolated leptons of same electric charge, a moderate  $E_T^{miss}$ , and two energetic jets of large invariant mass which are well separated in rapidity.

The lepton selection cuts are:

- Exactly two leptons ( $e^\pm$  or  $\mu^\pm$ ) of same electric charge with transverse momenta  $p_T > 25$  GeV, within pseudorapidity  $|\eta| < 2.7$ ,  $|\eta| < 3.2$ , or  $|\eta| < 4.0$ , depending on the tracker scenario.
- The angular separation between the leptons must fulfil:  $\Delta R_{ll} = \sqrt{(\Delta\phi)^2 + (\Delta\eta)^2} > 0.3$ .
- The invariant mass of the dilepton system must be  $m_{ll} > 20$  GeV.
- A veto on  $Z$  decays in the  $ee$  channel was set:  $|m_{ee} - m_Z| > 10$  GeV.
- A third lepton veto for electrons with  $p_T > 7$  GeV and for muons with  $p_T > 6$  GeV was set.

For the jets, the selection cuts were the following:

- There must be at least two jets with transverse momenta  $p_T > 30$  GeV.
- These two jets must be within pseudorapidity  $|\eta| < 4.5$ .
- The angular separation from the leptons must be  $\Delta R_{lj} > 0.3$ .
- The first two leading jets in  $p_T$  are the "tag jets".
- The separation in pseudorapidity between the two tag jets must be  $|\Delta\eta_{jj}| > 2.4$ .
- The invariant mass of the two tag jets must be  $m_{jj} > 500$  GeV.

Table 12: The EWK selection cuts are listed here as they were used in the cutflow for comparing the number of events after each cut.

Selection Name	Cut	Description
Lepton Sel.	lepton trigger	single lepton trigger
	single lepton sel.	lepton $p_T > 25$ GeV; $ \eta  < 2.7, 3.2, 4.0$ , $N_{lep} = 2$
	dilepton sel.	$\Delta R_{ll} > 0.3$ , $m_{ll} > 20$ GeV, like-sign leptons
	$eeZ$ veto	$ m_{ee} - m_Z  > 10$ GeV
MET Sel.	MET sel.	$E_T^{miss} > 40$ GeV
Jet Sel.	jet $p_T$ sel.	jet $p_T > 30$ GeV, $\Delta R_{lj} > 0.3$
	jet $\eta$ sel.	jet $ \eta  < 4.5$
	jet multiplicity sel.	$N_{jets} \geq 2$
	$ \Delta\eta_{jj} $	$ \Delta\eta_{jj}  > 2.4$
	3 <sup>rd</sup> lepton veto	remove events with $\geq 3$ leptons with $p_T > 6, 7$ GeV
	$m_{jj}$	$m_{jj} > 500$ GeV

On the missing transverse momentum, a cut of 40 GeV is applied.

All cuts listed before comprise the *EWK event selection*. They are summarized in Table 12.

In addition to the selection summarized in Table 12, the track confirmation tool was used to remove PU and HS jets.

Furthermore, a cut on the lepton centrality  $\zeta$ ,  $\zeta > 0$ , was applied. The lepton centrality is defined as

$$\zeta = \min[\max(\eta_{l_1}, \eta_{l_2}) - \min(\eta_{j_1}, \eta_{j_2}), \max(\eta_{j_1}, \eta_{j_2}) - \max(\eta_{l_1}, \eta_{l_2})]. \quad (37)$$

It is applied to select for  $W^\pm W^\pm jj$  -EW scattering using the relative kinematic signature between leptons and jets. This cut allows to obtain a highly pure  $W^\pm W^\pm jj$  -EW sample, but reduces significantly the size of the sample. All plots shown in this section are shown without lepton centrality cut. However, it is listed at the end of the cutflows for comparison.

#### 9.4.4 The significance method

The 3000 fb<sup>-1</sup> of integrated luminosity at the HL-LHC will provide enough data to reduce statistical uncertainties in the physics measurements, making their systematic uncertainties the dominant contribution to their precision. This study assumes an analytical form of the likelihood function  $\mathcal{L}$  defined in [69], where the observed number of events  $n$  follows a Poissonian distribution with a mean of  $S + B$  and is convoluted with a Gaussian distribution to account for the uncertainty on the background estimation.

$$\mathcal{L}(B) = \frac{(S + B)^n}{n!} e^{-(S+B)} \cdot \frac{1}{\sqrt{2\pi}\sigma_B} e^{-(M-B)^2/2\sigma_B^2} \quad (38)$$

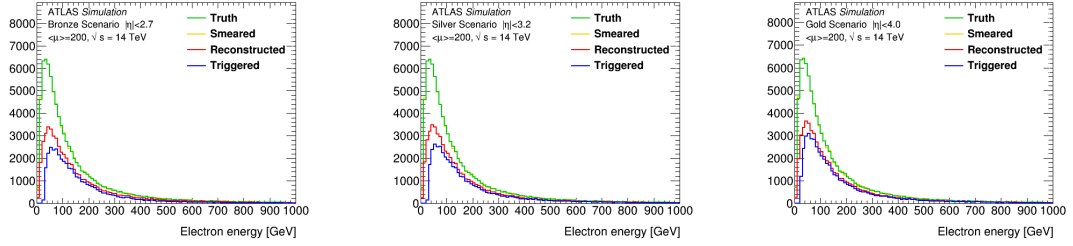


Figure 103: A comparison for smeared and unsmeared objects for the electron energy is shown for the Bronze, Silver, and Gold scenario for  $W^\pm W^\pm jj$ -EW events at  $\langle\mu\rangle = 200$ . After the smearing the trigger and ID efficiencies were also applied which is also shown.

$S$  represents the expected number of signal events,  $B$  is the unknown parameter and represents the expected number of background events, and  $M$  is the measured number of background events following the Gaussian distribution with a known standard deviation  $\sigma_B$ .

Signal significances were computed using  $Z_{\sigma B}$  which can be defined as

$$Z_{\sigma B} = \sqrt{2 \left[ (S + B) \log \left( \frac{S + B}{B_0} \right) + B_0 - S - B \right] + \frac{(B - B_0)^2}{\sigma_B^2}} \quad (39)$$

$$B_0 = \frac{1}{2} \left( B - \sigma_B^2 + \sqrt{(B - \sigma_B^2)^2 + 4(S + B)\sigma_B^2} \right). \quad (40)$$

where  $B_0$  maximises  $\mathcal{L}$  for the tested background-only hypothesis.

In this study, a background uncertainty of 15% was assumed for all calculations. The measurement precision was derived from the significance, assuming the precision is equal to  $1/Z_{\sigma B}$ .

## 9.5 Object validation

Before proceeding with the analysis, several validation studies were done in order to verify the Upgrade Smearing Functions. The smearing of the truth objects and the applied efficiencies were examined. All plots in this section were done with the  $W^\pm W^\pm jj$ -EW sample.

### 9.5.1 Leptons

The lepton objects are smeared according to the Bronze, Silver, and Gold scenarios. Figure 103 shows the smearing of the electron energy for the three scenarios. Figure 104 the smearing of the muon  $p_T$ . The truth values are smeared maintaining the same normalization and then the smeared values are used to apply the trigger and reconstruction ID efficiencies separately.

The electron trigger and reconstruction efficiencies are shown in Figure 105. For muons, the efficiencies are shown in Figure 106. The results are consistent with the expectations.

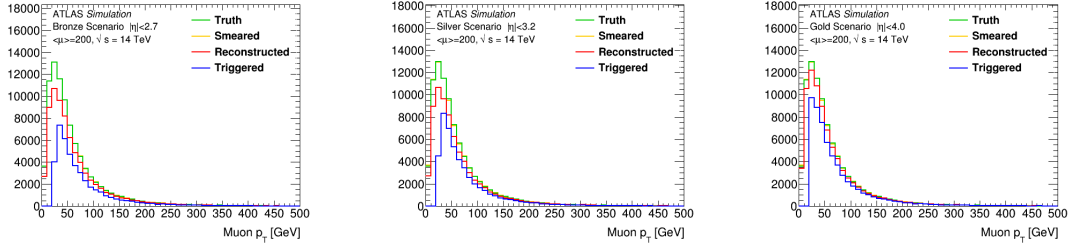


Figure 104: A comparison for smeared and unsmeared objects for the muon  $p_T$  is shown for the Bronze, Silver, and Gold scenario for  $W^\pm W^\pm jj$ -EW events at  $\langle\mu\rangle = 200$ . As for the electron energy, also here the ID and trigger efficiencies were applied to the smeared distributions.

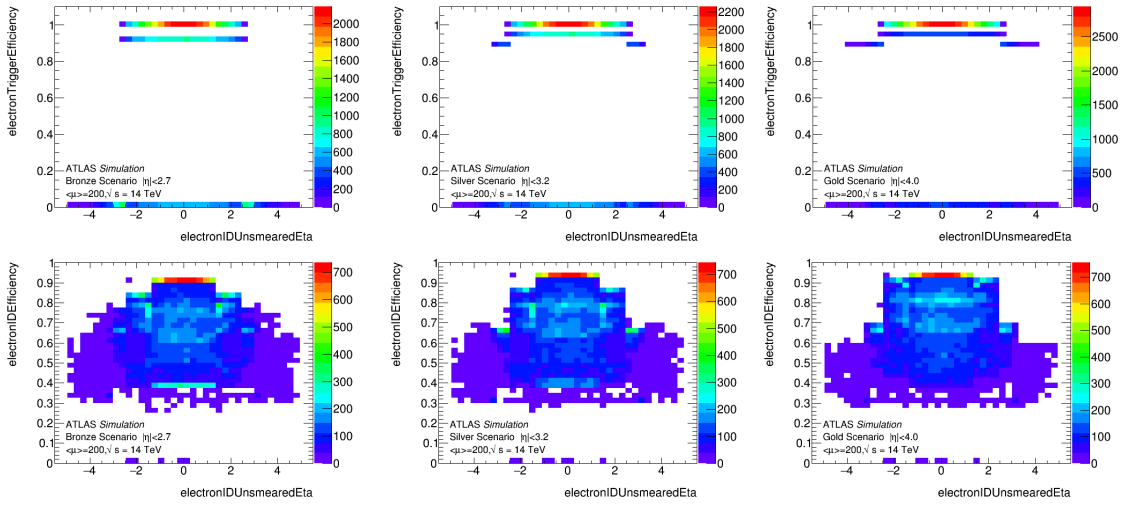


Figure 105: The trigger and ID efficiencies as a function of  $\eta$  are shown for all three scenarios for electrons.

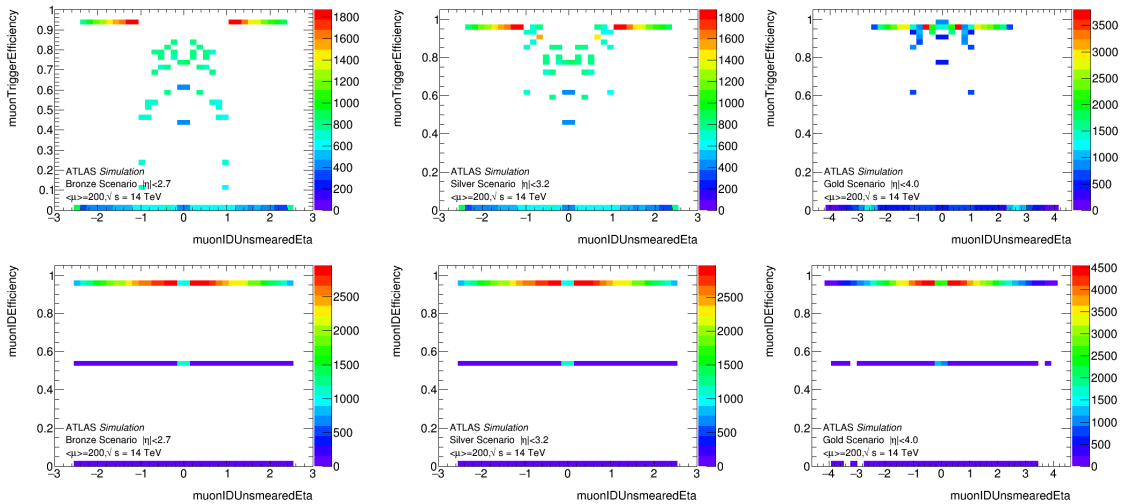


Figure 106: The trigger and ID efficiencies as a function of  $\eta$  are shown for all three scenarios for muons.

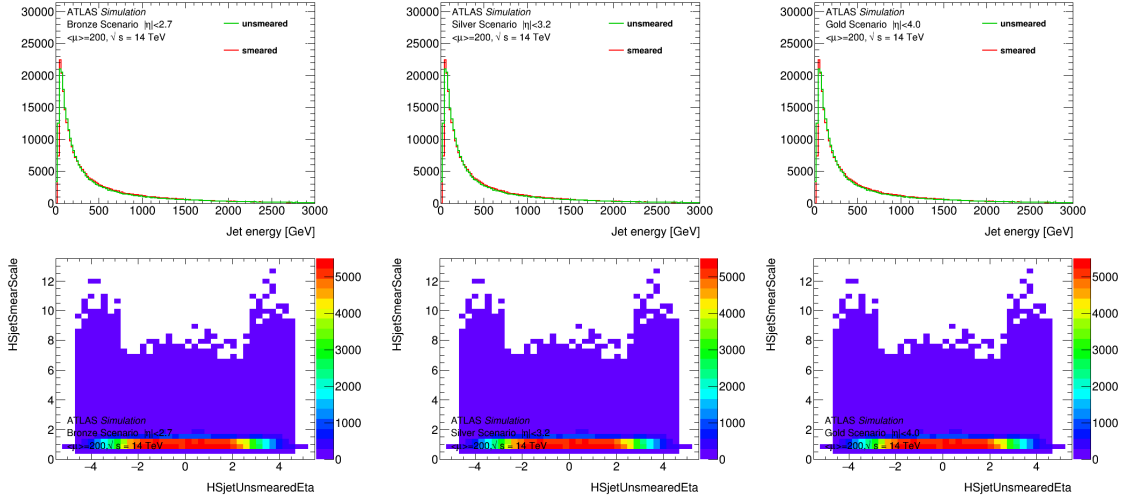


Figure 107: A comparison of smeared and unsmeared objects for the jet energy (top row) for Bronze, Silver, and Gold and the resulting scale factors for each jet as a function of pseudorapidity (bottom row).

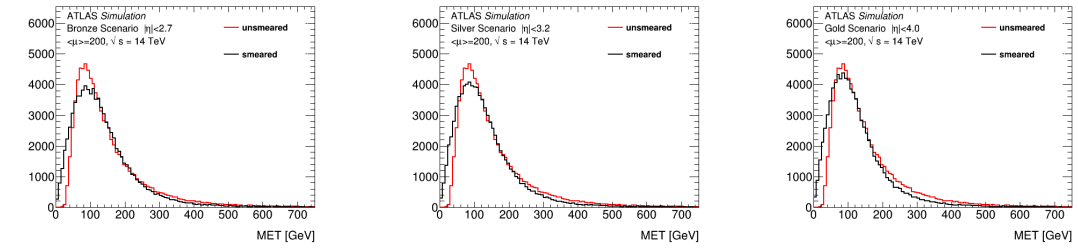


Figure 108: A comparison of smeared and unsmeared objects for the  $E_T^{miss}$  for the Bronze, Silver, and Gold scenarios.

### 9.5.2 Jets and $E_T^{miss}$

The jet energy and  $E_T^{miss}$  were smeared as well. Figure 107 shows the jet energy before and after smearing. Additionally, it shows the effective scale factor which was applied to extract the smeared jet  $p_T$  versus the  $\eta$  of the jet. The jet energy resolution was used to determine the smearing factor.

In Figure 108, the smearing of the  $E_T^{miss}$  is shown.

### 9.5.3 Pile-up subtraction

Extended tracker coverage can improve PU rejection whenever PU identification uses track information. The track confirmation tool for the subtraction of PU jets was implemented in the Upgrade Smearing Functions. It computes the vertices of jets and concludes from these whether a jet is originating from a hard collision or not. It applies an efficiency to remove PU and HS jets. A jet  $p_T$  threshold of 30 GeV was applied to the PU jet collection and a PU efficiency of 2% was applied in the region of the tracker. In Figure 109, the PU and HS jet track efficiencies as



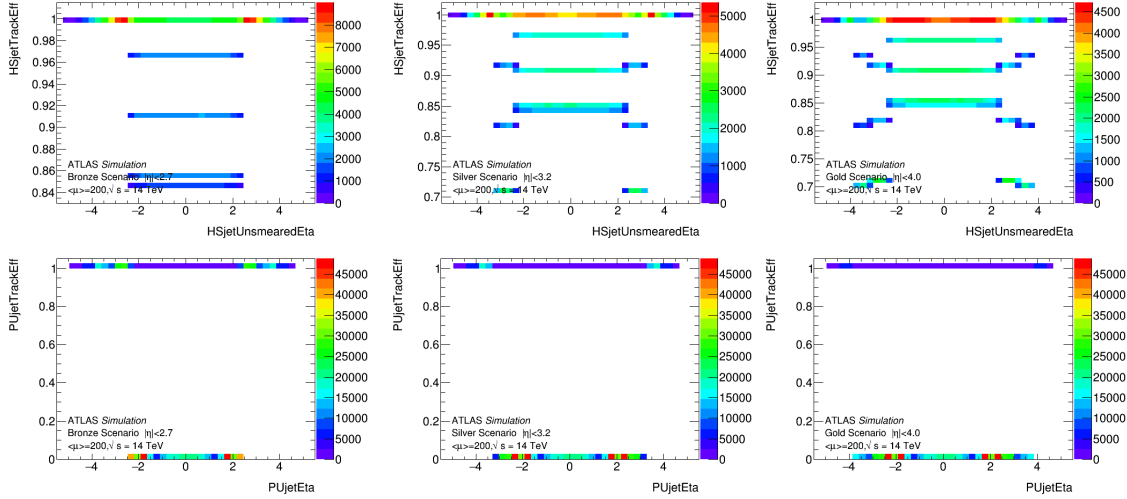


Figure 109: The HS (top row) and PU (bottom row) jet track efficiencies as a function of the jet  $\eta$  are shown for the Bronze, Silver, and Gold scenarios. A cut of  $p_T > 30$  GeV was applied to the PU jets.

a function of jet  $\eta$  are shown for all scenarios.

## 9.6 Performance studies

The performance of the reconstructed physics objects was compared for the Bronze, Silver, and Gold scenarios. The plots shown in this section refer to events before any selection cuts were imposed.

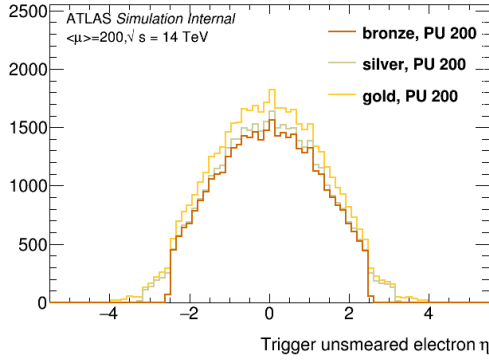
### 9.6.1 Leptons

The main advantage for the performance of the electrons and muons for the three upgrade scenarios arises from the increased acceptance of an extended tracker. The difference is mainly visible in the  $\eta$  distributions and the lower  $p_T$  thresholds. The acceptance for the muons benefits more markedly the Gold scenario where there is an addition of a forward muon spectrometer.

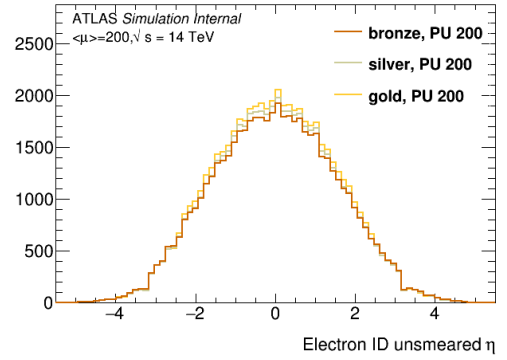
The Figures 110 and 111 show the performance of electrons and muons for the Bronze, Silver, and Gold scenarios for the  $W^\pm W^\pm jj$ -EW sample.

### 9.6.2 Additional leptons

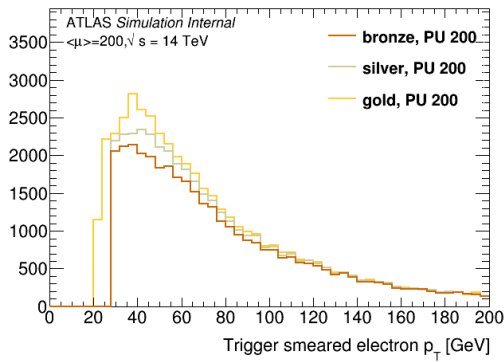
The third lepton veto removes a significant portion of the  $WZ/\gamma^* jj$  background contribution which contains three leptons in the final state. The veto rejects additional leptons defined as any lepton in addition to the two signal leptons that have  $p_T > 6$  GeV (for muons) and  $p_T > 7$  GeV (for electrons). An extended tracker will increase the acceptance for additional leptons leading to a more effective third lepton veto. In Figure 112, the  $\eta$  distribution for the additional leptons with  $p_T > 6$  or 7 GeV is shown.



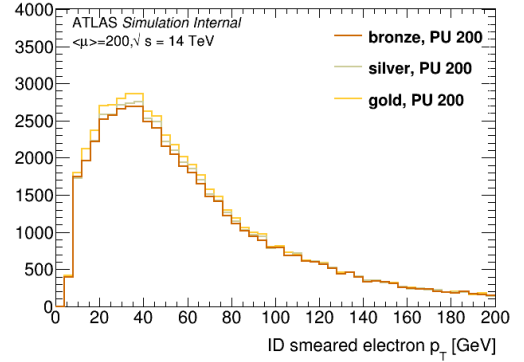
(a)



(b)



(c)



(d)

Figure 110: The  $\eta$  (top row) and  $p_T$  (bottom row) distributions are shown for triggered electrons (left column) and reconstructed (ID) electrons (right column). The plots compare the Bronze, Silver, and Gold scenarios for the  $W^\pm W^\pm jj$ -EW sample.

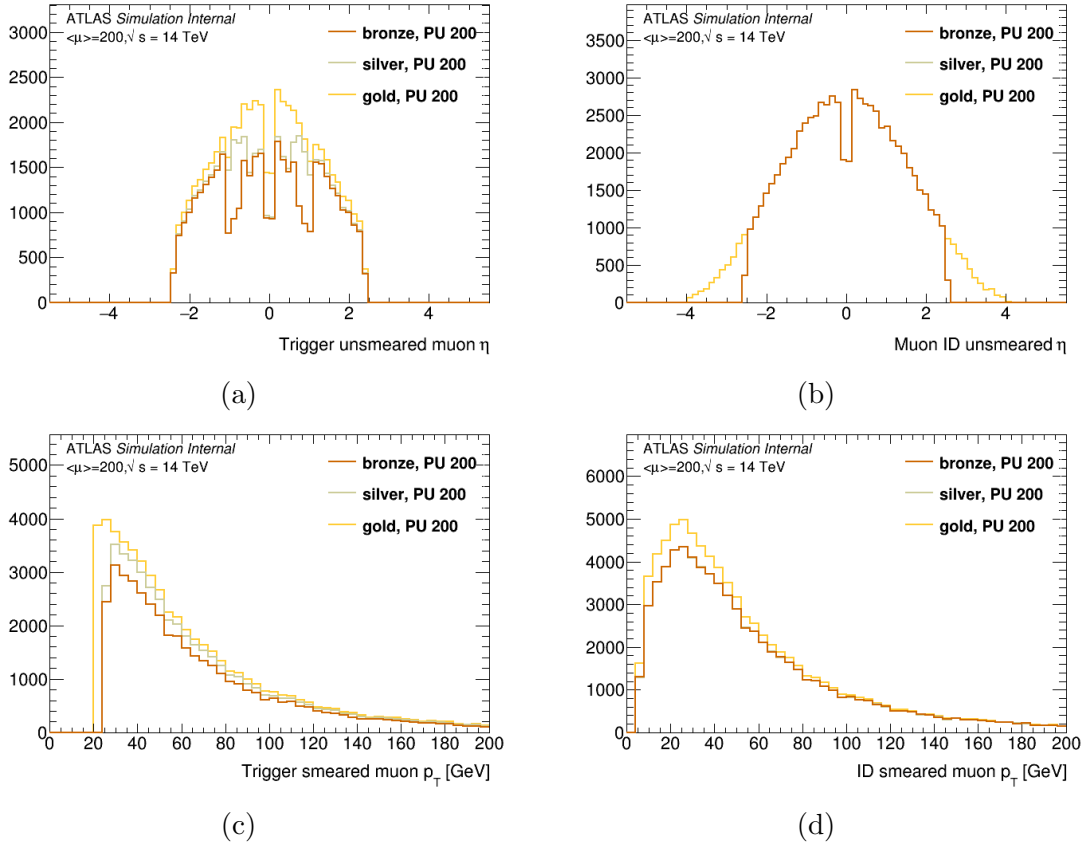


Figure 111: The  $\eta$  (top row) and  $p_T$  (bottom row) distributions are shown for triggered muons (left column) and reconstructed (ID) muons (right column). The plots compare the Bronze, Silver, and Gold scenarios for the  $W^\pm W^\pm jj$ -EW sample.

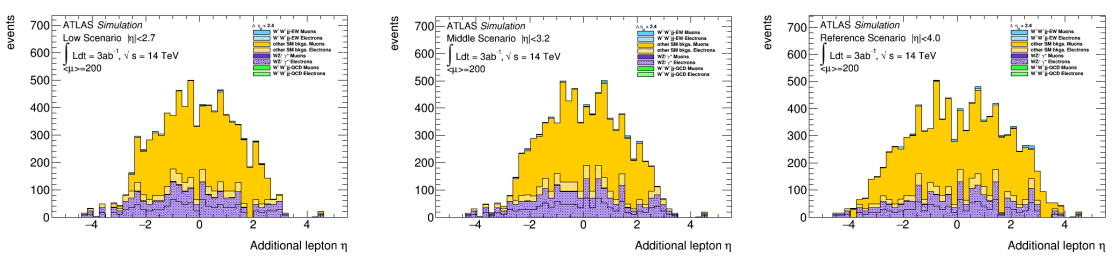


Figure 112:  $\eta$  distribution of additional (third or higher) leptons is shown for muons (electrons) with  $p_T > 6$  (7) GeV for all scenarios for  $\langle\mu\rangle = 200$  after the  $\Delta\eta_{jj}$  cut was applied.

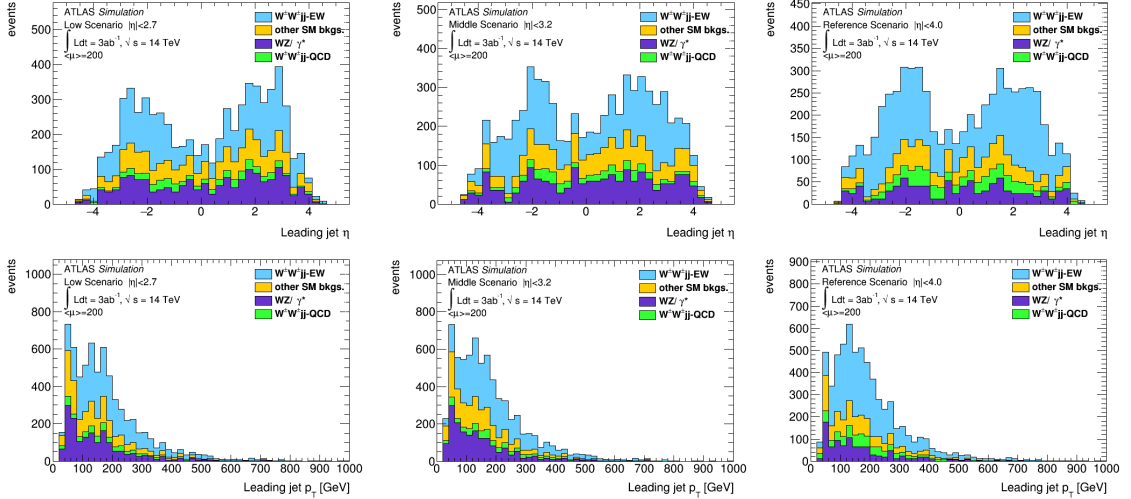


Figure 113: The  $\eta$  (top row) and  $p_T$  (bottom row) distributions of the Bronze, Silver, and Gold scenario for the leading HS jets are shown. The plots compare  $W^\pm W^\pm jj$ -EW,  $W^\pm W^\pm jj$ -QCD and  $WZ/\gamma^*$  events at  $\langle\mu\rangle = 200$ . EWK cuts are applied.

Due to the limited lepton coverage in the Silver and Bronze scenarios the efficiency of suppressing the WZ background through the third-lepton veto is reduced by a factor of  $\approx 2$  with respect to the Gold scenario.

### 9.6.3 Jets

The HS jets barely change for the Bronze, Silver, and Gold scenarios. Figure 113 shows the  $\eta$  and  $p_T$  distribution of the leading HS jets (ordered by  $p_T$ ) after the EWK cuts have been applied. The typical vector boson scattering signature is apparent in the leading jet  $\eta$  distribution. However, the additional jets arising from parton showering are obscuring the signature for the sub-leading jets as shown in Figure 114.

The presence of jets from parton showering is very noticeable in the HS jet multiplicity, as shown in Figure 115. The average number of jets is much greater than the two signature tag jets. In the scope of this analysis it was not planned to mitigate this effect. However, it is expected that an extended tracker will improve the z-vertex resolution and hence the underlying event identification. The possibility of an improved timing resolution may also help in this regard.

### 9.6.4 Pile-up

Jets are crucial to the vector boson scattering signature. Therefore, it is a key part of the analysis that the correct HS jets are identified. At high PU values it gets more difficult to distinguish the HS jets from the PU jets.

Figure 116 shows the PU jet  $\eta$  and  $p_T$  distributions. Figure 117 shows the PU jet multiplicity. The seemingly low jet multiplicity is due to the hard coded jet  $p_T$

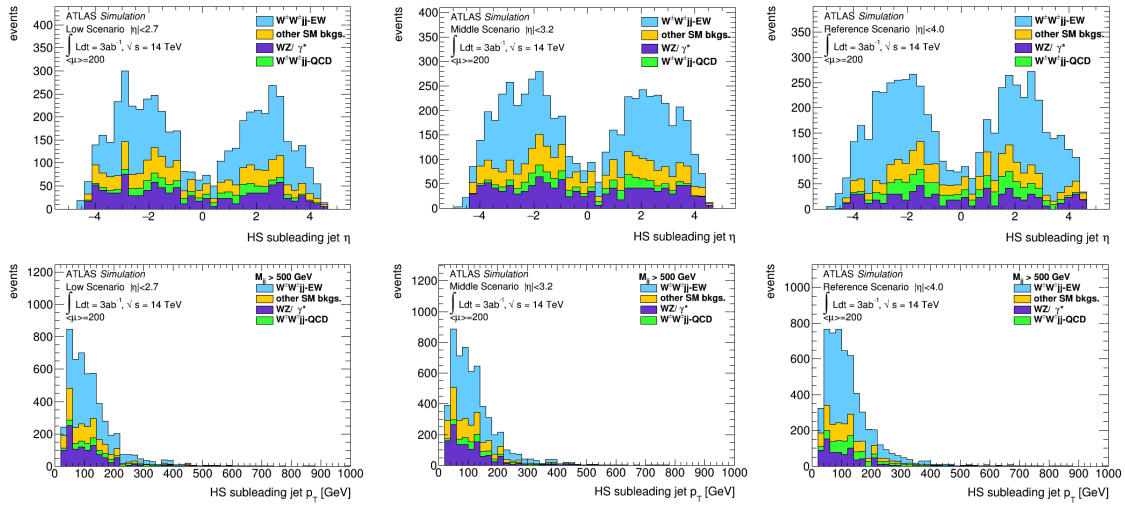


Figure 114: The  $\eta$  (top row) and  $p_T$  (bottom row) distributions of the Bronze, Silver, and Gold scenario for the subleading HS jets are shown. The plots compare  $W^\pm W^\pm jj$ -EW,  $W^\pm W^\pm jj$ -QCD and  $WZ/\gamma^*$  events at  $\langle\mu\rangle = 200$ . EWK cuts are applied.

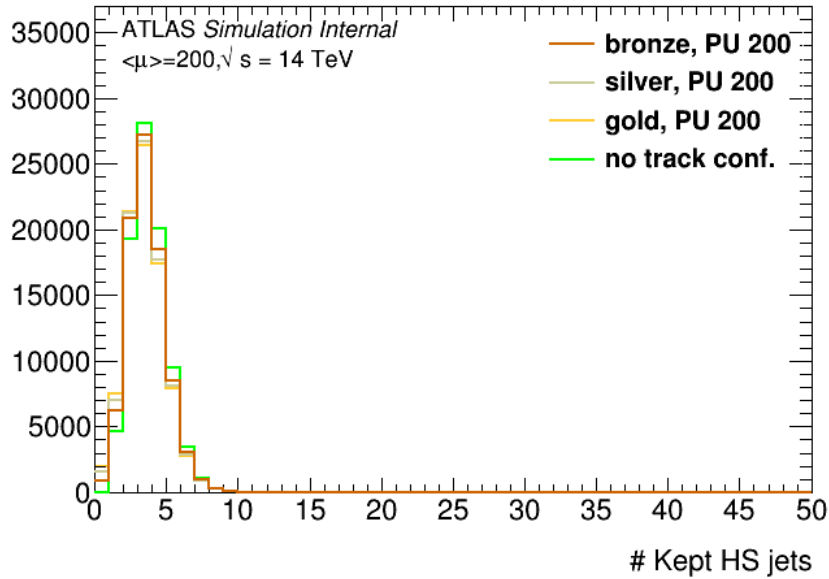


Figure 115: The HS jet multiplicity is shown for the Bronze, Silver, and Gold scenarios for  $W^\pm W^\pm jj$ -EW events. The y-axis indicates the number of events. In addition, the case where there is no track confirmation at all is shown. A jet  $p_T > 30$  GeV cut is applied.

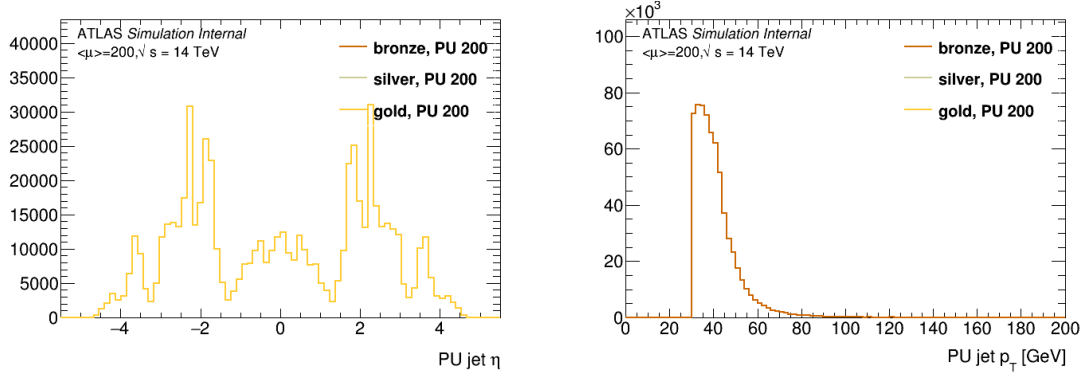


Figure 116: The  $\eta$  and  $p_T$  distributions of the PU jets are shown for the Bronze, Silver, and Gold scenarios for  $W^\pm W^\pm jj$ -EW events. The y-axis indicates the number of events. A jet  $p_T > 30$  GeV cut is applied.

cut of 30 GeV present in the Upgrade Smearing Functions PU overlay, which is part of the track confirmation package.

### 9.6.5 Pile-up suppression

The track confirmation tool plays a key role in enabling the measurement of the impact of the ability to suppress PU jets via track jet information. Several options for PU suppression efficiencies or HS jet efficiencies were available via the track confirmation tool. The overall performance for a PU jet efficiency of 2% is shown in Figures 118 and 119, where the impact of this tool is assessed based on the HS and PU jets, respectively, through the number of jets that are kept and removed by the tool. Figure 120 shows the HS and PU jets that comprise the  $W^\pm W^\pm jj$ -EW events before any cuts are applied (except jet  $p_T > 30$  GeV). The number of PU jets that pass the EWK selection cuts are shown in Figure 121 for the Gold scenario.

## 9.7 Results

The distributions of kinematic variables of Standard Model  $W^\pm W^\pm jj$ -EW events in the Gold, Silver, and Bronze scenarios are shown after the EWK event selection in Figures 122 - 124. Figure 122 shows the leading lepton  $\eta$  distributions for the different tracker scenarios, illustrating the increased acceptance of the Silver and Gold upgrades.

The leading and subleading jet  $\eta$  distributions are shown in Figure 123. The increased contribution of PU and other poorly reconstructed jets is noticeable in the very forward regions especially for the subleading jet.

The lepton centrality  $\zeta$  distributions are shown in Figure 124.

An improvement on the cross-section precision is possible by introducing a cut on the lepton centrality  $\zeta$ . A cut at  $\zeta > 0.0$  was selected to increase the significance, but as seen in Figure 124, it also greatly reduces the number of events.

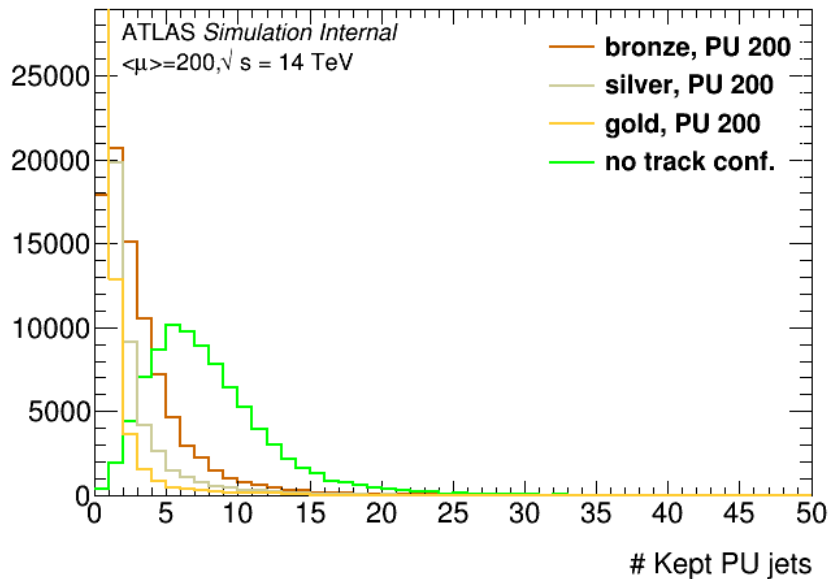


Figure 117: The PU jet multiplicity is shown for the Bronze, Silver, and Gold scenarios for  $W^\pm W^\pm jj$ -EW events. The y-axis indicates the number of events. In addition, the case where there is no track confirmation at all is shown. A jet  $p_T > 30$  GeV cut is applied.

Table 13 shows the event yields after different selection cuts for the signal and background for the Bronze, Silver, and Gold scenarios.

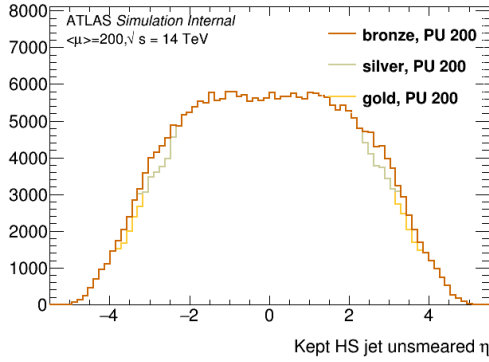
The percent statistical errors are reported, while, as already said, a 15% systematic uncertainty on the background was assumed in the cross-section precision calculation. The precision on a cross-section measurement improves in the Gold tracker scenario compared to the Bronze tracker especially for high PU scenarios as shown in Table 14. A 125% increase in cross-section precision is expected at  $\langle\mu\rangle = 200$  when moving from the Bronze to the Gold scenario.

The precision of the cross-section measurement in the Gold scenario is 5.9% and it is reduced in the Silver and Bronze ones to 11% and 13%, respectively. There are two dominant effects causing this deterioration of performance.

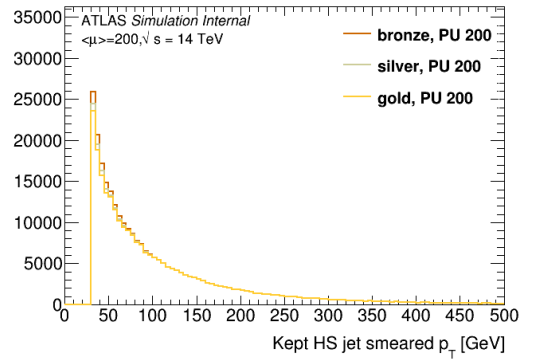
First, the limited lepton coverage in the Silver and Bronze scenarios reduces the efficiency of suppressing the WZ background through the third-lepton veto by a factor of  $\approx 2$  with respect to the Gold scenario.

Second, the limited  $\eta$ -coverage of the tracker in the Silver and Bronze scenarios causes a significant increase of the background with PU jets: the fraction of events where the selected jets originate from PU interactions increases from  $\approx 18\%$  in the Gold scenario to  $\approx 23\%$  ( $\approx 27\%$ ) in the Silver (Bronze) one.

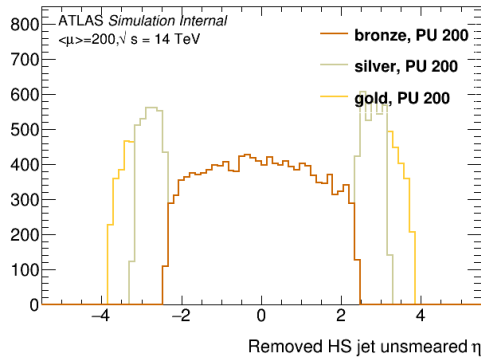
In conclusion, there is a clear correlation between the extension of the tracker and the precision of the measurement. Additionally, in the Gold scenario the cross-section measurement is more than twice as precise as in the Bronze scenario [62].



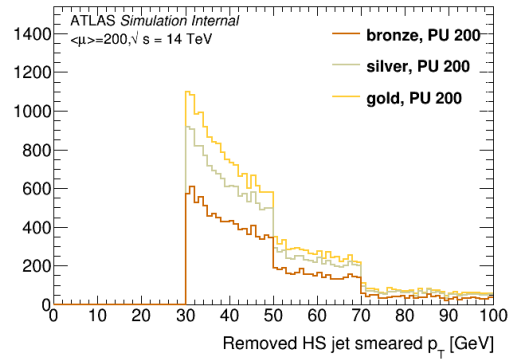
(a)



(b)



(c)



(d)

Figure 118: The  $\eta$  (left column) and  $p_T$  (right column) distributions of the HS jets are shown for the HS jets *kept* by the track confirmation tool (top row) and *removed* by the tool (bottom row). The y-axis indicates the number of events. The plots compare the Bronze, Silver, and Gold scenarios for the  $W^\pm W^\pm jj$ -EW sample.



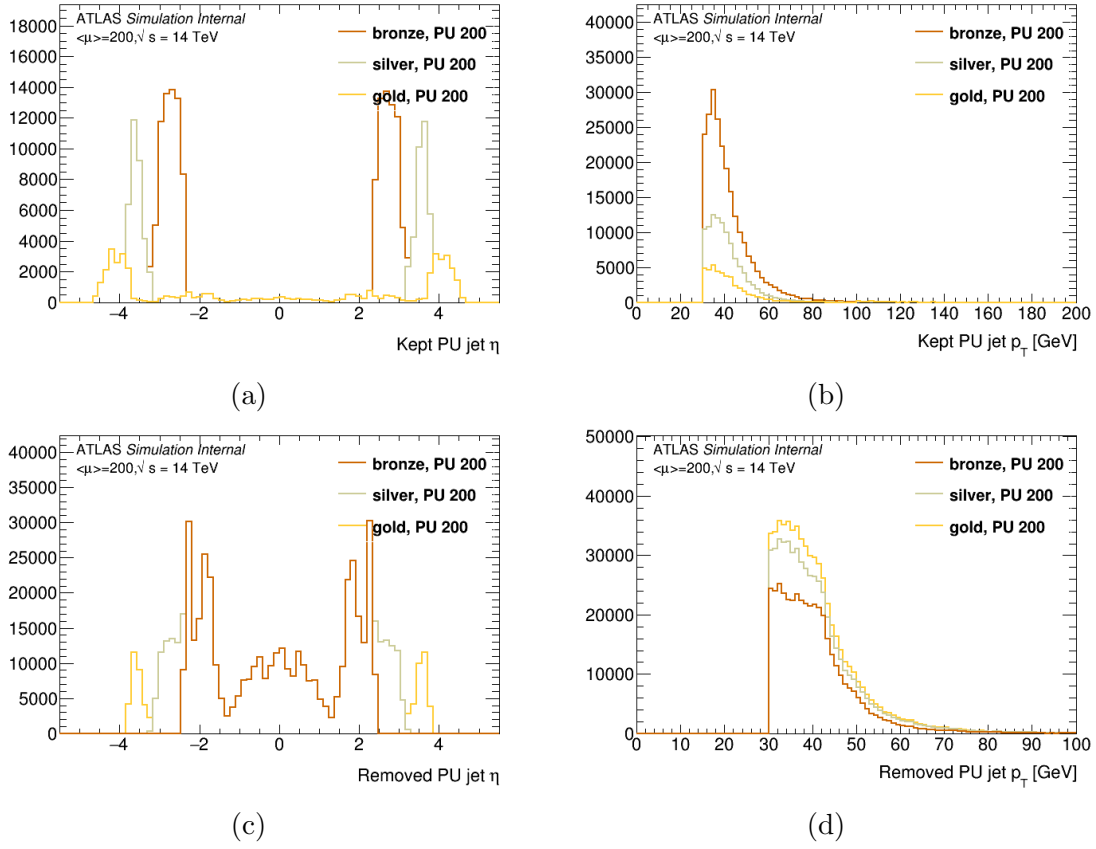


Figure 119: The  $\eta$  (left column) and  $p_T$  (right column) distributions of the PU jets are shown for the PU jets *kept* by the track confirmation tool (top row) and *removed* by the tool (bottom row). The y-axis indicates the number of events. The plots compare the Bronze, Silver, and Gold scenarios for the  $W^\pm W^\pm jj$ -EW sample.

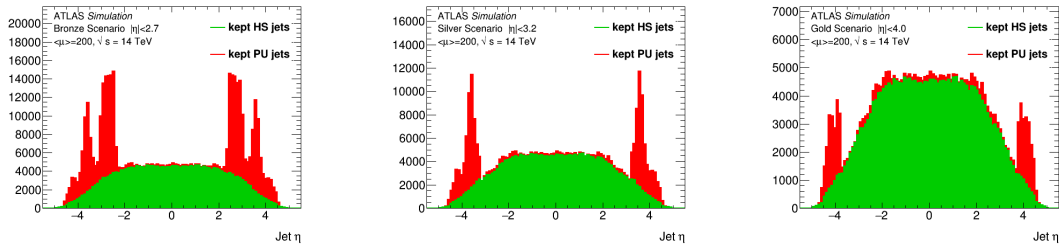


Figure 120: The  $\eta$  distribution of HS and PU jets is shown for the three scenarios for  $W^\pm W^\pm jj$ -EW events. The y-axis indicates the number of events.

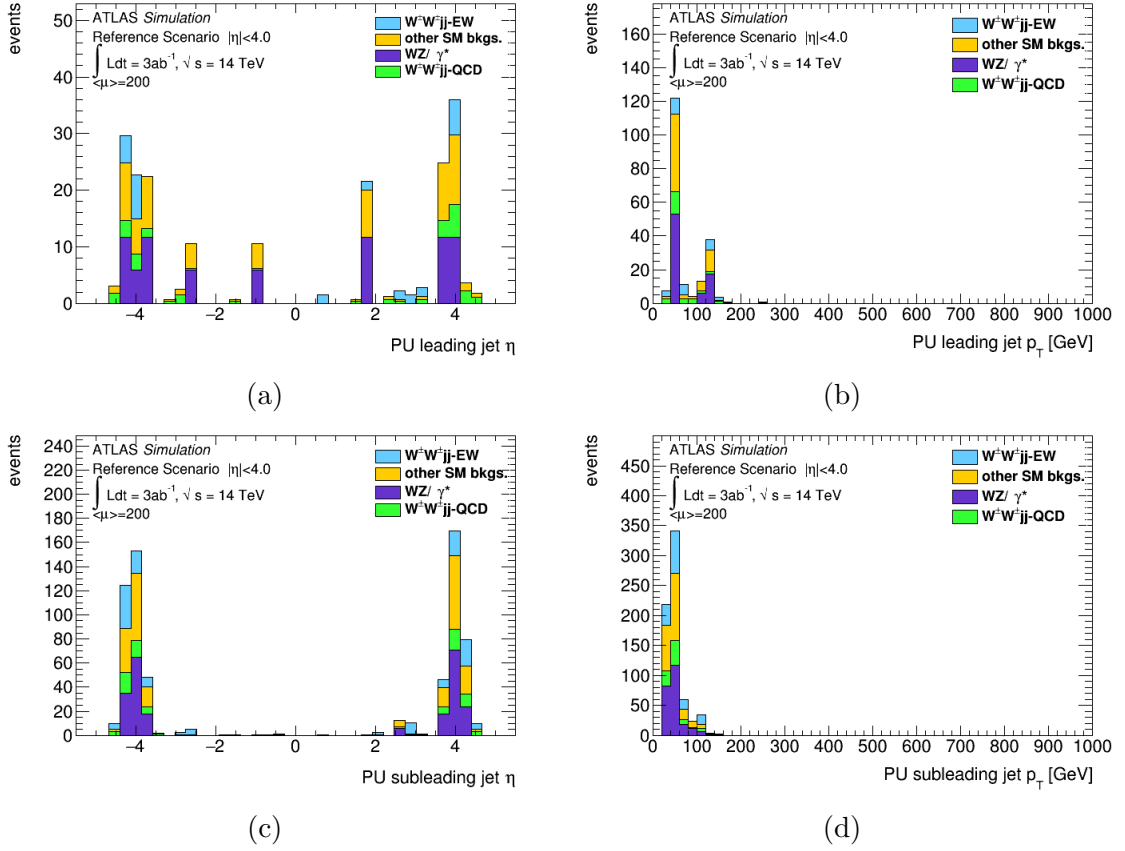


Figure 121: The  $\eta$  (left column) and  $p_T$  (right column) distributions of the tag jets are shown for events where there is a PU jet mistaken as the leading jet (top row) or subleading jet (bottom row). The plots show the Gold scenario for the  $W^\pm W^\pm jj$ -EW sample with the analysis cuts applied for the signal region.

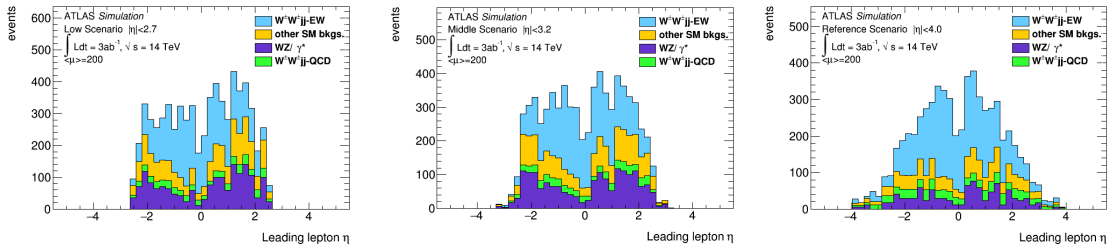


Figure 122: The leading lepton  $\eta$  distribution is shown for the three scenarios for  $W^\pm W^\pm jj$ -EW events with the EWK selection.

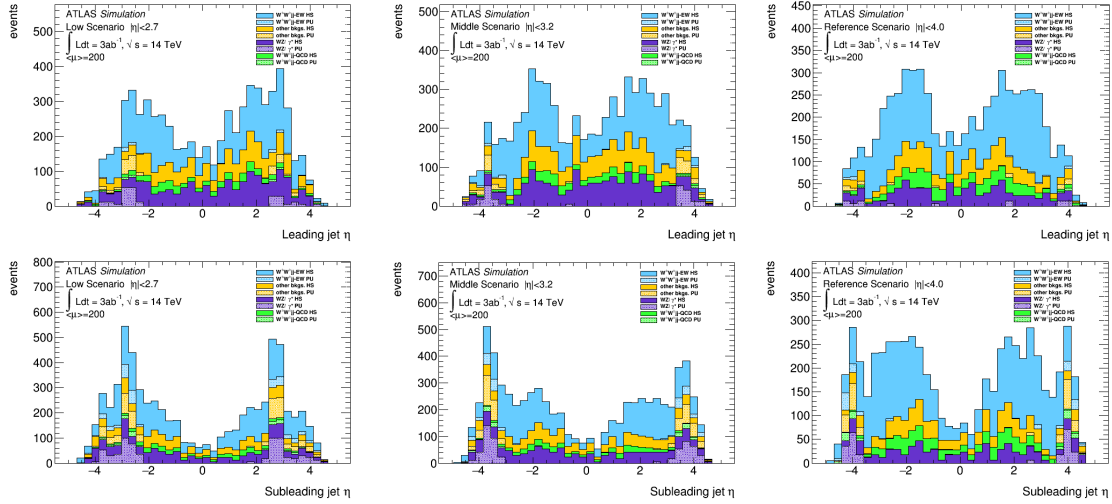


Figure 123: The leading (top row) and subleading (bottom row) jet  $\eta$  distributions are shown for the Bronze, Silver, and Gold scenarios with the EWK cuts applied.

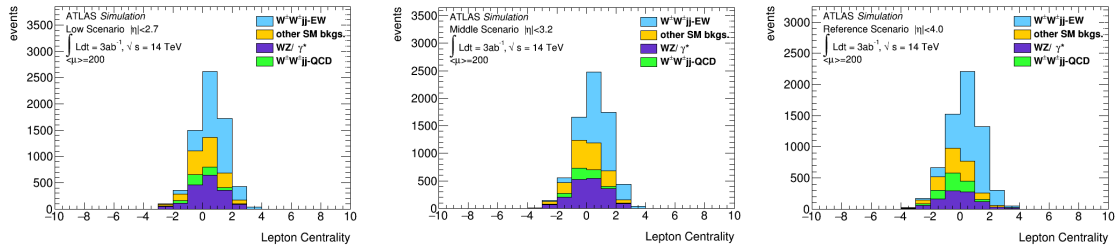


Figure 124: The lepton centrality  $\zeta$  distributions for the Bronze, Silver, and Gold scenarios with the EWK selection applied.

Table 13: The signal and background event yields and the corresponding significances are given for signal,  $W^\pm W^\pm jj$ -EW, and background,  $(WZ\gamma^* + W^\pm W^\pm jj$ -QCD)  $\cdot 1.7$  for  $\int \mathcal{L} dt = 3ab^{-1}$  for the Bronze, Silver, and Gold scenario. Only statistical errors are reported.

Cut	Bronze scenario		Silver scenario		Gold scenario	
	Signal	Background	Signal	Background	Signal	Background
Preselection	47035	2.45725e+06	47034.8	2.45725e+06	47035	2.45725e+06
Trigger	32191	1.27223e+06	34640	1.37247e+06	37946	1.55412e+06
LeptonSelection	15218	633415	16485	689574	18811	788241
DileptonSelection	14977	195520	16223	213633	18530	250279
METCut	13688	172792	14737	186505	16642	214108
JetPtCut	4330	51967	4426	50086	4878	54529
JetEtaCut	4314	51908	4405	49995	4840	54386
nJetsCut	4314	51908	4405	49995	4840	54386
DeltaEta,jj	2826	20153	2951	18956	3175	18362
ThirdLepVeto	2753	6498	2877	6241	3089	4299
Mjj	2311	3665	2447	3497	2634	2419
LepCntr	1946	2523	2011	2104	2061	1124

Table 14: The precision on the measurement of the Standard Model  $W^\pm W^\pm jj$ -EW cross-section is shown for the Bronze, Silver and Gold scenarios. The EWK event selection is used with the addition of a cut on the lepton centrality,  $\zeta > 0.0$ . The results are shown for  $\sqrt{s} = 14$  TeV and  $\int \mathcal{L} dt = 3ab^{-1}$  for  $\langle \mu \rangle = 200$ . Only statistical errors are reported. The precision is estimated by  $1/Z_{\sigma B}$ . A 15% systematic uncertainty is used in the cross-section precision calculation [70].

	Bronze	Silver	Gold
	$ \eta  < 2.7$	$ \eta  < 3.2$	$ \eta  < 4.0$
Significance $Z_{\sigma B}$	$5.0 \pm 0.2$	$6.1 \pm 0.3$	$11.3 \pm 0.6$
$\Delta\sigma/\sigma$	5.9%	11%	13%

## 10 Conclusions

After the successful installation of the demonstrator, it became a useful tool for testing the Phase-I upgrade electronics on the ATLAS detector. After first tests were done in order to ensure that the system was operating in a proper way, it was running in parallel with the ATLAS legacy readout during proton-proton and heavy ion collisions of the LHC. After the system was calibrated, the first physics objects could be identified by event-by-event comparison with the main readout.

Further work has to be done in order to fully automatize data taking with the upgrade system. Additionally, the back end firmware has to be further tested and stabilized in order to guarantee faultless data taking after replacing the whole ATLAS readout with the new system (Run 3).

The same-sign  $WW$  Vector Boson Scattering results were published in the Scoping Document for the Phase-II upgrade of ATLAS and were encouraging the extension of the upgraded tracker, the ITk, to  $\eta = 4.0$ .

The analysis is also a useful tool in order to evaluate the effect of a possible additional PU jet suppression in the forward region. There are many possible upgrades for Phase-II to be considered as the sFCal detector [62, p. 84] and the High Granularity Timing Detector (HGTD) [62, p. 91] which would mitigate PU jets in the forward region.

With an additional sFCal detector, the current performance in the forward region could be maintained or improved. The improvements would come from an increase in the readout granularity in this region, with a consequent improvement in the  $\eta$  and  $\phi$  resolutions for clusters of calorimeter cells. This would help to see the jet substructure and would lead to a reduced pile-up contribution per cell, which will help with pile-up mitigation strategies.

The pile-up conditions expected at the HL-LHC will significantly degrade the calorimeter performance in the region  $|\eta| > 2.5$ . This is caused mainly by the increase of the total noise in individual readout channels. Instrumenting the forward region with a high-granularity detector like the HGTD having an intrinsic time resolution on the order of a few tens of pico-seconds is a way to mitigate these pile-up effects. Precision timing would allow the association of clusters in the calorimeter to a small area around the primary vertex. A combination of timing and precision position information would enable ATLAS to develop algorithms for local pile-up subtraction on an event-by-event basis.

This analysis will be an easily adjustable tool in order to prove or disprove whether the significance improves with PU jet suppression in a certain region.

The discovery potential for new physics can also be evaluated in an effective field theory framework for the anomalous quartic gauge coupling parameter  $f_{T,1}$  [71].

## References

- [1] S. L. Glashow. *Partial-Symmetries of Weak Interactions*. 1961. Nuclear Physics 22, nr. 4, 579–588.
- [2] A. Salam. *Elementary Particle Theory*. 1968. Almqvist and Wiksell.
- [3] S. Weinberg. *A Model of Leptons*. 1967. Phys. Rev. Lett. 19, 1264–1266.
- [4] ATLAS Collaboration. *Observation of a new particle in the search for the Standard Model Higgs boson with the ATLAS detector at the LHC*. 2012. Phys. Lett. B 716, 1–29.
- [5] CMS Collaboration. *Observation of a new boson at a mass of 125 GeV with the CMS experiment at the LHC*. 2012. Phys. Lett. B 716 30.
- [6] L. Evans and P. Bryant. *LHC Machine*. 2008. Journal of Instrumentation 3, nr. 11, S08001.
- [7] The ALICE Collaboration. *The ALICE Experiment at the CERN LHC*. 2008. Journal of Instrumentation 3, nr. 08, S08002.
- [8] The LHCb Collaboration. *The LHCb Detector at the LHC*. 2008. Journal of Instrumentation 3, nr. 08, S08005.
- [9] The CMS Collaboration. *The CMS Experiment at the CERN LHC*. 2008. Journal of Instrumentation 3, nr. 08, S08004.
- [10] *Worldwide LHC Computing Grid*. <http://wlcg-public.web.cern.ch/>. Accessed: 2016-05-20.
- [11] *LHC/HL-LHC Plan*. [http://acceleratingnews.web.cern.ch/sites/acceleratingnews.web.cern.ch/files/pictures/issue%2012/new\\_timeplan\\_24Sept2014%20big.png](http://acceleratingnews.web.cern.ch/sites/acceleratingnews.web.cern.ch/files/pictures/issue%2012/new_timeplan_24Sept2014%20big.png). Accessed: 2016-03-10.
- [12] ATLAS Collaboration. *Studies of the performance of the ATLAS detector using cosmic-ray muons*. 2011. Eur.Phys.J. C71, 1593 arXiv:1011.6665.
- [13] ATLAS Inner Detector Collaboration. *ATLAS Inner Detector: Technical Design Report*. Number CERN-LHCC-97-016. ATLAS-TDR-4. Geneva, 1997.
- [14] ATLAS Pixel Collaboration. *ATLAS Pixel Detector Technical Design Report*. Number CERN-LHCC-98-013. ATLAS-TDR-11. Geneva, 1998.
- [15] ATLAS SCT Collaboration. *ATLAS Semiconductor Tracker Technical Design Report*. 1997. Nuclear Instrumentation Methods A409 161–166.
- [16] ATLAS TRT Collaboration. *ATLAS Transition Radiation Tracker (TRT) proportional drift tube: Design and performance*. 2008. JINST 3 P02013.

- [17] ATLAS Collaboration. *ATLAS Insertable B-Layer Technical Design Report*. Number CERN-LHCC-2010-013 ; ATLAS-TDR-19. Geneva, 2010.
- [18] Tomasz Hemperek. *The FE-I4 Pixel Readout System-on-Chip for ATLAS Experiment Upgrades*. <https://indico.cern.ch/event/83060/contributions/2101686/attachments/1069923/1525755/FE-I4.pdf>. Accessed: 2016-09-02.
- [19] ATLAS Collaboration. *ATLAS Calorimeter Performance Technical Design Report*. Number CERN/LHCC/96-40. Geneva, 1997.
- [20] ATLAS Muon Collaboration. *ATLAS Muon Spectrometer Technical Design Report*. Number CERN/LHCC/97-22. Geneva, 1997.
- [21] F. Bauer et al. *Construction and test of MDT chambers for the ATLAS muon spectrometer*. Number JINST 461 no. 1–3, 17 – 20. 8th Pisa Meeting on Advanced Detectors. 2001.
- [22] J. Wotschack. *ATLAS Muon Chamber Construction Parameters for CSC, MDT, and RPC chambers*. Number Tech. Rep. ATL-MUON-PUB-2008-006. ATL-COM-MUON-2008-008, CERN, Geneva, Back-up document for the ATLAS Detector Paper. 2008.
- [23] A. Dos Anjos, M. Abolins, S. Armstrong, J. T. Baines, M. Barisonzi, H. P. Beck, C.P. Bee, M. Beretta, M. Biglietti, and R. Blair et al. *The second level trigger of the ATLAS experiment at CERN's LHC*. Number IEEE TRANSACTIONS ON NUCLEAR SCIENCE, VOL. 51, NO. 3. June 2004.
- [24] H-P. Beck, C.P. Bee, C. Boissat, M. Caprini, P-Y. Duval, F. Etienne, R. Ferrari, D. Francis, F. Hemmer, and R. Jones et al. *The ATLAS event filter*. Number HAL Id: in2p3-00011494. May 2002.
- [25] ATLAS Collaboration. *ATLAS High-Level Trigger, Data Acquisition and Controls Technical Design Report*. Number ATLAS TDR-016. Geneva, Oct 2003.
- [26] Will Buttinger. *The ATLAS Level-1 Trigger System*. Number Journal of Physics: Conference Series 396, 012010. 2012.
- [27] C. Fabjan and F. Gianotti. *Calorimetry for particle physics*. 2003. Rev.Mod.Phys. 75 1243–1286.
- [28] ATLAS Liquid Argon Collaboration. *Liquid Argon Calorimeter Technical Design Report*. Number ATLAS-TDR-2 ; CERN-LHCC-96-041. Geneva, 1996.
- [29] M. Aleksa et al. *ATLAS Liquid Argon Calorimeter Phase-I Upgrade Technical Design Report*. Number CERN-LHCC-2013-017. ATLAS-TDR-022. Geneva, Sep 2013. Final version presented to December 2013 LHCC.

- [30] R. Wigmans. *Calorimetry: Energy Measurement in Particle Physics*. Number Clarendon Press, Oxford. 2000.
- [31] B. Rossi. *High Energy Particles*. 1952. Prentice-Hall, Inc., Englewood Cliffs, NJ.
- [32] Particle Data Group. *Review of Particle Physics, Physical Review D*. 2002.
- [33] *Gamma ray*. [https://en.wikipedia.org/wiki/Gamma\\_ray](https://en.wikipedia.org/wiki/Gamma_ray). Accessed: 2016-02-04.
- [34] Particle Data Group. *Review of Particle Physics*. Number Physical Review D. 2002.
- [35] C. Charlot. *Electron/Photon identification in ATLAS and CMS*. 2007. arXiv:0709.2479 [physics.data-an].
- [36] H. Zhang. *The ATLAS Liquid Argon Calorimeter: Overview and Performance*. 2011. Journal of Physics: Conference Series 293 no. 1, 012044.
- [37] ATLAS Liquid Argon Collaboration. *Drift time measurement in the ATLAS liquid argon electromagnetic calorimeter using cosmic muons*. 2011. J.Phys.Conf.Ser. 293 012050.
- [38] N. J. Buchanan et al. *Design and implementation of the Front End Board for the readout of the ATLAS liquid argon calorimeters*. 2008. Journal of Instrumentation 3, no. 03, P03004.
- [39] ATLAS Liquid Argon Back End Electronics Collaboration. *ATLAS liquid argon calorimeter back end electronics*. 2007. Journal of Instrumentation 2, nr. 06, P06002.
- [40] G. Perrot. *Installation and Commissioning of the ATLAS Liquid Argon Calorimeter Read-Out Electronics*. 2008. Topical Workshop on Electronics for Particle Physics, pp.215-219.
- [41] ATLAS Collaboration. *Letter of Intent for the Phase-I Upgrade of the ATLAS Experiment*. Number CERN-LHCC-2011-012 ; LHCC-I-020. Geneva, Nov 2011.
- [42] X. Li B. Deng and D. Gong. *A Low-latency and Low Overhead Encoder ASIC for the Serial Data Transmission in ATLAS LAr Calorimeter Readout Upgrade*. 2014. TWEPP 2014: Topical Workshop on Electronics for Particle Physics, Poster.
- [43] ATLAS Collaboration. *ATLAS Detector Control System User Requirements Document*. [http://atlas.web.cern.ch/Atlas/GROUPS/DAQTRIG/DCS/DDC/ddc\\_urd.pdf](http://atlas.web.cern.ch/Atlas/GROUPS/DAQTRIG/DCS/DDC/ddc_urd.pdf), 2000.



- [44] L. Levinson et al. *FELIX: Interfacing the GBT to general purpose networks (ATLAS-TDAQ)*. <http://twiki.cern.ch/twiki/bin/viewauth/Atlas/GBT2LAN>, 2000.
- [45] N. Letendre et al. *IPMC Mezzanine for ATCA boards*. <http://indico.cern.ch/getFile.py/access?contribId=7&resId=0&materialId=slides&confId=180573>.
- [46] Weiming Qian. *ATLAS Level-1 Calorimeter Trigger Upgrade for Phase-I*. 2012. ATL-DAQ-PROC-2012-052.
- [47] ATLAS Collaboration. *Letter of Intent for the Phase-II Upgrade of the ATLAS Experiment*. CERN-LHCC-2011-022. LHCC-I-020.
- [48] Ullrich Pfeiffer. *A Compact Pre-Processor System for the ATLAS Level-1 Calorimeter Trigger*. 1999. Dissertation, Institut für Hochenergiephysik, Universität Heidelberg.
- [49] *Flash ADC*. [https://en.wikipedia.org/wiki/Flash\\_ADC](https://en.wikipedia.org/wiki/Flash_ADC). Accessed: 2016-01-21.
- [50] *Understanding Flash ADCs*. <https://www.maximintegrated.com/en/app-notes/index.mvp/id/810>. Accessed: 2016-01-21.
- [51] ATLAS Collaboration. *ATLAS DAQ, High-Level Triggers and DCS Technical Proposal*. Number CERN-LHCC-2000-17. Geneva, 2000.
- [52] Adriana Milic. *Demonstrator for the ATLAS LAr calorimeter Phase-I Trigger Readout Upgrade*. Geneva, 2015. ATL-LARG-SLIDE-2015-030.
- [53] Pavol Strizenec. *Performance of the ATLAS Liquid Argon Calorimeter after three years of LHC operation and plans for a future upgrade*. 2014. JINST 9 C09007.
- [54] J. Colas et al. *Electronics Calibration Board for the ATLAS Liquid Argon Calorimeters*. 2008. Nuclear Instruments and Methods in Physics Research Section A: Accelerators, Spectrometers, Detectors and Associated Equipment, Elsevier, 593, pp.269-291.
- [55] C. Bee et. al. *The raw event format in the ATLAS Trigger and DAQ*. 2004. ATL-DAQ-98-129.
- [56] W.E. Cleland and E.G. Stern. *Signal processing considerations for liquid ionization calorimeters in a high rate environment*. 1994. Nuclear Instruments and Methods in Physics Research A 338, 467-497.
- [57] W. Walkowiak. *Drift Velocity of Free Electrons in Liquid Argon*. 1999. Atlas internal note, ATL-LARG-99-008.

- [58] D. Banfi, M. Delmastro, and M. Fanti. *Cell response equalization of the ATLAS electromagnetic calorimeter without the direct knowledge of the ionization signals*. 2004. ATL-LARG-2004-007.
- [59] ATLAS Computing Group. *ATLAS Computing Technical Design Report*. Number ATLAS TDR-017, CERN-LHCC-2005-022. Geneva, 2005.
- [60] Walter Lampl. *Optimizing the energy measurement of the ATLAS electromagnetic calorimeter*. 2005. Dissertation, Technische Universität Wien, Fakultät für Physik.
- [61] LAr demonstrator data taking during proton-proton collisions with trigger type 0x90. `file:///home/adriana/Downloads/2016-03-17-demonstrator-analysis-Robert.pdf`, 2016.
- [62] ATLAS Collaboration. *ATLAS Phase-II Upgrade Scoping Document*. 2015. CERN-LHCC-2015-020; LHCC-G-166.
- [63] ATLAS Collaboration. *Evidence for Electroweak Production of  $W^\pm W^\pm jj$  in  $pp$  Collisions at  $\sqrt{s} = 8$  TeV with the ATLAS Detector*. 2014. Phys. Rev. Lett. 113, 141803.
- [64] CMS Collaboration. *Study of vector boson scattering and search for new physics in events with two same-sign leptons and two jets*. 2015. Phys.Rev.Lett. 114, 051801, 1410.6315.
- [65] A. Alboteanu, W. Kilian, and J. Reuter. *Resonances and Unitarity in Weak Boson Scattering at the LHC*. 2008. JHEP 0811 010, doi: 10 . 1088 / 1126 - 6708 / 2008 / 11 / 010, arXiv: 0806.4145 [hep-ph].
- [66] J. Alwall et al. *MadGraph 5 : Going Beyond*. 2011. JHEP 1106 128, url: <http://arxiv.org/abs/1106.0522>.
- [67] T. Sjöstrand, S. Mrenna, and P. Skands. *A Brief Introduction to PYTHIA 8.1*. 2008. Comput.Phys.Commun 178 852–867, url: <http://arxiv.org/abs/0710.3820>.
- [68] *xAOD Analysis in EventLoop*. [https://twiki.cern.ch/twiki/bin/view/AtlasComputing/SoftwareTutorialxAODAnalysisInROOT#How\\_to\\_update\\_to\\_a\\_newer\\_Analysi](https://twiki.cern.ch/twiki/bin/view/AtlasComputing/SoftwareTutorialxAODAnalysisInROOT#How_to_update_to_a_newer_Analysi). Accessed: 2016-05-08.
- [69] G. Cowan. *Discovery sensitivity for a counting experiment with background uncertainty*. <http://www.pp.rhul.ac.uk/~cowan/stat/notes/medsigNote.pdf>, 2012.
- [70] Adriana Milic. *Impact of an Extended ATLAS Tracker on  $W^\pm W^\pm$  Scattering at a High-Luminosity LHC*. Geneva, 2016. ATL-PHYS-SLIDE-2016-084.

- [71] O. Eboli, M. Gonzalez-Garcia, and J. Mizukoshi.  $pp \rightarrow jje^\pm\mu^\pm\nu\nu$  and  $jje^\pm\mu^\pm\nu\nu$  at  $O(\alpha_{em}^6)$  and  $O(\alpha_{em}^4\alpha_s^2)$  for the study of the quartic electroweak gauge boson vertex at CERN LHC. 2006. Phys.Rev. D74 073005.

# Acknowledgements

To carry out the work for this thesis I have been staying at CERN since February 2013. During this time I had the opportunity to meet a lot of people whom I truly enjoyed working with. Without their support I could not have accomplished and completed this work.

First of all, I would like to thank Luis Hervas, who was my CERN thesis advisor. He introduced me to the interesting program of the Phase-I upgrade of the ATLAS LAr calorimeter and gave me the opportunity to work on the ambitious LAr demonstrator project.

I would also like to thank my university advisor Claudia-Elisabeth Wulz for her support, especially during the end phase of this work.

A special thanks goes to Pavol Strizenec, who has lent me a helping hand since the beginning of my PhD and introduced me to the world of the ATLAS offline reconstruction. He was never lacking a few kind words, so, I would not lose my will and motivation for the work.

I would like to explain my deep gratitude to Marco Leite, whom I worked with during the demonstrator tests and my stay in Sao Paolo. He managed to thrill me about my work like no one else during my PhD studies and I enjoyed and learned a lot from the numerous discussions we had.

Jessica Metcalfe has also played a very important role during my time as a PhD student. Apart from being a close friend and advisor, she got me involved in the Scoping document study on same-sign  $WW$  Vector Boson Scattering which allowed me to learn about all steps of an analysis. I am very grateful for having met her during one of the numerous social events at CERN.

I would also like to thank Martin Aleksa, Francesco Lanni, Christopher Marino, and Marc-Andre Pleier who were all excellent advisors and provided a big support during my PhD work.

Christos Anastopoulos, Walter Lampl, Henric Wilkens, and Stefanie Morgenstern, you were all great and helpful office mates.

I also deeply appreciate many great colleagues I met during the work on my PhD. I would like to thank Alessandra Camplani, Yuji Minegishi, Tatsuya Mori, Eleni Mountricha, Laura Pacheco-Rodriguez, and Steffen Stärz, for their collaboration, great company, and a lot of joyful moments.

Above all I would like to acknowledge all the efforts my parents made to ensure that I had an excellent education. I would like to thank them for this and for far more I could possibly describe here.

# Adriana Milic

## *Curriculum Vitae*

---

### Education

- 2016 **Consultant BNL, at CERN, Geneva, Switzerland.**  
Work on prospects for same-sign WW Vector Boson scattering for the ATLAS Phase-II Upgrade  
Advisor: Marc-Andre Pleier (BNL)
- 2013 – 2016 **CERN Doctoral Student, CERN, Geneva, Switzerland.**  
Graduation expected in October 2016 from Technical University of Vienna, Austria  
Advisors: Dr. Luis Hervas (CERN), Prof. Claudia-Elisabeth Wulz (Technical University of Vienna)  
Thesis title: *"Demonstrator System for the Phase-I Trigger Readout Upgrade of the ATLAS Liquid-Argon Calorimeter Readout at the LHC"*
- 2006 – 2012 **Diploma degree in experimental quantum physics.**  
5 year program  
University of Vienna, Vienna, Austria  
Advisor: Prof. Markus Arndt (University of Vienna)  
Thesis title: *"Fluorescence detection of far-field diffraction of large molecules"*

---

### Scholarships

- 2015 **EPLANET scholarship, University of Sao Paolo, Sao Paolo, Brazil.**  
One month stay at University of Sao Paolo, work on upgrade simulation studies for LAr Phase-I Upgrade  
Advisor: Dr. Marco Leite (University of Sao Paolo)
- 2011 **Studentship from HEPHY, High Energy Physics Institute, Vienna, Austria.**  
Two months stay at CERN for work in the SUSY research group of HEPHY  
Advisor: Wolfgang Adam (HEPHY)
- 2010 **Merit scholarship, University of Vienna.**
- 2007, 2008, 2009 **Studentship from IQOQI, Institute of Quantum Optics and Quantum Information, Vienna, Austria.**  
Experimental work in the Quantum Nanophysics & Molecular Quantum Optics group during summer  
Advisor: Prof. Markus Arndt (University of Vienna)

---

## Research Experience

2015-2016 **Analysis of the demonstrator data.**

After establishing a reliable readout system, I took demonstrator data in parallel with the ATLAS readout. I was able to match ATLAS events to demonstrator events and compare them. I worked on the calibration of the demonstrator system and compared the energies of measured showers of the main and the demonstrator readout. I was able to identify the same particles in the same event for the ATLAS and demonstrator readout.

2015-2016 **Hardware on call expert for Liquid Argon (LAr) and on call expert for LAr demonstrator.**

As hardware on call expert my main responsibilities were monitoring the high and low voltage systems and the temperature of the front end electronics. In case of a high voltage trip I ramped the high voltage lines back to their nominal voltage. I was also trained to exchange various power supplies in the electronics cavern. LAr achieved an efficiency of 99.6 % during data taking in 2015 where I played a crucial role with my responsibilities as hardware on call expert.

In addition to the LAr hardware on call duties, I was on call expert for the LAr demonstrator. Due to the unstable system, various interventions during data taking were required such as re-configuring and resetting the readout firmware. I successfully took first data with the demonstrator during stable beam runs despite a technically challenging integration and many instabilities of the demonstrator system.

2015-2016  **$W^\pm W^\pm$  scattering in the  $l^\pm \nu l^\pm \nu jj$  final state study for Phase-II.**

In a team of only two people, I evaluated the potential physics benefits of an extended ATLAS Inner Tracker on the electroweak Vector Boson Scattering via  $W^\pm W^\pm$  scattering in the  $l^\pm \nu l^\pm \nu jj$  final state. I generated the events with MadGraph and produced samples using the official ATLAS generation and reconstruction tools. I was also involved in writing the analysis code and preparing the final results. The outcome showed an improvement by a factor of two for the tracker scenarios to support the extended layout which involves an extension of the Inner Tracker up to  $\eta = 4.0$  and various additional forward detectors which will increase the overall acceptance. Hence, this channel provides a strong argument to expand the plans of the current ATLAS Inner Tracker Upgrade. In addition, I evaluated the possible impact of future detectors like the sFCal and the HGTD on this analysis.

2014-2016 **Installation, testing and data taking of the demonstrator system.**

After the installation of the demonstrator on the detector, I took the first data with the new system and performed the first analysis of the calibration data. I quantified the total noise on the main and trigger readout and performed connectivity checks and further tests to ensure the proper functionality. In September 2015, I was able to establish a sufficiently stable readout system of the demonstrator and take data during physics runs.

2015 **Super shifter for the Calo+Fwd desk.**

My duties as Super shifter included organizing and holding the training of new shifters for Liquid Argon, Tile and Fwd detectors such as LUCID. Furthermore, all documentation for the shifters had to be kept up-to-date. During data taking I interacted with shifters on an almost daily basis to help them with troubleshooting to ensure that good data is taken.

2013-2014 **Test setup for the demonstrator of the LAr Calorimeter Trigger Readout Upgrade for Phase-I.**

LAr opted for installing a demonstrator on ATLAS during the first long shutdown in order to test the performance of the upgraded front end electronics. Before the installation, I thoroughly tested the new components of the front end electronics to ensure that the installation of the new electronics would not have a negative effect on the ATLAS main readout and performance.

I was responsible for data taking of a test bench setup of the upgraded system and its analysis. I verified that the electronics noise level, the coherent noise fraction and the cross-talk among channels on the main and the trigger readout do not increase with the introduction of the new components in the current readout system. I also ensured the proper channel connectivity, and I quantified the linearity and saturation point of the trigger output.

My obtained results were the key to the successful ATLAS prototype review before the insertion of the demonstrator system in ATLAS.

2015-2016 **Bytestream converter for calibrating the demonstrator readout system.**

I adapted the standard bytestream converter package existing in the ATLAS software framework to the new demonstrator readout. For the package to work I had to ensure the compatibility of the demonstrator data format with the ATLAS data format. I changed the code for the converter to cope with the new byte packaging and implemented the new mapping from the LAr calorimeter cells to the readout channels. I could compute the calibration constants for the demonstrator electronics.

---

## Publications

2015 **ATLAS Collaboration**, "*ATLAS Phase-II Upgrade Scoping Document*". CERN-LHCC-2015-020; LHCC-G-166.

I evaluated the potential physics benefits of an extended Inner Tracker on the electroweak Vector Boson Scattering via  $W^\pm W^\pm$  scattering in the  $l^\pm \nu l^\pm \nu jj$  final state. I was involved in every step of the analysis, starting from the generation of the events using MadGraph and the official ATLAS event generation tools through the validation of the parametrization functions up to writing and running the analysis code, and preparing the final results.

2015 **A. Milic**, on behalf of the ATLAS collaboration, "*Radiation Tolerant Electronics and Digital Processing for the Phase-I Readout Upgrade of the ATLAS Liquid Argon Calorimeters*". ANNIMA 2015, ATL-COM-LARG-2015-004.

- 2012 T. Juffmann, **A. Milic**, M. Muellneritsch, P. Asenbaum, A. Tsukernik, J. Tuexen, M. Mayor, O. Cheshnovsky, M. Arndt, *"Real-time single-molecule imaging of quantum interference"*. In: *Nature Nanotechnology* 7, pp. 297-300. doi:10.1038/nnano.2012.34.

I completed the setup, data taking, and data analysis of the experiment. The outcome showed the in-situ built-up of an interference pattern with large, fluorescent molecules which is an important result for evaluating the boarder between the quantum and macroscopic world.

---

## Talks and posters

- Mar 2016 **LHCC meeting March 2016**, CERN.  
Poster: *"Impact of an Extended ATLAS Tracker on  $W^\pm W^\pm$  Scattering at a High-Luminosity LHC"*
- Feb 2016 **Liquid Argon Week**, CERN.  
Talk: *"First results of the Bytestream converter for the LAr demonstrator"*
- Nov 2015 **ATLAS Upgrade Week**, CERN.  
Talk: *"Bytestream converter for the LAr demonstrator"*
- Apr 2015 **ANNIMA 2015, Advancements in Nuclear Instrumentation Measurement Methods and their Applications**, Lisbon, Portugal.  
Talk: *"Radiation Tolerant Electronics and Digital Processing for the Phase-I Readout Upgrade of the ATLAS Liquid Argon Calorimeters"*
- Mar 2015 **LHCC meeting March 2015**, CERN.  
Poster: *"ATLAS LAr Calorimeter Trigger Phase-I Upgrade"*
- Sep 2014 **External Liquid-Argon week**, Marseille, France.  
Talk: *"Installation and current status of the demonstrator for the ATLAS LAr Calorimeter Trigger Phase-I Upgrade"*
- May 2014 **Liquid-Argon week**, CERN.  
Talk: *"Measurements at the EMF for testing the demonstrator for the ATLAS LAr Calorimeter Trigger Phase-I Upgrade"*
- Mar 2011 **DPG conference, German Physical society**, Dresden, Germany.  
Talk: *"Surface based detection schemes for molecular interferometry experiments - implications and possible applications"*
- Feb 2011 **SFB meeting, Foundations and Applications of Quantum Science**, Innsbruck, Austria.  
Poster: *"Fluorescence detection of far-field interference with large molecules"*
- Nov 2010 **atom2010, Atomic Physics Workshop**, Dresden, Germany .  
Poster: *"Fluorescence detection of far-field interference with large molecules"*



---

## Schools and academic training

- Sep 2014 **Danube School on Instrumentation in Elementary Particle & Nuclear Physics**, Novi Sad, Serbia.  
Poster: *"Demonstrator for the ATLAS LAr detector Phase-I Upgrade"*
- Nov 2014 **C++ hands-on training**, CERN.
- Mar 2013 **ATLAS Offline Software Tutorial**, CERN.
- Oct 2011 - **Internship at CERN**, CERN, work on SUSY background estimations in the  
Dec 2011 SUSY research group of HEPHY.

---

## Teaching and outreach

- 2015 **Super shifter for ATLAS Calo+Fwd desk**, Giving shifter trainings to new shifters and supervising them during their first shifts, CERN.
- 2015 **Participation in Serbian Teacher Programme at CERN**, giving guided tours of CERN and ATLAS, CERN.
- 2013 - present **Official ATLAS tour guide**, underground and visitor center, CERN.
- 2009-2011 **Physics lab for nutrition scientists**, Assisting small groups of students in preparing and conducting small experiments, University of Vienna.

---

## Computing skills

Linux, C/C++, Python, SQL, ROOT Framework, Madgraph, ATHENA, LabView, DCS,  $\text{\LaTeX}$

---

## Languages

- Native German, Serbo-Croatian  
Fluent English, Persian, Italian  
Intermediate French, Turkish